New Reactivity, New Mechanisms: Silicon–Chalcogen Bond Formation on Silicon Surfaces

by

Minjia Hu

A thesis submitted in partial fulfillment of the requirements for the degree of

Doctor of Philosophy

Department of Chemistry
University of Alberta

© Minjia Hu, 2020

Abstract

Silicon is the foundation of the electronics industry and is now the basis for a myriad of new hybrid electronics applications, such as sensing, silicon nanoparticle-based imaging and light emission, photonics, and applications in solar fuels. From interfacing of biological materials to molecular electronics, the nature of the chemical bond plays important roles in electrical transport and can have profound effects on the electronics of the underlying silicon itself, affecting its work function, band bending, and surface dipole. When a semiconductor device becomes small (on the nanoscale), the surface:bulk ratio increases dramatically, and thus surface functionalization can dominate the electronic properties.

Much attention has been focused on silicon surfaces functionalized with monolayers bound through Si–C or Si–O bonds, and experimental results have been complemented by many theoretical studies. However, the chemistry of oxygen's chalcogenide cousins, $\equiv$Si$-$E bonds (E = S, Se, and Te), has not been investigated extensively. These $\equiv$Si$-$E bonds could be of significance because the additional electronic states for the heavier atoms (Te versus Se versus S versus O) can affect electron transfer to and from molecules attached to a silicon surface. Furthermore, as is seen in the case of molecular silane chemistry, the chemistry of organochalcogenides on silicon surfaces could offer a variety of reactivity. This dissertation is focused on the formation of Si–E bonds on silicon surfaces via the reaction of hydride-terminated porous or flat silicon with dichalcogenides, the investigation of the mechanism of the reaction, and the quantification of the substitution level.

Hydride-terminated porous Si(100) surfaces were reacted first with a range of organochalcogenide reagents, including di-*n*-butyl disulfide, di-*t*-butyl disulfide, di-*n*-octadecyl disulfide, diphenyl disulfide, diphenyl diselenide, diphenyl ditelluride, and bis(4-chlorophenyl) disulfide, through fast microwave heating (10–15 s) or direct thermal heating (hot plate, 2 min), resulting in the formation of ≡Si−E bonds with low levels of oxidation. The research was followed by the second type of reaction between hydride-terminated flat Si(111) surfaces and dichalcogenides under UV irradiation accompanied by mild heating for 15 min. The mechanism of both types of reactions appears to be radical in nature, involving surface silyl radicals or dangling bonds that react with either the alkyl or aryl dichalcogenide directly or with their homolysis products, the alkyl or aryl chalcogenyl radicals. For the functionalized flat Si(111) surfaces, the coverage and electronic properties were investigated as well. The substitution level of the phenyl chalcogenide derivatives (≡Si−E−Ph) was lower than that of the aliphatic chalcogenide (≡Si−S−*n*-octadecyl) group, most likely due to the fact that the phenyl group blocks the surface Si–H groups and thus sterically prevents them from reacting. The XPS- and UPS-determined electronic properties of ≡Si−E−Ph surfaces, including surface dipoles and work function, did not change significantly compared to those of the starting ≡Si−H surface maybe due to the low level of substitution. The series of chalcogen–silicon bonds, from Si–O, to Si–S, to Si–Se, and now to Si–Te, can be accessed easily and applied to a variety of electronic applications on this semiconductor. The comparison of the errors in estimating the substitution level using the ratio of carbon to silicon versus the ratio of heteroatom to silicon was discussed. It is found that the usage of heteroatoms (F and S) as atomic tags will reduce the error by an order of magnitude in the quantification of the substitution level that resulted from the effect of adventitious carbon.

Preface

Chapter 1 provides a brief introduction to the basic principles of silicon surface chemistry and describes the development and mechanisms of formation of silicon–chalcogen bonds on silicon surfaces. Chapter 2 introduces the chemistry to produce $\equiv$Si$-$E (E = S, Se, and Te) bonds through very fast microwave heating and direct thermal heating via the reaction of hydride-terminated porous silicon surfaces with dialkyl or diaryl dichalcogenides. Chapter 3 describes the formation of $\equiv$Si$-$E bonds on flat Si(111) surfaces initiated by UV light coupled with gentle heating as well as the quantification of the substitution levels of the silicon–hydride on the starting Si(111)–H surface by an organochalcogen via XPS measurement and 2-dimensional stochastic simulation. Chapter 4 studies the quantification of the substitution levels of alkyl-terminated monolayers on flat Si(111) surfaces, using the carbon, fluorine, or sulfur linker atoms as the atomic labels. Chapter 5 summarizes the thesis and proposes several directions for future research.

Chapter 2 is based on the publication "Hu, M.; Liu, F.; Buriak, J. M. Expanding the Repertoire of Molecular Linkages to Silicon: Si–S, Si–Se, and Si–Te Bonds. *ACS Applied Materials & Interfaces* **2016**, *8*, 11091–11099." Dr. Fenglin Liu trained me on the preparation of porous silicon samples and on FTIR measurements and ran the first set of experiments with me. Dr. Cong Jin helped with the determination of the heating profile. I performed the experiments, analyzed the data, prepared the figures, and wrote the first draft. My supervisor, Prof. Jillian M. Buriak, assisted with manuscript writing. All authors have given approval to the final version of the manuscript.

Chapter 3 is based on the publication "Hu, M.; Hauger, T. C.; Olsen, B. C.; Luber,

E. J.; Buriak, J. M. UV-Initiated Si–S, Si–Se, and Si–Te Bond Formation on Si(111): Coverage, Mechanism, and Electronics. *The Journal of Physical Chemistry C* **2018**, *122*, 13803–13814." I carried out the experiments, measured the contact angles, and analyzed the data. Tate C. Hauger measured the UV-Vis spectra of molecules, the resistivity of the silicon wafer, and the intensity of UV light, and made the space-filling model. Brian C. Olsen and Tate C. Hauger helped with AFM image analysis. Dr. Erik J. Luber designed the model and wrote the code for the 2-dimensional stochastic simulations. Tate C. Hauger and Dr. Erik J. Luber derived the equations for the quantification of the substitution levels. Tate C. Hauger, Dr. Erik J. Luber, Brian C. Olsen, and I wrote the initial text draft. Tate C. Hauger and I prepared the figures. All authors contributed to the discussion and text editing.

Chapter 4 also was written as an article. I performed the experiments, analyzed the data, prepared the figures, and wrote most of the draft. Dr. Erik J. Luber derived the formulas for the quantification of the substitution levels. Prof Jillian M. Buriak, Dr. Erik J. Luber, and I contributed to the discussion and text editing.

All X-ray photoelectron spectroscopy (XPS) and ultraviolet photoelectron spectroscopy (UPS) measurements were performed by Dr. Anqiang He and Dr. Shihong Xu in the University of Alberta NanoFAB. Time-of-flight secondary ionization mass spectrometry (ToF-SIMS) measurements also were performed by Dr. Anqiang He.

Acknowledgements

I would like to thank my supervisor, Prof. Jillian Buriak, for her mentorship throughout the five-year graduate studies. I really admire your rigorous attitude towards science and appreciate your support and encouragement. You always stand by our side and have faith in us. You always can discover the highlights of your students even when sometimes we don't realize it.

I am grateful to all Buriak Group lab mates who give me so many good memories during and after work. Special gratitude goes out to Dr. Erik Luber; I would still be lost in the unknown science without your intelligent insight and analysis. Thank you Tate Hauger for always being the first to lend a helping hand when we met any problems. Dr. Fenglin Liu, thank you for taking me into the real world of silicon. Thanks to Brian Olsen for your diverse technical skills. Thank you Dr. Cong Jin for your generous and sincere help even before I entered the university. Thank you Kelli Luber for all your efforts with Jillian to make the team stick together closer.

A very big thank you to the previous and current group members, Dr. Bing Cao, Dr. Jeffrey Murphy, Dr. Lawrence Huck, Jennifer Ozdoba, Dr. Binbin Yu, Dr. Gang He, Dr. Chris Fetterly, Dr. Peter Kalisvaart, Dr. Sayed Youssef Sayed, Chengcheng Rao, Hezhen Xie, Mahmoud Almadhoun, Gayashani Ginige, Dr. Dong Wang, Dr. Delwar Sikder, Yaqi Tu, Dan Yang, Hao Wang, Jasper Woodard, Aaron Kirkey, Oliver Zamponi, and Miriam Fenniri.

I am also grateful to my supervisory committee, Prof. Steven Bergens and Prof. Michael Serpe, and faculty members in the Department of Chemistry, Prof. Jonathan

Veinot, Prof. Mark McDermott, Prof. Eric Rivard, and Prof. Sarah Styler for their guidance and support. I want to thank Prof. Susan Kauzlarich for taking the time to be my external examiner. Thank you Prof. Karl Kopecky for being my defence chair. I am also grateful to the NanoFAB staff, Dr. Anqiang He and Dr. Shihong Xu, for their technical support. Also, thank you Dr. Anna Jordan for the thesis editing. You are such an elegant and thoughtful lady, like my grandma but also like a good friend whom I can share anything with.

Last but by no means least, I must express my very profound gratitude to my parents for their continuous support and encouragement. I should have spent more time with you, my dear dad and mom. My biggest thanks goes to my fiancé, Haoyang Yu. Thank you for always accompanying me to face various challenges in research and life, see all the stars and mountains, and experience the prosperity of the world.

Contents

1 Introduction **1**

1.1 The Interface Is the Device 1

1.2 Flat Silicon and Porous Silicon 3

1.2.1 Flat Silicon 3

1.2.2 Porous Silicon 3

1.3 Hydride-Terminated Silicon Surfaces 6

1.4 Functionalization of Si–H-Terminated Surfaces 9

1.4.1 Radical-Based Chemistry 9

1.4.2 Exciton-Based Chemistry 13

1.4.3 Photoemission 16

1.5 Silicon–Chalcogen Bond Formation 17

1.5.1 Si–E Bond Formation on Silicon Surfaces 17

1.5.2 Radical-Based Mechanisms of Si–E Bond Formation: The Connection Between Molecules and Surfaces 17

1.6 Characterization Techniques for Functionalized 24

1.6.1 Fourier-Transform Infrared Spectroscopy (FTIR) 24

1.6.2 X-Ray Photoelectron Spectroscopy (XPS) 26

1.6.3 Time-of-Flight Secondary Ion Mass Spectrometry (ToF-SIMS) . 27

1.6.4 Contact Angle Measurement 29

1.6.5 Atomic Force Microscopy (AFM) Scribing 30

1.7 Summaries and Outlook 31

2 Direct Thermal and Microwave Initiated Si–E (E = S, Se and Te) Bond Formation 33

2.1 Recent Development in Si−E Bond Formation 33

2.2 Materials and Methods 35

2.2.1 Materials 35

2.2.2 Porous Silicon Preparation 36

2.2.3 Determination of Heating Rate and Profile 36

2.2.4 Reactions with the Dichalcogenides and Thiols 38

2.2.5 Analytical Techniques 39

2.3 Results and Discussion 39

2.3.1 Hydrogen-terminated Surfaces 39

2.3.2 Rapid Silicon−Chalcogen Bond Formation 40

2.3.3 Mechanism 47

2.4 Conclusions 51

3 Coverage, Mechanism, and Electronic Properties of UV-Initiated Si–S, Si–Se, and Si–Te Bond Formation on Si(111) Surface 52

3.1 Introduction 52

3.2 Materials and Methods 54

3.2.1 Materials 54

3.2.2 Flat Si(111)−H Preparation 55

3.2.3 Reactions with Dichalcogenides 55

3.2.4 Estimation of Light Absorption by Molecules Above the Silicon Surface 56

3.2.5 Analytical Techniques 57

3.2.6 Calculation of Silicon Energy Levels 58

3.2.7 Determination of Work Function, Band Bending, and Surface Dipole . . . 58
3.2.8 Simulation . . . 60
3.3 Results and Discussion . . . 61
3.3.1 Silicon–Chalcogen Bond Formation via UV Irradiation and Gentle Heating . . . 61
3.3.2 Determination of Layer Thickness . . . 67
3.3.3 Quantification of Substitution Level of ≡Si–H with ≡Si–ER Groups . . . 72
3.3.4 Calculations of Constants . . . 74
3.3.5 Calculations of Substitution Levels . . . 75
3.3.6 Discussion and Simulation . . . 77
3.3.7 Proposed Mechanism . . . 80
3.3.8 Work Function and Surface Dipoles . . . 82
3.4 Conclusions . . . 86

4 Reevaluating the Quantification of Substitution Level of Monolayers on Silicon Surfaces 87

4.1 Introduction . . . 87
4.1.1 Substitution Levels of Organic Alkyl Monolayers on Si(111) Surfaces . . . 87
4.1.2 Molecular Models . . . 89
4.1.3 Techniques for the Determination of Substitution Levels . . . 92
4.2 Materials and Methods . . . 95
4.2.1 Materials . . . 95
4.2.2 Preparation of Flat Si(111)–H . . . 96
4.2.3 Reactions with Organic Molecules . . . 96
4.2.4 Analytical Techniques . . . 98

4.3 Results and Discussion . . . 98

4.3.1 Functionalized Silicon Surface: Contact Angle Measurements . 99

4.3.2 Functionalized Silicon Surface: XPS . . . 101

4.3.3 ≡Si−CH=CH−$(CH_2)_n$–F Surfaces from Literature . . . 102

4.4 Reconsideration of the Models and Calculations used for XPS-based Determination of Surface Coverage . . . 104

4.4.1 Calculations of Constants . . . 104

4.4.2 Connection between Attenuation Length and Atomic Density . 106

4.4.3 Monolayer with an ω-Fluorine Tag: the ≡Si–$(CH_2)_{11}$–F Surface 107

4.4.4 Monolayers without Heteroatomic Tags: ≡Si–$(CH_2)_n$–CH_3 Surfaces . . . 112

4.4.5 Monolayers with an α-Heteroatom, Surface-Bound Tag: the ≡Si−S−$(CH_2)_{17}$−CH_3 Surface . . . 113

4.4.6 Results and Discussion . . . 115

4.5 Conclusions . . . 118

5 Thesis Summary and Outlook 120

5.1 Summary of Chapters . . . 120

5.1.1 Chapter 1 . . . 120

5.1.2 Chapter 2 . . . 121

5.1.3 Chapter 3 . . . 121

5.1.4 Chapter 4 . . . 122

5.2 Future Work . . . 123

5.2.1 Control of the Electronic Properties of Chalcogenide-modified Silicon Surfaces . . . 123

5.2.2 Monolayer Doping of Silicon Surfaces with Chalcogens for Water Splitting . . . 124

5.2.3 Functionalization of Porous and Flat Germanium Surfaces with Dichalcogenides 126

List of Figures

1.1 (a) A composed scheme of silicon nanocrystals showing tunable photoluminescence via surface functionalization. (Reprinted with permission from ref 1, copyright 2016 American Chemical Society.) (b) A scheme of a single-wire pull-out test of a modified silicon microwire to obtain the interfacial mechanical shear strength. (Reprinted with permission from ref 2, copyright 2015 American Chemical Society.) (c) A scheme of bacterial recognition of silicon nanowire arrays. (Reprinted with permission from ref 3, copyright 2013 American Chemical Society.) (d) Tunable work function of the silicon surface via the choice of the head group or tail group attached to silicon. (Reprinted with permission from ref 4, copyright 2015 American Chemical Society.) 2

1.2 Upper: unit cells of Si(100), Si(110) and Si(111). Lower: the view along the different directions of the diamond cubic lattice. The black marked silicon atoms belong to a particular plane. (Reprinted with permission from ref 5. Copyright 2015 The Electrochemical Society.) 4

1.3 Electrochemical etching system. (a) Silicon sample (working electrode). (b) Reference electrode. (c) Counter electrode, made of Pt. (d) Electrolyte (etchant). (e) An actual cell used for the electrochemical functionalization of porous silicon. 4

1.4 A schematic diagram of a porous silicon sample with an average pore diameter of 60 nm. (Reprinted with permission from ref 6. Copyright 2009 Wiley-VCH.) 5

1.5 Scanning electron microscope (SEM) images of the morphology of porous silicon (100) samples varied by the applied current density. (a) Pore diameter $\sim$95 nm $\pm$ 10 nm, pore distance $\sim$45 nm; (b) Pore diameter $\sim$60 nm $\pm$ 8 nm, pore distance $\sim$50 nm; (c) Pore diameter $\sim$45 nm $\pm$ 10 nm, pore distance $\sim$55 nm; (d) Pore diameter $\sim$25 nm, pore distance $\sim$60 nm. The anodization time was kept constant at 10 min. (Reprinted with permission from ref 7. Copyright 2007 Elsevier.) . 5

1.6 Etching conditions for obtaining (a) a flat Si(100)–H_2 surface, (b) a flat Si(111)–H surface, (c) a porous Si–H_x surface, and (d–e) a hydride-terminated silicon nanoparticle. 7

1.7 ATR-FTIR spectra of a Si(111)–H surface, etched in the 40% NH_4F (aq), taken with both s- and p-polarized IR light. (Reprinted with permission from ref 8. Copyright 1990 American Institute of Physics.) 8

1.8 FTIR spectrum (transmission mode) of a freshly etched porous Si(100) surface. 8

1.9 (a) Photodecomposition of di-*t*-butyl peroxide and the reaction of *t*-BuO· radical with $(Me_3Si)_3SiH$. (b) Reactions of a silyl radical with a silyl radical, halides, alkenes, and carbonyl groups, respectively, from top to bottom. 10

1.10 (a) Decomposition of a radical initiator, a diacyl peroxide, and the reaction between the formed $CH_3(CH_2)_n\bullet$ radical and a hydride-terminated silicon surface. (b) Reaction of the diazonium reagent with a hydride-terminated silicon surface. (c) Cleavage of a Si–H bond under thermal heating. (d) Cleavage of a Si–H bond under UV irradiation. 11

1.11 Reaction of surface silyl radical with alkene. 12

1.12 (a) Decomposition of an alkene under UV light irradiation, forming an alkyl radical. (b) Reaction of the radical with a hydride-terminated silicon surface. 12

1.13 Mechanism for the exciton-mediated hydrosilylation event. 14

1.14 (a) The exciton-based mechanism for an enhanced hydrosilylation rate: electron abstraction by RX from the photogenerated exciton in the porous silicon hole, h^+, in the silicon nanocrystal that then is attacked by the alkene. (b) Energy level diagram showing the approximate positions of the conduction and valence bands in a silicon nanocrystallite and LUMOs of select oxidizing agents. (Reprinted with permission from ref 9. Copyright 2012 American Chemical Society.) 15

1.15 Exciton-driven hydrosilylation on a flat silicon surface involving both radical- and hole (h^+)- based mechanisms. 16

1.16 Reaction of a hydride-terminated silicon surface with an alkene driven by photoemission. 16

1.17 Reactions of molecular (a and b) or surface (c and d) silyl radical with di-*n*-butyl disulfide or sulfide. 18

1.18 (a and b) Reactions of molecular alkyl radicals with dipheneyl disulfide and diphenyl diselenide. (c and d) Reactions of surface silyl radicals with diphenyl disulfide and diphenyl diselenide. 19

1.19 Lack of reaction of a surface silyl radical with di-*t*-butyl disulfide. Steric hindrance between the bulky *t*-butyl group and the surface prevented the reaction from proceeding. 20

1.20 (a and b) Reaction of molecular silyl redicals with indicated Ph–E–alkyl molecules, where E = S and Se. (c) Lack of reaction of the surface silyl radical with phenylethyl sulfide (PhSEt). (d) Reaction of the surface silyl redical with phenylethyl selenide. 21
1.21 Lack of reaction of the surface silyl radical with di-*n*-butyl sulfide (bu–S–bu), diphenyl sulfide (PhSPh), or disphenyl selenide (PhSePh). 21
1.22 (a) Equilibria between thiols and molecular silane. (b) Equilibria between thiols and a hydride-terminated silicon surface. (c) Reaction of a surface silyl radical with 1-octadecanethiol. (d) Direct coupling of a surface silyl radical with a free thiyl radical. (e) Lack of reaction of a surface silyl radical with *t*-butylthiol. 23
1.23 Transmission FTIR spectra of porous silicon samples before and after reaction with the reagent indicated, initiated by 4-bromobenzenediazonium tetrafluoroborate. The spectra on the left show the full mid-IR range, and the spectra on the right show the ν(Si–H_x) region before the reaction (red curve) and after the reaction (black). (Reprinted with permission from ref 10. Copyright 2015 American Chemical Society.) 25
1.24 XPS spectra for a mixed methyl/3,4,5-trifluoropheny-lacetylenyl (MMTFPA)-terminated n-Si(111) surface. (a) Survey spectrum and an inset scheme of the Si(111)-MMTFPA surface. (b–d) High-resolution XPS spectra of C 1s, Si 2p, and F 1s, respectively. (Reprinted with permission from ref 11. Copyright 2016 American Chemical Society.) 27

1.25 Depth-profiled SIMS of porous silicon surfaces before functionalization (red curves) and after reaction. Top: SIMS showing the level of carbon on surfaces functionalized with phenylsilane (black), 4-fluorophenylsilane (green), and 4-fluorophenethyl (pink) groups. Bottom: the signal level of fluorine in a 4-fluorophenylsilane-terminated surface (green) compared to that in a 4-fluorostyrene-reacted surface (pink) and a native, hydride-capped surface (red).(Reprinted with permission from ref 12. Copyright 2006 American Chemical Society.) 29

1.26 Schematic of static and dynamic angles. The static contact angle (a) is measured when a droplet is standing on the surface, while the advancing (b) and receding (c) contact angles are measured when the volume of the droplet is gradually increased or decreased, respectively. 30

1.27 Left: an AFM scribing test. The AFM tip is brought into contact with the surface with a set force and moved across the surface. Right: an example of thickness measurment by AFM scribing on a dodecyl-terminated surface, indicating the film thickness is 1.4 nm thick. (Reprinted with permission from ref 13. Copyright 2005 Elsevier.) 31

2.1 Reaction approach to functionalize silicon. (a) Overall reaction scheme outlining the approach to Si−S, Si−Se, and Si−Te bond formation on silicon surfaces. (b) Seven dichalcogenide molecules that were screened for reactivity under microwave irradiation or direct thermal heating (hot plate) on hydride-terminated porous silicon. 35

2.2 (a) Photo of the microwave irradiation apparatus used for determination of the heating profile (Figure 2.3c). (b) Photo of a glass vial with a small hole drilled in the side to enable the fiber optic temperature probe to be threaded into the interior of the vial and make contact with the silicon sample. For the actual experiments with chalcogenide compounds, a completely sealed vial was used. 37

2.3 (a) Photograph of the microwave heating apparatus, comprised of a microwave for domestic use, a fiber optic temperature probe, and the sample vial residing within the Teflon chamber. (b) Photograph of the direct thermal heating apparatus (hot plate). (c) Temperature profiles for the heating rates of 1.2×1.2 cm^2 porous silicon samples that were heated in the absence of reagents under microwave and direct heating. Temperature profiles were determined on dummy porous silicon samples in the absence of reagents because the vials are sealed to prevent contamination, oxidation, and damage to the polyimide probe. 37

2.4 Top view (left) and cross-section SEM images of freshly prepared porous silicon. 39

2.5 FTIR spectra (transmission mode) of (a) freshly etched unfunctionalized porous silicon and (b–m) porous silicon samples reacted with the chalcogenide reagents for the time indicated under microwave irradiation (left) and hot plate heating (right). Hot plate temperature was set to 250 °C; sample temperature reaches 230 °C. 41

2.6 XPS of porous silicon samples after reaction with (a–h) the disulfide reagents, (i and j) diphenyl diselenide, and (k and l) diphenyl ditelluride under microwave irradiation for the time indicated. The data from this figure and supporting literature references are tabulated in Tables 2.1 and 2.2. 43

2.7 XPS of porous silicon samples after reaction with the reagents under microwave irradiation for the time indicated. 44

2.8 ToF-SIMS analysis of functionalized porous silicon samples. The thick curves represent the porous silicon samples after reaction with (a–d) the disulfide reagents, (e) diphenyl diselenide, and (f) diphenyl ditelluride, all under microwave irradiation for 15 s. The same sample of unfunctionalized porous silicon was used as the comparison (reference sample, dotted line) in all spectra. 46

2.9 ToF-SIMS analysis of functionalized porous silicon samples. The thick curves represent the porous silicon samples after reaction with bis(4-chlorophenyl) disulfide under microwave irradiation for 15 s. The same sample of unfunctionalized porous silicon was used as the comparison (reference sample, dotted line). 47

2.10 Possible mechanisms that could play a role in formation of ≡Si–E bonds (E = S, Se, and Te) on silicon surfaces. (a) Direct homolysis of Si−H bonds by heat, leading to formation of silicon radicals on the surface, and subsequent reaction with a dichalcogenide or a chalcogenyl radical. (b) Scheme for hemolysis of $Si-SiH_3$ bonds on the surface, leading to silicon radicals. (c) Radical-based chalcogenol-silane equilibrium. (d) Homolysis of dichalcogenides, leading to chalcogenyl radical formation. 48

2.11 FTIR spectra of modified porous silicon, prepared with 1-octadecanethiol under microwave irradiation for 15 s and 20 s. 49

2.12 FTIR spectra of modified porous silicon, prepared with *t*-butylthiol under microwave irradiation for 10 s, 15 s, and 20 s. 50

2.13 FTIR spectra of modified porous silicon, prepared with 1-octadecanethiol under heat for 1 min, 2 min, 5 min, and 10 min on the hot plate. 50

2.14 FTIR spectra of modified porous silicon, prepared with *t*-butylthiol under heat for 1 min, 2 min, 5 min, and 10 min on the hot plate. 50

2.15 XPS spectra, C 1s, of porous silicon after microwave irradiation with a) di-*n*-butyl disulfide, b) di-*t*-butyl disulfide, c) di-*n*-octadecyl disulfide, d) diphenyl disulfide, e) diphenyl diselenide, f) diphenyl ditelluride, g) 1-octadecanethiol, h) *t*-butylthiol, i) bis(4-chlorophenyl) disulfide for the time indicated. 51

3.1 Overall reaction scheme summarizing the formation of Si−S, Si−Se, and Si−Te bonds on Si(111)−H surfaces. 54

3.2 Schematic of assembly process for the reaction of dichalcogenides with the Si(111)−H surface. 56

3.3 (a and b) A "sandwich" apparatus consists of quartz, reagent, and silicon wafer. (c) The apparatus was placed on a hot plate under a UV pen lamp. 56

3.4 XPS spectra of Si(111) surfaces after the UV-mild thermal (80 °C) treatment with indicated diphenyl dichalcogenides and di-*n*-octadecyl disulfide reagents for 15 min. Orange dashed curves are the envelope fittings. The data from this figure and supporting literature are tabulated in Tables 3.2 and 3.3. E^a = S, Se, Te, as well as H. 62

3.5 XPS spectra of Si(111)−H surfaces after reaction with diphenyl dichalcogenides reagents under indicated reaction times and temperatures. . . . 64

3.6 Water contact angle images of a Si(111)−H surface reacted with indicated reagents corresponding to Table 3.4. 65

3.7 Water contact angles of di-*n*-octadecyl disulfide-functionalized silicon surfaces with different reaction times (black dots) and the fitting curve according to the contact angle data (red curve). Each black dot represents a unique sample that had been reacted for the indicated reaction time. The error bars represent the standard deviation of five measurements on the same sample. 66

3.8 AFM scribing of Si(111) surfaces. All scale bars are 400 nm. (a) Scribing on a hydride-terminated Si(111) surface. (b–d) Functionalized Si(111) surfaces reacted with PhSSPh, PhSeSePh, and PhTeTePh, respectively. (e) Functionalized Si(111) surfaces reacted with di-*n*-octadecyl disulfide. A smaller area was etched for the di-*n*-octadecyl disulfide molecule due to the rapid buildup of residue on the tip. 68

3.9 Side-view space-filling model of the ≡Si−E−Ph (E = S, Se, Te) interfaces on a flat hydride-terminated Si(111) surface. The chalcogenide-based functionalities were placed randomly on the surface, as would be the case for kinetically trapped, irreversible Si–E bond formation. . . . 70

3.10 Theoretical monolayer thicknesses of ≡Si−S−Ph-, ≡Si−Se−Ph-, ≡Si−Te−Ph-, and ≡Si−S–*n*-octadecyl-modified silicon surfaces calculated based upon the indicated bond lengths and angles. H_{vdw} is the van der Waals radius of the hydrogen para to the chalcogenide. Red lines indicate steric hindrance between the phenyl ring and underlying hydrogen atoms on the silicon surface. 71

3.11 (a) Idealized close-packed configuration of ≡Si−S−Ph groups on a Si(111) surface. (b) Configuration resulting from a simulation of stochastically packed ≡Si−S−Ph groups on a Si(111) surface. Silicon-hydride groups are represented by small black dots, chalcogen atoms by medium blue disks, and phenyl rings by large gray disks. 79

3.12 "Photolysis–diffusion–abstraction–addition" mechanism leads to the ≡Si–ER bond formation. (a) Photolysis of REER molecules near the top of the organic layer results in RE• radicals. Because this film has been melted and is thus a liquid, these radicals can diffuse throughout the film and can abstract a hydrogen from a surface ≡Si–H bond, leading to ≡Si• radicals. (b) Addition of REER molecules to surface ≡Si• radicals via S_H2 addition leads to ≡Si–E bond formation. (c) Direct combination of a ≡Si• radical with a RE• radical also can yield ≡Si–ER bond formation. 81

3.13 UV absorption spectra of diphenyl and dialkyl dichalcogenides. Dashed vertical lines = 254 nm. 82

3.14 (a) XPS spectrum of the Au reference used for binding energy calibration. (b) Cross-section SEM image of the Au film on the Si(111) surface, from reference 14. 83

3.15 XPS spectra of the Si 2p peak from Si(111) surfaces, with indicated terminations. Four identical batches of silicon samples were prepared for XPS measurement. Each batch contained four samples, which were ≡Si−H, ≡Si−S−Ph, ≡Si−Se−Ph, and ≡Si−Te−Ph surfaces. For each sample, two spots were measured by XPS. Consequently, each functionalization of silicon surfaces contains eight measurements, giving eight XPS curves, in which every two curves with same color means they are from the same sample. The curves are all from raw data without normalization. 84

3.16 UPS He I spectra of the Si(111) surfaces, with indicated terminations, for the determination of work function. Four identical batches of silicon samples were prepared for UPS measurement. Each batch contained four samples, which were ≡Si−H, ≡Si−S−Ph, ≡Si−Se−Ph, and ≡Si−Te−Ph surfaces. For each sample, two spots were measured by UPS. Consequently, each functionalization of silicon surfaces contains eight measurements, giving eight UPS curves, in which each two curves with same color means they are from the same sample. The curves are all from raw data without normalization. 85

3.17 Energy band diagram of functionalized n-type Si(111) with band bending, qV_{bb}, and surface dipole, δ. The values of black markings, including BE^B (Si $2p_{3/2}$), E^B_{vbm} and χ_B, are constant for a specific silicon. In the present case, the values of BE^B (Si $2p_{3/2}$), E^B_{vbm}, and χ_B are 98.74 eV, 0.82 eV, and 4.05 eV, respectively. The values labeled in red are obtained from XPS and UPS data. 86

4.1 (a) Different linkages of organic monolayers on the Si(111)–H: alkyl monolayer (left) and alkenyl monolayer (right). (b) Surface coverage obtained by ATR-dichroism (diamond) and XPS (circle) of 1-alkene (lower black curves) and 1-alkyne (upper red curves) monolayers on Si(111)–H. (Reprinted with permission from ref 15. Copyright 2010 American Chemical Society.) 88

4.2 STM image of Si(111)–CH_3 collected at 4.7 K (inset: 77 K) with a sample bias of –2.5 V and a constant current of 0.050 nA (dark = low; light = high). Directions of low-index planes determined by X-ray crystallography are shown. The surface unit cell is represented by the parallelogram, and four methyl groups are drawn. (Reprinted with permission from ref 16. Copyright 2005 American Chemical Society.) . 89

4.3 Structures of monolayers as obtained by the polymer consistent force field (PCFF) calculations with (a) 50% and (b) 33.3% substitution levels. (Reprinted with permission from ref 17. Copyright 2001 American Chemical Society.) 90

4.4 (a) Simulation cells for various percentages of molecular substitution. (b) Packing energy per chain vs percent substitution for octadecyl groups (C_{18}) on Si(111) from molecular mechanics simulations. (Reprinted with permission from ref 18. Copyright 2001 American Chemical Society.) 91

4.5 FTIR spectra of porous silicon coated with 0.5 M CBr_4 in dodecene (a) before and (b) after an 8-min white light photolysis ($\sim$175 mW cm^{-2}). (Reprinted with permission from ref 9. Copyright 2011 American Chemical Society.) 92

4.6 Monolayer coverages of $\equiv$Si$-$$OCH_3$ surfaces determined from (a) transmission infrared spectroscopy measurements and (b) X-ray photoelectron spectroscopy measurements as a function of the oxidizing conditions. (Reprinted with permission from ref 19. Copyright 2017 American Chemical Society.) 94

4.7 Reaction of Si(111)–H with (a) neat alkenes, (b) 11-fluoro-1-undecene diluted in mesitylene, and (c) di-*n*-octadecyl disulfide. Overview of experimental setup for reaction of Si(111)–H with an alkene via (d) direct heating using neat molecules, (e) UV irradiation, and (f) direct heating with an alkene diluted in mesitylene. 97

4.8 Water contact angle images of a Si(111)–H surface reacted with indicated reagents corresponding to Table 4.1. 100

4.9 Kinetic profile of hydrosilylation of 1-octadecene on Si(111)–H with UV irradiation. Each black dot represents a unique sample that had been reacted for the indicated reaction time. The error bars represent the standard deviation of five measurements on the same sample. 100
4.10 XPS spectra of Si(111)–H surfaces after thermal hydrosilylation with 1-octene, 1-dodecene, 1-octadecene, and 11-fluoro-1-undecene (10% in mesitylene solutions, v/v) at 200 °C for 2 h. Orange dashed curves are envelope fittings. 101
4.11 (a) C1s and (b) Si 2p XPS narrow scan of $\equiv$Si$-$CH$=$CH$-$(CH_2)$_n$–F surfaces. (Reprinted with permission from ref 20. Copyright 2013 American Chemical Society.) 102
4.12 Schematic models of the $\equiv$Si$-$(CH_2)$_{11}$$-$F, $\equiv$Si$-$(CH_2)$_n$–CH_3, and $\equiv$Si$-$S$-$(CH_2)$_{17}$$-$$CH_3$ surfaces, from left to right, respectively. 104
4.13 Scheme of the cross-section of the organic monolayer comprising $\equiv$Si–(CH_2)$_{11}$–F groups, an ω-heteroatomic tag. 108
4.14 A representative scheme of the Si–(CH_2)$_n$–CH_3 surface. 112
4.15 Scheme of the cross-section of the organic monolayer comprising $\equiv$Si–S–(CH_2)$_{17}$–CH_3 groups. 114
4.16 A scheme of the relationship between substitution levels and the thickness of adventitious carbon of (a) the $\equiv$Si$-$(CH_2)$_{11}$$-$F surface, derived using the C/Si ratio (black) or the F/Si ratio (blue) from XPS data, and (b) the $\equiv$Si$-$S$-$(CH_2)$_{17}$$-$$CH_3$ surface, derived using the C/Si ratio (black) or the S/Si ratio (orange) from XPS data. 118

5.1 FTIR spectra of freshly prepared hydride-terminated porous silicon (red), and the porous silicon after reaction with dimethyl disulfide on a 100 °C hot plate for 1 h (black). 124

5.2 (a) Schematic illustration of the single silicon nanowire for the photoelectrochemical process. Photoexcited electron-hole pairs are produced under illumination and are subsequently separated at the nanowire/electrolyte interface because of band bending. The electrons then move to the platinum catalytic sites and carry out proton reduction. (b) Scanning electron microscope (SEM) image of individually addressable single nanowires. Scale bar is 10 µm. (Reprinted with permission from ref 21. Copyright 2016 Springer Nature.) 125
5.3 Schematic diagram of the monolayer contact doping process for Si substrates. 126
5.4 (a) Schematic representation of the bipolar electrochemical etching to produce porous Ge(100) wafers. (b) Schematic representation of preparation of hydride-terminated flat Ge(100) wafers. 127
5.5 Top (left) and cross-sectional (right) views of n^+ type derived porous germanium. Reprinted with permission of ref 22. Copyright 2000 the Royal Society of Chemistry. 128
5.6 Functionalization of hydride-terminated germanium with dialkyl/diaryl dichalcogenides under UV irradiation or thermal heating. 128

List of Tables

2.1 Summary of XPS Data, Corresponding to Figure 2.6 44

2.2 Representative Peaks of S 2p, Se 3d, and Te 3d, Corresponding to Figure 2.6 45

3.1 Estimated Light Absorption by Dichalcogenide Molecules Above the Silicon Surface 57

3.2 Summary of XPS Data Corresponding to Figure 3.4 63

3.3 Representative Peaks of S 2p, Se 3d and Te 3d Data From the Literature 63

3.4 Contact Angles for the Functionalized Silicon Surfaces Reacted with the Indicated Reagents under UV Irradiation at 80 °C 64

3.5 Representative Contact Angles of Indicated Phenyl-Terminated and Long Alkyl Chain-Terminated Silicon or Gold Surfaces from Literature 66

3.6 Contact Angles[a] for the Control Experiments with Indicated Conditions 66

3.7 Representative C–E–C[a] and Si–S–R[b] Bond Angles for Various Compounds from Literature 69

3.8 List of All Constants Used for the Calculation of Substitution Levels from XPS Data 75

3.9 The Ratio of XPS Counts Carbon to Silicon of Si(111)–H Samples[a] . . 75

3.10 The Ratio of XPS Counts Carbon to Silicon of ≡Si–S–*n*-octadecyl Terminated surfaces[a] 76

3.11 The ratio of XPS counts for each element compared to silicon[a] 77

3.12 Substitution Level Measured from XPS Data and Simulation 77

3.13 Binding Energy, Work Function, and Surface Dipole of Functionalized Silicon Surfaces[a] 84

4.1 Static and Dynamic Contact Angles for the Functionalized Silicon Surfaces Reacted with the Indicated Reagents under Different Reaction Conditions 99

4.2 Summary of XPS Data Corresponding to Figure 4.10 102

4.3 Quantitative XPS Data of Indicated ≡Si−CH=CH−$(CH_2)_n$−F Surfaces from Reference 20 103

4.4 Quantitative XPS Data of Indicated Functionalized Silicon Surfaces . . 104

4.5 List of All Constants Used for the Calculation of Substitution Levels from XPS Data 106

4.6 Quantification of Substitution Level for Different Functionalized Silicon Surfaces 116

List of Symbols

Symbol	Meaning
I	XPS intensity
σ	Relative sensitivity factor
ρ	Atomic density
λ	Electron attenuation length
d	Thickness
ϕ	Substitution level
n	Surface density
$q\mathrm{V}_{\mathrm{bb}}$	Band bending energy
WF	Work function
χ	Electron affinity
δ	Surface dipole
θ_a	Advancing contact angle
θ_r	Receding contact angle

List of Abbreviations

Abbreviation	Meaning
AFM	Atomic force microscopy
BE	Binding energy
FTIR	Fourier transform infrared spectroscopy
SAM	Self-assembled monolayer
SEM	Scanning electron microscopy
STM	Scanning tunneling microscopy
ToF-SIMS	Time-of-flight secondary ionization mass spectrometry
UPS	Ultraviolet photoelectron spectroscopy
UV-vis	Ultraviolet and visible
XPS	X-ray photoelectron spectroscopy

Chapter 1

Introduction

1.1 The Interface Is the Device

Silicon as a material dominates the entire microelectronic industry worldwide due to its abundance on the earth's crust, ideal band gap, oxide surface chemistry, and etching properties that enable the manufacture of incredibly powerful integrated circuitry.[23,24] The previous historical "age" periods, stone age, bronze age, and iron age, now have become the "silicon age", which also is called the "age of information." The functionalization of silicon surfaces is of significance because of the resulting effect on the physical, chemical, and electrical properties. These changes can improve the viability of this semiconductor for a myriad of practical applications, including silicon-based devices for solar energy conversion,[25] modulation of the electronic properties of bulk and nanocrystalline silicon structures,[26–28] light-emitting devices,[29,30] sensing applications,[31,32] and many others.[33,34]

In 2001, Herbert Kroemer opened his Nobel lecture by stating: "Often, it may be said that the interface is the device."[35] Indeed, electronics is based on asymmetries induced by interfaces. As the feature sizes on silicon devices continuously decrease, especially on the nanoscale where new physical properties emerge via breaking a "bulk" into very small objects, the interfaces play a more important role in the properties of the devices.[36–38] Silicon nanocrystals will show various photoluminescence when they are functionalized with different surface groups (Figure 1.1a).[1] Additionally, the interfacial mechanical shear strength between silicon microwires and ionomer membranes can be tailored via chemical modification of the silicon surface with different surface functionalities and tunable surface density (Figure 1.1b).[2] From a biomedical and bioenergy perspective, silicon nanowires can control bacterial motion and attachment on surfaces (Figure 1.1c),[3] which affords great opportunities to treat tumor and cancer cells and to detect specific

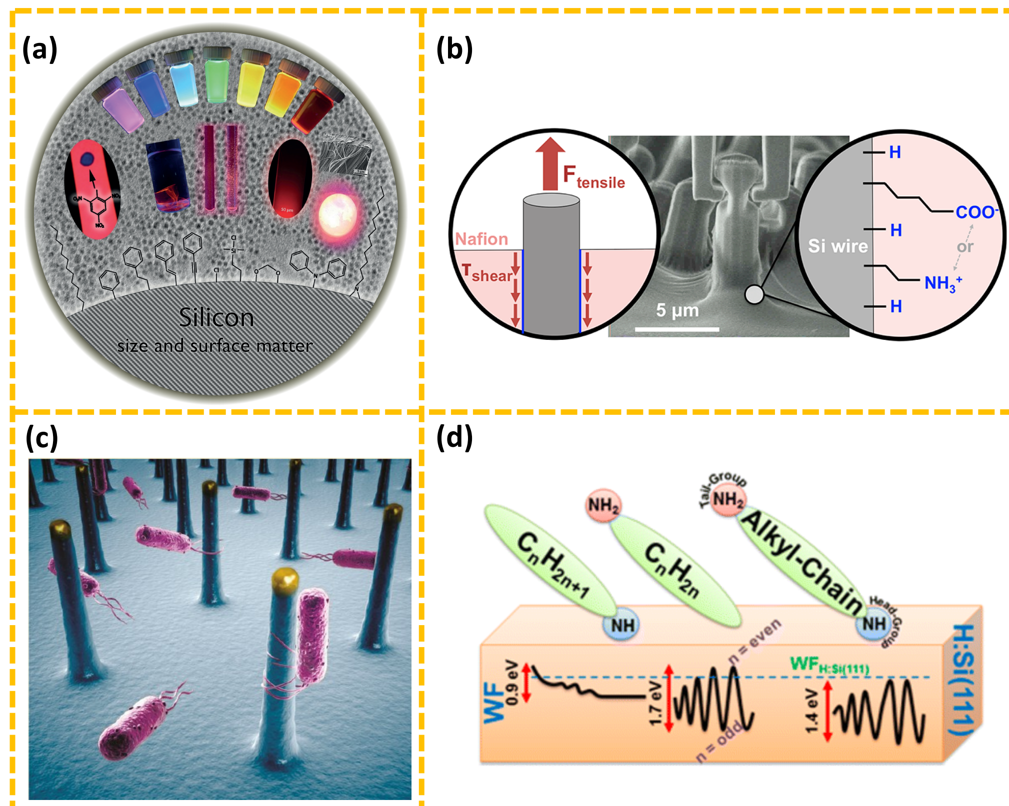

Figure 1.1. (a) A composed scheme of silicon nanocrystals showing tunable photoluminescence via surface functionalization. (Reprinted with permission from ref 1, copyright 2016 American Chemical Society.) (b) A scheme of a single-wire pull-out test of a modified silicon microwire to obtain the interfacial mechanical shear strength. (Reprinted with permission from ref 2, copyright 2015 American Chemical Society.) (c) A scheme of bacterial recognition of silicon nanowire arrays. (Reprinted with permission from ref 3, copyright 2013 American Chemical Society.) (d) Tunable work function of the silicon surface via the choice of the head group or tail group attached to silicon. (Reprinted with permission from ref 4, copyright 2015 American Chemical Society.)

biomolecules electrically. Moreover, by changing the head or tail group attached on the silicon surface, it was calculated that the work function of the silicon surface can be tuned by up to 1.73 eV (Figure 1.1d).[4] Other surface-based electronic properties, including band bending and surface dipole, also will be influenced upon surface functionalization treatments, as demonstrated by experimental measurements[39,40] or calculation.[4,41,42]

The distinguished physicist, Wolfgang Pauli, used to say, “God made the bulk; the surface was invented by the devil." Pauli explained that the diabolical characteristic of surfaces was due to the simple fact that a solid surface shares its border with the external world. While the bulk silicon provides intrinsic properties, the surface offers infinite possibilities.

1.2 Flat Silicon and Porous Silicon

1.2.1 Flat Silicon

Silicon wafers are used widely in electronic devices as they have proven to be reliable and effective in conducting integrated circuits. Silicon wafers are highly pure single crystalline materials, generally formed by the Czochralski growth process.[43] A trace of donor impurity atoms can be incorporated chemically into molten intrinsic silicon, dramatically changing the electronic properties of silicon, producing n-type and p-type silicon.[44–46] Impurity atoms with five valence electrons, such as phosphorus or arsenic, produce n-type semiconductors by contributing one extra electron to the lattice for each atom of dopant. P-type silicon is created by doping an intrinsic semiconductor with an electron deficient element, such as boron or gallium, during manufacture.

When a silicon wafer is sliced from the bulk diamond cubic structure crystal, the surface is aligned in one of several relative directions, known as the orientation. The orientation is important for the electronic and surface properties of the wafer. The different planes have different arrangements of atoms and lattices that will affect the manner by which electricity travels in the circuit.[47] The orientations of silicon wafers are classified using Miller indices (hkl), and the most common surface orientations are Si(100), Si(110), and Si(111), as shown in Figure 1.2.[5]

Bare silicon wafers are covered with a thin layer of native oxide, which can be removed by flashing under UHV conditions and with fluoride treatment.[48–50] Further lithography and etching steps provide silicon microscale and nanoscale roughness and structure as desired.

1.2.2 Porous Silicon

The demonstration in 1990 by Canham that porous silicon could emit visible light through photoluminescence at room temperature was attributed to quantum-confinement effects in crystalline silicon.[51] It induced considerable worldwide research activities to understand the fundamental basis of the luminescence phenomenon of this material.[52–55] Starting from the study of emissive properties, research on other properties (e.g., surface area, Young's modulus, bandgap, infrared refractive index, conductivity, and resistivity) all emphasize the high tunability of porous silicon, either via manipulation of its structural parameters, the chemistry of the large internal surface area, or the impregnation of other materials.[56–58]

Porous silicon is fabricated mainly by "top-down" etching techniques, such as

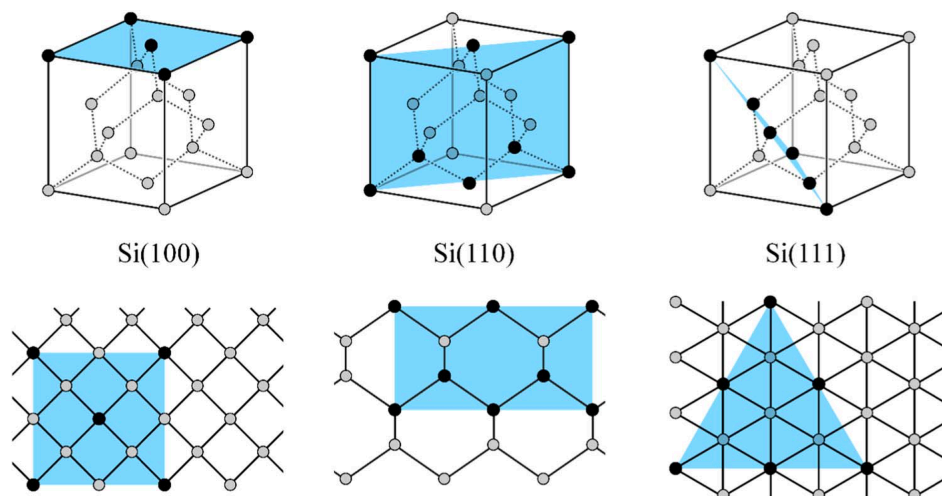

Figure 1.2. Upper: unit cells of Si(100), Si(110) and Si(111). Lower: the view along the different directions of the diamond cubic lattice. The black marked silicon atoms belong to a particular plane. (Reprinted with permission from ref 5. Copyright 2015 The Electrochemical Society.)

galvanic etching, metal nanoparticle-assisted etching, anodization, and HF vapor etching,[56] which results in highly directional porosity, so that properties that can be highly anisotropic. The most commonly used etching system is an electrochemical system, as illustrated in Figure 1.3. In this etching set up, the silicon wafer (Figure 1.3a) is at the bottom, making contact with the electrolyte (Figure 1.3d) through a hole in a container (commonly sealed with a O-ring). The counter electrode (Figure 1.3c) usually is made of Pt, which is not corroded during the etching process. The reference electrode (Figure 1.3b) can be any standard electrode used as a reference (Ag/AgCl, saturated calomel, etc.) or a noble metal like Pt. The electrolyte (Figure 1.3d) enables the ionic transport from the cathode to the anode and contains etching species, primarily aqueous solutions of HF with ethanol, as a co-additive to reduce surface tension. Illumination can be used to increase the etching rate. It generates electron-hole pairs that are separated by the

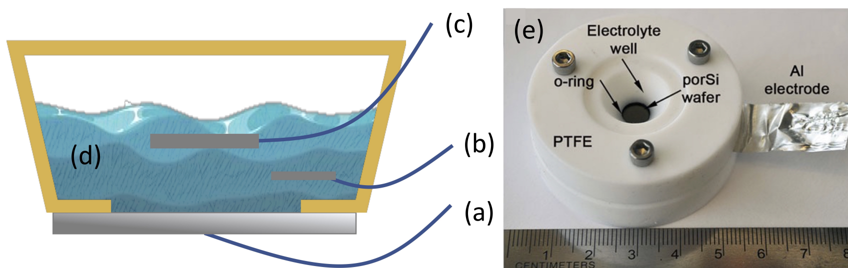

Figure 1.3. Electrochemical etching system. (a) Silicon sample (working electrode). (b) Reference electrode. (c) Counter electrode, made of Pt. (d) Electrolyte (etchant). (e) An actual cell used for the electrochemical functionalization of porous silicon.

electrostatic barrier at the silicon/electrolyte interface. Then the generated holes migrate to the surface of the n-type silicon and increase the etching rate.[59] This is the simplest and usual way of arranging the set up to assure that the electrolyte will always make an even contact with Si. Teflon is a good material for fabricating the container due to its excellent chemical stability, even in very concentrated HF solutions. An example of an actual cell used for the electrochemical functionalization of porous silicon is shown in Figure 1.3e.

Figure 1.4 shows the top view and the cross-section view of a typical porous silicon sample with an average pore diameter of 60 nm.[6] Pore size can be tuned via changing the applied current density for etching. As seen in the scanning electron microscope (SEM) images in Figure 1.5, for the same 10-min etching, when the current density decreases from 125 mA/cm^2 to 50 mA/cm^2, the pore size also decreases from an average diameter of 95 nm to that of 25 nm.[7]

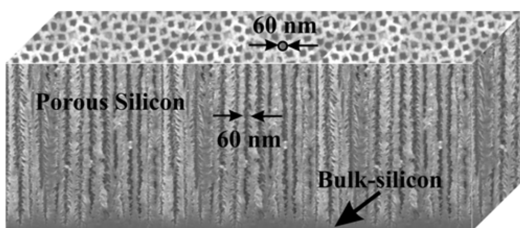

Figure 1.4. A schematic diagram of a porous silicon sample with an average pore diameter of 60 nm. (Reprinted with permission from ref 6. Copyright 2009 Wiley-VCH.)

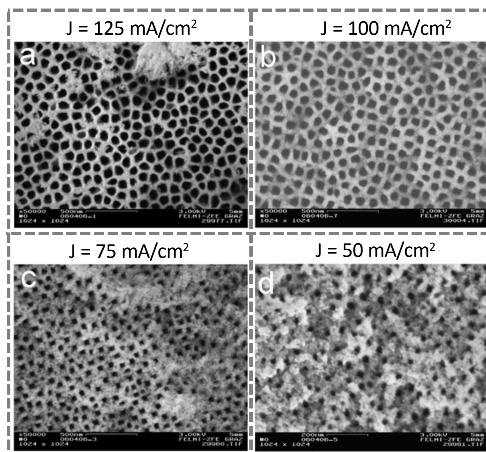

Figure 1.5. Scanning electron microscope (SEM) images of the morphology of porous silicon (100) samples varied by the applied current density. (a) Pore diameter ∼95 nm ± 10 nm, pore distance ∼45 nm; (b) Pore diameter ∼60 nm ± 8 nm, pore distance ∼50 nm; (c) Pore diameter ∼45 nm ± 10 nm, pore distance ∼55 nm; (d) Pore diameter ∼25 nm, pore distance ∼60 nm. The anodization time was kept constant at 10 min. (Reprinted with permission from ref 7. Copyright 2007 Elsevier.)

1.3 Hydride-Terminated Silicon Surfaces

Freshly etched silicon–hydrogen bond-terminated silicon surfaces are good candidates as a surface reactive precursor for further functionalization because they are relatively stable in ambient atmosphere for short periods. Fluoride-based etching methods for preparing hydride-terminated silicon surfaces have been harnessed for more than 30 years, as shown in Figure 1.6. Dihydride-terminated Si(100) $=SiH_2$ surfaces (Figure 1.6a) are prepared by etching commercial, native oxide-capped flat crystal silicon (100) wafers with a low concentration of (1–2%) aqueous HF.[8] Si(100) wafers etched by this method show a relatively high rough surface at nanoscale,[8] however, they can be smoothed via high-temperature (850$\sim$1200°C) annealing in pure argon at atmospheric pressure for 30–60 min.[60,61] Flat Si(111) samples etched in highly buffered HF solutions, such as in a 40% ammonium fluoride solution (pH = 7.8),[8,62,63] show homogeneous and atomically flat monohydride-terminated characteristic surfaces (Figure 1.6b). Upon etching, a very sharp, narrow stretch ν_{Si-H} at 2083.7 cm^{-1} (line width = $\sim$1 cm^{-1}) is observed in attenuated total reflectance (ATR)-FTIR (Figure 1.7), indicating an atomically smooth surface over nanometer-scale distances.[8]

For porous silicon, after electrochemical, chemical, or photochemical etching of Si(100) wafer (vide supra), the surface of porous Si contains a mixture of $-SiH_3$, $=SiH_2$, and $\equiv$SiH groups in a variety of different local orientations and environments due to the roughened surface morphology (Figure 1.6c).[64] FTIR spectroscopy characterization (Figure 1.8) shows that the surface comprises absorptions due to Si–H_x stretching modes (2088 cm^{-1} for $\equiv$SiH, 2117 cm^{-1} for $=SiH_2$, and 2138 cm^{-1} for $-SiH_3$) and $=SiH_2$ scissor modes, δ_{Si-H_2} at 912 cm^{-1} and δ_{Si-H_x} at 669 and 629 cm^{-1}. A small Si$-$O$-$Si stretching mode peak at $\sim$1037 cm^{-1}, which is present in all porous silicon samples, results most likely from a small oxidation of the reactive surface or is due to interstitial oxygen in the original silicon substrate lattice.[65]

As one of the nanostructured silicon materials, silicon nanoparticles (Si NPs) have attracted much attention because of their unique optoelectronic and chemical properties. Hydride-terminated Si NPs typically are obtained by etching the SiNPs/SiO_2 composite using concentrated HF (49%) with stirring (Figure 1.6d)[66,67] or by etching the silicon nanoparticles in a mixture of HNO_3 and HF (Figure 1.6e).[68,69]

All the freshly etched silicon hydride-terminated surfaces are chemically homogeneous (>99% H termination).[48] The hydrogen-passivated silicon surface is of good electronic quality, but the Si–H termination does not protect the surface fully from oxidation and corrosion. After a few hours in air, some initial oxidation often is observed,

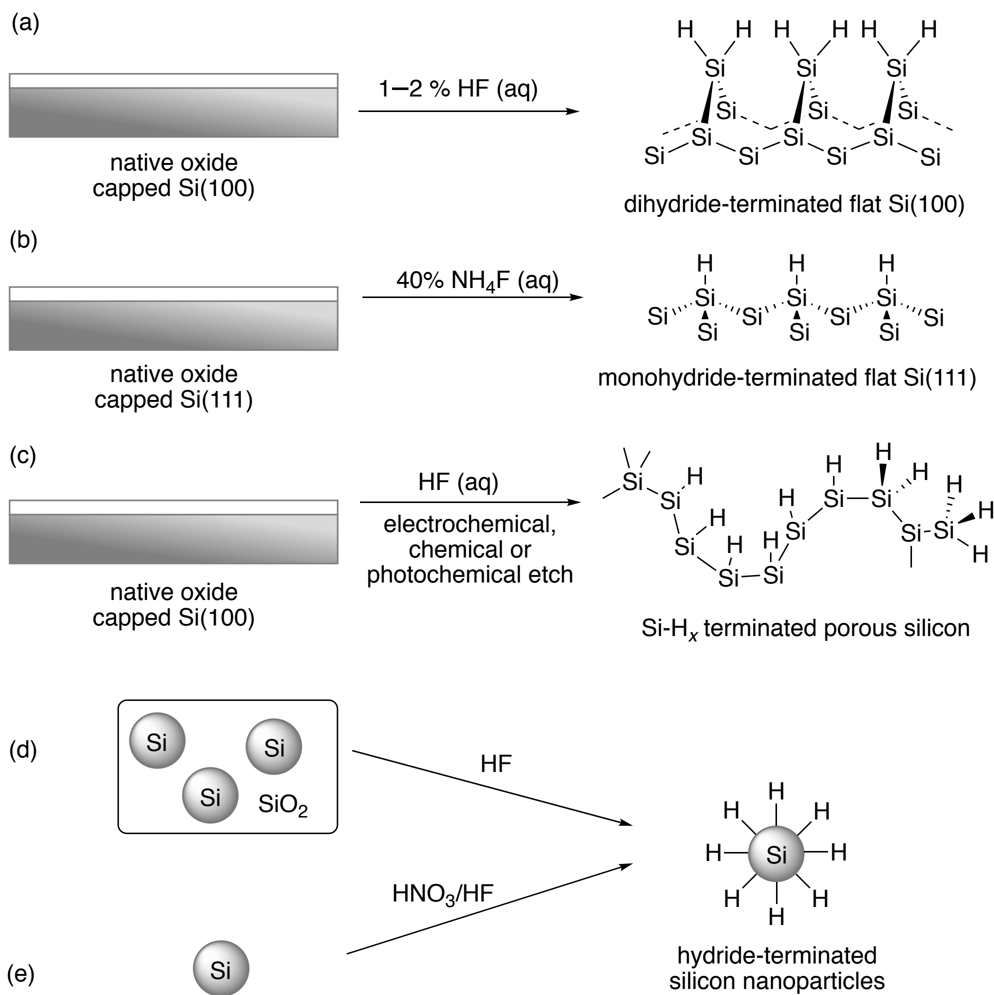

Figure 1.6. Etching conditions for obtaining (a) a flat Si(100)–H_2 surface, (b) a flat Si(111)–H surface, (c) a porous Si–H_x surface, and (d–e) a hydride-terminated silicon nanoparticle.

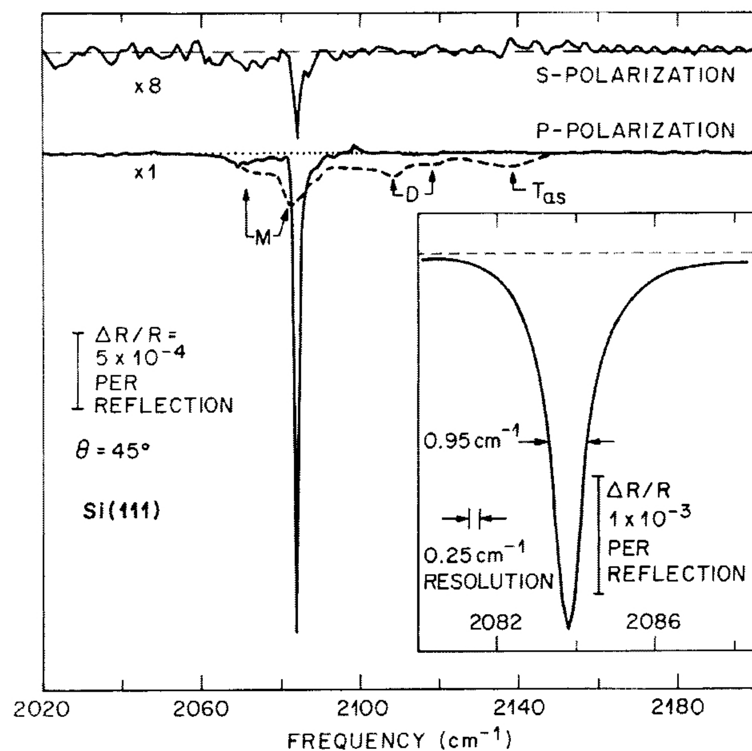

Figure 1.7. ATR-FTIR spectra of a Si(111)–H surface, etched in the 40% NH_4F (aq), taken with both s- and p-polarized IR light. (Reprinted with permission from ref 8. Copyright 1990 American Institute of Physics.)

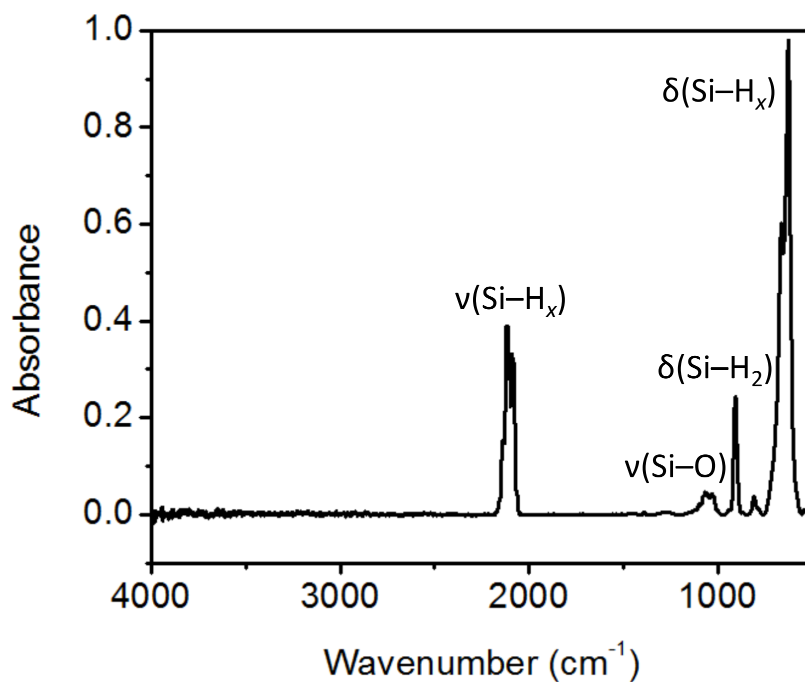

Figure 1.8. FTIR spectrum (transmission mode) of a freshly etched porous Si(100) surface.

although H-terminated Si surfaces remain stable in pure O_2, H_2O, and N_2 gases at temperatures above 300 °C.[70–72] It is believed that degradation in air is due to reactive species (i.e., radicals, ozone) that react with Si–H, leaving the surface susceptible to oxidation.

1.4 Functionalization of Si–H-Terminated Surfaces

Chemical functionalization of the surface with organic monolayers is used to stabilize the porous silicon with respect to demanding chemically- and biologically-relevant environments and can enable precise tailoring of properties to endow the material with particular characteristics, on demand. Two research directions of organic monolayers on Si surfaces have been studied: monolayers on native or thin silicon oxide (SiO_x) surfaces, prepared mostly through silane chemistry, and monolayers on oxide-free Si, prepared mostly via Si–C chemistry.[48,73] Between the two categories, oxide-free interfaces, typically using Si–H-terminated surfaces as a reactive surface precursor, are worth pursuing. For many potential molecular electronic applications, the oxide is not desirable as it presents an additional insulating barrier between the organic layer and the bulk silicon.[74,75] In addition, unless grown under carefully controlled conditions, the silicon–silicon oxide interface has a high density of electronic defects, which limit its usefulness in future devices.[76,77] Different mechanisms are involved upon functionalization, including radical-based chemistry, exciton-based chemistry, and photoemission.

1.4.1 Radical-Based Chemistry

Thirty years ago, Chatgilialoglu and co-workers demonstrated that tris(trimethylsilyl)silane, $(Me_3Si)_3SiH$, is an effective reducing agent for organic halides, selenides, xanthates, and isocyanides, as well as an effective hydrosilylating agent for dialkyl ketones and alkenes.[78] As shown in Figure 1.9a, a radical precursor, di-*t*-butyl peroxide, decomposes into *t*-BuO• radical under irradiation, and the radical then reacts with $(Me_3Si)_3SiH$ to produce tris(tri-methylsilyl)silyl radicals, $(Me_3Si)_3Si$•.[78,79] The formed silyl radical can react with various organic compounds via radical–radical reactions, halogen atom abstraction, or addition to unsaturated carbon–carbon bond or carbonyl groups (Figure 1.9b).[78] Similarly, bond dissociation of a Si–H bond also ocurrs on the hydride-terminated silicon surface, forming a surface-based silyl radical (vide infra).

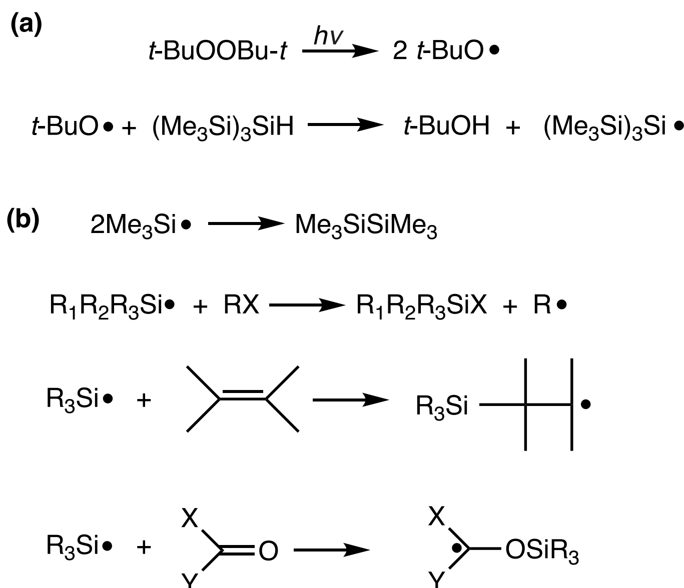

Figure 1.9. (a) Photodecomposition of di-*t*-butyl peroxide and the reaction of *t*-BuO· radical with $(Me_3Si)_3SiH$. (b) Reactions of a silyl radical with a silyl radical, halides, alkenes, and carbonyl groups, respectively, from top to bottom.

Radical Initiation

In 1993, Linford and Chidsey first carried out the hydrosilylation on flat crystal Si(111)–H surfaces.[80] It was proposed that the key intermediate is the surface silyl radical, or dangling bond, represented by ≡Si•. Figure 1.10 shows four ways that will lead to the formation of the silyl radical. As shown in Figure 1.10a, thermal decomposition of the radical initiator, a diacyl peroxide, produces alkyl radicals, $CH_3(CH_2)_n$•, via $CH_3(CH_2)_nCOO$•. The alkyl radical will abstract a hydrogen atom from a Si–H group, yielding the silicon surface-based radical, ≡Si•.[80,81] Another type of radical initiator utilized for silicon surface functionalization is a diazonium salt. In 2006, Buriak and co-workers showed that diazonium reagents could act as a radical initiator on hydrogen-terminated silicon surfaces, at room temperature, to produce surface silyl radicals that could be harnessed for further functionalization.[82] As shown in Figure 1.10b, the electrophilic diazonium reagent is reduced by the silicon, leading to the decomposition and formation of the aryl radical and release of N_2. The resulting positive charge on the silicon surface may be neutralized via release of HX and formation of a surface silyl radical.

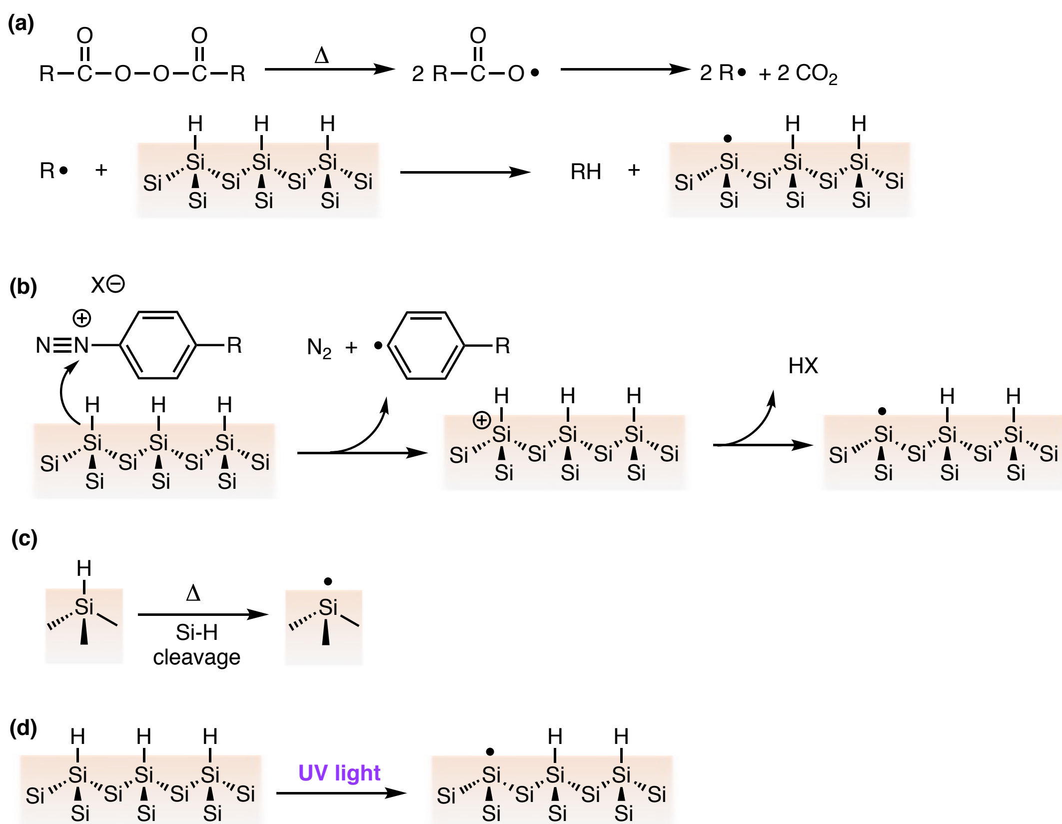

Figure 1.10. (a) Decomposition of a radical initiator, a diacyl peroxide, and the reaction between the formed $CH_3(CH_2)_n$• radical and a hydride-terminated silicon surface. (b) Reaction of the diazonium reagent with a hydride-terminated silicon surface. (c) Cleavage of a Si–H bond under thermal heating. (d) Cleavage of a Si–H bond under UV irradiation.

Silyl Radical from Thermal Heating

Thermal functionalization methods make up the majority of methods reported in the literature to produce SAM on a silicon surface due to the straightforward procedures and no requirements for a catalyst or special equipment. Samples can be placed in a small flask or vial, immersed in or coated with the reactant, and heated on a hot plate (≥150 °C) for hours to days.[33] If a vial is used, the cap should be lined with a material that is inert to the vapors from the liquid. As shown in Figure 1.10c, the mechanism also involves direct homolytic silicon–hydrogen bond cleavage at high temperature, giving a silyl radical, or dangling bond, ≡Si•.[83]

Silyl Radical from UV illumination

UV light illumination is another practical and easily implemented method to achieve hydrosilylation. UV light was harnessed first to successfully graft SAM on a silicon

surface via a Si–C bond by Chidsey and co-workers more than 30 years ago.[84,85] The mechanism was presumed to involve homolytic cleavage of the silicon–hydrogen bond to generate a silicon-based radical (Figure 1.10d). It was believed initially that the energy of the light needs to be at least ∼81 kcal/mol (354 nm)[86–88] to cleave a Si–H bond that has an equivalent bond dissociation energy.[89] Later in 2010, Hamers and co-workers proposed an alternative mechanism to Si–H dissociation for UV light promoted hydrosilylation, a mechanism driven by photoemission (vide infra).[90]

The silyl radical will react extremely rapidly with olefins, forming a carbon-based radical, which can abstract a hydrogen atom either from a neighboring Si–H group or from the allylic position of an unreacted olefin, as shown in Figure 1.11.[89] During thermal hydrosilylation, about 50–55% of the surface hydrides on an Si(111)–H surface are replaced by alkyl chains.[17,91] Through a careful process,[80,92,93] the alkyl-SAM-passivated surfaces could be more stable than hydrogen-terminated silicon and have high photoluminescence (PL) intensities and minimal interfacial oxide.

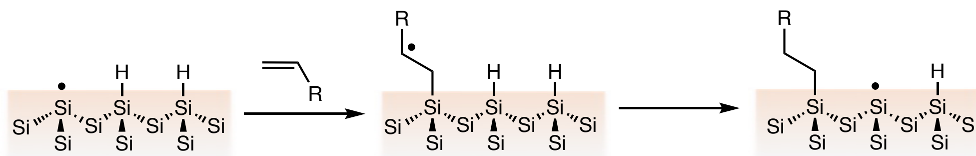

Figure 1.11. Reaction of surface silyl radical with alkene.

Gas Phase Radical Generation

When the alkene is in a gas phase over a silicon wafer under UV irradiation, another different reaction pathway is proposed.[94] The UV light cleaves the reactant to generate a hydrogen radical and an alkyl radical that can then pull hydrogen from the surface, generating a surface silyl radical, as shown in Figure 1.12. Monolayer growth can occur through either a radical chain reaction mechanism or through direct radical attachment to the silicon dangling bonds.

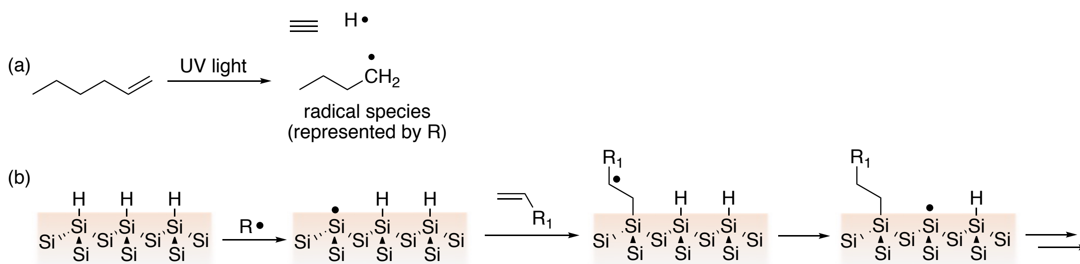

Figure 1.12. (a) Decomposition of an alkene under UV light irradiation, forming an alkyl radical. (b) Reaction of the radical with a hydride-terminated silicon surface.

Silyl Radical from Microwave Irradiation

In 2003, Boukherroub and co-workers demonstrated microwave-assisted chemical functionalization of a silicon surface using various 1-alkenes terminated with different functionalities (acid and ester).[95] In their work, a remarkable increase in the rate of the hydrosilylation reaction and surface coverage was shown when utilizing microwave irradiation as a source of energy. The functionalized porous silicon showed a very good stability in different aqueous and organic media. Later in 2008, the Boukherroub group extended the same system to other organic reagents, including alkenes, aldehydes, and alkyl halides.[96] A mechanistic approach was proposed for an alkyl halide reaction with porous silicon surfaces, involving two distinct initiation schemes. The temperature of silicon can reach a very high value within seconds to minutes under microwave irradiation, inducing the dissociation of Si–H bonds to generate silyl radicals, which propagate chain reactions, similar to those shown in Figure 1.11. Theoretically, the absorption efficiency by porous silicon is much higher than that by flat silicon because of the specific nanoscale architecture with networks of numerous nanoscale pores among nanocrystallites that can capture microwave energy.[96] One the other hand, microwave heating also leads to homolytic decomposition of the alkyl halide to yield both alkyl radicals, R•, and halide radicals, X•. These radicals are able to react with the Si–H bonds, terminating the porous silicon surface by hydrogen abstraction followed by formation of a Si–C bond.[96]

1.4.2 Exciton-Based Chemistry

Nanocrystalline Porous Silicon

Although white light is not expected to be sufficiently energetic to cleave Si–H bonds, it still can promote hydrosilylation of alkenes and alkynes on photoluminescent silicon nanoparticles in minutes via the generation excitons in the substrate, which can then initiate the reaction.[87,97] Exciton is the combination of an electron, e^-, and a positive hole, h^+ (an empty electron state in a valence band), which is free to move through a nonmetallic crystal as a unit.[51,98–100] Unlike the reaction of a molecular silane or bulk single silicon, excition-based chemistry only occurs in nanocrystalline porous silicon. Photoluminescent porous silicon is an ensemble or matrix of isolated silicon nanocrystallites and so has substantially different electronic properties than those of bulk single crystalline silicon. The exciton in porous silicon and silicon nanoparticles is relatively long-lived (microseconds) and, upon recombination, can emit light via

photoluminescence. As shown in Figure 1.13, upon absorption of a photon of sufficient energy by a nanocrystallite of silicon within the porous silicon matrix, an electron/hole pair is formed. Alkenes or alkynes can interact with the photogenerated holes, forming a Si–C bond and a β-silyl-substituted carbocation that can then be neutralized with a neighboring H and the electron derived from the original exciton.[9,101]

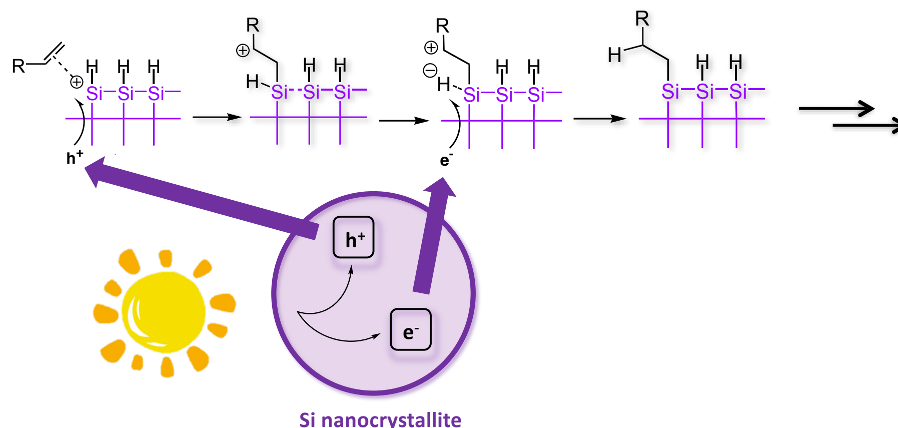

Figure 1.13. Mechanism for the exciton-mediated hydrosilylation event.

It is worth noting that the addition of electron acceptors would increase the rate of the hydrosilylation reaction and the final yield.[9] As shown in Figure 1.14a, additive RX abstracts an electron from the photogenerated exciton, and then the hole, h^+, in the silicon nanocrystal is attacked by the alkene. Figure 1.14b shows a number of different additives, with a range of LUMO energy levels from below the conduction band of a silicon nanocrystallite to far above. In 2012, the Buriak group demonstrated that those additives whose LUMO levels are below that of the conduction band by $\sim$0.2 eV will cause a strong increase in the rate of the hydrosilylation reaction, while those additives whose LUMOs were higher than the conduction band of a silicon nanocrystallite showed no effects on either the rate or the yield of the reaction.[9]

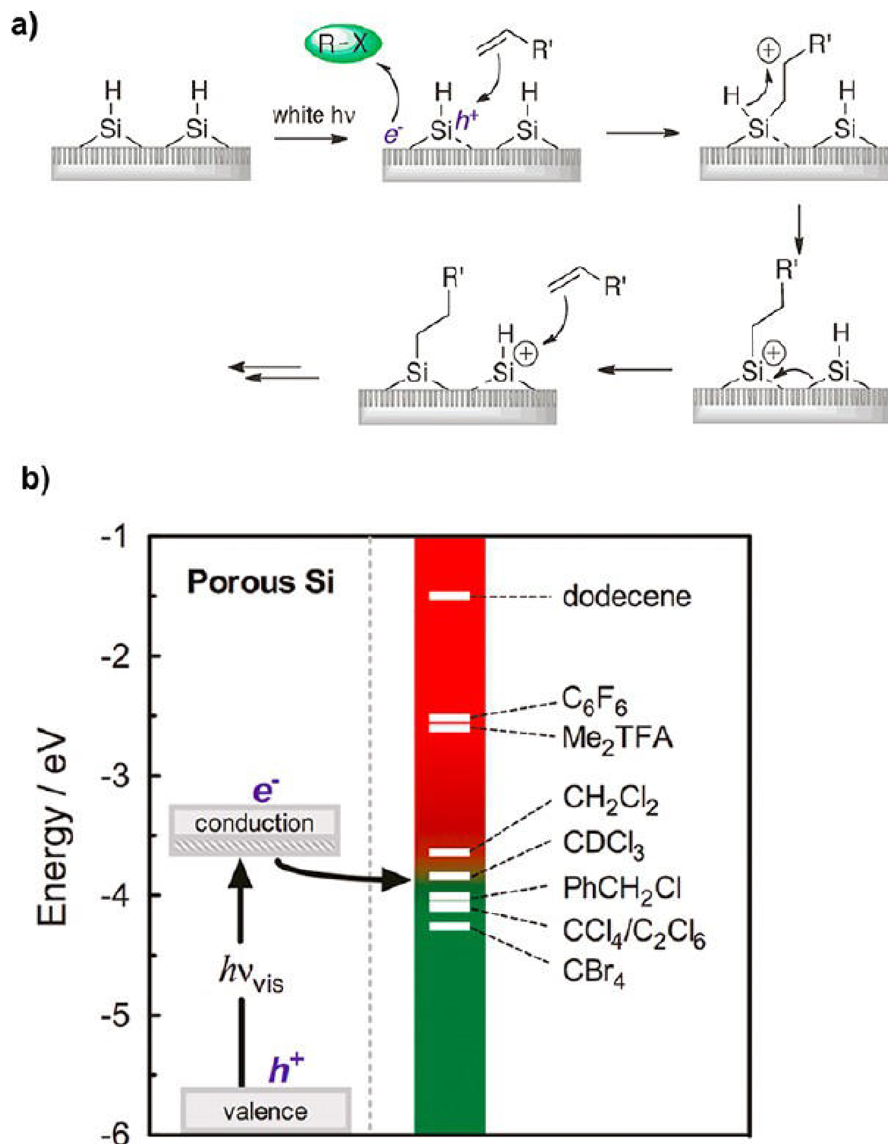

Figure 1.14. (a) The exciton-based mechanism for an enhanced hydrosilylation rate: electron abstraction by RX from the photogenerated exciton in the porous silicon hole, h^+, in the silicon nanocrystal that then is attacked by the alkene. (b) Energy level diagram showing the approximate positions of the conduction and valence bands in a silicon nanocrystallite and LUMOs of select oxidizing agents. (Reprinted with permission from ref 9. Copyright 2012 American Chemical Society.)

Flat Silicon

Longer white light irradiation time (>10 h) is required to activate hydrosilylation of alkenes on both flat Si(111)–H and Si(100)–H surfaces,[102] and the mechanism for the reaction on flat silicon is different from that on nanocrystalline porous silicon. As shown in Figure 1.15, the mechanism incorporated both radical- and hole (h^+)-based mechanisms.[103,104] The first step is quite similar to the one occurring in porous silicon, where an electron/hole pair is formed upon absorption of a photon. The hole weakens a

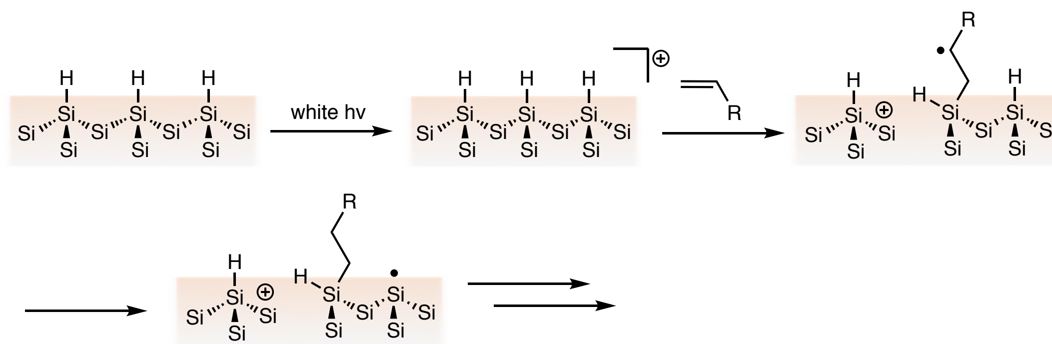

Figure 1.15. Exciton-driven hydrosilylation on a flat silicon surface involving both radical- and hole (h^+)-based mechanisms.

surface Si–Si bond, which is then attacked by the alkene to produce the Si–C bond, and the positive charge remains in the silicon. It is proposed that the carbon has more radical character and will abstract a hydrogen from the silicon surface to complete the reaction.

1.4.3 Photoemission

In 2010, Hamers and co-workers proposed an alternative and concurrent mechanism to Si–H dissociation for UV light promoted hydrosilylation, a mechanism that begins with UV-induced photoemission of a valence electron from the silicon surface.[90] Silicon has a work function of ~4.7 eV, and 254-nm photons possess sufficient energy to eject an electron directly from the conduction band. Ejection of the electron leaves the silicon surface with a net positive charge that then is attacked by the π-electrons of the alkene, leading to formation of the Si–C bond.

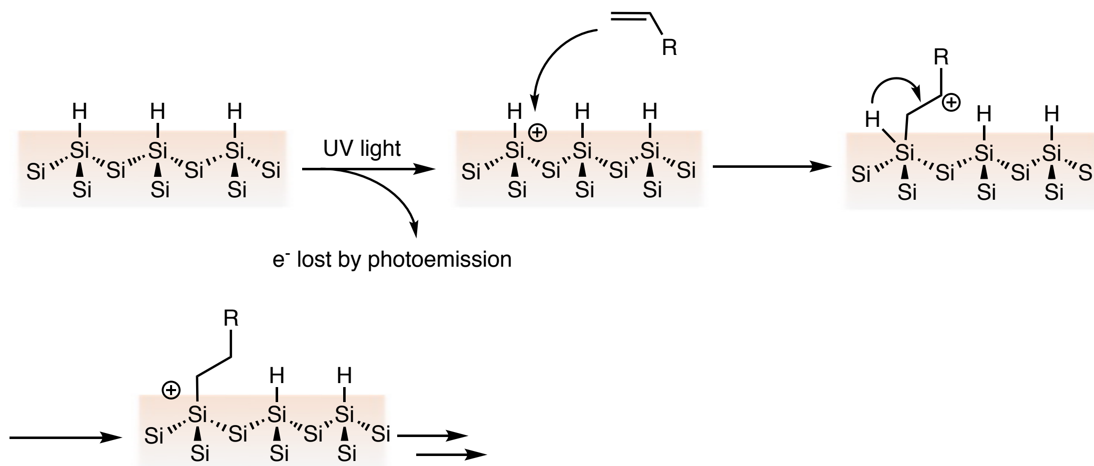

Figure 1.16. Reaction of a hydride-terminated silicon surface with an alkene driven by photoemission.

1.5 Silicon–Chalcogen Bond Formation

1.5.1 Si–E Bond Formation on Silicon Surfaces

The chemistry of organic molecules bound to silicon surfaces through silicon–chalcogen bonds on surfaces is relatively new compared to the widely studied silicon–oxygen and silicon–carbon bonds, and it has focused for the most part on sulfur-containing molecules.[105] Silicon-chalcogenide bonds could be important to the device that requires a specific electrochemically active interface. A heavier atom (S, Se, and Te versus O) provides more possibilities arising from the bond length and availability of additional electronic states.[4,106] Moreover, the chemistry of organochalcogenides on silicon surfaces has not been investigated extensively and could offer a rich and diverse repertoire of reactivity, as is seen in the case of molecular organosilane chemistry.[107,108]

Functionalization of silicon with organosulfur compounds, resulting in surface-bound silicon–sulfur bonds, was initiated first under ultrahigh vacuum conditions.[109] More recently, solution-phase approaches toward silicon–sulfur bound alkyl monolayers were shown to be accessible through reactions of alkanethiols, driven by UV,[110,111] white light,[112] or heat.[113,114] Using heat and supercritical carbon dioxide as an alkanethiol carrier fluid, monolayers on silicon surfaces bound through $\equiv$Si$-$SR bonds were shown to be stable to prolonged exposure to ambient atmosphere.[115] To access silicon–selenium bonds, Bocian and co-workers used a very short (2 min), high-temperature (400 °C) baking procedure to attach acetylchalcogenidoarene-derivatized (Ar–EAc, E = S, Se) porphyrins covalently on Si(111) surfaces through Si–O, Si–S, and Si–Se linkages.[105,106] However, until recently, the complete series of S, Se, and Te linkers remained elusive due to the difficulty of making $\equiv$Si$-$TeR bonds. The chemistry of silicon–chalcogenide-based interfacing of molecules on silicon surfaces is still in its very early stages.

1.5.2 Radical-Based Mechanisms of Si–E Bond Formation: The Connection Between Molecules and Surfaces

Radical-based functionalization of silicon surfaces always starts with a surface silyl radical, $\equiv$Si•, so the well-established molecular chemistry of silyl radicals with organochalcogenides should be a guide to the explanation of mechanisms of Si–E bond formation on a silicon surface. Molecules containing S- and Se- based substituents have played a significant role in radical chemistry, including the molecular chemistry of silyl radicals.

Silyl Radical with Alkyl Disulfide and Alkyl Sulfide

More than 30 years ago, Platz and co-workers showed that the homolytic displacement reaction of the silyl radical $Et_3Si\bullet$ with di-*n*-butyl disulfide, *n*-bu–SS–*n*-bu, leads to the formation of a Si–S bond, accompanied by the release of the *n*-butyl thiyl radical, as shown in 1.17a.[116] The reaction proceeds almost 100 times faster than the reaction with di-*n*-butyl sulfide (1.17b) due to the lower bond dissociation energy of the S–S bond versus the S–C bond (53–57 and 74 kcal/mol, respectively).[116] The longer bond length of S–S relative to S–C (0.21 nm versus 0.18 nm) also can decrease steric encumbrance and accelerate the rate of homolytic displacement. Similarly, the formed ≡Si• on the silicon surface also could react with *n*-bu–SS–*n*-bu via homolytic dispacement, followed by S–S bond cleavage, forming the ≡Si−S−bu termination on the surface.[10] However, according to the FTIR spectrum, di-*n*-butyl sulfide did not give successful incorporation of butyl sulfide with silicon under the same conditions (Figure 1.17d) (vide infra).

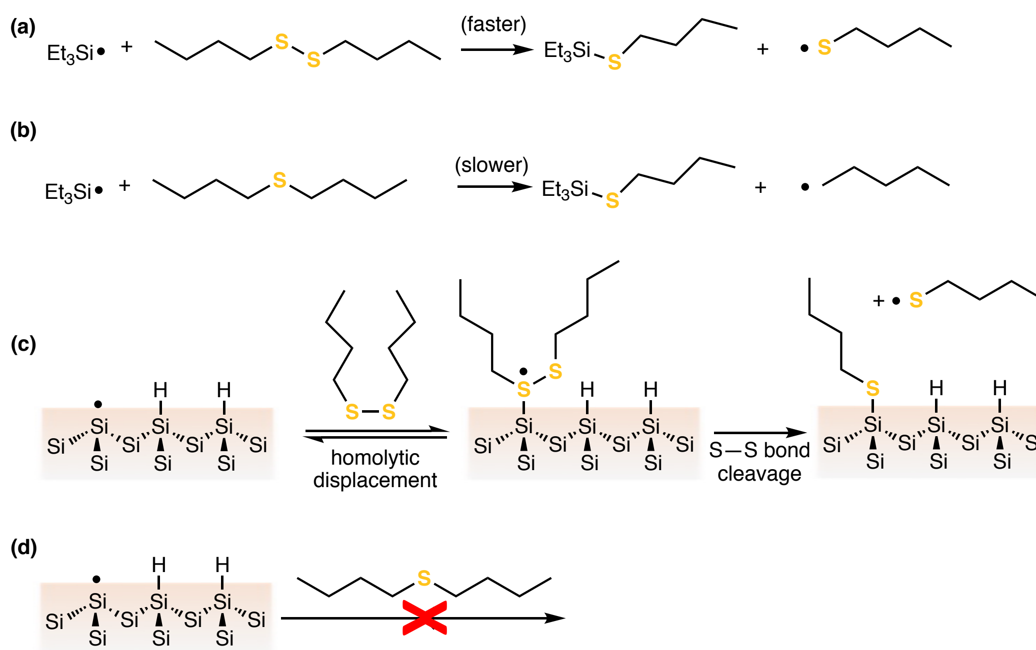

Figure 1.17. Reactions of molecular (a and b) or surface (c and d) silyl radical with di-*n*-butyl disulfide or sulfide.

Silyl Radicals with Aryl Disulfide

Diaryl disulfides and diselenides are also well-known radical traps that can react with an alkyl radical and form thiyl and selenyl radicals, as shown in Figure 1.18a and b. The reactivity of an alkyl radical with PhSeSePh is 160 times faster than that with

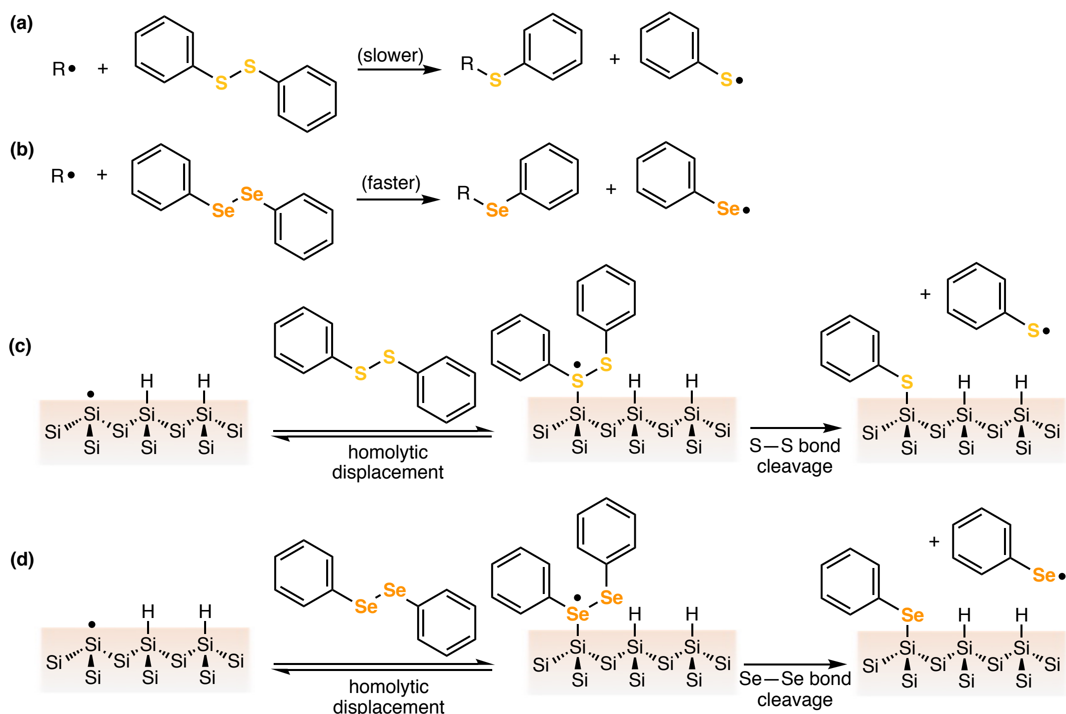

Figure 1.18. (a and b) Reactions of molecular alkyl radicals with dipheneyl disulfide and diphenyl diselenide. (c and d) Reactions of surface silyl radicals with diphenyl disulfide and diphenyl diselenide.

PhSSPh.[117–119] For a silicon surface silyl radical, a silimar mechanism was postulated to occur between the surface silicon radicals and both PhSeSePh and PhSSPh (Figure 1.18c and d).[10,83]

Silyl Radical with Di-*t*-butyl Disulfide

Di-*t*-butyl disulfide is an exception to the successful incorporation of a sulfide monolayer onto a silicon surface when using disulfide as a reagent (Figure 1.19). The reason can be explained from the literature on molecular silyl radical reactions with sulfides. Platz and co-workers studied the reactivity of the $Et_3Si\bullet$ radical with various sulfide compounds and found that the transition structure for the reaction of a radical with a *t*-butyl compound involves more S–Si bond making than C–S bond breaking.[116] They concluded that the kinetics of the reaction are more sensitive to steric effects than to the stability of the radical reaction product.[116] Similarly, for di-*t*-butyl disulfide with a silicon surface, the bulky *t*-butyl group on the sulfur first undergoes the S_H2 addition onto the silicon surface, and the surface prevents the reaction from proceeding because of the steric hindrance.[10]

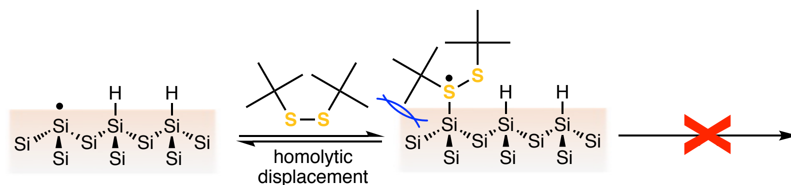

Figure 1.19. Lack of reaction of a surface silyl radical with di-*t*-butyl disulfide. Steric hindrance between the bulky *t*-butyl group and the surface prevented the reaction from proceeding.

Silyl Radical with Aryl–E–Alkyl

Another form of sulfides and selenides are phenyl–E–alkyl, PhER, where E is S or Se. Work from Chatgilialoglu and co-workers showed that the reaction of molecular silyl radicals ($(Me_3Si)_3Si\bullet$ and $Et_3Si\bullet$) with $PhSeC_{10}H_{21}$ was at least an order of magnitude faster than that with $PhSC_{10}H_{21}$ (Figure 1.20a and b).[78,107] The latter involves the formation of a sulfuranyl or seleranyl radical intermediate upon addition, followed by collapse to produce ≡Si−SePh molecules upon α-cleavage of the Se–C_{alkyl} bond. Because of the stronger C_{sp^2}–E bond compared to the C_{sp^3}–E bond,[120] the C_{alkyl}–E bond is cleaved rather than the E–C_{phenyl} bond. The mechanism for the silicon surface reaction with PhSeEt is similar to the molecular version, starting from the S_H2 addtion of selenoether onto the silyl radical and the formation of the seleranyl intermediate that collapses to form the final products (Figure 1.20d).[78,107]

However, no obvious incorporation of the alkyl monolayer with the silicon surface was observed from FTIR spectroscopy by the Buriak group when the silicon surface reacted with phenylethyl sulfide (PhSEt), di-*n*-butyl sulfide (bu–S–bu), diphenyl sulfide (PhSPh), or disphenyl selenide (PhSePh) (Figure 1.20c and 1.21).[10,82] This result again supports the fact that α-cleavage of the E–C_{alkyl} bond is inclined to occur in the selenium derivatives, as opposed to the sulfur variants.[78,107,116]

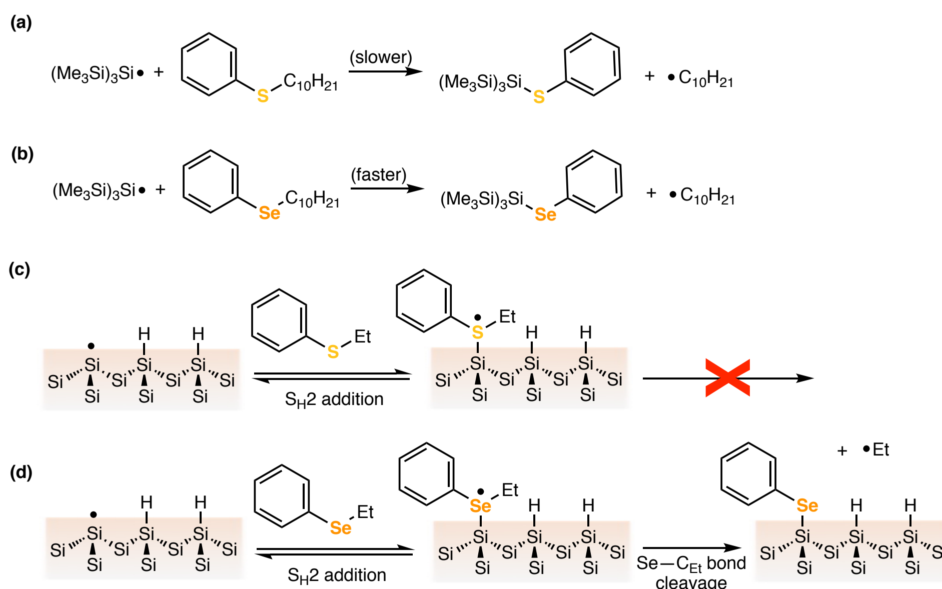

Figure 1.20. (a and b) Reaction of molecular silyl redicals with indicated Ph–E–alkyl molecules, where E = S and Se. (c) Lack of reaction of the surface silyl radical with phenylethyl sulfide (PhSEt). (d) Reaction of the surface silyl redical with phenylethyl selenide.

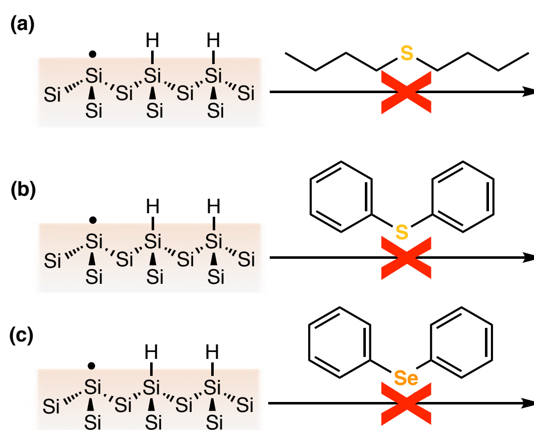

Figure 1.21. Lack of reaction of the surface silyl radical with di-*n*-butyl sulfide (bu–S–bu), diphenyl sulfide (PhSPh), or disphenyl selenide (PhSePh).

Silyl Radical with Thiols

Among various organic precursors for deposition of SAM on a silicon surface, alkylthiols also have been demonstrated to be tethered to the Si surface through a Si–S bond under photochemical activation, thermal reaction, or radical initiation. From a molecular perspective, the hydrogen-exchange equilibria between silanes and thiols under radical conditions have been studied extensively, as shown in Figure 1.22a.[88,108,121,122] When R is an alkyl, the equilibrium with RSH is slightly exothermic by approximately –3.5

kcal/mol, but slightly endothermic by 5.0 kcal/mol when R is a phenyl.[122] Similarly, the equilibria between a surface silyl radical and thiols are possible. Presumably, there are two possible pathways to produce the final product on the silicon surface, namely, the same stepwise S_H2-based mechanism described for thioethers (Figure 1.22c)[10] and the direct coupling of a surface silyl radical with a free thiyl radical in solution (Figure 1.22d).[123] Because of the equilibria between thiols and silanes, the substitution level of surface Si–H with alkanethiol is relatively low compared to the disulfides or diselenides under the same reaction conditions. Lack of reaction of a silicon surface with *t*-butylthiol was observed by the Buriak group (Figure 1.22e);[10] this is due to steric hindrance, similar to the result using di-*t*-butyl disulfide as a reagent (Figure 1.19).

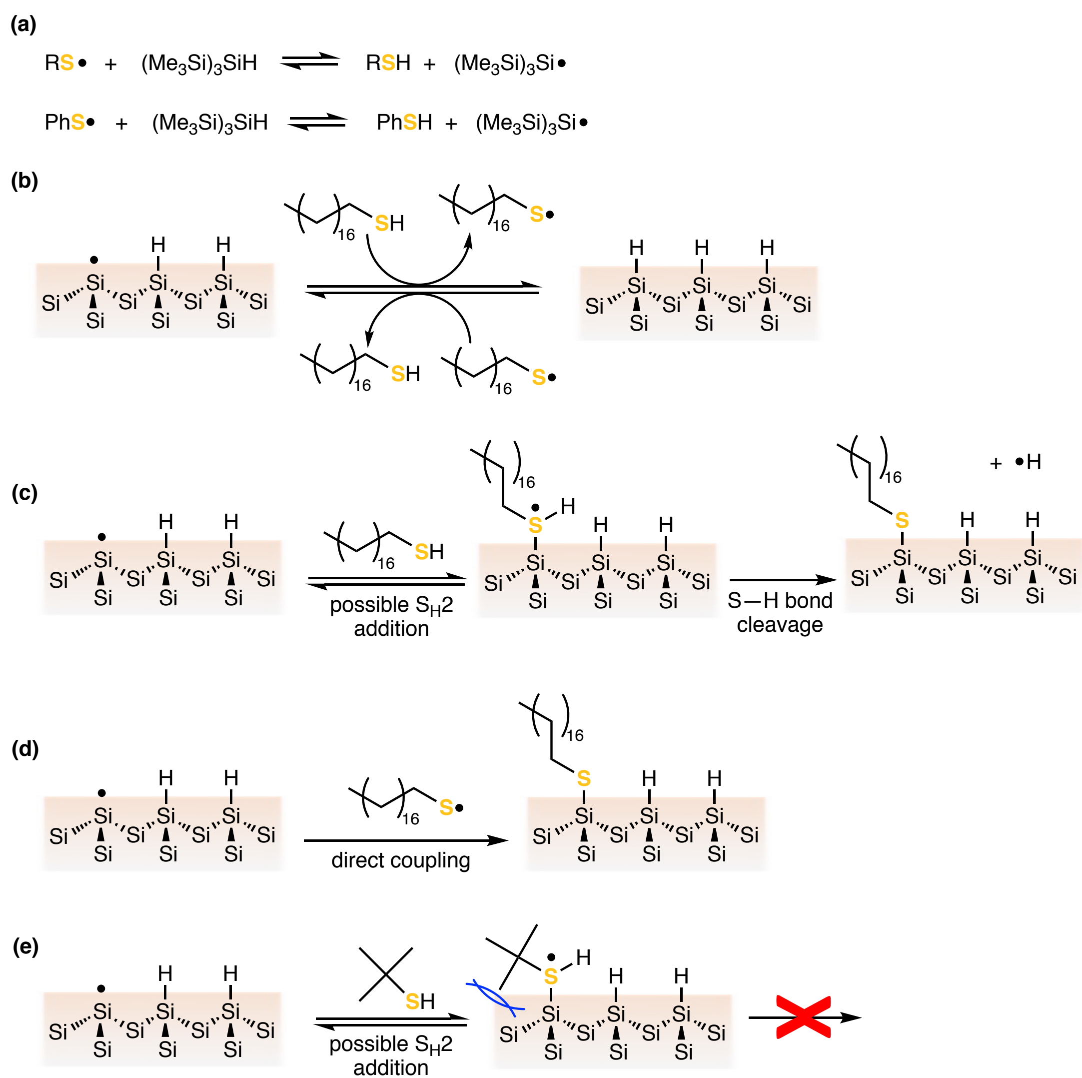

Figure 1.22. (a) Equilibria between thiols and molecular silane. (b) Equilibria between thiols and a hydride-terminated silicon surface. (c) Reaction of a surface silyl radical with 1-octadecanethiol. (d) Direct coupling of a surface silyl radical with a free thiyl radical. (e) Lack of reaction of a surface silyl radical with *t*-butylthiol.

1.6 Characterization Techniques for Functionalized Silicon Surfaces

1.6.1 Fourier-Transform Infrared Spectroscopy (FTIR)

FTIR is a powerful and extensively used tool to identify chemical functional groups attached on a silicon surface due to their characteristic vibrational modes, making it possible to track the progress of surface reactions easily.

Porous silicon can be analyzed rapidly by conventional transmission FTIR due to the high surface area and good signal to noise ratio of the functionalized surface. An example of FTIR spectra of porous silicon before and after reaction with the indicated reagents is shown on the left-hand side of Figure 1.23.[10] Figure 1.23a shows the characteristic features of a freshly prepared porous silicon sample (vide supra), the ν(Si–H$_x$) stretching mode centered around 2100 cm^{-1} and the bending modes, δ(Si–H$_x$), just above 800 cm^{-1}. Figure 1.23c, e, g, i, and k show the spectra of porous silicon grafted with different functional groups, all of which have distinct C–H$_x$ stretches around 3000 cm^{-1} (above 3000 cm^{-1} for C–H$_x$ on aryl groups and below 3000 cm^{-1} for that on alkyl chains). Partial Si–H bonds are consumed after the reaction, as can be seen on the right-hand side of Figure 1.23, so the decrease of the integrated intensity of the ν(Si–H$_x$) peak can be converted easily to the efficiency (%E) of the reaction via the following equation[124,125]

$$\%E = \frac{(A_{\text{Si–H, before}} - A_{\text{Si–H, after}})}{A_{\text{Si–H, before}}} = \frac{\Delta A_{\text{Si–H}} \times 100}{A_{\text{Si–H, before}}} \tag{1.1}$$

where A is the area of the integrated intensity of the absorption of the specified feature.

This semiquantitative analysis assumes that all the reacted S–H bonds are converted to the Si–R (R = C, S, N, etc.) groups as desired, so air and water should always be avoided during the preparation of samples. Dry and deoxygenated reagents are necessary prerequisites for the reaction, which should be performed in a glove box or using a Schlenk line, both of which provide an inert atmosphere.[126]

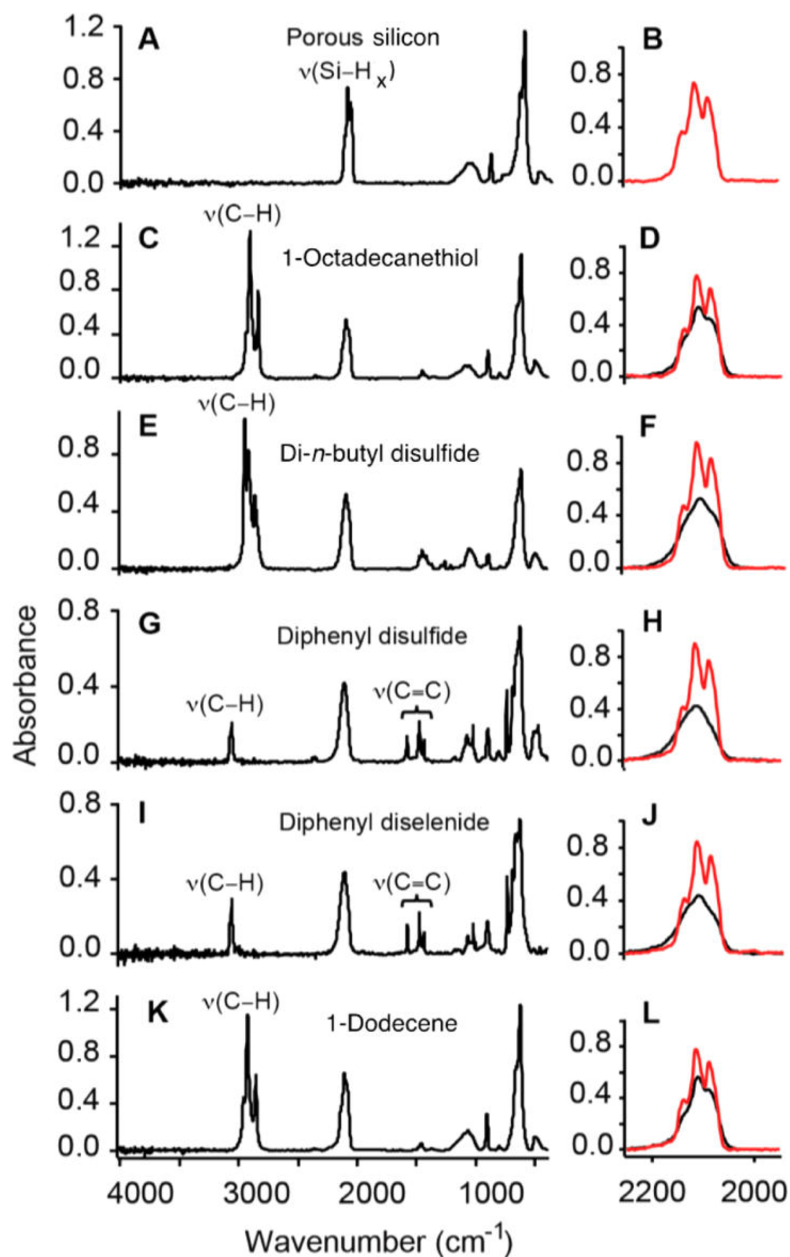

Figure 1.23. Transmission FTIR spectra of porous silicon samples before and after reaction with the reagent indicated, initiated by 4-bromobenzenediazonium tetrafluoroborate. The spectra on the left show the full mid-IR range, and the spectra on the right show the ν(Si–H$_x$) region before the reaction (red curve) and after the reaction (black). (Reprinted with permission from ref 10. Copyright 2015 American Chemical Society.)

The study on the substitution level of hydride-terminated silicon began in the 1990s. For flat Si(111) surfaces, the maximum coverage that can be obtained is ∼50–55% due to the steric hindrance between alkyl chains bonded to the silicon atom on the surface, as demonstrated by experimental research and theoretical calculation.[15,127] A higher substitution level (>55%), in other words, a higher packing density, requires the

atomic distance to be smaller than the van der Waals radii of the atoms in the chain, which is energetically unacceptable. Steric hindrance also is expected when organic groups are attached to porous silicon, although porous silicon is different from flat silicon. Moreover, porous silicon may contain some crevices and regions that cannot be accessible by molecular reagents for reaction, further lowering the substitution level. The size of the reagent also is a consideration because larger molecules are less able to migrate effectively within the porous framework and also will block the Si–H underneath the grafted molecules for reaction.

1.6.2 X-Ray Photoelectron Spectroscopy (XPS)

XPS is a very useful measurement technique to investigate the chemical composition on the surface of a sample (usually within 10 nm).[33,76] XPS detects the kinetic energy of an emitted photoelectron under an X-ray beam irradiation and gives the binding energy of the core electron. For a specific core electron, its binding energy shifts with a change in chemical binding with surrounding elements. As a result, the oxidation state of the elements as well as the electronic structure of a modified silicon surface can be obtained from XPS.

An example in Figure 1.24 shows the XPS spectra for an n-Si(111) surface terminated with a mixed methyl/3,4,5-trifluorophenylacetylenyl (MMTFPA) monolayer.[11] The survey spectrum in Figure 1.24a concisely shows all the elements present in the sample surface (Si, C, O, and F) without any contamination elements. A high resolution C 1s peak was deconvoluted into four peaks, belonging to C bound to F (C_F) , C bound to O (C_O), C bound to C (C_C), and C bound to Si (C_{Si}) from left to right, respectively, due to the different binding energy of C 1s under different chemical environments. Because of its low dipole moment, the Si–C bond is too weak to be detected via FTIR, while it can be observed by XPS, enabling XPS as a complementary technique to prove the surface functionality.

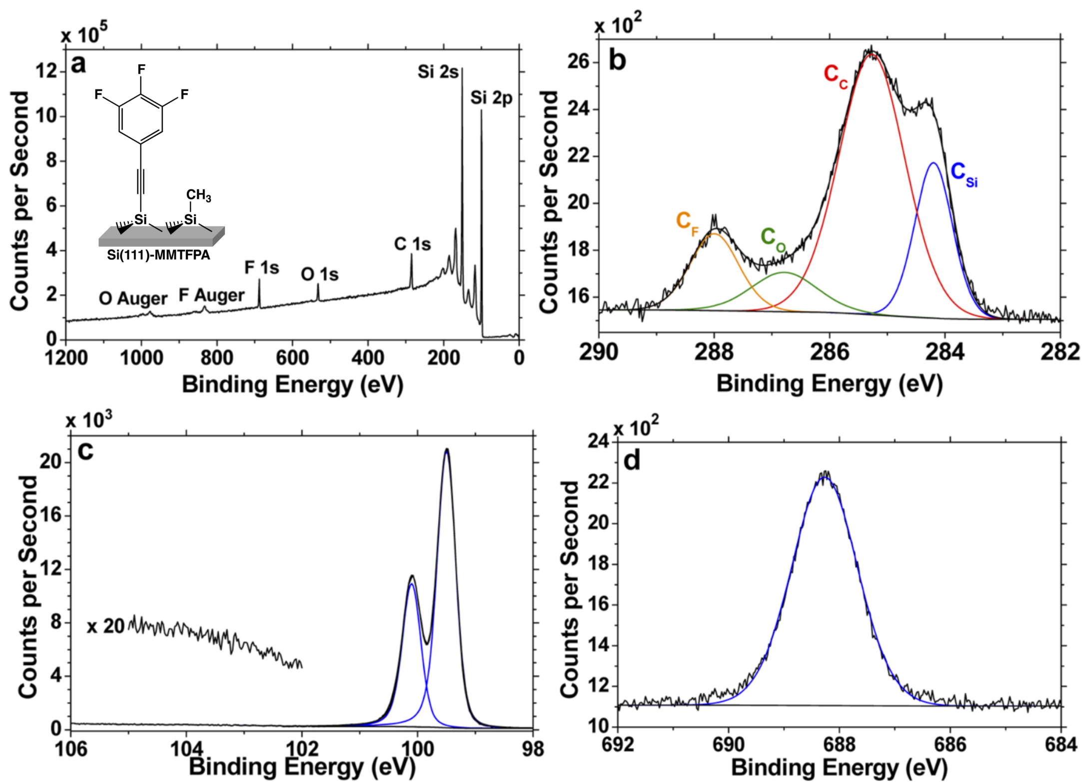

Figure 1.24. XPS spectra for a mixed methyl/3,4,5-trifluoropheny-lacetylenyl (MMTFPA)-terminated n-Si(111) surface. (a) Survey spectrum and an inset scheme of the Si(111)-MMTFPA surface. (b–d) High-resolution XPS spectra of C 1s, Si 2p, and F 1s, respectively. (Reprinted with permission from ref 11. Copyright 2016 American Chemical Society.)

For the Si 2p high resolution spectrum, the region between 101 eV and 104 eV is used to determine if any oxidation (Si^{1+} to Si^{4+}, separated by $\sim$ 1 eV per formal oxidation state) occurs during surface reaction. Figure 1.24c shows peaks attributed to bulk Si^0 with no detectable high-order SiO_x (magnified region). The F 1s high-resolution spectrum exhibited a single peak (Figure 1.24d), indicative of a single source of F on the surface (F bound to C).

With the information of instrumental parameters and measured data as well as the rational design of the model for a silicon surface covered with a self-assembled monolayer (SAM), it is possible to use XPS to quantify the substitution level of Si–H by organic groups (see Chapter 3 and 4).

1.6.3 Time-of-Flight Secondary Ion Mass Spectrometry (ToF-SIMS)

Time-of-flight secondary ion mass spectrometry (ToF-SIMS) is a very sensitive surface analytical technique that provides elemental and molecular information about the surface, thin layers, and interfaces of the sample, and gives a full three-dimensional

analysis.[128] ToF-SIMS uses a finely focused ion beam to bombard a sample surface, causing the emission of secondary ions and ion clusters from the surface. Then, the ions are accelerated into a "flight tube", and their mass/charge ratios are measured by the detector.[129,130]

ToF-SIMS is essentially a destructive technique because it relies on the removal of atoms from the sample surface. However, this technique is ideally suitable for depth profiling to determine the distribution of a reaction throughout the porous structure of functionalized silicon, from the top of the film to the underlying bulk silicon. SIMS can be used to compare the quantity of a specific atom or molecular fragment by comparing the counts of functionalized porous silicon with freshly etched silicon under identical etching conditions.[10,12,83] Figure 1.25 shows an example of the depth-profiled SIMS of porous silicon surfaces before and after functionalization.[12] The reacted porous silicon has much higher intensities of C and F than the hydride-terminated silicon. The flat lines show that the relative quantities of C and F in the functionalized samples appear consistent throughout the film, suggesting even coverage throughout the porous silicon matrix.

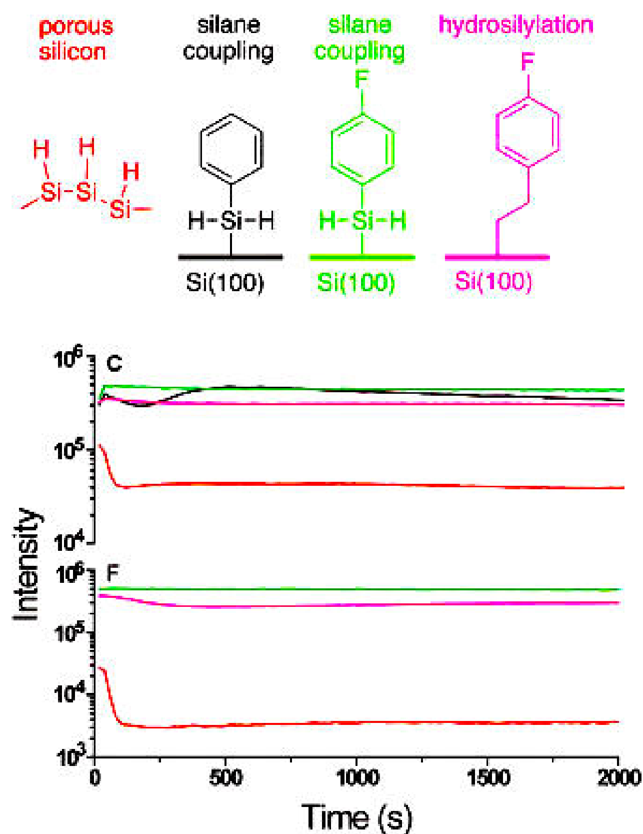

Figure 1.25. Depth-profiled SIMS of porous silicon surfaces before functionalization (red curves) and after reaction. Top: SIMS showing the level of carbon on surfaces functionalized with phenylsilane (black), 4-fluoro-phenylsilane (green), and 4-fluorophenethyl (pink) groups. Bottom: the signal level of fluorine in a 4-fluorophenylsilane-terminated surface (green) compared to that in a 4-fluorostyrene-reacted surface (pink) and a native, hydride-capped surface (red).(Reprinted with permission from ref 12. Copyright 2006 American Chemical Society.)

1.6.4 Contact Angle Measurement

Contact angle is the angle formed by a liquid at the three-phase boundary where a liquid, gas, and solid intersect.[131] As shown in Figure 3.6a, the static contact angle (or equilibrium contact angle, θ_e) is measured when a droplet is standing on the surface and the three-phase boundary is not moving. The dynamic contact angle includes two forms, the advancing contact angle (θ_a) and the receding contact angle (θ_r).[132] Continuously adding liquid into a static droplet on the surface and increasing its size gives the value of the advancing contact angle (Figure 3.6b). In contrast, the contact angle measured during a droplet shrinking is referred to as the receding contact angle (Figure 3.6c). Contact angle hysteresis is the difference between the advancing and the receding contact angle, which is a means to assess the mean roughness of the sample. If the surface is chemically homogeneous, the advancing and receding contact angles are constant and do not depend

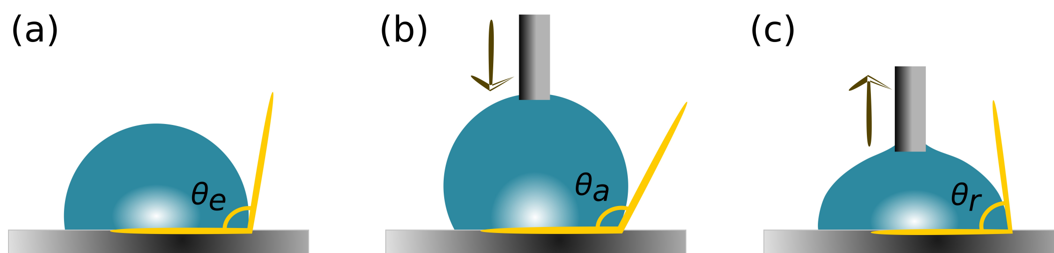

Figure 1.26. Schematic of static and dynamic angles. The static contact angle (a) is measured when a droplet is standing on the surface, while the advancing (b) and receding (c) contact angles are measured when the volume of the droplet is gradually increased or decreased, respectively.

on the size of the droplet.

A freshly etched hydride-terminated silicon surface has a contact angle of ~83°,[133] while the value will increase or decrease after surface modification, depending on the functional group on the silicon surface, the length of carbon chain, and the density of packing. For instance, work by the Kakkar group showed that, as the chain length of the monolayer decreased from $-(CH_2)_{17}-CH_3$ to $-(CH_2)_7-CH_3$, the water contact angle dropped from 110° to 90°.[134] Yu and co-workers showed that the water contact angle of the monolayer surface was determined largely by the end-group, and the less hydrophobic phenyl-terminated silicon surface has a water contact angle of ~80°.[135] Additionally, other liquids, including hexadecane, diiodomethane, and *n*-tetradecane, were used in contact angle measurements to determine the level of packing order, density, and coverage of SAM on the silicon surface.[136,137]

1.6.5 Atomic Force Microscopy (AFM) Scribing

The thickness of SAM on silicon can be determined by a variety of techniques, among which AFM scribing, an intentional scratch on the SAM layer with an AFM tip, has been used to access the monolayer thickness.[12,13,138] If the applied force is sufficient to disrupt the monolayer but not to damage the substrate, it is possible to "carve out" a rectangular trench in the monolayer, as shown in the left image of Figure 1.27. The surface was imaged first at a contact mode with minimized force (< 5 nN) with a larger scan scale. Then, the AFM tip was pushed to scratch the surface with a greater force of ~200 nN in a zoomed area. Finally, the area was imaged with a minimized force again to evaluate the film thickness or via tapping mode. The height difference between the scratched and unscratched areas is the measured film thickness, as shown at the right of Figure 1.27.[13]

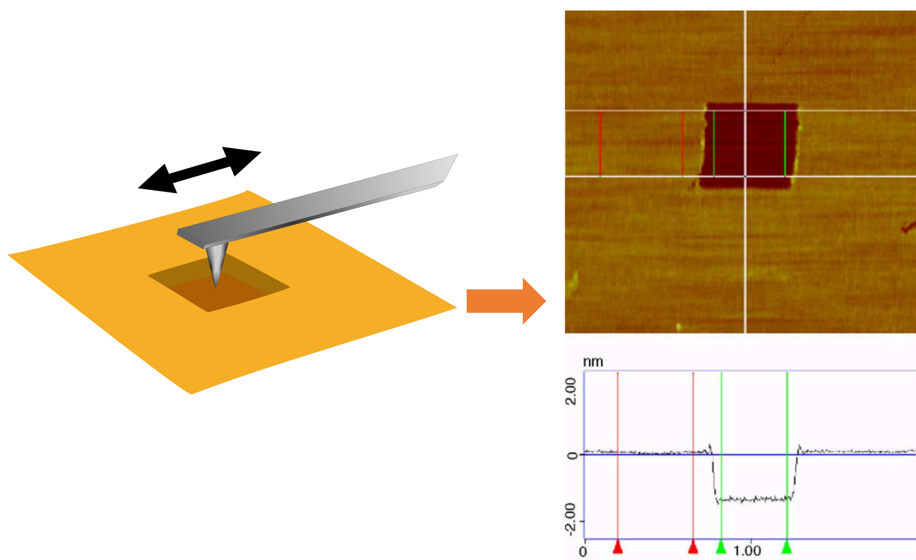

Figure 1.27. Left: an AFM scribing test. The AFM tip is brought into contact with the surface with a set force and moved across the surface. Right: an example of thickness measurment by AFM scribing on a dodecyl-terminated surface, indicating the film thickness is 1.4 nm thick. (Reprinted with permission from ref 13. Copyright 2005 Elsevier.)

1.7 Summaries and Outlook

Silicon is the foundation of the electronics industry and is now the basis for a myriad of new hybrid electronics applications, including sensing, silicon nanoparticle-based imaging and light emission, photonics, and applications in solar fuels, among others.[23,24,33,139,140] As electronic devices on silicon become progressively smaller, the fraction of atoms residing on or near the surface becomes even more significant. Various wet chemical methods have been developed for the manufacture of SAM possessing desired chemical and physical properties on oxide-free Si substrates.

Compared to the richness of the literature pertaining to silicon–carbon and silicon–oxygen bond formation, the chemistry of organic molecules bound to silicon surfaces through silicon–chalcogen bonds on surfaces is relatively new and has focused for the most part on sulfur-containing molecules. Our group functionalized silicon surfaces using dialkyl and diaryl disulfides and diselenides via radical initiation, but the sterically hindered *t*-butyl-contained disulfides did not proceed successfully. Until recently, the complete series of S, Se, and Te linkers remains elusive due to the difficulty of making $\equiv$Si$-$TeR bonds. Diorganodichalcogenides (REER, where E = S, Se, Te) are the promising molecular precursors that would secure the $\equiv$Si$-$Te bond and complete the series of chalcogenides.

The extent of the electronic property change of a monolayer-grafted silicon surface largely depends on the substitution level of the monolayer. FTIR and XPS are two methods used to calculate the coverage of the monolayer on a silicon surface. While FTIR is harnessed as a semiquantitative analysis method that assumes all reacted Si–H bonds are converted to Si–R groups and uses the decrease in the integrated intensity of the ν(Si–H) peak to obtain the substitution level,[126] XPS is a technique that truly can quantify the substitution level when one rationally designs the model of a SAM-grafted silicon surface and carefully derives equations.[141] Most work shows calculation methods using the ratio of carbon to silicon derived from XPS spectra, while the effect from unavoidable adventitious carbon during the processing and measurement was usually neglected. For monolayers that contain elements other than carbon, for instance chalcogens in chalcogenide functionalized silicon surfaces, the calculation using these heteroatoms as the atomic label is much less. However, the signals from these heteroatom labels could be very promising parameters for a more precise coverage calculation because all of them are directly from the monolayers.

Chapter 2

Direct Thermal and Microwave Initiated Si–E (E = S, Se, and Te) Bond Formation*

2.1 Recent Development in Si–E Bond Formation

The nature of the connection to silicon for electronic applications is critical as the chemical identity of this linkage can have profound effects on the electronics of the underlying semiconductor.[142,143] For instance, the junction resistance of silicon-based solar generators can be reduced by surface functionalization, thus optimizing the electrical transport throughout the system.[25] The thickness of a self-assembled monolayer (SAM) or the length of molecular wires on a functionalized surface also will have a significant impact on electron-transport mechanisms.[144] For quantum dots composed of crystalline silicon, the chemical nature of the silicon interface greatly affects the underlying electronics, thus modulating the wavelength of emission of photoluminescence.[29,145] Recent experimental and theoretical results have provided insights into the fundamentals and have shown that the work function of silicon surfaces can be tuned through the choice of head groups through which a self-assembled monolayer (SAM) can be bonded.[42,146] Fagas and co-workers predict that tuning of the work function by up to 1.73 eV is possible through tailoring of the chemical nature of the SAM as a result of modulation of surface dipoles.[4] Bonding of SAMs through Si–O, Si–S, Si–Se, Si–Te, and Si–N bonds, as well as Si–X (X = halide) coverage were examined. For heavier atoms (Te versus Se versus S versus O), additional electronic states are available, which can affect electron transfer to and from molecules attached to a silicon surface.[42,106]

In contrast to the vast literature of SAMs bonded to silicon through ≡Si–C[147,148]

*The contents of this chapter have been copied and/or adapted from the following publication: Hu, M.; Liu, F.; Buriak, J. M. Expanding the Repertoire of Molecular Linkages to Silicon: Si–S, Si–Se, and Si–Te Bonds. *ACS Applied Materials & Interfaces* **2016**, *8*, 11091–11099.

and ≡Si−O[149,150] linkages, the development of silicon-chalcogenide bond-forming reaction schemes on silicon surfaces has only just begun, in spite of the strong impetus to study, understand, and apply them. The field of Si−S- and Si−Se-based SAMs on surfaces via solution (non-vacuum) chemistry can be summarized in one paragraph. The first literature report of ≡Si−SR bond formation on a hydrogen-terminated flat silicon was driven by UV irradiation in the presence of alkanethiols.[110–112] 1-Dododecanethiol forms monolayers on Si(111)−H with 2–4 h of illumination with UV light[110,111] or 90 min of white light.[112] 1-Octadecanethiol was shown to react with Si(111)−H at 150 °C, overnight when used as a solution[113] or within 1–2 h when applied neat.[114] Acetylchalcogenidoarene- derivatized (Ar-EAc, E = O, S, and Se) porphyrins can be attached covalently to silicon surfaces via ≡Si−S and ≡Si−Se bonds through a 2-min high-temperature reaction at 400 °C.[105,106] Recently, Korgel and co-workers showed that silicon nanoparticles could be functionalized with a monolayer of ≡Si−S−*n*-dodecyl through a 12-h thermal reaction at 190 °C.[151] Our group showed how porous silicon could be functionalized through a room-temperature radical-initiated process using dialkyl and diaryl disulfides and diselenides, but the chemistry did not proceed with sterically hindered disulfides (i.e., with *t*-butyl substituents) or ditellurides (the latter because of very low solubility).[10] Finally, to the best of our knowledge, there are no reports of SAMs attached to silicon through ≡Si−Te bonds. To summarize, the chemistry of silicon-chalcogenide-based interfacing of molecules on silicon surfaces is still in its very early stages when compared to the richness of the literature pertaining to silicon−carbon and silicon−oxygen bond formation.

In this chapter, we describe the 15-s to 2-min functionalization chemistry of readily accessible and commercially available dichalcogenide molecules, those containing S−S, Se−Se, and Te−Te bonds, with hydrogen-terminated silicon (Figure 2.1). These dialkyl and diaryl dichalcogenide molecules are practical to work with and are far less odorous than the corresponding chalcogenols (thiols and selenols). In the case of the tellurium compounds,unhindered tellurols are unstable,[152,153] whereas the ditellurides are stable and easy to work with.[154] Thus, the direct reaction with the ditellurides may be one of the only viable routes to SAMs based upon Si−Te bonds. The reactions are driven by either microwave irradiation in 15 s or less or on a hot plate in 2 min or less. Comparison with the molecular literature of silanes and chalcogenides provides insights into the mechanism.

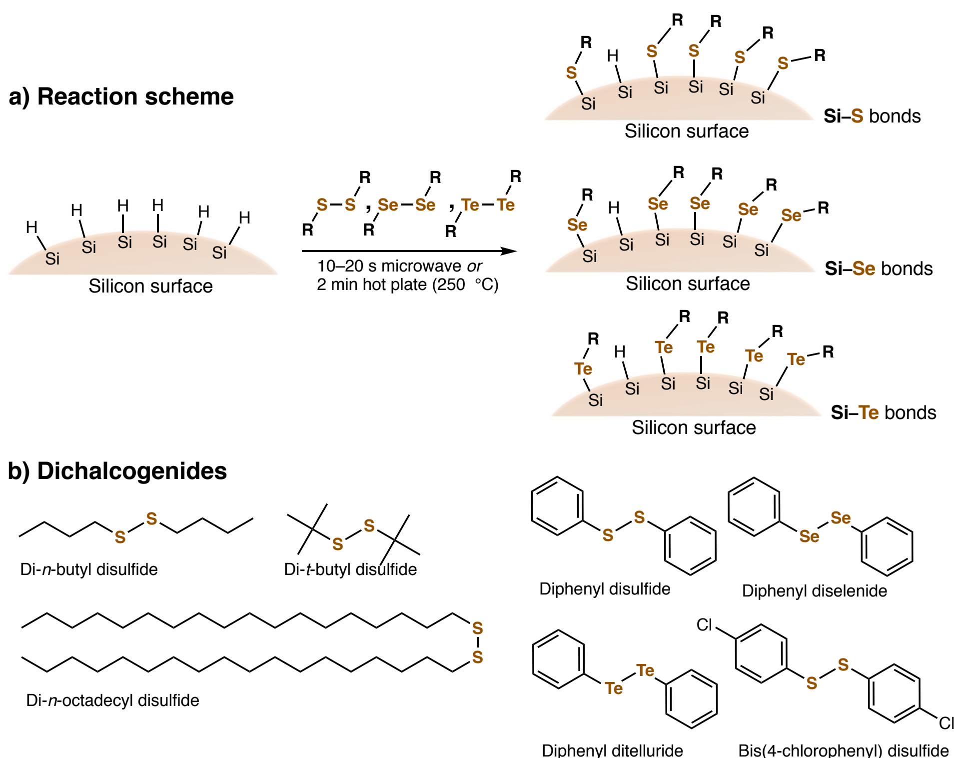

Figure 2.1. Reaction approach to functionalize silicon. (a) Overall reaction scheme outlining the approach to Si–S, Si–Se, and Si–Te bond formation on silicon surfaces. (b) Seven dichalcogenide molecules that were screened for reactivity under microwave irradiation or direct thermal heating (hot plate) on hydride-terminated porous silicon.

2.2 Materials and Methods

2.2.1 Materials

Silicon wafers (100, prime-grade, n-type, P-doped, 1–3 Ω·cm, 450 ± 25 μm) were obtained from Virginia Semiconductor, Inc. Di-*n*-butyl disulfide (97%), di-*t*-butyl disulfide (97%), diphenyl disulfide (99%), diphenyl diselenide (98%), diphenyl ditelluride (98%), bis(4-chlorophenyl) disulfide (97%), 1-octadecanethiol (98%), *t*-butylthiol (2-methyl-2-propanethiol, 99%), and aluminum oxide (activated, neutral, Brockmann Neutral I, standard grade, ∼150 mesh, 58 Å) were purchased from Sigma-Aldrich. Alumina was dried in a 100 °C oven for more than 24 h before being transferred into a glovebox while still hot. Di-*n*-octadecyl disulfide (98%) was purchased from Alfa Aesar. All the reagents were stored at –20 °C inside an argon-filled glovebox. Molecular sieves (type 4A, 1/16 in. pellets, for selective adsorption) were purchased from Caledon Laboratories, Ltd. Ethanol (absolute) and acetone (reagent) were purchased from Fisher. HF (aqueous, 49%, semiconductor grade) was purchased from J. T. Baker. Degassed

and dry dichloromethane was obtained from a solvent purification system (Innovative Technologies, Inc.), taken into a glovebox in a standard dry Schlenk flask, and dried over molecular sieve for 24 h in the glovebox prior to use. All liquid chemicals were passed through a fresh column of alumina prior to use in the glovebox.

2.2.2 Porous Silicon Preparation

Porous silicon was prepared according to the method previously described in the literature.[155,156] Silicon wafers were cut into 1.4 cm^2 (1.2 cm $\times$ 1.2 cm) pieces, cleaned by sonication (10 min in 1:1 acetone/ethanol), rinsed with ethanol, and dried with an argon stream. The unpolished side of the silicon wafer was in contact with an aluminum foil tongue electrode to act as the anode, and a Pt wire loop electrode was used as the cathode. Using a 24.5% HF/25.5% H_2O/50% EtOH solution as an electrolyte/etchant, the silicon was anodized at 7.6 mA cm^{-2} for 90 s and then 76 mA cm^{-2} for 120 s with full white-light illumination ($\sim$40 mW cm^{-2}) using an ELH bulb. The freshly etched silicon was rinsed with excess ethanol, immersed in pentane, dried with an argon stream, and stored in an argon-filled airtight glass vial in the dark.

2.2.3 Determination of Heating Rate and Profile

The heating rate and heating profiles of the porous silicon samples were determined before the actual chemical reaction on dummy porous silicon samples, without the dichalcogenide or thiol reagents because of the potential of reactivity of the polyimide fluorescence optical fiber temperature sensor with these reagents (vide infra). A porous silicon sample was prepared in an identical fashion and was heated under the same conditions to determine the heating rate and heating profile. The fiber optic probe cannot exceed 250 °C without succumbing to permanent damage.

Reactions under microwave irradiation were performed in a modified domestic Panasonic microwave oven (model number NNST651W, purchased from Walmart), as described previously.[157] A mortar containing 100 g of SiC powder (200–450 mesh, purchased from Sigma-Aldrich) was placed in the right side of the microwave oven to absorb excess microwave radiation and prevent damage to the microwave. A fluorescence-based fiber optic temperature probe (model number PRB-G40-2.0M-ST-C with polyimide tip and calibration to 250 °C and accuracy of ±0.5 °C obtained from OSENSA Inc.) was inserted through small holes drilled in the side of the microwave oven and Teflon chamber (Figure 2.2a and ref[157]). A freshly prepared porous silicon piece was placed in the Teflon chamber, and the fiber optic probe was placed in direct physical contact

with the silicon for in situ monitoring (Figure 2.3a). The temperature profile is plotted in Figure 2.3c. After the microwave oven was turned on, a 4-s lag was required to activate the cavity magnetron, so the temperature of the silicon wafers did not change in the first 4 s. After 4 s, the silicon wafer increased in temperature, reaching 240 °C in 12 s, after which the microwave oven was shut off manually. This was followed by a cooling down of the wafer to 50 °C in 88 s and reaching 30 °C in 198 s. The temperature was monitored and recorded until the wafer had cooled to around 25 °C. It is assumed that samples irradiated for longer than 12 s will increase further in temperature, above 240 °C.

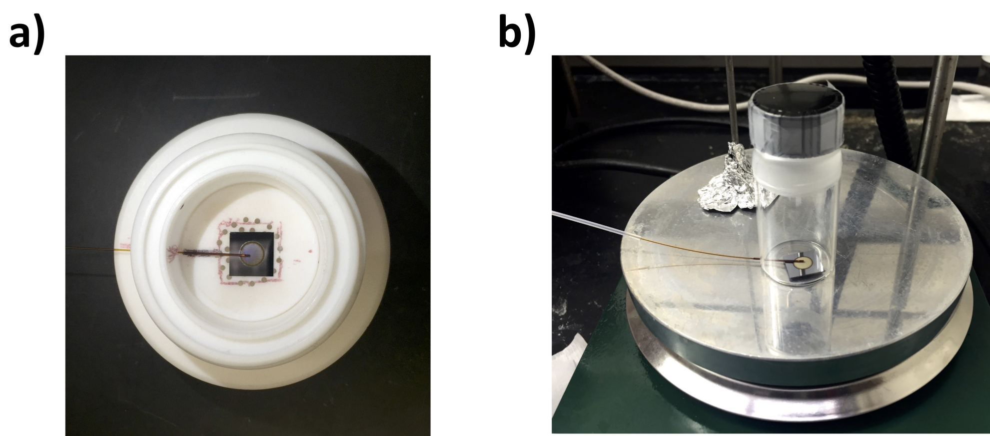

Figure 2.2. (a) Photo of the microwave irradiation apparatus used for determination of the heating profile (Figure 2.3c). (b) Photo of a glass vial with a small hole drilled in the side to enable the fiber optic temperature probe to be threaded into the interior of the vial and make contact with the silicon sample. For the actual experiments with chalcogenide compounds, a completely sealed vial was used.

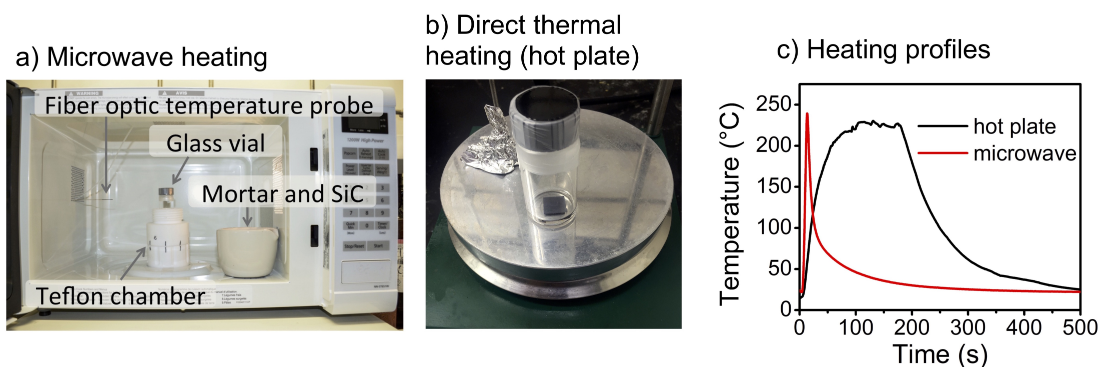

Figure 2.3. (a) Photograph of the microwave heating apparatus, comprised of a microwave for domestic use, a fiber optic temperature probe, and the sample vial residing within the Teflon chamber. (b) Photograph of the direct thermal heating apparatus (hot plate). (c) Temperature profiles for the heating rates of 1.2 $\times$ 1.2 cm^2 porous silicon samples that were heated in the absence of reagents under microwave and direct heating. Temperature profiles were determined on dummy porous silicon samples in the absence of reagents because the vials are sealed to prevent contamination, oxidation, and damage to the polyimide probe.

Determination of the heating profile of porous silicon on a hot plate was carried out by placing a fiber optic probe in direct contact with a porous silicon wafer inside the same type of glass vial used for the experiments with chalcogenide. A small hole was, however, drilled into the vial to enable the fiber optic probe to be threaded through the hole to make direct contact with the dummy piece of porous silicon (Figure 2.2b). The hot plate temperature was set to 250 °C. After 2 min, the wafer and the probe were removed from the hot plate. The temperature was monitored and recorded until the wafer had cooled to around 25 °C.

2.2.4 Reactions with the Dichalcogenides and Thiols

Before carrying out each reaction, the liquid molecules to be used, including the di-*n*-butyl disulfide, di-*t*-butyl disulfide, and *t*-butylthiol were passed through a fresh column of alumina before use. Solids (generally the diaryl dichalcogenides) were used with no further purification. Twenty drops of liquid reagent or about 0.05 g for solids, were placed on a porous silicon substrate inside a 20-mL glass vial. The melting points of all the solids used here were lower than the maximum temperature reached, and thus they would liquefy in situ; the melting points of PhEEPh are 61 °C (E = S), 61 °C (E = Se), and 66 °C (E = Te). The face of the silicon with the etched porous silicon was placed upside down to enforce spreading of the reagent, thus forming a sandwich of glass–reagent–porous silicon. The glass vials were then sealed with multilayers of parafilm entwined round the cap (Figure 2.3a,b).

For the microwave reaction, the sealed glass vial containing the reagent and porous silicon substrate was removed from the glovebox and put in the center of a Teflon chamber, which was marked and fixed in the center of the microwave oven (Figure 2.3a), followed by microwave irradiation. When the microwave oven was shut off, the glass vial was transferred to the glovebox for rinsing. For the hot plate reactions, the sealed glass vial containing the reagent and the porous silicon substrate was put on a 250 °C hot plate for the desired reaction time (Figure 2.3b). On completion of the reactions (microwave or hot plate), the porous silicon samples were soaked in dry dichloromethane for 5 min and rinsed three times with a forceful stream of dry dichloromethane from a pipet to remove excess unreacted reagents. The samples were removed from the glovebox (in the sealed glass vial), dried with argon gas, and then analyzed.

2.2.5 Analytical Techniques

Scanning electron microscopy (SEM) images were obtained with a Hitachi S-4800 FE-SEM with an accelerating voltage of 15 kV. FTIR spectra were collected with a Nicolet Nexus 760 spectrometer with a MCT detector cooled with liquid nitrogen and a nitrogen-purged sample chamber (32 scans, 4 cm^{-1} resolution). X-ray photoelectron spectroscopy (XPS) was taken on a Kratos Axis 165 X-ray photoelectron spectrometer in the Alberta Centre for Surface Engineering and Science (ACSES), now part of the University of Alberta NanoFAB. Time-of-flight secondary ion mass spectroscopy (ToF-SIMS) depth analysis was obtained on a ToF-SIMS IV-100 (ION-TOF GmbH) at ACSES. The pSi samples were sputtered with a 1 keV Cs^+ ion source, leading to a crater size of 150 μm × 150 μm, with analysis by Ga^+ at 25 keV, 35 μm × 35 μm.

2.3 Results and Discussion

2.3.1 Hydrogen-terminated Surfaces

Porous silicon was applied as the test bed for surface chemistry development because it enables exquisite analysis by FTIR, XPS, and the depth profiling using techniques such as ToF-SIMS, among others.[126,158] The surface of hydride-terminated porous silicon is related closely to that of other hydride-terminated nanocrystalline surfaces (e.g., silicon nanocrystals) and hydride-terminated Si(100) because they are capped by Si−H, Si−H_2, and Si−H_3 groups; their FTIR spectra, as a result, are very similar.[159–161] Porous silicon was etched electrochemically from single-crystal Si(100) wafers with ethanolic HF (aqueous) to provide high-surface-area, hydride-terminated silicon samples whose surface is essentially oxide-free.[155,156] The etched porous layer showed a thickness of around 20 μm (Figure 2.4). The chemistry of porous silicon is related closely to the reactivity of other hydride-terminated flat and nanocrystalline surfaces; thus, observed

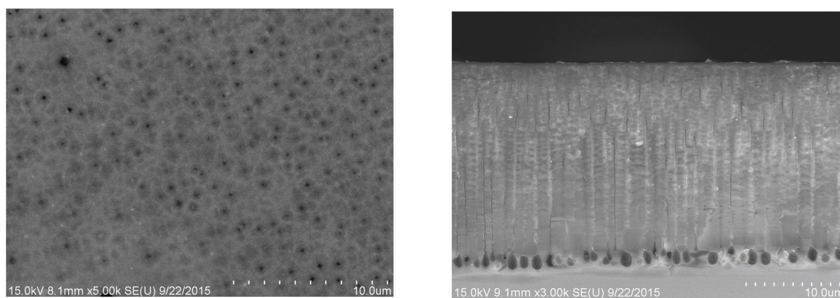

Figure 2.4. Top view (left) and cross-section SEM images of freshly prepared porous silicon.

reactions are typically generalizable to other morphologies.[48,158] Because hydrogen-terminated silicon surfaces are metastable in laboratory ambient room temperature and can resist oxidation on a time scale of minutes, they are an ideal interface for more sophisticated functionalization of silicon. Si−H-terminated surfaces are, however, still sensitive with respect to low concentrations of dissolved oxygen, particularly under conditions required to promote functionalization (e.g., heat, illumination, radical initiators), and so even very low oxygen levels (ppm) can compete effectively with the desired chemistry, leading to mixed oxide surfaces.[162] To favor efficient and clean reactions and to compete with oxidation, neat reagents and very short reaction times were preferred.

2.3.2 Rapid Silicon−Chalcogen Bond Formation

As shown in Figure 2.1, the reaction approach to functionalize the silicon involves rapid thermal heating of a dialkyl or diaryl dichalcogenide, a molecule containing a S−S, Se−Se, or Te−Te bond, with hydride-terminated porous silicon. A small quantity of the neat dichalcogenide molecule was placed on the porous silicon in a glass vial under an inert atmosphere (sealed inside an argon-filled glovebox) and then placed in a standard domestic microwave for 10–15 s or on a hot plate set to 250 °C for 2 min, as outlined in Figure 2.3. The use of microwave irradiation to promote heating on silicon is well-established; it is known that lightly doped silicon wafers heat up rapidly upon microwave irradiation, that the rate of heating is dependent upon doping levels, and that in the extreme case silicon can reach melting temperatures.[157] Boukherroub and co-workers used microwave irradiation to reduce the time required for alkene hydrosilylation on lightly doped porous silicon from hours to about 10 min.[95] In this work, 1.2×1.2 cm^2 samples of n-type, P-doped, 1–3 Ω·cm Si(100) reach 240 °C in approximately 10–12 s with microwave irradiation, as monitored with a fiber optic temperature probe in direct contact with the silicon. In the second approach to heating, the same sample size of porous silicon in a glass vial is placed onto a hot plate set to 250 °C; monitoring of the temperature with the fiber optic probe shows that it takes approximately 100 s to reach 230 °C (Figure 2.3c).

Figure 2.1 shows the seven dialkyl and diaryl dichalcogenide molecules examined in this work. Analysis of the microwave and hot plate reactions was carried out first by transmission mode FTIR (Figure 2.5). In all cases, the reactions were carried out for different lengths of time, and the best spectra, in terms of low oxidation and high incorporation levels, are shown here. The full series of spectra for each compound with

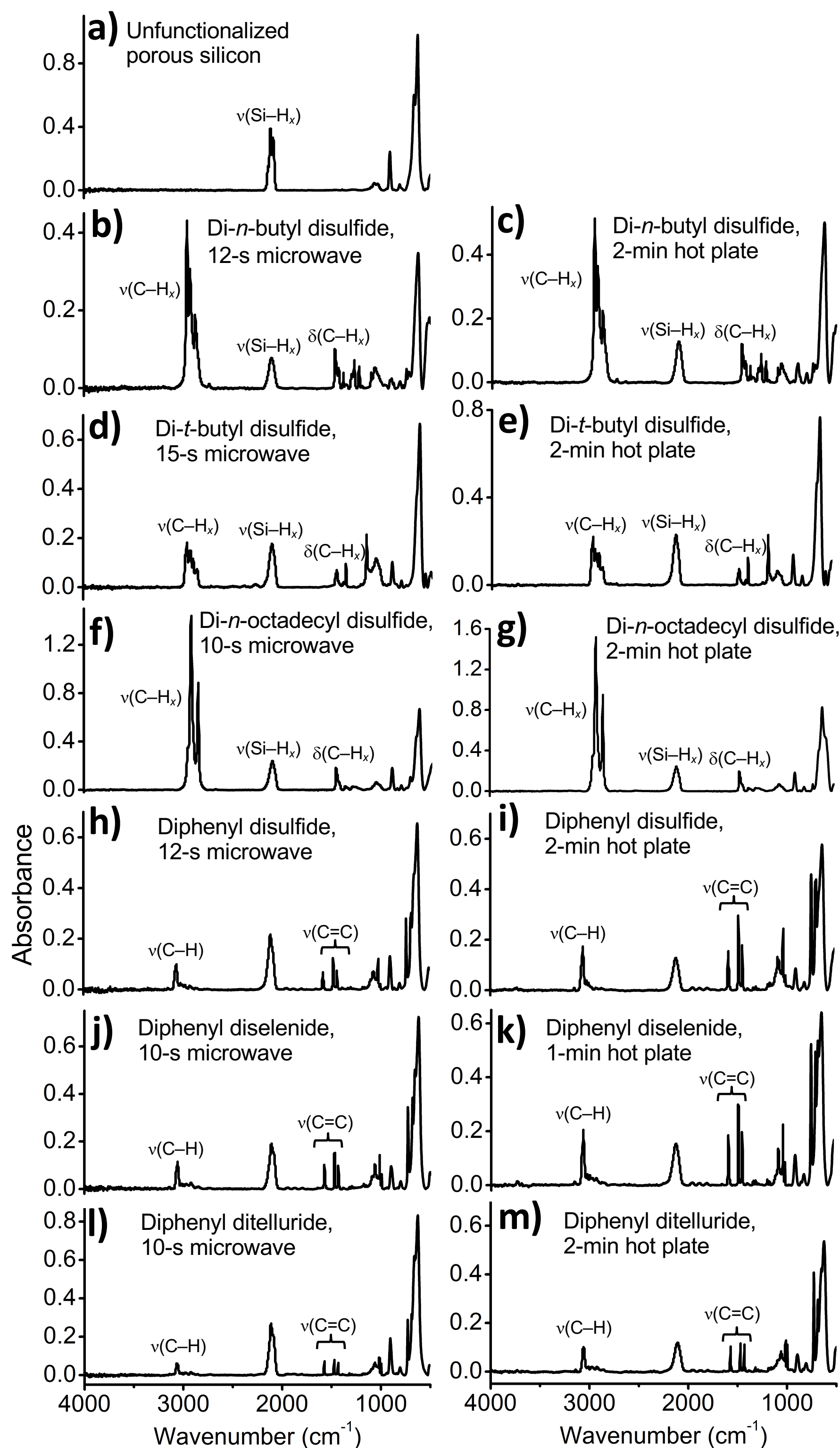

Figure 2.5. FTIR spectra (transmission mode) of (a) freshly etched unfunctionalized porous silicon and (b–m) porous silicon samples reacted with the chalcogenide reagents for the time indicated under microwave irradiation (left) and hot plate heating (right). Hot plate temperature was set to 250 °C; sample temperature reaches 230 °C.

different thermal treatment times is shown in the supporting information of the published paper.[83] Functionalized surfaces were determined to have low oxidation levels by comparing the ν(Si−O) feature at 1000–1100 cm^{-1} to that of the freshly etched, unfunctionalized porous silicon sample in Figure 2.5a as well as the features corresponding to the ν(Si−H$_x$) of oxygen-back-bonded Si−H groups above 2200 cm^{-1} that result from oxygen insertion into nearby Si−Si bonds.[155,163] In all cases, the broad compilation of ν(Si−H$_x$) modes, centered around 2100 cm^{-1}, decreases in intensity upon reaction. The three RSSR molecules, where R is aliphatic (Figure 2.5b–g, R = *n*-butyl, *t*-butyl, and *n*-octadecyl), exhibit profiles for their ν(C−H$_x$) modes in the region of 2850–2960 cm^{-1} that correspond to their respective functional groups upon comparison to the FTIR spectra of the neat parent chalcogenide molecules. The linear di-*n*-butyl and di-*n*-octadecyl disulfides react cleanly without obvious oxidation (Figure 2.5b,c,f,g). The highly hindered di-*t*-butyl disulfide, however, consistently shows some oxidation in the ν(Si−O) stretching region at ∼1000 cm^{-1} upon microwave irradiation (Figure 2.5d) as well as the appearance of a small feature corresponding to oxygen-back-bonded Si−H$_x$ groups above 2200 cm^{-1}, and it requires more time (15 s of microwave irradiation versus 10 or 12 s for all other reagents). Less oxidation is noted, however, for the hot plate reaction of di-*t*-butyl disulfide (Figure 2.5e). The diphenyl chalcogenides, PhSSPh, PhSeSePh, and PhTeTePh, all reacted cleanly to yield FTIR spectra corresponding to expected modes of a phenyl ring, presumably Ph−S−Si≡, Ph−Se−Si≡, and Ph−Te−Si≡ moieties, with little oxidation.

To determine the elemental nature of the bond to the silicon (S, Se, or Te) and the level of oxidation, X-ray photoelectron spectroscopy (XPS) was carried out. The RSSR molecules all result in sulfur incorporation on the silicon surfaces (Figures 2.6a,c,e,g, and 2.7), the energy of which corresponds to the known binding energy of ≡Si−S−R groups.[10,111] The corresponding silicon Si 2p spectra reveal little oxidation, which would appear as conspicuous higher energy features above 102 eV.[25,125] The XPS spectra of the products of the reaction of PhSeSePh and PhTeTePh are shown in Figure 2.6i–l and reveal the presence of Se and Te, respectively, with little accompanying oxidation, at the expected binding energies.[10,164] The disulfide molecule, bis(4-chlorophenyl) disulfide, which has a chlorine tag, also was reacted with the porous silicon, and the distinctive Cl 2p doublet was observed at 200.6 and 202.2 eV, in addition to the sulfur feature (Figure 2.7). XPS data for the chalcogenide features of the starting materials (molecules REER, E = S, Se, and Te), as well as reported values for ≡Si−ER when known, are shown in Figure 2.6 and Tables 2.1 and 2.2.

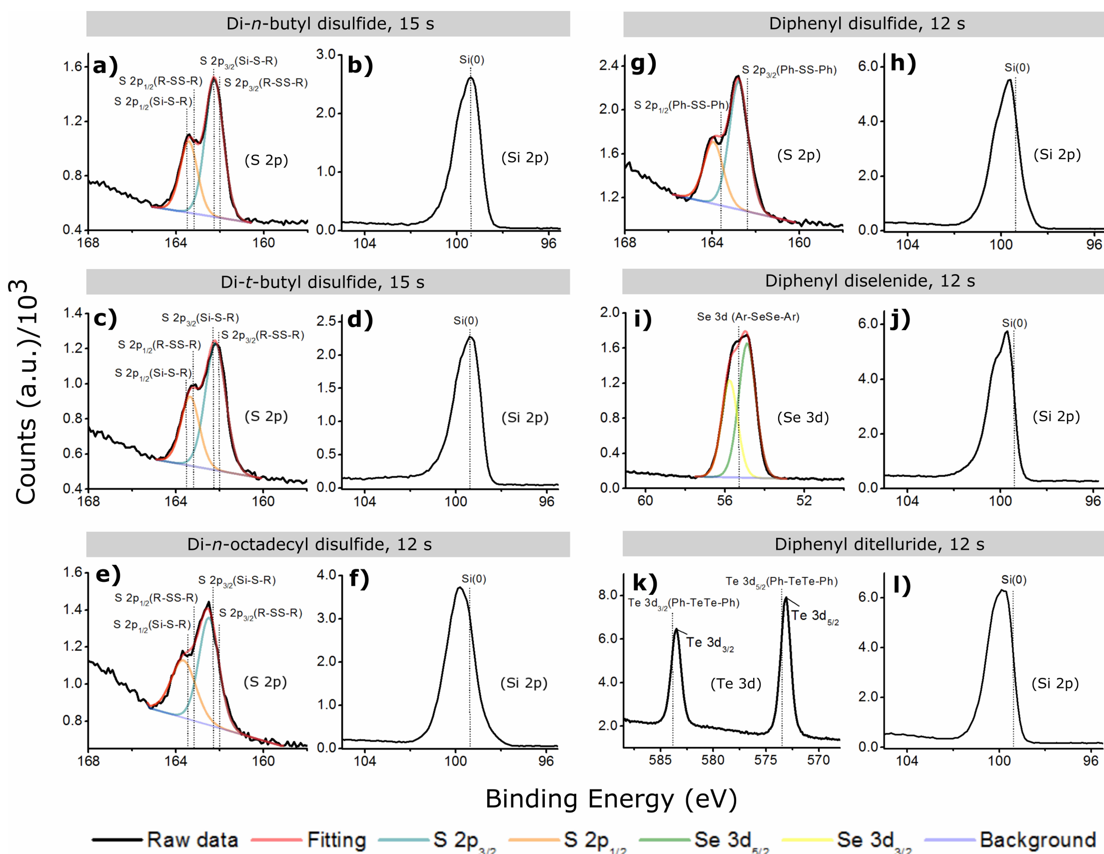

Figure 2.6. XPS of porous silicon samples after reaction with (a–h) the disulfide reagents, (i and j) diphenyl diselenide, and (k and l) diphenyl ditelluride under microwave irradiation for the time indicated. The data from this figure and supporting literature references are tabulated in Tables 2.1 and 2.2.

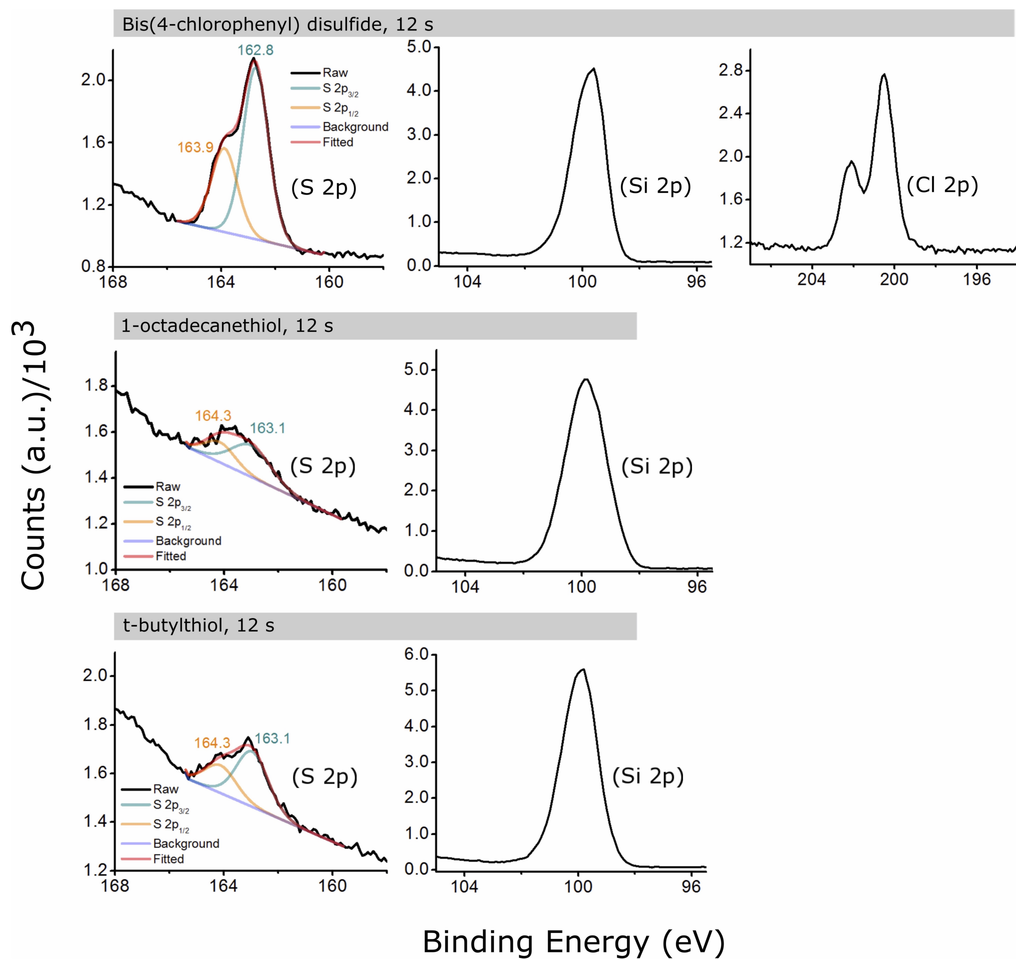

Figure 2.7. XPS of porous silicon samples after reaction with the reagents under microwave irradiation for the time indicated.

Table 2.1. Summary of XPS Data, Corresponding to Figure 2.6

	Si 2p (eV)	S 2p (eV)	Se 3d (eV)	Te 3d (eV)	Cl 2p (eV)
Di-*n*-butyl disulfide	99.5	162.3, 163.4			
Di-*t*-butyl disulfide	99.5	162.2, 163.4			
Di-*n*-octadecyl disulfide	99.8	162.5, 163.7			
Diphenyl disulfide	99.7	162.8, 164.0			
Diphenyl diselenide	99.7		54.9, 55.8		
Diphenyl ditelluride	99.8			573.1, 583.5	
Bis(4-chlorophenyl) disulfide	99.7	162.8 163.9			200.6, 202.2
1-Octadecanethiol	99.8	163.1,164.3			
t-Butylthiol	99.9	163.1, 164.3			

Table 2.2. Representative Peaks of S 2p, Se 3d, and Te 3d, Corresponding to Figure 2.6

	S 2p (eV)	Se 3d (eV)	Te 3d (eV)	Reference
R–SS–R	162.0 and 163.2			165
Si–S–R	162.3 and 163.5			111
Ph–SS–Ph	162.4 and 163.6			166
Ar–SeSe–Ar		55.3		167
Ph–TeTe–Ph			573.5 and 583.9	168

XPS analyses were complemented by depth profiling with ToF-SIMS, which provides information regarding elemental content, uniformity of functionalization throughout the layer, and comparative information regarding substitution levels. In all of the ToF-SIMS spectra in Figure 2.8a–f, the baseline carbon level of a freshly etched porous silicon sample is shown (dotted black line) in each panel for comparison. It should be noted that because of the thickness of the porous silicon layer (20 μm) on the bulk wafer, the 2500-s of etching by ToF-SIMS here does not reach the porous silicon−bulk silicon interface. As can be seen for the porous silicon samples functionalized disulfides, RSSR (Figure 2.8a–d), the level of carbon and sulfur increases by 1 or more orders of magnitude when contrasted with the unfunctionalized control. The substitution levels appear consistent and flat throughout the porous silicon film. The diphenyl diselenide- and ditelluride-functionalized porous silicon surfaces show similar results for both C and Se (Figure 2.8e) and C and Te (Figure 2.8f). Bis(4-chlorophenyl) disulfide, with its chlorine label, also was reacted with porous silicon and shows 2–3 orders of magnitude increase in the level of chlorine compared to that of the unfunctionalized control, as well as much higher levels of carbon and sulfur (Figure 2.9). In all cases, the levels corresponding to the Si−E fragments (E = S, Se, and Te) increase by 2 orders of magnitude over those in the unfunctionalized sample, providing further evidence to support the claim of a ≡Si−E bond.

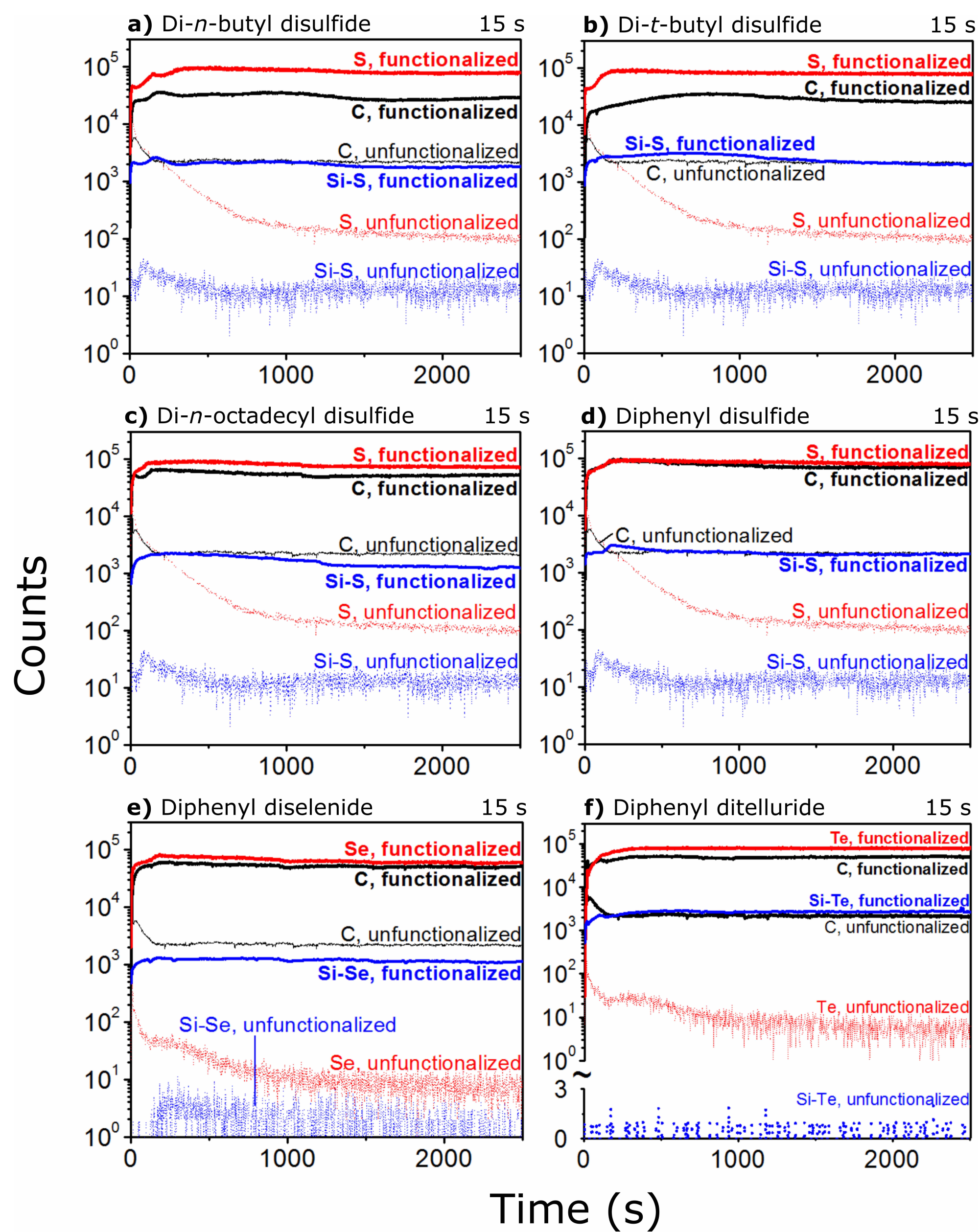

Figure 2.8. ToF-SIMS analysis of functionalized porous silicon samples. The thick curves represent the porous silicon samples after reaction with (a–d) the disulfide reagents, (e) diphenyl diselenide, and (f) diphenyl ditelluride, all under microwave irradiation for 15 s. The same sample of unfunctionalized porous silicon was used as the comparison (reference sample, dotted line) in all spectra.

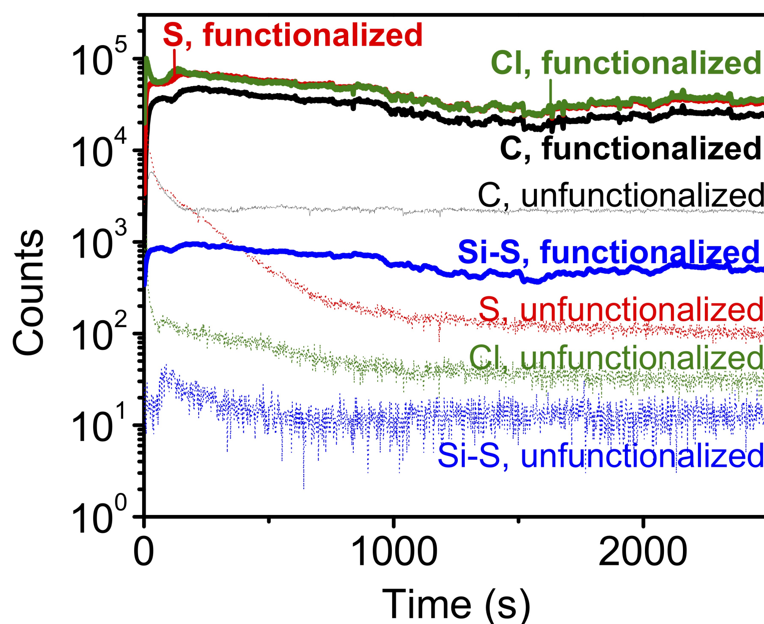

Figure 2.9. ToF-SIMS analysis of functionalized porous silicon samples. The thick curves represent the porous silicon samples after reaction with bis(4-chlorophenyl) disulfide under microwave irradiation for 15 s. The same sample of unfunctionalized porous silicon was used as the comparison (reference sample, dotted line).

2.3.3 Mechanism

Possible reactions that could play a role in the mechanism of ≡Si−E (E = S, Se, and Te) bond formation on silicon surfaces are shown in Figure 2.10. Four different reactions need to be considered, including thermally driven homolytic silicon−hydrogen bond and silicon−silicon bond cleavage (Figures 2.10a,b), well-established radical equilibria between thiols and silanes (Figure 2.10c), and dichalcogenide homolysis to cleave the E−E bond (Figure 2.10d). Because there is a rich body of literature pertaining to the molecular reactivity of disulfides with silane radicals,[78,88,107,108,122] it is proposed that the key intermediate is the surface silyl radical, or dangling bond, represented by ≡Si•. This surface radical can be accessed via three possible routes. The first route is a direct thermally driven homolytic bond cleavage, as shown in Figure 2.10a, which has been postulated as a key step in thermally driven hydrosilylation on hydride surfaces.[81,124] The second route to a surface-bound ≡Si• is the more recently proposed Si−Si bond cleavage of ≡Si−SiH_3 species, resulting in loss of •SiH_3 , shown in Figure 2.10b.[169] Porous silicon is terminated with ≡SiH, =SiH_2, and −SiH_3 groups, of which the single Si−Si bond is the weakest bond present (bond dissociation energy is 70–80 kcal/ mol)[86] compared to the Si−H bonds (bond dissociation energies of 85–90 kcal/mol).[86] Neale and co-workers[169] have shown that cleavage of ≡Si−SiH_3 groups

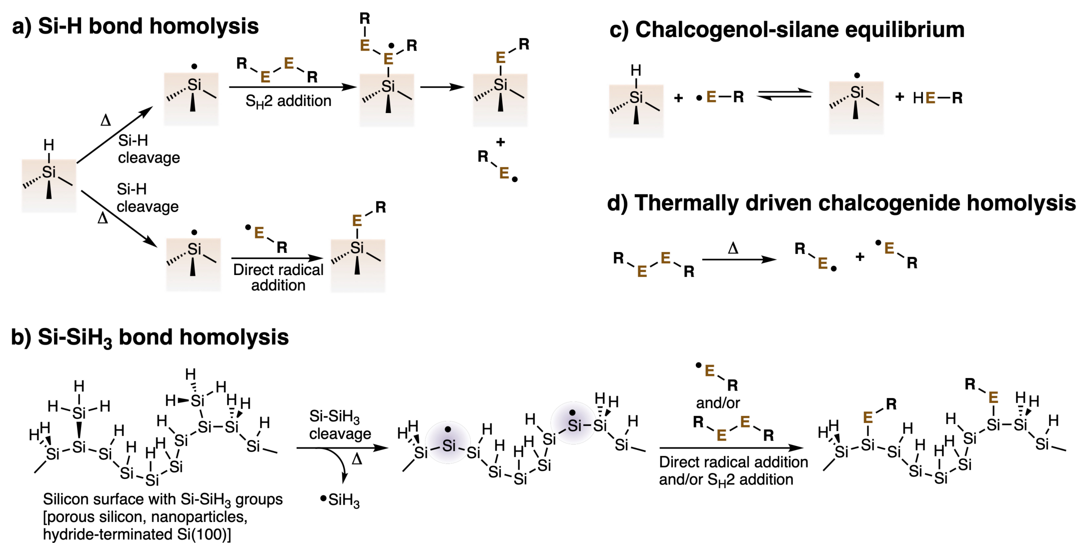

Figure 2.10. Possible mechanisms that could play a role in formation of ≡Si–E bonds (E = S, Se, and Te) on silicon surfaces. (a) Direct homolysis of Si−H bonds by heat, leading to formation of silicon radicals on the surface, and subsequent reaction with a dichalcogenide or a chalcogenyl radical. (b) Scheme for hemolysis of Si−SiH_3 bonds on the surface, leading to silicon radicals. (c) Radical-based chalcogenol-silane equilibrium. (d) Homolysis of dichalcogenides, leading to chalcogenyl radical formation.

on hydride-terminated silicon nanoparticles may be the dominant initiation step for hydrosilyation with alkenes. The third route to formation of ≡Si• is removal of the silicon-bound H• by a chalcogenyl radical, shown in Figure 2.10c.[108,169,170] The thiyl, selenyl, and telluryl radicals would result from homolysis of the weak S−S, Se−Se, or Te−Te bond, which have bond dissociation energies of 53–57, ∼40, and ∼30–35 kcal/mol, respectively, under these high-temperature conditions (Figure 2.10d).[171] Thiyl and selenyl radicals are known radical propagators, therefore, telluryl radicals could play a similar role, plucking hydrogen atoms from the silicon surface to produce silyl surface radicals, particularly under high concentrations of reagents.[119,172,173]

Assuming the central role of the ≡Si• radical species, the formation of the ≡Si−E bond could occur through two possible pathways. As is well-established in the molecular silane radical literature,[10,107] dialkyl and diaryl disulfides and diselenides can add to the silyl radical through an S_H2 mechanism (Figure 2.10a), producing a sulfuranyl or seleranyl intermediate that then collapses to form the ≡Si−ER final product, releasing an equivalent of •ER (E = S and Se). The equilibria between silanes and thiols under radical conditions have been studied extensively, and although there are few examples of direct coupling of a silane radical, ≡Si•, and a chalcogenide radical, •ER, to produce ≡Si−ER bonds, there is precedent.[123] Thus, the possibility of direct coupling is shown in Figure 2.10a.

To help provide insight into the mechanism, the reactivity of the alkanethiols, 1-

octadecanethiol and *t*-butyl thiol, via microwave heating was examined by FTIR and XPS (shown in Figures 2.11, 2.12, 2.13, 2.14, 2.15, and 2.7). Both reactions resulted in low incorporation levels on the basis of comparison with the spectra of the reaction with di-*n*-octadecyl disulfide (Figure 2.5f,g), in spite of a slightly longer exposure to microwave irradiation (10 s for the disulfide versus 15 s for the thiol). The low yield of ≡Si−SR formation with the thiol precursor compared to that of the corresponding dialkyl disulfide suggests that the stronger S−H bond[174] (bond dissociation energy ∼ 84 kcal/mol) translates to lower yields of the homolysis product, RS•, and hence slower kinetics. Korgel and co-workers recently proposed that during the thermal reaction of dodecanethiol with hydrogen-terminated silicon nanoparticles, the thiol could be oxidized in situ to produce di-*n*-dodecyl disulfide, which then reacts with the surface.[151] Although the mechanism involving dichalcogenides proposed here requires further investigation, it appears that the dialkyl and diaryl disulfides are more reactive under these conditions than the corresponding thiols and that this difference of reactivity could be due to the ease of homolysis of the dichalcogenide bond, E−E, compared to that of the RE−H bond, which then enables radicals to propagate and react.

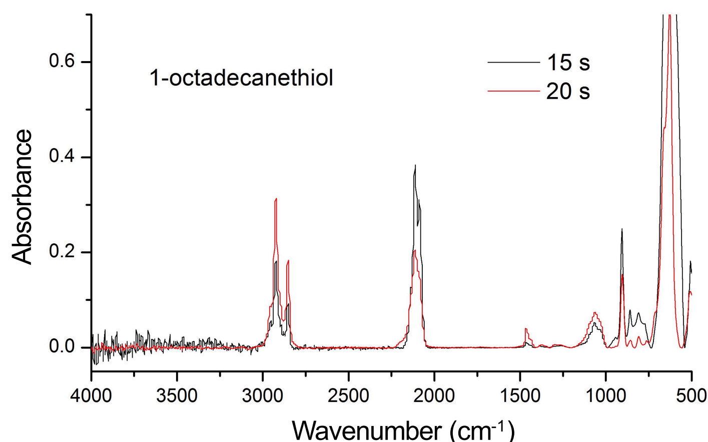

Figure 2.11. FTIR spectra of modified porous silicon, prepared with 1-octadecanethiol under microwave irradiation for 15 s and 20 s.

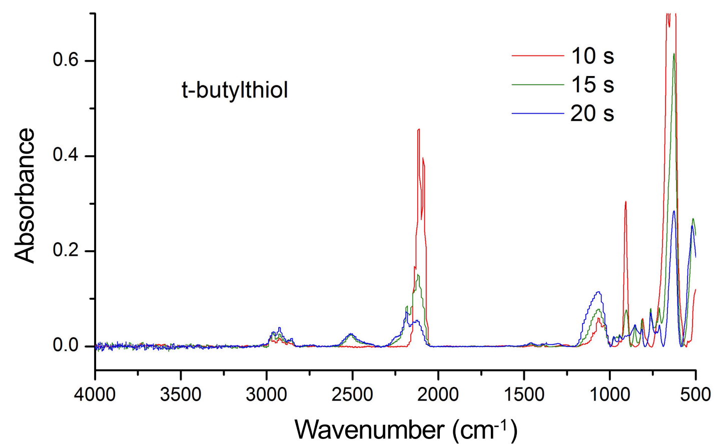

Figure 2.12. FTIR spectra of modified porous silicon, prepared with *t*-butylthiol under microwave irradiation for 10 s, 15 s, and 20 s.

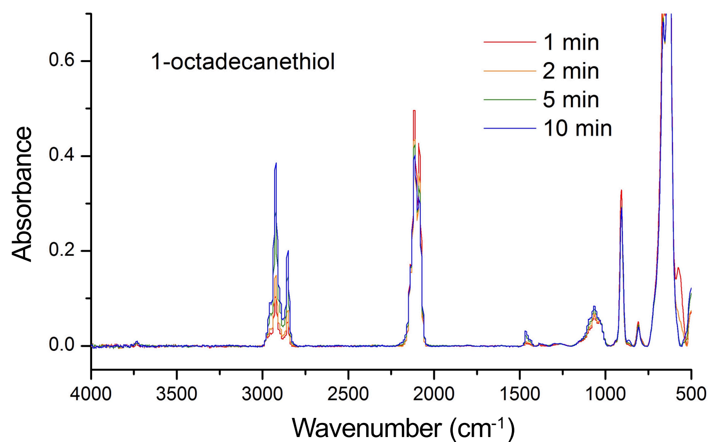

Figure 2.13. FTIR spectra of modified porous silicon, prepared with 1-octadecanethiol under heat for 1 min, 2 min, 5 min, and 10 min on the hot plate.

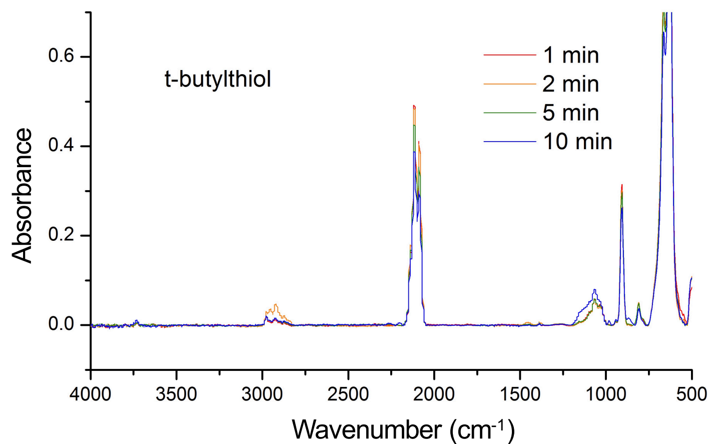

Figure 2.14. FTIR spectra of modified porous silicon, prepared with *t*-butylthiol under heat for 1 min, 2 min, 5 min, and 10 min on the hot plate.

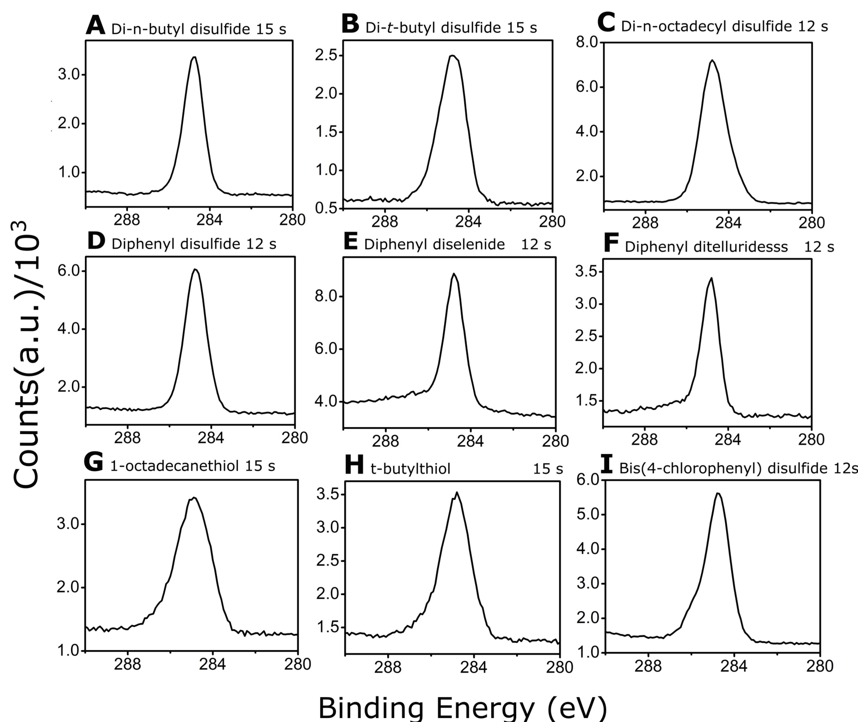

Figure 2.15. XPS spectra, C 1s, of porous silicon after microwave irradiation with a) di-*n*-butyl disulfide, b) di-*t*-butyl disulfide, c) di-*n*-octadecyl disulfide, d) diphenyl disulfide, e) diphenyl diselenide, f) diphenyl ditelluride, g) 1-octadecanethiol, h) *t*-butylthiol, i) bis(4-chlorophenyl) disulfide for the time indicated.

2.4 Conclusions

In this work, we described a very fast thermal functionalization strategy for silicon surfaces to enable the covalent interfacing of molecules and self-assembled monolayers through ≡Si−ER bonds, where E = S, Se, and Te. Through either a microwave or hot plate thermal heating approach with dichalcogenide compounds that contain S−S, Se−Se, or Te−Te bonds, well-defined molecular bonds with low levels of oxidation are produced easily. The alkyl and aryl dichalcogenide molecules are practical to work with because they are stable, commercially available, and of low odor compared to thiols. The series of chalcogen-silicon bonds, from Si−O, to Si−S, to Si−Se, and now to Si−Te, now can be accessed easily and applied to a variety of electronic applications on this semiconductor. Modulation of work function, monolayer doping of silicon, and expansion of the repertoire of hybrid organic–semiconductor electronic devices is possible through this applied surface chemical approach.

Chapter 3

Coverage, Mechanism, and Electronic Properties of UV-Initiated Si–S, Si–Se, and Si–Te Bond Formation on Si(111) Surface*

3.1 Introduction

Control of the electronic properties of a semiconductor surface is critical for device applications.[11,25,175]Functionalization of a semiconductor surface will affect various fundamental properties of the material, including band bending, an effect that has seen much attention for various semiconductor contacts ranging from metals, solutions, vacuum, and covalently bound molecules.[39,40,176,177] When a semiconductor device becomes small (on the nanoscale), the surface:bulk ratio increases dramatically, and thus surface functionalization can dominate the electronic properties.[36–38] For a given semiconductor, doping density and type determine the Fermi level relative to valence and conduction bands in the bulk.[178,179] In the case of a molecular monolayer covalently bound to a semiconductor surface, a new energy level at the interface is created due to hybridization of the semiconductor and molecule. Band bending and alignment alter both work function and electron affinity of the surface, thus creating surface dipoles that can enhance or attenuate the ability to extract electrons from the surface.[180] The complete energy band diagram can be determined using a combination of X-ray photoelectron spectroscopy (XPS) and ultraviolet photoelectron spectroscopy (UPS).[39,40,113,179]

Among various substrates developed for molecular electronics, silicon is of particular interest not only due to its ubiquity in microelectronics but also due to the feasibility of

*The contents of this chapter have been copied and/or adapted from the following publication: Hu, M.; Hauger, T. C.; Olsen, B. C.; Luber, E. J.; Buriak, J. M. UV-Initiated Si–S, Si–Se, and Si–Te Bond Formation on Si(111): Coverage, Mechanism, and Electronics. *The Journal of Physical Chemistry C* **2019**, *122*, 13803–13814.

interfacing organic molecules through direct, covalent bonds on the silicon surface.[181] Much attention has been focused on silicon surfaces functionalized with monolayers bound through Si−C bonds,[20,48,182] and experimental results have been complemented by many theoretical studies.[39,41,183] Systematic preparation and evaluation of other covalent bonds on silicon are, however, much more limited but equally intriguing. Computational DFT work has suggested that the nature of the atom through which an organic monolayer is bonded to a silicon surface, the headgroup, can have profound effects on underlying electronics of the silicon.[4,42,184] These predictions for chalcogenides have not been tested experimentally yet.

The chemistry of organic molecules bound to silicon surfaces through silicon–chalcogen bonds on surfaces is relatively new, as described in Chapter 2. Until recently, the complete series of S, Se, and Te linkers remained elusive due to the difficulty of making ≡Si−TeR bonds. In order to secure the ≡Si−Te bond and complete the series of chalcogenides, we turned to diorganodichalcogenides (REER, where E = S, Se, Te) as synthetically useful molecular precursors.[10,83] These molecules are readily available both commercially and synthetically and have a weak dichalcogenide bond that can be cleaved easily to enable silicon surface functionalization through radical-based mechanisms. Diorganodisulfides and diselenides react with porous silicon at room temperature with a diazonium radical initiator, but these conditions are incompatible with diphenyl ditelluride due to its lower solubility.[10] Diorganodichalcogenide molecules, however, very efficiently and cleanly form ≡Si−ER bonds (E = S, Se, and Te) on high surface area hydride-terminated porous silicon through microwave heating (10–15 s) or direct thermal heating (230 °C, 2 min), temperatures at which silicon radicals are generated directly through homolytic Si−H bond cleavage.[83] Extension of this chemistry from porous silicon to flat Si(111)−H surfaces with these heat-driven approaches failed due to severe contamination with other decomposition products of the diorganodichalcogenide molecules (vide infra).

In this chapter, we describe the chemistry to functionalize Si(111)−H surfaces with ≡Si−ER bonds (E = S, Se, Te) in a manner that is fast and free from both oxidation and contamination from decomposition products of the starting diorganodichalcogenide molecules (Figure 3.1). A combination of mild heating and UV irradiation resulted in a “sweet spot” of desired reactivity to enable clean functionalization of silicon with a series of ≡Si−S−Ph, ≡Si−Se−Ph, and ≡Si−Te−Ph groups. Both the substitution levels and electronic properties of these surfaces were analyzed via XPS. This method also was used with a saturated aliphatic variant, ≡Si−S−*n*-octadecyl.

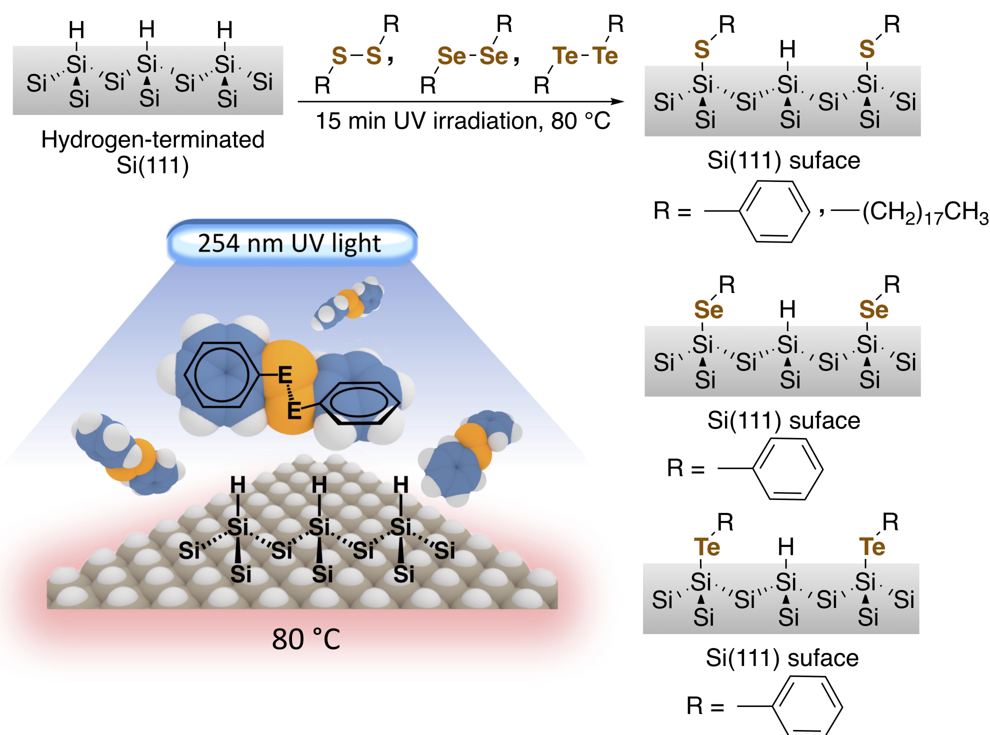

Figure 3.1. Overall reaction scheme summarizing the formation of Si–S, Si–Se, and Si–Te bonds on Si(111)–H surfaces.

3.2 Materials and Methods

3.2.1 Materials

Si(111) wafers (n-type, phosphorus doped, 1–10 Ω·cm, 525 ± 25 μm) were obtained from Virginia Semiconductor, Inc. Diphenyl disulfide (99%), diphenyl diselenide (98%), and diphenyl ditelluride (98%) were purchased from Sigma-Aldrich. Di-*n*-octadecyl disulfide (98%) was purchased from Alfa Aesar. All reagents were stored in a –20 °C freezer inside an argon-filled glovebox. Dichloromethane was purified by a solvent purification system (Innovative Technology, Inc.) and dried over molecular sieves for 24 h in a glovebox prior to use. Molecular sieves (type 4A, 1/16 in. pellets, for selective adsorption), NH_4OH (aqueous, 30%), and HCl (aqueous, 37%) were purchased from Caledon Laboratories, Ltd. NH_4F (aqueous, 40%, semiconductor grade) was purchased from Transene Company, Inc. H_2O_2 (aqueous, 30%) and 2-propanol (≥99.5%) were obtained from Sigma-Aldrich. $KAuCl_4{\cdot}xH_2O$ was purchased from Strem Chemicals. HF (49% aqueous, semiconductor grade) was purchased from J. T. Baker.

3.2.2 Flat Si(111)−H Preparation

Silicon wafers were cut into 1 cm × 1 cm squares using a dicing saw (Disco DAD 321) and then sonicated in 2-propanol for 10 min. Each chip was cleaned by a standard RCA procedure: the chips were immersed first in a fresh solution of H_2O/30% NH_4OH (aq)/30% H_2O_2 (aq) (6:1:1) at 80 °C for 10 min, rinsed with water, and then immersed in a fresh solution of H_2O/37% HCl (aq)/30% H_2O_2 (aq) (5:1:1) at 80 °C for another 10 min. The chips were rinsed with water and dried with a stream of argon gas. The cleaned silicon chips were immersed in argon-saturated 40% NH_4F for 5 min and then dipped into deionized water for 10 s. After being dried with an argon stream, each chip was transferred immediately into a glovebox via a sealed argon-filled vial.

3.2.3 Reactions with Dichalcogenides

All reactions, except for the etching of silicon surfaces, were performed in the argon-filled glovebox. Each of the dichalcogenides, including diphenyl disulfide (PhSSPh), diphenyl diselenide (PhSeSePh), diphenyl ditelluride (PhTeTePh), and di-*n*-octadecyl disulfide (C18SSC18), was dissolved in dichloromethane to form a solution with a concentration of 20 mg/mL. The 1 cm × 1 cm silicon chip was placed on a hot plate, heated to 80 °C, in the glovebox. A 40-µL solution of a specific dichalcogenide was dropped onto the silicon and then covered with a UV grade quartz disc (from University Wafer), forming a sandwich of quartz coverslip–chalcogenide reagent–silicon wafer. The assembly process is shown in Figure 3.2, and the apparatus is shown in Figure 3.3. The dichloromethane evaporated immediately upon contact with the silicon because of its low boiling point, and the small volume of the solution spread over a large area, leaving a solid film between the quartz and silicon. The melting points of PhSSPh, PhSeSePh, PhTeTePh, and di-*n*-octadecyl disulfide are 61 °C, 61 °C, 66 °C, and 62 °C, respectively, and thus the chalcogenide compounds melted to form a film. Then, the samples were irradiated with the light from a UVP Pen-Ray lamp (254 nm, model 11SC-1) held 1 cm above the samples for 15 min. The intensity of a 254-nm light reaching the quartz surface was measured to be $\sim$2 mW cm^{-2}. On completion of the reactions, the quartz coverslip was removed, and the silicon chips were soaked in dry dichloromethane for 3 min, followed by three rinses with a stream of dichloromethane from a pipet to remove the unreacted reagents. The samples were removed from the glovebox in sealed vials, dried further under an argon gas stream, and analyzed immediately.

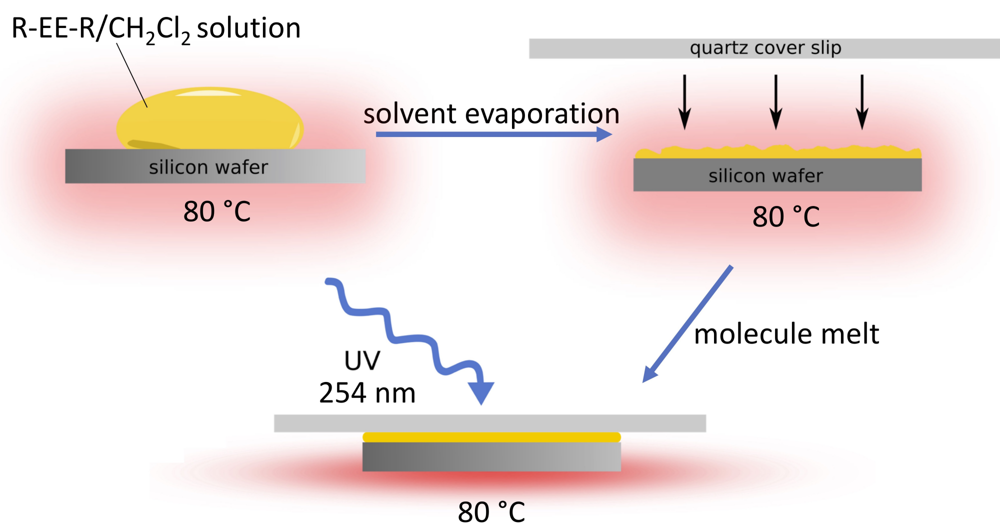

Figure 3.2. Schematic of assembly process for the reaction of dichalcogenides with the Si(111)−H surface.

3.2.4 Estimation of Light Absorption by Molecules Above the Silicon Surface

A 1 cm × 1 cm silicon chip was placed on a hot plate heated to 80 °C. A 40-μL solution of a dichalcogenide with a concentration of 20 mg/mL was dropped on the silicon wafer and quickly covered with a quartz disc, forming a sandwich of quartz–reagent–silicon wafer. The solvent, dichloromethane, evaporated immediately upon contact with the silicon, resulting in a solid film between quartz and silicon (see Figure 3.3). The chalcogenide compounds melted to form a film because of their low melting points.

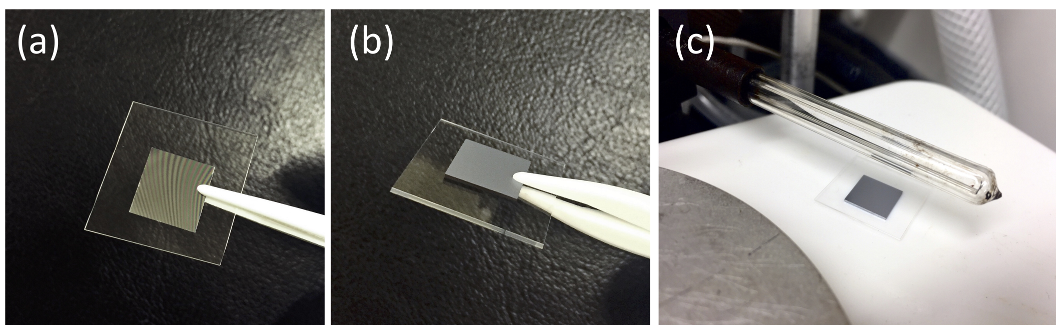

Figure 3.3. (a and b) A "sandwich" apparatus consists of quartz, reagent, and silicon wafer. (c) The apparatus was placed on a hot plate under a UV pen lamp.

Next, the samples were irradiated with the light from a UV lamp.

Taking PhSSPh as an example, the film thickness (h) of molecules during the reaction is given by the volume/area as

$$h = \frac{40\ \mu\text{L}(\frac{\text{mL}}{1000\ \mu\text{L}})(20\ \text{mg mL}^{-1})}{1.35\ \text{g cm}^{-3}(1\ \text{cm}^2)} = 5.9 \times 10^{-4}\ \text{cm}$$

where 40 μL and 20 mg/mL is the added volume and the concentration of the PhSSPh solution, 1.35 g/cm^3 is the density of PhSSPh molecule, and 1 cm^2 is the surface area of the silicon wafer. Since the film only contains pure molecules, the molar concentration (c) for PhSSPh is given as

$$c = \frac{1.35\ \text{g cm}^{-3}}{218.34\ \text{g mol}^{-1}} = 0.00619\ \text{mol cm}^{-3} = 6.19\ \text{mol L}^{-1}$$

We calculated absorbance and transmission values for the diphenyl and dialkyl dichalcogenides used throughout the experiments via the Beer-Lambert law

$$A = -\log(T) = \varepsilon hc \tag{3.1}$$

The estimated light absorption by dichalcogenide molecules above the silicon surface are shown in Table 3.1. The molar absorption coefficients at 254 nm for the dichalcogenides, $\varepsilon_{254\ \text{nm}}$, were measured from UV absorption spectra (Figure 3.13).

Table 3.1. Estimated Light Absorption by Dichalcogenide Molecules Above the Silicon Surface

	c(M)	$\varepsilon_{254\ \text{nm}}$(M^{-1}cm^{-1})	h (cm)	$A_{254\ \text{nm}}$	$\%T_{254\ \text{nm}}$
Diphenyl disulfide	6.19	6493	5.9×10^{-4}	23.8	1.62×10^{-22}
Diphenyl diselenide	5.89	18600	4.3×10^{-4}	47.7	2.13×10^{-46}
Diphenyl ditelluride	5.45	26891	3.6×10^{-4}	52.5	2.84×10^{-51}
Di-*n*-octadecyl disulfide	1.54	1577	9.1×10^{-4}	2.2	0.62

3.2.5 Analytical Techniques

X-ray photoelectron spectroscopy (XPS) spectra were taken on a Kratos Axis Ultra X-ray photoelectron spectroscopy system with a power of 14 kV, 12 mA, and 168 W using an Al source with an energy of 1487 eV, in the University of Alberta NanoFAB, with binding energies calibrated to Au 4f$_{7/2}$ = 84.0 eV. Photoelectrons were collected using a takeoff angle of 90° relative to the sample surface. Although samples were not rotated during XPS measurements (to eliminate photodiffraction effects), multiple measurements of identically prepared samples in separate XPS runs were used for all quantitative XPS

calculations. From these results, it was found that there was generally less than a 10% difference in calculated substitution levels. Ultraviolet photoelectron spectroscopy (UPS) spectra were taken on a Kratos Axis Ultra XPS system with a power of 3 kV, 20 mA, and 60 W. Advancing and receding contact angle measurements were taken on an FTA200 video system. Sessile drop contact angles for the stability monitoring of the functionalized silicon surfaces were measured using 3 μL of water on a Ramé-Hart Mode 100–00 contact-angle goniometer. Film thicknesses were determined by contact mode atomic force microscopy (AFM) scribing. AFM scribing and images were captured using a Veeco/Digital Instruments Multi-Mode NanoScope IV. The intensity of the 254 nm UV light was measured by a Solo 2 energy and power meter with a XLPF12-3S-H2-D0 head (Gentec Electro-Optics Inc.). The resistivity of silicon wafers (oxide layer was removed by HF) was measured using a Keithley 2400 Source Meter in conjunction with a Jandel four-point probe (serial number LB25907) with 0.5 mm probe spacing.

3.2.6 Calculation of Silicon Energy Levels

The resistivity was measured to be 11 $\pm$ 0.8 Ω-cm via a 4-point probe. The dopant level was calculated to be $4.05 \pm 0.37 \times 10^{14}$ cm^{-3} with the following equation

$$n_\mathrm{d} = \frac{1}{q\mu_\mathrm{e}\rho} \tag{3.2}$$

Where n_d is the dopant density, q is the elementary charge, μ_e is the electron mobility in silicon, and ρ is the resistivity of the silicon. The change in work function from intrinsic Si, is then calculated by

$$\Delta WF = k_\mathrm{B} T \ln(\frac{n_\mathrm{d}}{n_\mathrm{i}}) \tag{3.3}$$

where k_B is Boltzmann's constant, T is temperature, and n_d and n_i are the dopant carrier density and the intrinsic carrier density, respectively.

3.2.7 Determination of Work Function, Band Bending, and Surface Dipole

The work function at the silicon surface, represented by $\mathrm{WF^S}$, was determined from the secondary electron cutoff from UPS spectra,

$$\mathrm{WF^S} = h\nu - E_\mathrm{cutoff} \tag{3.4}$$

where $h\nu$ is the energy emitted from a helium discharge lamp (He I), which equals to 21.2 eV, and E_{cutoff} is the secondary electron emission edge measured from the UPS data.

The band gap (E_{g}) is the energy difference of the valence band maximum and the conduction band minimum, which is 1.12 eV for silicon. The absolute energy differences from the valence band to the Fermi level in bulk silicon, from the conduction band to the Fermi level in bulk silicon, from the valence band to the Fermi level at the silicon surface, and from the conduction band to the Fermi level at the silicon surface are represented by $E^{\text{B}}_{\text{vbm}}$, $E^{\text{B}}_{\text{cbm}}$, $E^{\text{S}}_{\text{vbm}}$, $E^{\text{S}}_{\text{cbm}}$, respectively. The band energy is given by

$$E_{\text{g}} = E^{\text{B}}_{\text{vbm}} + E^{\text{B}}_{\text{cbm}} = E^{\text{S}}_{\text{vbm}} + E^{\text{S}}_{\text{cbm}} = 1.12 \text{ eV} \tag{3.5}$$

and $E^{\text{S}}_{\text{vbm}}$ is determined by

$$E^{\text{S}}_{\text{vbm}} = \text{BE (Si 2p}_{3/2}) - \text{BE}^{\text{B}} \text{ (Si 2p}_{3/2}) \tag{3.6}$$

where BE^{B} (Si $2p_{3/2}$) is the binding energy of the Si $2p_{3/2}$ peak of bulk crystalline silicon, namely the energy difference from the Si $2p_{3/2}$ core level to the valence band in bulk silicon (98.74 eV), and BE (Si $2p_{3/2}$) is the binding energy of the Si $2p_{3/2}$ peak at the surface as measured by XPS.

Band bending ($q\text{V}_{\text{bb}}$) is observed for the functionalized silicon surfaces as well as the hydride-terminated silicon surface because of the charged surface states. Band bending can be defined as the energy difference between $E^{\text{B}}_{\text{vbm}}$ and $E^{\text{S}}_{\text{vbm}}$

$$q\text{V}_{\text{bb}} = E^{\text{B}}_{\text{vbm}} - E^{\text{S}}_{\text{vbm}} \tag{3.7}$$

In this work, n-type Si(111) wafers with a resistivity of 1–10 Ω·cm were chosen for the reaction, and the exact resistivity measured was 11 Ω cm, which gives $E^{\text{S}}_{\text{vbm}} = 0.82$ eV according to dopant density calculations. The binding energy BE^{B} (Si $2p_{3/2}$) mentioned before is 98.74 eV, determined by using Au as a Fermi level reference. The band bending in the present case can be expressed by 3.7 as

$$q\text{V}_{\text{bb}} = E^{\text{B}}_{\text{vbm}} - E^{\text{S}}_{\text{vbm}}$$

$$q\text{V}_{\text{bb}} = E^{\text{B}}_{\text{vbm}} + \text{BE}^{\text{B}}(\text{Si 2p}_{3/2}) - \text{BE (Si 2p}_{3/2})$$

$$q\text{V}_{\text{bb}} = 99.56 \text{ eV} - \text{BE (Si 2p}_{3/2})$$

The electron affinity χ is the difference in energy between the vacuum level and the conduction band minimum. For bulk silicon, the electron affinity χ^{B} was taken as 4.05 eV (references 185 and 186) For the silicon surface, as shown in the band diagram, the electron affinity χ^{S} can be calculated as the difference between WF^{S} and E^{S}_{cbm}

$$\chi^{S} = WF^{S} - E^{S}_{cbm} = WF^{S} - (E_{g} - E^{S}_{vbm}) \tag{3.8}$$

The surface dipole, δ, is obtained as the energy difference of electron affinity at the surface, χ^{S}, and the electron affinity in bulk silicon, χ^{B}

$$\delta = \chi^{S} - \chi^{B} = WF^{S} - (E_{g} - E^{S}_{vbm} - \chi^{B}) = WF^{S} + E^{S}_{vbm} - 5.17 \text{ eV} \tag{3.9}$$

A band diagram regarding to the binding energy, band bending, surface dipole, electron affinity, and work function is shown in Figure 3.17.

3.2.8 Simulation

Stochastic packing of phenylchalcogenides on the Si(111) surface was simulated by assuming the steric interactions to be 2-dimensional, where the ≡Si−E−Ph groups were represented by the union of two hard disks. The respective radii of these disks were set by using the van der Waals radii of the chalcogen and the phenyl ring. Briefly, the packing algorithm works according to the following procedure. First, a sufficiently large Si(111) surface is generated (results were found to be effectively invariant for more than 14,000 Si atoms), and a random Si site is chosen. Then, a ≡Si−E−Ph group is placed at this random Si site at multiple random orientations with uniform spacing (results were found to be invariant for more than 7 different orientations) and is checked to see if it overlaps with any of the other ≡Si−E−Ph groups on the surface. If an orientation with no overlaps is found, it is left permanently in that position and orientation. This process is repeated at different randomly chosen Si surface sites until all silicon surface sites have been checked. The final substitution level is simply the number of ≡Si−E−Ph groups divided by the number of silicon sites. The substitution levels determined from simulation are the average of 150 independent simulation runs, each having a simulation size of 14,000 silicon sites and checking 13 different orientations for the ≡Si−E−Ph group at each silicon site. It should be noted that the sites at the edge of the simulation volume were not used to calculate the substitution level as the amount of steric interactions will be lower in these regions. Specifically, sites within three silicon lattice parameters of the simulation boundaries were not used. Nonetheless,

given the large simulation volume, the edge effects were very small, leading to a less than ∼3% difference after edge correction.

3.3 Results and Discussion

3.3.1 Silicon–Chalcogen Bond Formation via UV Irradiation and Gentle Heating

To drive selective chemistry on Si(111)−H with dialkyl or diaryl dichalcogenides, low intensity 254-nm UV irradiation was coupled with gentle heating to enable the use of neat molecular reagents, with no additional solvent or other additives. A small volume (40 μL) of dichloromethane solution was placed on a 1-cm^2 chip of freshly etched Si(111)−H and then heated to 80 °C to evaporate the solvent and melt the film (all four molecules have melting points below this temperature). A quartz window was pressed on top of the melted reagent to spread it evenly over the face of the silicon wafer, as shown in Figures 3.2 and 3.3. Then, the sample was then irradiated by a Hg pen-lamp with a wavelength of 254 nm (intensity 2 mW cm^{-2}). X-ray photoelectron spectroscopy (XPS) was carried out on the silicon samples reacted with the PhSSPh, PhSeSePh, PhTeTePh, and di-*n*-octadecyl disulfide precursors to determine the nature of the bonding atom to the silicon (S, Se, or Te) and the level of oxidation. As shown in Figure 3.4, the narrow Si 2p feature of all four silicon samples reveals little oxidation, which would appear at a higher binding energy, above 102 eV.[25,125] Figure 3.4a,c shows the S 2p spectra, revealing the characteristic S $2p_{3/2}$ and S $2p_{1/2}$ peaks at 162.6 and 163.8 eV for the PhSSPh-functionalized silicon surface, respectively, and 162.5 and 163.7 eV, for the di-*n*-octadecyl disulfide-functionalized silicon surface, respectively. The Se 3d spectrum (Figure 3.4e) also reveals a doublet of the Se 3d peak that has been fit to the Se $3d_{5/2}$ and Se $3d_{3/2}$ peaks located at 54.9 and 55.7 eV, respectively. Two separate Te 3d peaks (Figure 3.4g) with binding energies of 573.1 and 583.5 eV correspond to Te $3d_{5/2}$ and Te $3d_{3/2}$, respectively. The binding energies for these chalcogens agree with previous results for surfaces functionalized with Si−S, Si−Se, and Si−Te bonds on porous silicon surfaces.[83,106] The features of the starting reagents, PhEEPh (E = S, Se, Te) and di-*n*-octadecyl disulfide, are shown in Figure 3.4 and summarized in Tables 3.2 and 3.3.

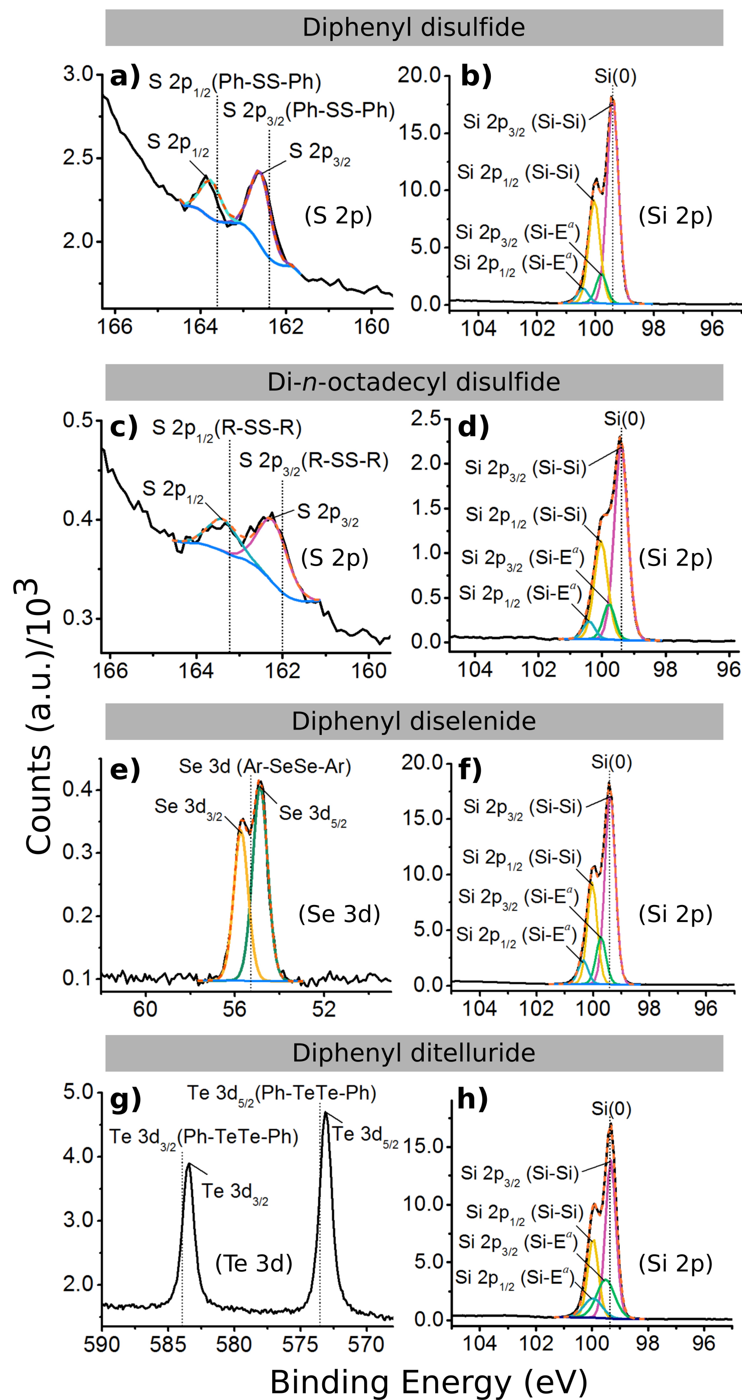

Figure 3.4. XPS spectra of Si(111) surfaces after the UV-mild thermal (80 °C) treatment with indicated diphenyl dichalcogenides and di-*n*-octadecyl disulfide reagents for 15 min. Orange dashed curves are the envelope fittings. The data from this figure and supporting literature are tabulated in Tables 3.2 and 3.3. E^a = S, Se, Te, as well as H.

Table 3.2. Summary of XPS Data Corresponding to Figure 3.4

	Si $2p_{3/2}$ (bulk, eV)	Si $2p_{3/2}$ (surface, eV)	S 2p (eV)	Se 3d (eV)	Te 3d (eV)
Di-*n*-octadecyl disulfide	99.41	99.78	162.2, 163.3		
Diphenyl disulfide	99.43	99.76	162.6, 163.8		
Diphenyl diselenide	99.34	99.65		54.9, 55.7	
Diphenyl ditelluride	99.37	99.68			573.1, 583.5

Table 3.3. Representative Peaks of S 2p, Se 3d and Te 3d Data From the Literature

	S 2p (eV)	Se 3d (eV)	Te 3d (eV)	Reference
Ph-SS-Ph	162.4, 163.6			166
R-SS-R	162.0, 163.2			165
Ar-SeSe-Ar		55.3		167
Ph-TeTe-Ph			573.5, 583.9	168

Prior work in our group showed that dialkyl and diaryl dichalcogenides react very rapidly (seconds to minutes) and cleanly with hydride-terminated porous silicon at high temperatures in the range of 200–230 °C under an inert atmosphere to form ≡Si−E−R (E = S, Se, Te) groups with no apparent oxidation.[83] On flat Si(111)−H, however, contamination was determined by XPS to be a serious issue in the case of the tellurium derivative. Thermally driven reactions with diphenyl dichalcogenides on Si(111)−H were carried out first at 200 °C for 90–120 s. The XPS spectra, shown in Figures 3.5a, b, c, and d, for the reactions with diphenyl disulfide and diphenyl diselenide on silicon surfaces proceed with little contamination or oxidation. For diphenyl ditelluride, however, the Te 3d XPS spectrum is complicated by two sets of Te 3d doublets, as seen in Figure 3.5e, as well as oxidation of the silicon surface (feature at 103 eV in Figure 3.5f). Lowering the temperature to 150 °C also resulted in oxidation of the silicon surface (Figures 3.5g and h). The set of doublets with a higher binding energy is consistent with the formation of Te−O bonds.[168] Previous work has shown that phenylchalcogenides decompose upon heating to yield chalcogenide metal due to cleavage of the chalcogenide–phenyl bond.[187] While the reactions were carried out in an inert atmosphere glovebox (O_2 < 1 ppm), if Te(0) indeed was formed under these conditions, brief exposure of the surfaces to air upon loading them into the XPS could result in oxidation of the tellurium metal. In order to keep the chemistry consistent across the sulfur, selenium, and tellurium derivatives, mild UV irradiation combined with gentle heating to 80 °C was used throughout this work.

Table 3.4. Contact Angles for the Functionalized Silicon Surfaces Reacted with the Indicated Reagents under UV Irradiation at 80 °C

	θ_e^{wa} (°)	θ_e^{HDa} (°)	$\theta_a^{wa}/\theta_r^{wa}$ (°)
Si(111)–H surface	83.5 ± 1.1	2.8 ± 0.7	95 ± 0.8 / 75 ± 0.9
Diphenyl disulfide	82.6 ± 1.3	7.5 ± 0.6	90 ± 1.1 / 69 ± 0.8
Diphenyl diselenide	82.2 ± 1.2	6.8 ± 0.5	95 ± 1.3 / 64 ± 1.1
Diphenyl ditelluride	80.2 ± 1.8	9.1 ± 0.7	88 ± 1.2 / 60 ± 0.7
Di-*n*-octadecyl disulfide	105.1 ± 0.4	43.4 ±1.4	108 ± 1.0 / 88 ± 0.8

[a]e, a and r refer to equilibrium, advancing and receding, respectively, and w and HD represent water and hexadecane, respectively. Each value is the average of five separate measurements and the error listed is the standard deviation.

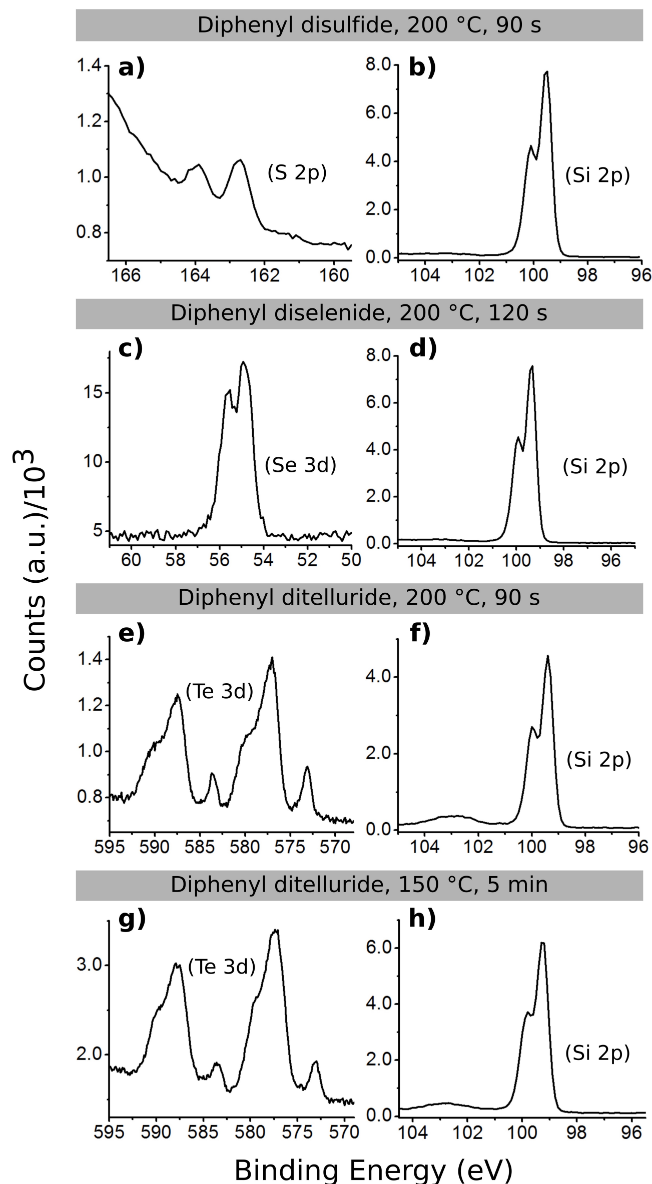

Figure 3.5. XPS spectra of Si(111)−H surfaces after reaction with diphenyl dichalcogenides reagents under indicated reaction times and temperatures.

Contact angle measurements of functionalized surfaces typically are used to obtain information regarding surface energy,[188] monolayer order,[189] and kinetics.[190] Static (θ_e) and dynamic (θ_a/θ_r) water contact angles of all the freshly prepared diphenyl dichalcogenide-functionalized samples fall between 80° and 83° (Table 3.4 and Figure 3.6), which are very close to that of the starting hydride-terminated silicon surface (∼83°) and hence not an informative metric to quantify surface functionalization. As such, the aliphatic disulfide, di-*n*-octadecyl disulfide, was used to provide insights into the rate of the reaction.[101,190,191] As shown in Figure 3.7, the Si(111)−H surface reacted with di-*n*-octadecyl disulfide at 80 °C with UV irradiation appears to follow classic Langmuir kinetics,[192] and a maximum contact angle of ∼105° is reached after 10 min, a value similar to that of other silicon surfaces functionalized with long alkyl chains (contact angles range from ∼105° to 110°).[147,193,194] Representative contact angles of phenyl- and long alkyl chain-terminated silicon and gold surfaces from the literature are shown in Table 3.5. Control experiments, summarized in Table 3.6, showed that both heat and UV irradiation are necessary to reach this high contact angle with di-*n*-octadecyl disulfide. With only heat (80 °C) or UV irradiation, the contact angles fell within the range of 83–88°, indicating that both are required in order to enable the reaction to

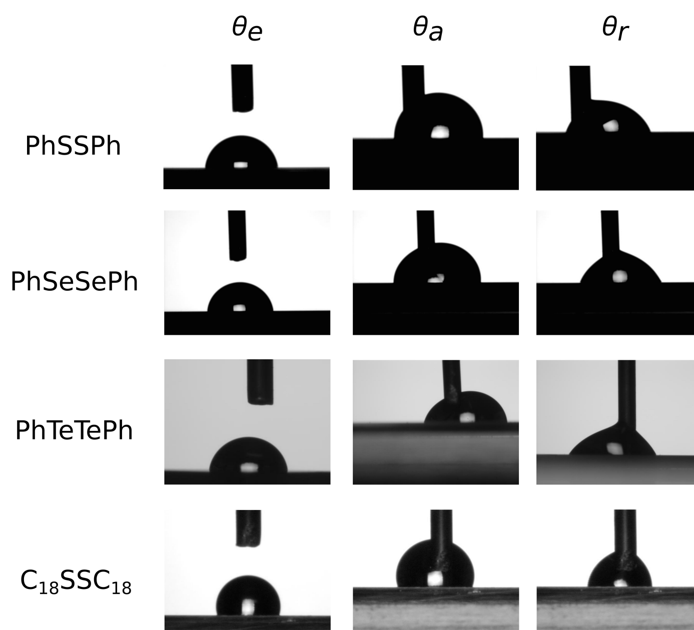

Figure 3.6. Water contact angle images of a Si(111)−H surface reacted with indicated reagents corresponding to Table 3.4.

proceed to high coverage within 15 min. With hexadecane as the probe liquid for contact angle measurements, the contact angles of all ≡Si−E−Ph surfaces were low ($\theta < 10°$),

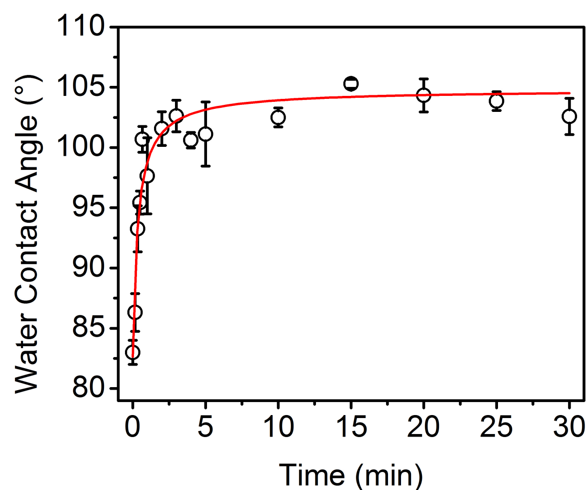

Figure 3.7. Water contact angles of di-*n*-octadecyl disulfide-functionalized silicon surfaces with different reaction times (black dots) and the fitting curve according to the contact angle data (red curve). Each black dot represents a unique sample that had been reacted for the indicated reaction time. The error bars represent the standard deviation of five measurements on the same sample.

while for the ≡Si−S−*n*-octadecyl surface, the average contact angle was 43.4° (Table 3.4), a value that is consistent with previous work investigating monolayers on silicon,[195] gold,[196] or hydroxylated silicon surfaces.[197]

Table 3.5. Representative Contact Angles of Indicated Phenyl-Terminated and Long Alkyl Chain-Terminated Silicon or Gold Surfaces from Literature

	θ_e^w(°)	θ_a^w/θ_r^w(°)	θ_a^{HD}(°)	Reference
≡Si(100)–O–Si–O-Ph	85	$\theta_a^w \sim 90$	- -	134
Au/HS–Ph	- -	80/76	- -	198
≡Si(111)–S–C_{18}	∼103	- -	- -	112
≡Si(100)–C_{18}	- -	110/96	- -	147
≡Si(100)–O–Si$(Me)_2$–C_{18}	- -	103/91 and 107/95 (two conditions)	- -	199
≡Si(100)–O–Si–O–C_{18}	110	$\theta_a^w \sim 115$	- -	197
≡Si(100)–O–Si–O–C_{16}	105	$\theta_a^w \sim 110$	- -	196
≡Si–O–Si–C_{18}	- -	θ_a^w=111	45	200
Au/HS–C_{16}	- -	θ_a^w=118	48	201

Table 3.6. Contact Angles[a] for the Control Experiments with Indicated Conditions

	θ_e^w (°) (80 °C, no UV)	θ_e^w (°) (room temperature, UV)	θ_e^w (°) (80 °C + UV)
Diphenyl disulfide	82.9 ± 0.6	82.9 ± 1.0	82.6 ± 1.3
Diphenyl diselenide	82.3 ± 1.0	81.7 ± 0.9	82.2 ± 1.2
Diphenyl ditelluride	81.8 ± 1.2	80.5 ± 1.1	80.2 ± 1.8
Di-*n*-octadecyl disulfide	87.6 ± 1.0	82.6 ± 0.7	105.1 ± 0.4

[a]Each value is the average of five separate measurements and the error listed is the standard deviation.

3.3.2 Determination of Layer Thickness

The thicknesses of the resulting films was measured by scribing with an AFM tip, a commonly used technique that can be used to remove soft organic monolayers from the hard inorganic surface by scratching the surface with a hard silicon AFM tip.[12,13,138,202] The scratched hydride-terminated silicon surface in Figure 3.8a reveals a small height difference of ~0.2 nm, most likely due to physisorbed hydrocarbon contaminants upon exposure to laboratory ambient conditions. As shown in Figure 3.8b–d, the scribed areas of the diphenyl dichalcogenide-treated surfaces capped with ≡Si−E−Ph groups are ~0.8 nm deep, as determined from both line profiles and histogram analysis. For the ≡Si−S−*n*-octadecyl-terminated surface, the measured depth is ~2.5 nm; a smaller area could be scribed only due to buildup of residue on the AFM tip.

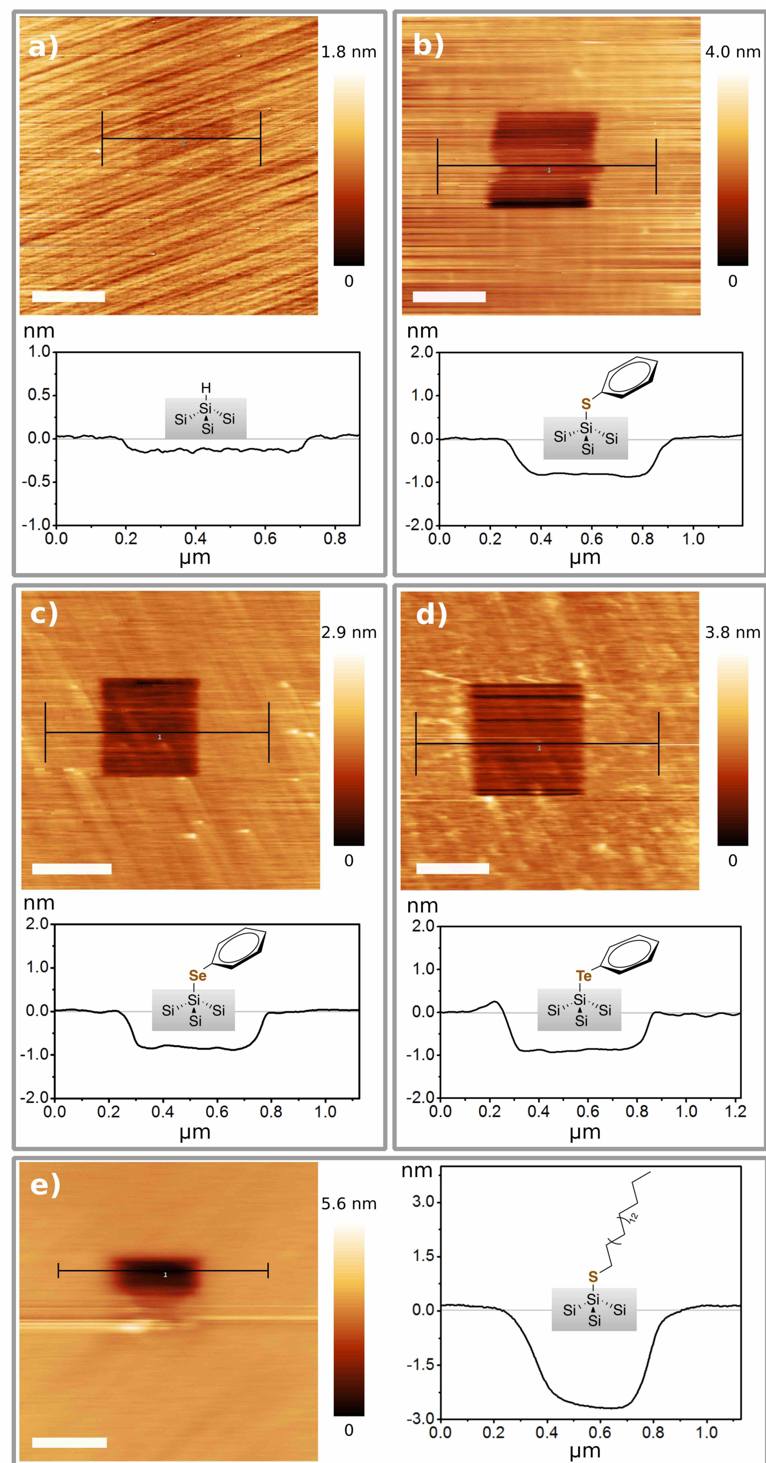

Figure 3.8. AFM scribing of Si(111) surfaces. All scale bars are 400 nm. (a) Scribing on a hydride-terminated Si(111) surface. (b–d) Functionalized Si(111) surfaces reacted with PhSSPh, PhSeSePh, and PhTeTePh, respectively. (e) Functionalized Si(111) surfaces reacted with di-*n*-octadecyl disulfide. A smaller area was etched for the di-*n*-octadecyl disulfide molecule due to the rapid buildup of residue on the tip.

In order to calculate the predicted thickness of the molecular layer on the Si(111) surface, the ≡Si−E bond length, the size of the phenyl ring, and the ≡Si−E−C bond angle need to be known or assumed. The value with the greatest uncertainty is the bond angle about the chalcogen, the ≡Si−E−C bond angle; a table of comparable molecules is provided in Table 3.7. Only a small number of molecules with silicon–chalcogenide bonds has been characterized sufficiently to evaluate bond angles (e.g., by single-crystal X-ray diffraction). For instance, the Si−S−H bond angle in tri(mesityloxy)silanethiol has been reported to be 95.4°,[210] and that of Si−S−CH_3 in the S-methyl ether of tributoxysilanethiol is 106°,[209] both of which were determined from crystal structures. For thioethers, the C−S−C bond angles for both Ph−S−CH_3 and Ar−S−Ar molecules are around 100° to 104°.[200,201,203–205] Selenoethers, Ar−Se−Ar and C(sp^3)−Se−C(sp^2), have a C−Se−C bond angle of ∼101°.[206,207] The C−Te−C bond angle for the telluroethers, Ph−Te−CH_3 and Ph−Te−Ph, is ∼96°.[208] When ≡Si−E−C bond angles of 103°, 101°, and 96° were imposed upon ≡Si−S−Ph, ≡Si−Se−Ph, and ≡Si−Te−Ph groups on the Si(111)−H surface, severe steric interference between underlying ≡Si−H groups and the overlying phenyl rings resulted. As shown in the space-filling representations in Figure 3.9, only when the bond angle about the chalcogenide of the ≡Si−E−Ph was increased to 125° (≡Si−S−Ph), 124° (≡Si−Se−Ph), and 117° (≡Si−Te−Ph) was there no overlap of the van der Waals radii of the phenyl rings and the underlying ≡Si−H groups. The higher angle of the ≡Si−S−Ph group results from having the shortest ≡Si−E bond of the trio, as it needs to have a higher tilt to avoid overlap with the underlying silicon hydrides. These calculations are summarized in Figure 3.10 and are shown with the smallest possible angle about the chalcogen atom. The calculated thicknesses for the ≡Si−E−Ph surfaces, therefore, represent the thinnest possible monolayer; with a higher angle about the chalcogenide linker atom, the monolayer could

Table 3.7. Representative C–E–C[a] and Si–S–R[b] Bond Angles for Various Compounds from Literature

Compound	C–E–C Bond Angles (°)	Reference
Ph–S–CH_3	102.9 ∼ 105.6	200
Ph–S–CH_3	100 ∼ 104	201
Ph–S–Ar	104.1	203
Ar–S–Ar	101 ∼ 104	204
Ar–S–Ar	102.9	205
C(sp^3)–Se–C(sp^2)	∼101.0 (ϕ^c = 0°), ∼97.2 (ϕ^c = 90°)	206
Ar–Se–Ar	101.7	207
Ph–Te–CH_3	95.6	208
Ph–Te-Ph	96.1	208
Compound	**Si–S–R Bond Angles (°)**	**Reference**
Si–S–CH_3	106	209
Si–S–H	95.4	210

[a]E = S, Se, and Te. [b]R = C and H. [c]ϕ is the torsion angle, the angle between the planes of the benzene ring and C–Se–C bond.

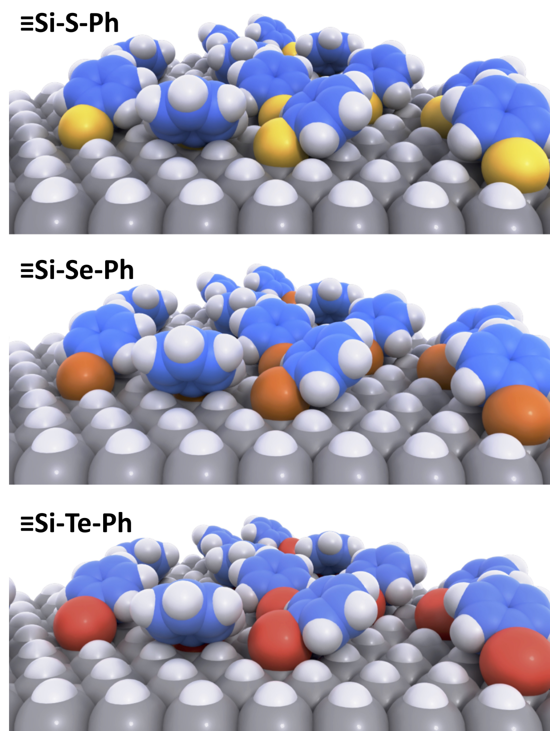

Figure 3.9. Side-view space-filling model of the ≡Si−E−Ph (E = S, Se, Te) interfaces on a flat hydride-terminated Si(111) surface. The chalcogenide-based functionalities were placed randomly on the surface, as would be the case for kinetically trapped, irreversible Si–E bond formation.

be thicker. For the aliphatic variant, the ≡Si−S−*n*-octadecyl-terminated surface, a tilt angle of the *n*-octadecyl group of 33° from the surface normal was used, based upon prior experimental results by Lou and co-workers for a similar surface formed via the reaction of 1-dodecanethiol on Si(111)−H.[111]

The calculations in Figure3.10 differ to a small degree from the results observed by AFM scribing. To repeat, it must be stated that we cannot determine the exact bond angle about the chalcogenide for these ≡Si−E−R-functionalized surfaces, and thus the observed difference of ∼0.2 nm between the calculated thicknesses and the measurements from AFM scribing could be due to physisorbed contamination but also could result from a higher ≡Si−E−C bond angle about the chalcogen. Indeed, it has been claimed that ≡Si−O−Ph-terminated surfaces have a Si−O−C bond angle close to 180° at high substitution levels,[211] but for the sulfur, selenium, and tellurium versions, the bond angle for RER molecules decreases going down the chalcogen group, so a bond angle closer to 180° about the chalcogen seems unlikely. Detailed quantification of substitution level by XPS, complemented by simulations that assume spatially stochastic covalent bonding (kinetic trapping), is described vide infra.

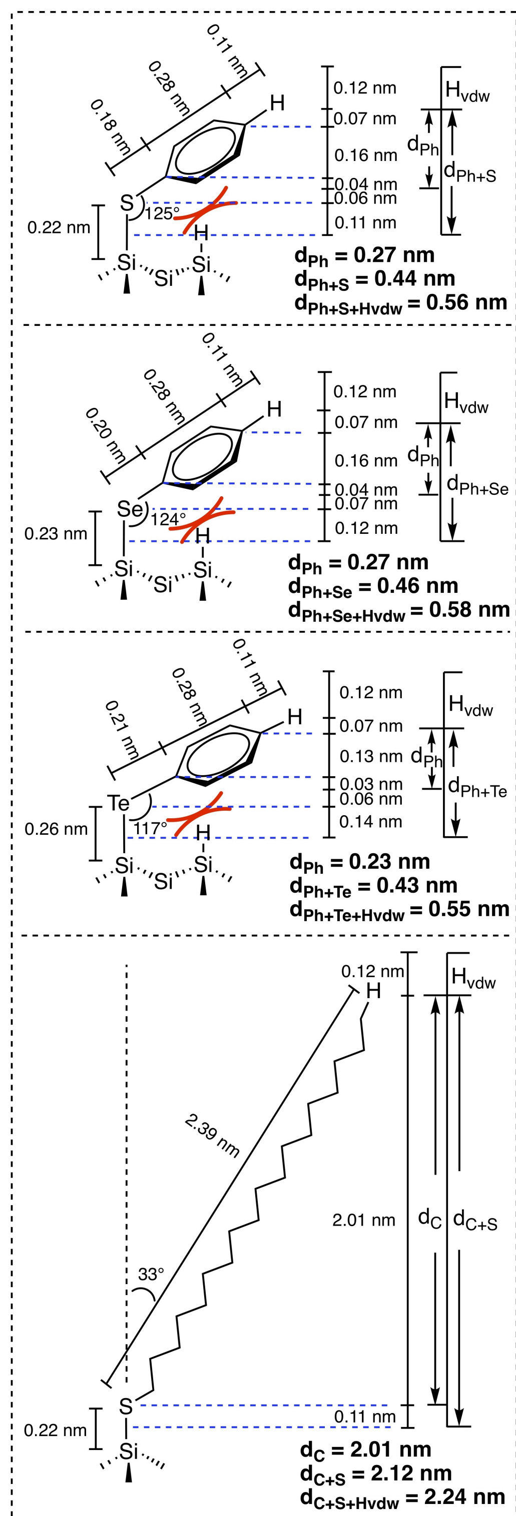

Figure 3.10. Theoretical monolayer thicknesses of ≡Si−S−Ph-, ≡Si−Se−Ph-, ≡Si−Te−Ph-, and ≡Si−S–*n*-octadecyl-modified silicon surfaces calculated based upon the indicated bond lengths and angles. H_{vdw} is the van der Waals radius of the hydrogen para to the chalcogenide. Red lines indicate steric hindrance between the phenyl ring and underlying hydrogen atoms on the silicon surface.

3.3.3 Quantification of Substitution Level of ≡Si–H with ≡Si–ER Groups

While the AFM scribing for all four ≡Si−E−R surfaces suggests uniform films, quantitative determination of the level of substitution of Si−H groups with chalcogenides was desired. XPS has been employed previously to estimate the substitution level of alkyl groups on silicon bound through silicon–carbon bonds.[15,141,212] In order to determine the substitution level, Θ, analytical expressions for the relative peak intensity areas of the silicon, carbon, and chalcogen signals were derived first. As is conventionally done, the silicon substrate and corresponding alkyl/phenyl molecular overlayers can be approximated by continuum layers that have a uniform atomic density, ρ_i, electron attenuation coefficient, λ_i, and thickness d_i. By making this continuum approximation, the measured intensity of photoelectrons can be calculated by simple application of the Beer–Lambert law. In the case of a silicon substrate (atomic density, ρ_{Si}, electron attenuation length, λ_{SiSi}) with a chalcogen overlayer (atomic density, ρ_E, electron attenuation length, λ_{EE}) capped by a phenyl/alkyl overlayer (atomic density, ρ_C, electron attenuation length, λ_{CC}), the total XPS intensity of the silicon peak is given by

$$I_{\mathrm{Si}} = A\sigma_{\mathrm{Si}}\rho_{Si}(\int_0^{\infty} \exp(-x/\lambda_{\mathrm{SiSi}})\mathrm{d}x)\exp(-d_{\mathrm{E}}/\lambda_{\mathrm{SiE}})\exp(-d_{\mathrm{C}}/\lambda_{\mathrm{SiC}})$$

$$I_{Si} = A\sigma_{\mathrm{Si}}\rho_{\mathrm{Si}}\lambda_{\mathrm{SiSi}}\exp(-d_{\mathrm{E}}/\lambda_{\mathrm{SiE}})\exp(-d_{\mathrm{C}}/\lambda_{\mathrm{SiC}}) \tag{3.10}$$

where A is the areal footprint of the X-ray beam and σ_{Si} is the relative sensitivity factor for silicon. Likewise, the signal from the chalcogen layer is given by

$$I_{\mathrm{E}} = A\sigma_{\mathrm{E}}\rho_{\mathrm{E}}(\int_0^{d_{\mathrm{E}}} \exp(-x/\lambda_{\mathrm{EE}})\mathrm{d}x)\exp(-d_{\mathrm{C}}/\lambda_{\mathrm{EC}})$$

$$I_{\mathrm{E}} = A\sigma_{\mathrm{E}}\rho_{\mathrm{E}}\lambda_{\mathrm{EE}}(1-\exp(-d_{\mathrm{E}}/\lambda_{\mathrm{EE}}))\exp(-d_{\mathrm{C}}/\lambda_{\mathrm{EC}}) \tag{3.11}$$

Lastly, the signal from the carbon layer is given by

$$I_{\mathrm{C}} = A\sigma_{\mathrm{C}}\rho_{\mathrm{C}}(\int_0^{d_{\mathrm{C}}} \exp(-x/\lambda_{\mathrm{CC}})\mathrm{d}x)$$

$$I_{\mathrm{C}} = A\sigma_{\mathrm{C}}\rho_{\mathrm{C}}\lambda_{\mathrm{CC}}(1-\exp(-d_{\mathrm{C}}/\lambda_{\mathrm{CC}})) \tag{3.12}$$

Taking the ratio of the silicon and carbon intensities (eqs 3.10 and 3.12) gives

$$\frac{I_{\mathrm{Si}}}{I_{\mathrm{C}}} = \frac{\sigma_{\mathrm{Si}}\rho_{\mathrm{Si}}\lambda_{\mathrm{SiSi}}\exp(-d_{\mathrm{E}}/\lambda_{\mathrm{SiE}})}{\sigma_{\mathrm{C}}\rho_{\mathrm{C}}\lambda_{\mathrm{CC}}(\exp(d_{\mathrm{C}}/\lambda_{\mathrm{SiC}})-\exp(d_{\mathrm{C}}(1/\lambda_{\mathrm{SiC}}-1/\lambda_{\mathrm{CC}})))} \tag{3.13}$$

Equation 3.13 can be simplified in two ways. First, we can assume that $\exp(d_C(1/\lambda_{SiC} - 1/\lambda_{CC})) \approx 1$ since the attenuation length of photoemitted electrons from the silicon layer passing through the carbon layer, λ_{SiC}, will be very close to that for photoemitted electrons from the carbon layer passing through the carbon layer, λ_{CC}. Second, we also assume that $d_E/\lambda_{SiE} \ll 1$ since the thickness of the chalcogen layer will be less than twice the van der Waals radius (~0.4 nm), while the attenuation length of the chalcogen will be on the order of 3–4 nm. From these simplifying assumptions, eq 3.13 becomes

$$\frac{I_{Si}}{I_C} = \frac{\sigma_{Si}\rho_{Si}\lambda_{SiSi}}{\sigma_C\rho_C\lambda_{CC}(\exp(d_C/\lambda_{SiC}) - 1)} \tag{3.14}$$

Finally, this expression can be used to calculate the substitution level by determining an effective thickness d_C^{eff} of a carbon layer with attenuation length, λ_{SiC}^{Si}, and atomic density, ρ_C^{Si}, equal to that of a monolayer with 100% coverage of the silicon (111) surface. The values of λ_{SiC}^{Si} and ρ_C^{Si} can be estimated by scaling the values for gold surfaces with 100% coverage

$$\rho_C^{Si} = \frac{n_{Si}}{n_{Au}}\rho_C^{Au} \tag{3.15}$$

$$\lambda_{SiC}^{Si} = \frac{n_{Au}}{n_{Si}}\lambda_{SiC}^{Au} \tag{3.16}$$

$$\lambda_{CC}^{Si} = \frac{n_{Au}}{n_{Si}}\lambda_{CC}^{Au} \tag{3.17}$$

where n_{Si} and n_{Au} are the atomic surface densities of (111) silicon (7.8×10^{14} atoms/cm^2) and the $(\sqrt{3} \times \sqrt{3})$R30 surface of (111) gold (4.6×10^{14} atoms/cm^2). Combining eqs 3.14, 3.15, 3.16 and 3.17 gives

$$d_C^{eff} = \frac{n_{Au}}{n_{Si}}\lambda_{SiC}^{Au} \ln\left(\frac{I_C\sigma_{Si}\rho_{Si}\lambda_{SiSi}}{I_{Si}\sigma_C\rho_C^{Au}\lambda_{CC}^{Au}} + 1\right) \tag{3.18}$$

Using eq 3.18, we can divide the effective thickness by the theoretical monolayer thickness (2.01 nm for ≡Si−S−*n*-octadecyl at a tilt angle of 33°) to obtain the substitution level. The average substitution level determined is 50 ± 2%, which agrees well with previously reported values for hydrosilylation of alkyl chains on the (111) silicon.[17,89,91,141,213]

When using XPS data to determine the substitution level of alkyl chains on a silicon surface, analysis typically is limited to the silicon and carbon photoelectron signals. However, in the case of ≡Si−S−*n*-octadecyl, we also can utilize the silicon and sulfur

peak intensities to derive a second expression for the substitution level. If we divide eq 3.10 by eq 3.11 we arrive at the following expression

$$\frac{I_{\mathrm{Si}}}{I_{\mathrm{E}}} = \frac{\sigma_{\mathrm{Si}}\rho_{\mathrm{Si}}\lambda_{\mathrm{SiSi}}\exp(-d_{\mathrm{E}}/\lambda_{\mathrm{SiE}})\exp(-d_{\mathrm{C}}/\lambda_{\mathrm{SiC}})}{\sigma_{\mathrm{E}}\rho_{\mathrm{E}}\lambda_{\mathrm{EE}}(1-\exp(d_{\mathrm{E}}/\lambda_{\mathrm{EE}}))\exp(d_{\mathrm{C}}/\lambda_{\mathrm{EC}})} \tag{3.19}$$

If we again assume that $\exp(d_{\mathrm{E}}(1/\lambda_{\mathrm{SiE}} - 1/\lambda_{\mathrm{EE}})) \approx 1$, $\exp(d_{\mathrm{C}}(1/\lambda_{\mathrm{SiC}} - 1/\lambda_{\mathrm{EC}})) \approx 1$, and $d_{\mathrm{E}}/\lambda_{\mathrm{SiE}} \ll 1$, we arrive at the simplified expression of

$$\frac{I_{\mathrm{Si}}}{I_{\mathrm{E}}} = \frac{\sigma_{\mathrm{Si}}\rho_{\mathrm{Si}}\lambda_{\mathrm{SiSi}}}{\sigma_{\mathrm{E}}\rho_{\mathrm{E}}d_{\mathrm{E}}} \tag{3.20}$$

Given that $\rho_{\mathrm{E}}d_{\mathrm{E}} = n_{\mathrm{E}}$, where n_{E} is the atomic surface density of chalcogen atoms, and the substitution level is defined as $\Theta = n_{\mathrm{E}}/n_{\mathrm{Si}}$, we can solve for the substitution level

$$\Theta = \frac{\rho_{\mathrm{Si}}\lambda_{\mathrm{SiSi}}\sigma_{\mathrm{Si}}I_{\mathrm{E}}}{n_{\mathrm{Si}}\sigma_{\mathrm{E}}I_{\mathrm{Si}}} \tag{3.21}$$

3.3.4 Calculations of Constants

The atomic density of carbon on gold, ${\rho_{\mathrm{C}}}^{\mathrm{Au}}$, can be calculated by assuming that the functional layer would have the same areal density as the surface (Au), 4.6×10^{14} atoms/cm^2, and dividing that by the average thickness per carbon atomic plane or the theoretical thickness (2.01 nm) of each chain normalized by the number of carbons per chain (18)

$$\rho_{\mathrm{C}}^{\mathrm{Au}} = \frac{n_{\mathrm{Au}}}{d_{\mathrm{C}}/N_{\mathrm{Chain}}} = \frac{4.6\times 10^{14}}{2.01\times 10^{-7}/18} = 4.1\times 10^{22}\ \mathrm{atoms/cm^3}$$

The attenuation length of photoelectrons in alkyl monolayers on gold, $\lambda_{\mathrm{ML}}^{\mathrm{Au}}$, is given by

$$\lambda_{\mathrm{ML}}^{\mathrm{Au}} = 9 + 0.022E_{\mathrm{k}} \tag{3.22}$$

where E_{k} is the difference between the light source energy and the binding energy of the specific element, and the result is in Å. Therefore, the attenuation length of Si 2p electrons in alkyl monolayer on gold is given by

$$\lambda_{\mathrm{SiC}}^{\mathrm{Au}} = 9 + 0.022E_{\mathrm{k}} = 9 + 0.022(1487\ \mathrm{eV} - 99.4\ \mathrm{eV}) = 39.5\ \text{Å}$$

The uncertainties in the substitution levels are calculated based on the standard deviations in the substitution levels. For the di-*n*-octadecyl disulfide, the uncertainty

Table 3.8. List of All Constants Used for the Calculation of Substitution Levels from XPS Data

Constant	Value
Sensitivity factor σ_{Si}, σ_{S}, σ_{Se}, σ_{Te}, σ_{C}	0.328, 0.668, 0.853, 0.508, 0.278
Atomic surface density n_{Si}, ${}^{a}n_{Au}$	7.8×10^{14} atoms/cm^2, 4.6×10^{14} atoms/cm^2
Attenuation coefficients λ_{SiSi}, ${}^{b}\lambda_{SiC}^{Au}$, ${}^{b}\lambda_{CC}^{Au}$	1.8 nm, 3.95 nm, 3.54 nm
Atomic density ρ_{Si}, ${}^{c}\rho_{C}^{Au}$	5×10^{22} atoms/cm^3, 4.1×10^{22} atoms/cm^3

[a] $(\sqrt{3} \times \sqrt{3})R30$ surface of (111). [b] Calculated based on an empirical formula eq 3.22 from Whitesides (reference 214). [c] Calculated based on the gold surface.

of the substitution level derived from the silicon and carbon signals is calculated as the standard deviation in film thickness added in quadrature to the uncertainty in the adventitious carbon thickness. All of the utilized constants are listed in Table 3.8.

3.3.5 Calculations of Substitution Levels

This section shows the detailed calculations of the substitution levels of functionalized silicon surfaces. Table 3.9 shows the intensity ratios of C to Si of ≡Si−H surfaces, measured from XPS, and the calculated effective thicknesses. The average effective thickness of adventitious carbon is 0.42 ± 0.06 nm, calculated by averaging all d_{C}^{adv}. An example of using eq 3.18 to calculate the thickness of adventitious carbon is given by

$$d_{C}^{adv} = \frac{n_{Au}}{n_{Si}} \lambda_{SiC}^{Au} \ln\left(\frac{I_{C}\sigma_{Si}\rho_{Si}\lambda_{SiSi}}{I_{Si}\sigma_{C}\rho_{C}^{Au}\lambda_{CC}^{Au}} + 1\right) \tag{3.23}$$

$$d_{C}^{adv} = \frac{4.6 \times 10^{14}}{7.8 \times 10^{14}}(3.95) \ln\left(\frac{0.246(0.328)(5 \times 10^{22})(1.8 \times 10^{-7})}{0.278(4.1 \times 10^{22})(3.54 \times 10^{-7})} + 1\right) = 0.39 \text{ nm}$$

Table 3.10 shows the intensity ratios of C to Si of ≡Si−S–*n*-octadecyl surfaces measured from XPS. The average substitution of di-*n*-octadecyl disulfide is 29.5 ± 3.8 %, calculated by averaging all substitution levels. Each substitution level was calculated

Table 3.9. The Ratio of XPS Counts Carbon to Silicon of Si(111)–H Samples[a]

Adventitious Carbon								
C:Si XPS ratio	0.246	0.239	0.328	0.330	0.228	0.230	0.295	0.301
Effective thickness (nm)	0.39	0.37	0.49	0.50	0.35	0.36	0.45	0.46

[a] Numbers highlighted in blue are those used in the sample calculations.

Table 3.10. The Ratio of XPS Counts Carbon to Silicon of ≡Si–S–*n*-octadecyl Terminated surfaces[a]

Di-*n*-octadecyl disulfide						
C:Si XPS ratio	0.749	0.808	0.727	0.711	0.830	0.724
Substitution level (%)	29.7	32.4	28.1	27.2	33.6	28.0

[a]Numbers highlighted in blue are those used in the sample calculations.

individually as follows. First the total thickness of the carbon layer is calculated by

$$d_{\mathrm{C}}^{\mathrm{total}} = \frac{n_{\mathrm{Au}}}{n_{\mathrm{Si}}} \lambda_{\mathrm{SiC}}^{\mathrm{Au}} \ln\left(\frac{I_{\mathrm{C}} \sigma_{\mathrm{Si}} \rho_{\mathrm{Si}} \lambda_{\mathrm{SiSi}}}{I_{\mathrm{Si}} \sigma_{\mathrm{C}} \rho_{\mathrm{C}}^{\mathrm{Au}} \lambda_{\mathrm{CC}}^{\mathrm{Au}}} + 1 \right) \tag{3.24}$$

$$d_{\mathrm{C}}^{\mathrm{total}} = \frac{4.6 \times 10^{14}}{7.8 \times 10^{14}} (3.95) \ln\left(\frac{0.749(0.328)(5 \times 10^{22})(1.8 \times 10^{-7})}{0.278(4.1 \times 10^{22})(3.54 \times 10^{-7})} + 1 \right) = 1.02 \text{ nm}$$

Subtracting the average thickness of adventitious carbon from this value yields the effective thickness of the alkyl layer

$$d_{\mathrm{C}}^{\mathrm{eff}} = d_{\mathrm{C}}^{\mathrm{total}} - d_{\mathrm{C}}^{\mathrm{adv}} = 1.02 \text{ nm} - 0.42 \text{ nm} = 0.6 \text{ nm}$$

Finally, the effective thickness can be turned into a substitution level by

$$\Theta = \frac{d_{\mathrm{C}}^{\mathrm{eff}}}{d_{\mathrm{C}}^{\mathrm{Th}}} = \frac{0.6}{2.01} = 29.7\% \tag{3.25}$$

Table 3.11 shows the intensity ratios of E (E = S, Se, or Te) to Si of ≡Si−E−Ph surfaces measured from XPS. An example of using the chalcogen signal to calculate a substitution level from eq 3.21 is

$$\Theta = \frac{\rho_{\mathrm{Si}} \lambda_{\mathrm{SiSi}} \sigma_{\mathrm{Si}} I_{\mathrm{E}}}{n_{\mathrm{Si}} \sigma_{\mathrm{E}} I_{\mathrm{Si}}} = \frac{(5 \times 10^{22})(1.8 \times 10^{-7})(0.328)(0.030)}{(7.8 \times 10^{14})0.668} = 17\%$$

Table 3.11. The ratio of XPS counts for each element compared to silicon[a]

Method								
Diphenyl disulfide								
S:Si Counts ratio	0.028	0.029	0.027	0.024	0.028	0.029	0.024	0.026
Substitution level (%)	16.0	16.7	15.5	13.9	16.0	16.7	14.0	14.5
Diphenyl diselenide								
Se:Si XPS ratio	0.033	0.032	0.031	0.030	0.031	0.030	0.034	
Substitution level (%)	14.5	13.9	13.7	13.2	13.8	13.4	15.0	
Diphenyl ditelluride								
Te:Si XPS ratio	0.764	0.487	0.415	0.394	0.351	0.375	0.460	0.366
Substitution level (%)	30.2	19.3	16.4	16.6	13.9	14.9	18.3	14.5
Di-*n*-octadecyl disulfide								
S:Si XPS ratio	0.030	0.052	0.061	0.055	0.043	0.043		
Substitution level (%)	17.1	29.5	34.6	31.1	24.4	23.2		

[a]Numbers highlighted in yellow indicate values rejected using Peirce's Criterion. Numbers highlighted in blue are those used in the sample calculations.

3.3.6 Discussion and Simulation

The ≡Si−S−*n*-octadecyl substitution level determined using eq 3.21 are found to be 27 ± 6% (see Table 3.12), which appears to be significantly different from those determined using eq 3.18. However, this discrepancy can be resolved by adjusting for the fact that unavoidable amounts of adventitious carbon will contribute to the integrated peak intensity of the C 1s signal. This can be done by first subtracting the effective thickness of the adventitious carbon layer from eq 3.18, then calculating the substitution level. Using eq 3.18, the thickness of the adventitious carbon layer is estimated by utilizing the silicon and carbon XPS spectra for hydride-terminated silicon, ≡Si(111)−H, which is found to be 0.42 ± 0.06 nm (Table 3.9). After correcting for the additional signal from the adventitious carbon, the substitution level determined using the silicon and carbon signals (eq 3.18) is found to be 30 ± 4% (Tables 3.12 and 3.10), which agrees very well with the values of 27 ± 6% determined using the silicon and sulfur signals (eq 3.21). In the case of ≡Si−E−Ph-modified silicon surfaces, the substitution level can

Table 3.12. Substitution Level Measured from XPS Data and Simulation

Functional group	substitution level (%) (XPS data)	substitution level (%) (simulation)
Si−S−Ph	15 ± 1[a]	14.9 ± 0.1
Si−Se−Ph	13.9 ± 0.6[a]	14.7 ± 0.1
Si−Te−Ph	16 ± 2[a]	13.2 ± 0.1
Si−S−*n*-octadecyl	27 ± 6[a]	N/A
Si−S−*n*-octadecyl	30 ± 4[b]	N/A

[a,b]Calculated using eqs 3.21 and 3.18, respectively. Substitution levels are displayed as the average ± standard deviation. Four identical samples were prepared for each type of silicon surface. For each sample, two spots were measured by XPS, leading to each functionalization of silicon surfaces containing eight measurements. Table 3.11 includes the substitution level for each measurement. Substitution levels measured from simulation are the mean of 150 independent simulation runs (14,000 Si atoms and 13 different possible orientations for each ≡Si–E–Ph group).

be determined using the silicon and chalcogen signals via application of eq 3.21. The average substitution levels are all found to be ∼15% (Table 3.12).

From these data it is found that the substitution level of the ≡Si−E−Ph-modified silicon surfaces (∼15%) is low compared to the aliphatic variant, ≡Si−S−*n*-octadecyl (∼30%). These lower substitution levels can be understood better by inspection of Figure 3.9, where the bulky phenyl rings are shown to be nearly parallel to the silicon surface. Such a molecular surface configuration would shield a significant number of Si−H bonds from further reactivity, thereby reducing the maximum possible ≡Si−E−Ph groups that can bind to the silicon surface. In order to understand/validate the substitution levels measured by XPS better, Figure 3.11a shows an idealized close-packed representation of ≡Si−S−Ph groups on a Si(111) surface. It can be seen from this tiling that the substitution level is 25%, which gives a useful reference for the upper theoretical limit of the substitution level. In reality, this close-packed configuration of ≡Si−E−Ph groups cannot be achieved due to the covalent nature of the silicon–chalcogen bond and the spatially stochastic nature of silicon–chalcogen bonding events. Once the ≡Si−E−Ph groups are bonded to the silicon surface, they are trapped kinetically and cannot diffuse to other sites in order to achieve a lower energy/more densely packed configuration. As such, there will be a significant fraction of silicon surface atoms that are not bonded to a chalcogen or directly underneath a phenyl ring and are unavailable to form silicon–chalcogen bonds.

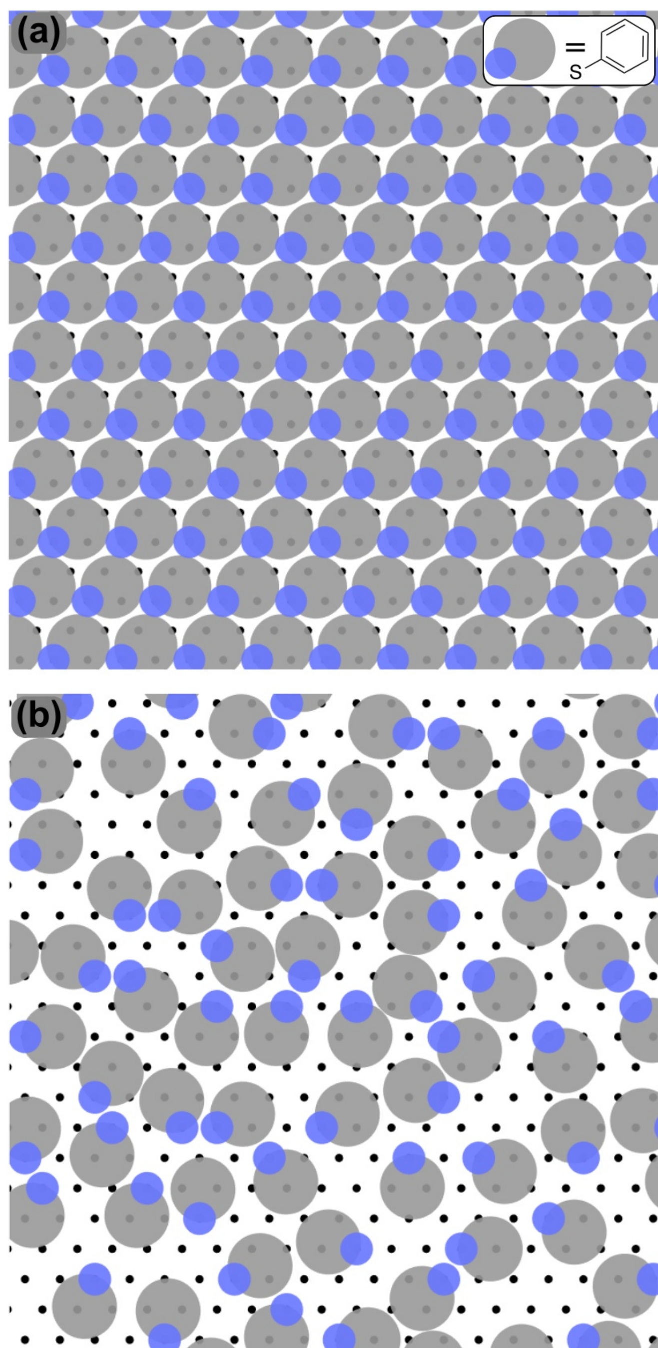

Figure 3.11. (a) Idealized close-packed configuration of ≡Si−S−Ph groups on a Si(111) surface. (b) Configuration resulting from a simulation of stochastically packed ≡Si−S−Ph groups on a Si(111) surface. Silicon-hydride groups are represented by small black dots, chalcogen atoms by medium blue disks, and phenyl rings by large gray disks.

This proposed mechanism of spatially stochastic covalent bonding of ≡Si−E−Ph groups on the silicon (111) surface was simulated, with a representative configuration shown in Figure 3.11b. In these simulations, the surface packing is assumed to be a

2-dimensional problem, where the ≡Si−E−Ph groups are represented by the union of two hard disks with respective radii corresponding to the bond lengths shown in Figure 3.10. Briefly, the stochastic bonding of ≡Si−E−Ph groups is simulated using the following method. First, a sufficiently large silicon (111) surface is generated (results were found to be effectively invariant for more than 14,000 Si atoms), and a random Si site is chosen. Then, a ≡Si−E−Ph group is placed at this random Si site at multiple random orientations, with uniform spacing (results were found to be invariant for more than seven different orientations), and checked to see if it overlaps with any of the other ≡Si−E−Ph groups on the surface. If an orientation with no overlaps is found, it is left permanently in that position and orientation. This process is repeated at different randomly chosen Si surface sites until all silicon surface sites have been checked. A time series visualization of a stochastic simulation of ≡Si−E−Ph groups packing the Si(111) surface is shown in Movie S1 in the Supporting Information of the published paper.[215] The substitution levels measured from these simulations are shown in Table 3.12 and found to be ∼15%, which is in excellent agreement with the experimentally measured values derived from XPS data. These results support the claim of near-parallel configurations of the phenyl rings, as well as the stochastic nature of ≡Si−E−Ph groups bonding to the silicon surface.

3.3.7 Proposed Mechanism

As mentioned earlier, the reaction of a ≡Si(111)−H surface with di-*n*-octadecyl disulfide with only UV irradiation or only 80 °C heating, resulted in a small increase of contact angle versus the unfunctionalized hydride-terminated silicon surface (Table 3.6), indicating that successful functionalization requires that the UV illumination be coupled with gentle heating. The key intermediate in silicon–chalcogen bond formation is most likely a silicon radical formed via homolytic cleavage, as shown in Figure 3.12, as has been postulated earlier on both surfaces and in silane molecules.[10,78,83,107,112,194] This silicon radical then can add to the dichalcogenide through an S_H2 reaction, followed by collapse of the trivalent intermediate to product and an organochalcogen radical.[10,78,83,107] The silicon radical also could react directly with an organochalcogen radical to form a silicon–chalcogen bond, although this pathway is expected to be less likely due to the improbability of having both species, present in low concentrations, in close proximity.

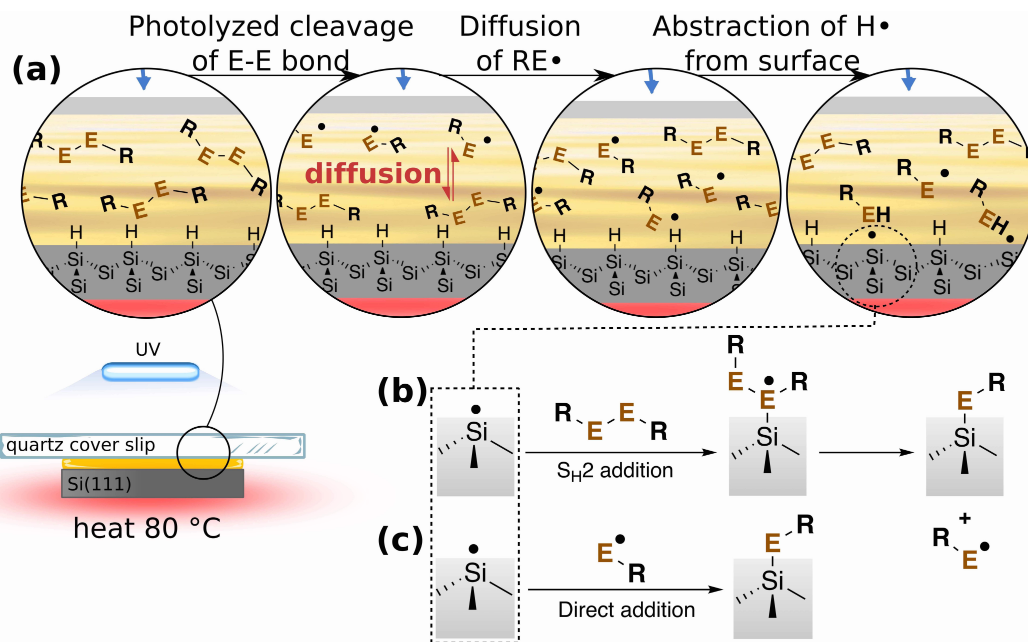

Figure 3.12. "Photolysis–diffusion–abstraction–addition" mechanism leads to the ≡Si–ER bond formation. (a) Photolysis of REER molecules near the top of the organic layer results in RE• radicals. Because this film has been melted and is thus a liquid, these radicals can diffuse throughout the film and can abstract a hydrogen from a surface ≡Si–H bond, leading to ≡Si• radicals. (b) Addition of REER molecules to surface ≡Si• radicals via S_H2 addition leads to ≡Si–E bond formation. (c) Direct combination of a ≡Si• radical with a RE• radical also can yield ≡Si–ER bond formation.

The central question is the driving force for homolytic cleavage of the surface silicon–hydride bond. The temperature required to initiate productive homolytic cleavage of the Si−H bond is typically in the range of 150–200 °C, as shown through numerous studies on hydrosilylation of alkenes and alkynes on silicon surfaces.[81,147,216] Similarly, heating to 80 °C does not induce Si−EC bond formation, as shown by the control experiment with only heat (vide supra); heating to 80 °C appears to serve only to liquefy the chalcogenide molecules to form an even layer on the silicon surface. The 254-nm UV light, however, is of sufficient energy (112.6 kcal/mol) to induce cleavage of both the diaryl/dialkyl dichalcogenide E−E bond[116,171,217] and the Si−H bond.[84,86–88,218] Because of the high absorption coefficients at 254 nm for the three diphenyl dichalcogenides as well as the di-*n*-octadecyl disulfide (Figure 3.13, and corresponding calculations in Section 3.2.4), essentially all of the incident UV light would be absorbed by this molecular layer, and no UV light would directly impinge upon the silicon surface. The role of the 254 nm UV light, then, must be to cleave S−S, Se−Se, or Te−Te bonds (bond energies of 53–57, 40, and 30–35 kcal/mol, respectively)[10,171,217] at the surface of the melted REER layer, in close proximity to the quartz coverslip, to yield thiyl, selenyl, or telluryl radicals, RE• (E = S, Se, and Te), respectively, as outlined in Figure 3.12.

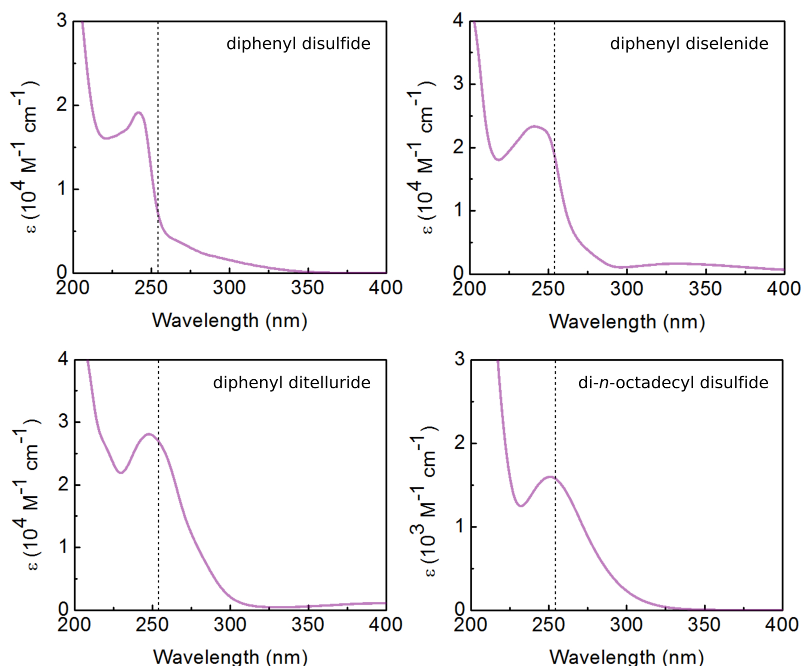

Figure 3.13. UV absorption spectra of diphenyl and dialkyl dichalcogenides. Dashed vertical lines = 254 nm.

Diffusion of these radicals throughout the layer then could lead to formation of silyl radicals, ≡Si•, at the surface through removal of H• from surface-bound ≡Si−H groups (Figure 3.12a)

Upon formation of ≡Si• species, two possible pathways would realize the formation of ≡Si−ER bonds, as has been described previously.[83] The first route involves a stepwise S_H2 addition of REER to a silyl radical, producing trivalent sulfuranyl, seleranyl, or telluranyl radical intermediates, followed by collapse of the intermediate to form the final ≡Si−ER product and an RE• radical (Figure 3.12b). This reaction pathway most likely would be favored due to the high abundance of REER molecules near the surface. The second pathway involves the direct combination of a surface silyl radical, ≡Si•, and a free chalcogenide radical, RE•, to produce ≡Si−ER (Figure 3.12c).[83] Both may be in operation and would be difficult to distinguish.

3.3.8 Work Function and Surface Dipoles

The effect of surface functionalization was examined for the series ≡Si−S−Ph, ≡Si–Se–Ph, and ≡Si−Te−Ph since these groups contain the same consistent phenyl termination. Functionalization of the silicon surface can alter its electronics, resulting from band bending due to charged surface states and surface dipoles,[40,133,219] thus we wished to ex-

amine the effect of the series of chalcogenide linkers on the properties of the silicon since earlier predictions had suggested large effects.[4,42,184] XPS can be used to determine the band bending, and work function can be obtained from UPS measurements.[39,40,113,179] Measurements required multiple samples to account for measurement variability as well as the use of gold-on-silicon as the reference for XPS, as outlined by Lewis and co-workers.[40] Figure 3.14a and b show the XPS spectra and cross-sectional SEM image of the Au reference used for binding energy calibration. Since the interfacial dipoles depend upon the doping level,[178] moderately doped n-type Si(111) was chosen because it would be expected to have the greatest range of Si $2p_{3/2}$ values depending upon surface functionality.[40]

Average values of electronic properties measured for the functionalized silicon surfaces are listed in Table 3.13. Raw data without normalization of all measurements, including XPS and secondary electron He I UPS, are shown in Figures 3.15 and 3.16. The data for the ≡Si−E−Ph-terminated surfaces, as reported in Table 3.13, are similar to that of the starting ≡Si−H-terminated surface. Figure 3.17 depicts the energy band diagram of Si $2p_{3/2}$ binding energy, with upward band bending corresponding to the measured band bending values. The measured work function of the ≡Si−H-terminated surface is 4.27 ± 0.03 eV, which is similar to that reported earlier, 4.29 eV for hydride-terminated Si(111) of the same doping.[40] Upon functionalization with the phenyl chalcogenide moiety, the work functions were relatively unchanged, in the range of 4.16 ± 0.09 eV for ≡Si−S−Ph to 4.31 ± 0.06 for ≡Si−Te−Ph. Other electronic characteristics, including surface electron affinity (χ^S) and surface dipole (δ), also are largely unchanged compared to the starting ≡Si−H interface. A ≡Si−CH_3-terminated Si(111) surface with similar (moderate n-type) doping, with full substitution of all ≡Si−H groups enabled by the small size of the methyl group, caused only a small drop of the work function to 4.04 eV.[40] A large shift of work function compared to starting ≡Si−H was, however,

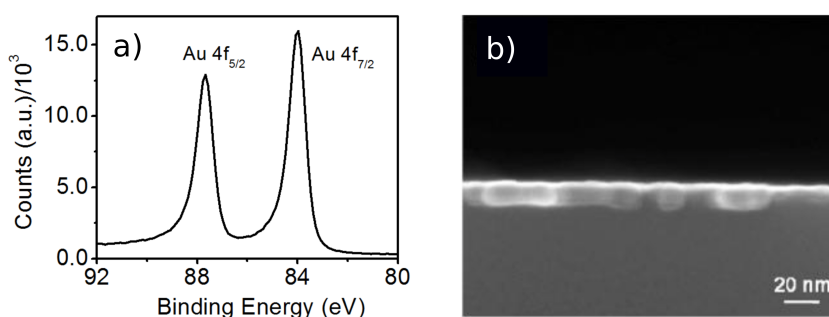

Figure 3.14. (a) XPS spectrum of the Au reference used for binding energy calibration. (b) Cross-section SEM image of the Au film on the Si(111) surface, from reference 14.

Table 3.13. Binding Energy, Work Function, and Surface Dipole of Functionalized Silicon Surfaces[a]

Surfaces	BE(Si $2p_{3/2}$)[b] (eV)	E^{S}_{vbm} (eV)	qV_{bb} (eV)	WF^{S} [b] (eV)	χ^{S} (eV)	δ[b] (eV)
≡Si−H	99.44 ± 0.07	0.70	0.12	4.27 ± 0.03	3.85	–0.20 ± 0.08
≡Si−S−Ph	99.43 ± 0.06	0.69	0.13	4.16 ± 0.09	3.73	–0.32 ± 0.11
≡Si−Se−Ph	99.34 ± 0.06	0.60	0.22	4.26 ± 0.06	3.74	–0.31 ± 0.08
≡Si−Te−Ph	99.37 ± 0.05	0.63	0.19	4.31 ± 0.06	3.82	–0.23 ± 0.08

[a]BE(Si $2p_{3/2}$) is the binding energy of the Si $2p_{3/2}$ peak at the surface as measured by XPS. E^{S}_{vbm} is the energy difference from the valence band to Fermi level at the surface. Band bending energy is represented as qV_{bb}. WF^{S} is the dark work function at the silicon surface measured in the dark by UPS. χ^{S} and δ represent surface electron affinity and the surface dipole, respectively. [b]Binding energy, work function, and surface dipole are displayed as "average ± standard deviation". The standard deviations of E^{S}_{vbm} and qV_{bb} have the same values as the ones of BE (Si $2p_{3/2}$), and the standard deviations of χ^{S} have the same values as the ones of δ. Four identical samples were prepared for each type of silicon surface. For each sample, two spots were measured by XPS as well as UPS, leading to each functionalization of silicon surfaces containing eight measurements. A gold-on-silicon sample was used as the reference for XPS.

observed upon substitution of hydrides with bromine atoms, ≡Si−Br, to 4.86 eV.[40] Thus, the chalcogenide terminations, which do not have the large dipole of the bromide termination and are more akin to the methyl termination in terms of electronegativity and surface dipole, do not induce much change. The small effect of ≡Si−E−Ph-termination also may result from the low substitution levels (∼15%);[11,220–223] the electronics of the silicon are thus dominated by the majority ≡Si−H termination.

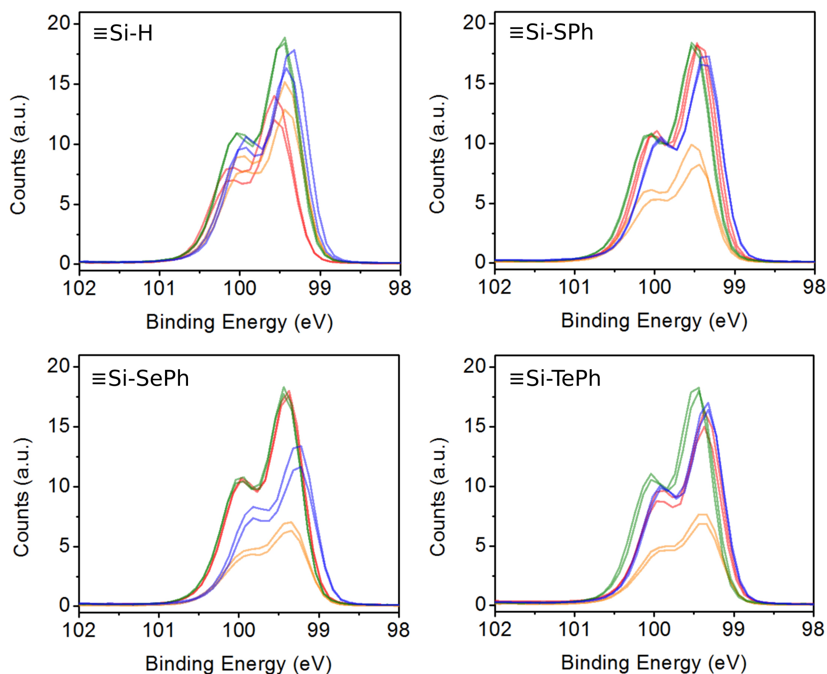

Figure 3.15. XPS spectra of the Si 2p peak from Si(111) surfaces, with indicated terminations. Four identical batches of silicon samples were prepared for XPS measurement. Each batch contained four samples, which were ≡Si−H, ≡Si−S−Ph, ≡Si−Se−Ph, and ≡Si−Te−Ph surfaces. For each sample, two spots were measured by XPS. Consequently, each functionalization of silicon surfaces contains eight measurements, giving eight XPS curves, in which every two curves with same color means they are from the same sample. The curves are all from raw data without normalization.

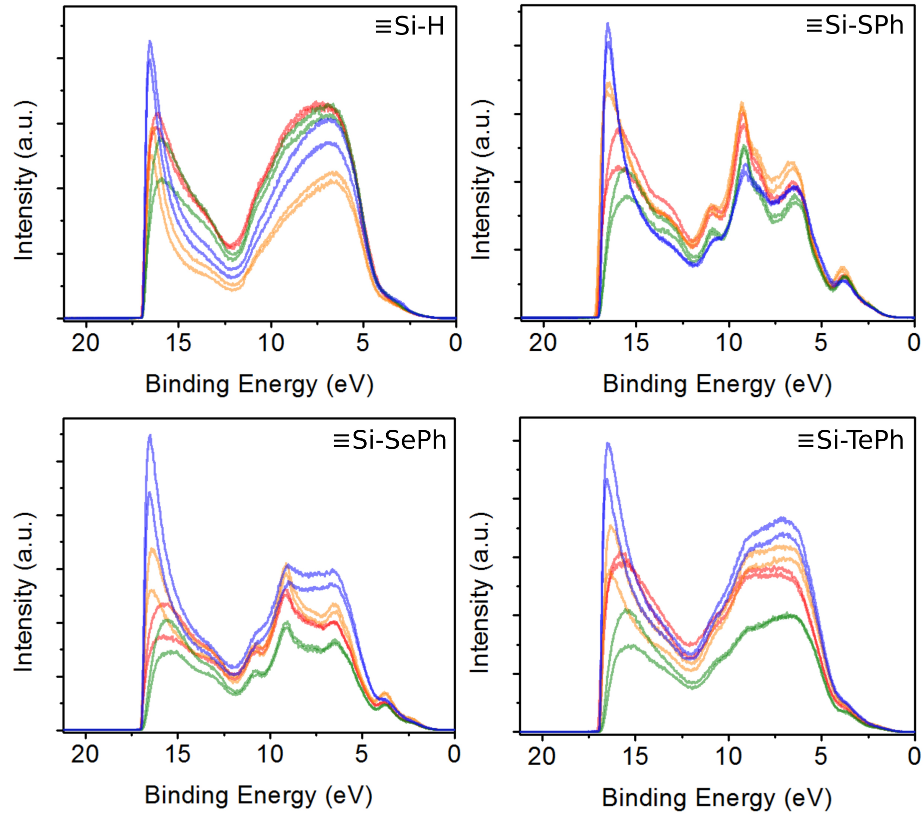

Figure 3.16. UPS He I spectra of the Si(111) surfaces, with indicated terminations, for the determination of work function. Four identical batches of silicon samples were prepared for UPS measurement. Each batch contained four samples, which were ≡Si−H, ≡Si−S−Ph, ≡Si−Se−Ph, and ≡Si−Te−Ph surfaces. For each sample, two spots were measured by UPS. Consequently, each functionalization of silicon surfaces contains eight measurements, giving eight UPS curves, in which each two curves with same color means they are from the same sample. The curves are all from raw data without normalization.

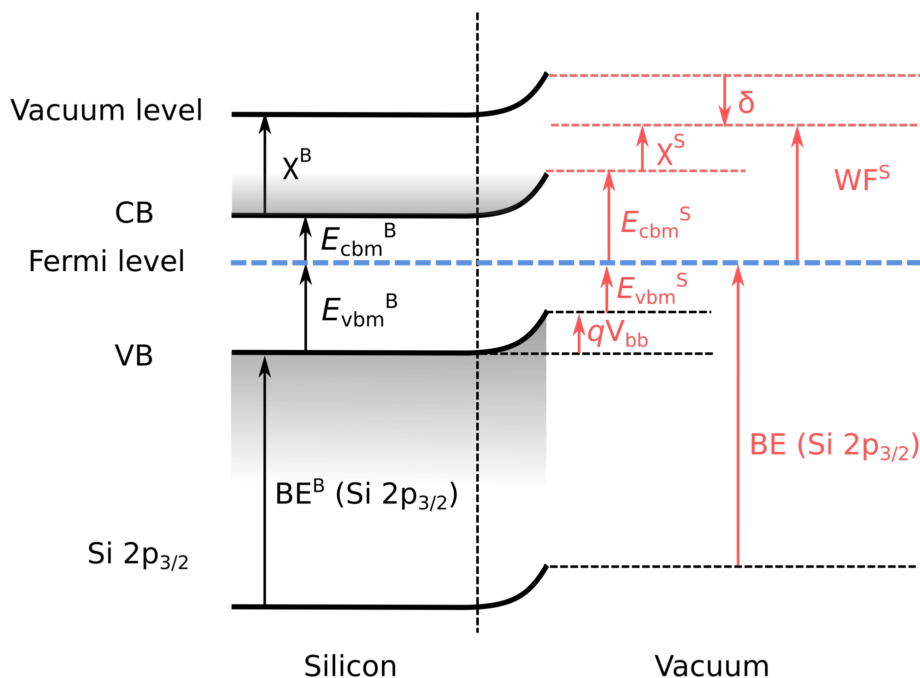

Figure 3.17. Energy band diagram of functionalized n-type Si(111) with band bending, qV_{bb}, and surface dipole, δ. The values of black markings, including BE^{B} (Si $2p_{3/2}$), E^{B}_{vbm} and χ_{B}, are constant for a specific silicon. In the present case, the values of BE^{B} (Si $2p_{3/2}$), E^{B}_{vbm}, and χ_{B} are 98.74 eV, 0.82 eV, and 4.05 eV, respectively. The values labeled in red are obtained from XPS and UPS data.

3.4 Conclusions

A straightforward approach to form ≡Si−E−R (E = S, Se, Te) functionalities on Si(111)−H surfaces has been described using UV irradiation and gentle thermal heating with synthetically practical dialkyl/diaryl chalcogenide precursors. The mechanism of reactivity of the dichalcogenides appears to be radical in nature and is related closely to the observed reactivity in silane molecules. The substitution level of the phenyl chalcogenide derivatives, ≡Si−E−Ph, was lower than that of the aliphatic chalcogenide (≡Si−S−*n*-octadecyl) group, most likely due to the fact that the phenyl group obscures neighboring silicon–hydride bonds and thus sterically prevents them from reacting. Use of larger flat aromatic precursors with dichalcogenide linkages could enable access to interesting interfaces that have few linker atoms to the surface of the silicon that shield the silicon surface with potentially electronically active moieties. Higher substitution levels will need to be achieved through use of less bulky dialkyl dichalcogenide groups in order to better study the effects of ≡Si−E bonds on the electronics of silicon.

Chapter 4

Reevaluating the Quantification of Substitution Level of Monolayers on Silicon Surfaces

4.1 Introduction

Modification of silicon surfaces via the grafting of organic molecules is of great interest to tailor the physical and chemical properties of the underlying silicon. The quality of the formed monolayers will be critical in determining the interfacial electronic properties and to obtain a chemically and electrochemically stable surface. Precise quantification of substitution levels of Si–H groups by organic molecules bound through Si–C bonds is important to determine the suitability of the modified surface for a specific application. Maximum coverage by specific functionalities is not always ideal for all the applications. For instance, Gooding and co-workers studied the effect of the monolayer coverage on the stability, optical, and chemical properties of porous silicon-based rugate filters.[224] They demonstrated that surfaces with low monolayer coverage have short-term stability in aqueous environments but are amenable to a high degree of biological functionalization. When the coverage is high, the sample is well-passivated but no longer sufficiently reactive toward biomolecules. By adjusting the level of surface coverage, the balance between stabilization and degree of biofunctionalization can be tuned.

4.1.1 Substitution Levels of Organic Alkyl Monolayers on Si(111) Surfaces

The substitution levels of hydrosilylation on silicon surfaces have been studied since the early work of Chidsey and co-workers from 1993 to 1995.[80,81] It was reported that

only 50–55% of the reactive Si–H sites on the Si(111) surface can be substituted by alkyl chains owing to the steric hindrance near the surface, leaving 45–50% of the Si–H sites unreacted after completion of the monolayer.[17,18,81,89,91,141,213,225,226] In 2010, Zuilhof and co-workers investigated the influence of the different linkage groups on the monolayer structure and found that the substitution levels for the alkenyl monolayers increased with the chain length from 55% for C_{12} to 65% for C_{18},[15] as shown in Figure 4.1. The higher coverage of alkenyl monolayers (60–65%) compared to alkyl monolayers (50–55%) may be attributed to the smaller van der Waals radius of the Si−C=C group compared to the Si–C–C group, allowing for the coverage of alkenyl monolayers not restricted by steric constraints near the surface.[15] The larger bond angle and rigidity of the C=C bond may enhance the chain to stand more upright. The purported higher reactivity of 1-alkynes than 1-alkenes toward Si(111)–H could also be another reason for more densely packed monolayers. Moreover, the Zuilhof group demonstrated that the C_{16} dienyl monolayers (≡Si−C=C−C=C−R, R = alkyl) show a higher coverage than the C_{16} alkenyl layers (≡Si−C=C−R, R = alkyl), 63% vs 59%,[104] although this difference may not be statistically significant.

A 100% coverage of the Si(111) surface by methyl groups has been reported by the Lewis group using a two-step halogenation/alkylation procedure of Si(111)–H.[16,34,227–229] With its 2.2 Å van der Waals radius, the methyl group is the only straight chain saturated alkyl group that sterically can terminate every atop site on an Si(111)–H surface, which has a distance of 3.8 Å between Si atop sites.[34] Figure 4.2 shows the low-temperature scanning tunneling microscopy (STM) images of Si(111)–CH_3 surfaces, with very few defects on the surface and a high degree of order.[16] For an ethyl-terminated Si(111) surface, ∼80% of the Si atop atoms were substituted by Si–C

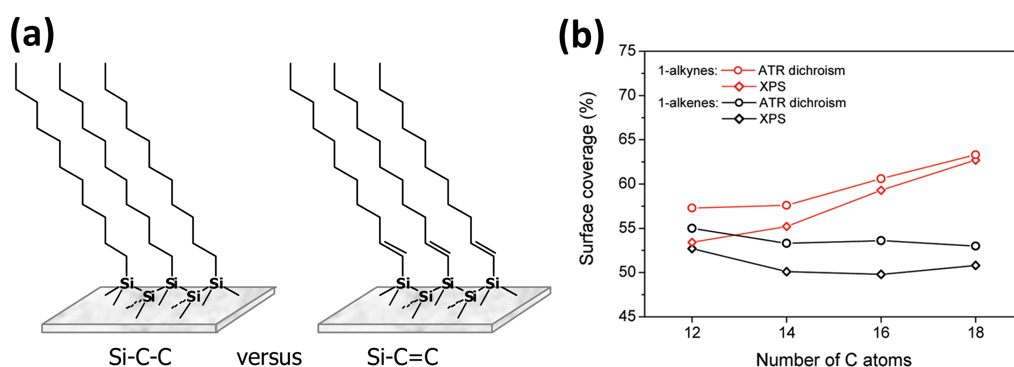

Figure 4.1. (a) Different linkages of organic monolayers on the Si(111)–H: alkyl monolayer (left) and alkenyl monolayer (right). (b) Surface coverage obtained by ATR-dichroism (diamond) and XPS (circle) of 1-alkene (lower black curves) and 1-alkyne (upper red curves) monolayers on Si(111)–H. (Reprinted with permission from ref 15. Copyright 2010 American Chemical Society.)

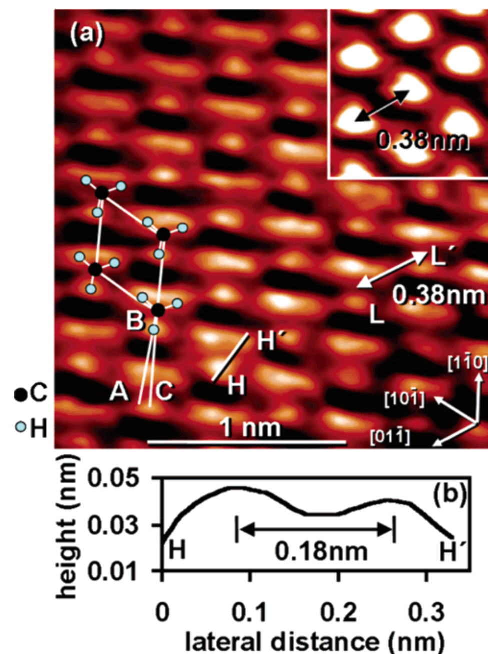

Figure 4.2. STM image of Si(111)–CH_3 collected at 4.7 K (inset: 77 K) with a sample bias of –2.5 V and a constant current of 0.050 nA (dark = low; light = high). Directions of low-index planes determined by X-ray crystallography are shown. The surface unit cell is represented by the parallelogram, and four methyl groups are drawn. (Reprinted with permission from ref 16. Copyright 2005 American Chemical Society.)

bonds due to the steric constrains.[229] Other than the methyl group, the acetylenyl group also gives a 100% substitution level on Si(111) surface, as demonstrated by Lewis and co-workers.[230] Furthermore, the ethynyl-terminated Si(111) surface can be functionalized further with electroactive groups via "click" chemistry between an azide-substituted electroactive molecule and the surface-bound alkyne.[231] Recently, the Zuilhof group developed a catalyst-free gas-phase hydrosilylation method and showed a linear attachment of 1-propenyl chains ($\equiv$Si$-$CH$=$CH$-CH_3$), with a reported 92% surface coverage.[232]

4.1.2 Molecular Models

Molecular modeling simulation is a useful way to obtain information about the structure of alkyl monolayers on the silicon surface. In 2001, using two-dimensionally repeating boxes to mimic the modified surface, the Zuilhof group studied the effects of various substitution levels (33.3%, 50%, 66.7%, and 100%) of the Si–H groups by octadecyl monolayers on the Si(111) surface.[17] The result was that only with a substitution level of $\sim$50% is there a good agreement between the structure obtained from molecular modeling and the available experimental data, as shown in the Figure 4.3a structure.

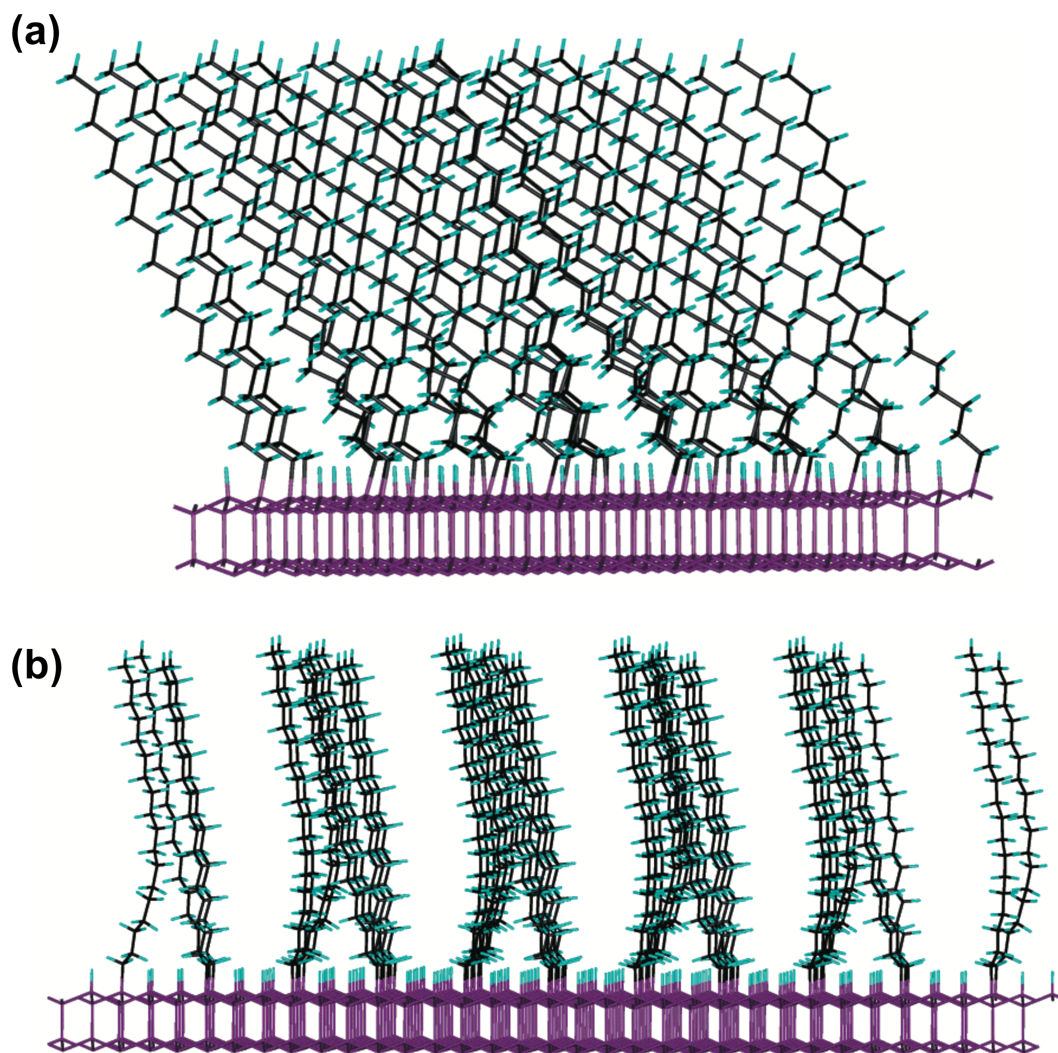

Figure 4.3. Structures of monolayers as obtained by the polymer consistent force field (PCFF) calculations with (a) 50% and (b) 33.3% substitution levels. (Reprinted with permission from ref 17. Copyright 2001 American Chemical Society.)

Although steric hindrance between alkyl chains makes the 50% substitution level seem energetically unfavorable because all the alkyl chains have to penetrate the van der Waals radii of other alkyl groups, it is compensated by larger attractive van der Waals forces between the alkyl chains. However, a lower substitution level of 33.3% gives an energetically less favorable configuration (Figure 4.3b); the molecules are tilted far away from each other ($\sim$60° for 33.3% vs. $\sim$30° for 50%) and form small clusters on the surface. High substitution levels (66.7% and 100%) give crowded surfaces with the molecules oriented perpendicular to the silicon surface, with high energies. This work was followed by molecular mechanics simulations for the optimal packing structure of octadecyl alkyl monolayers on a Si(111) surface by Zhang and co-workers.[18] Figure

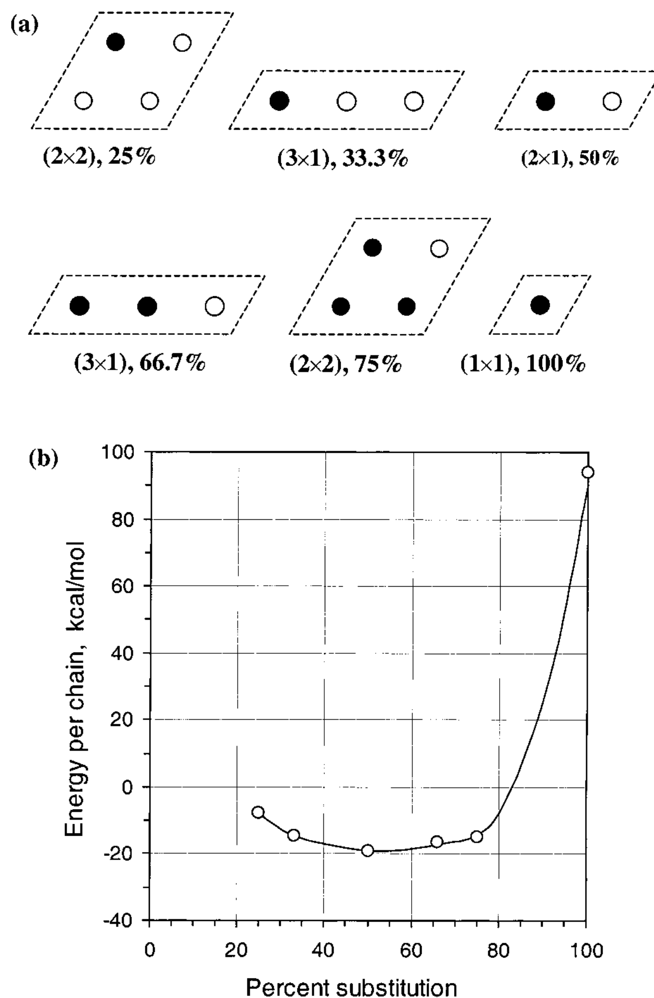

Figure 4.4. (a) Simulation cells for various percentages of molecular substitution. (b) Packing energy per chain vs percent substitution for octadecyl groups (C_{18}) on Si(111) from molecular mechanics simulations. (Reprinted with permission from ref 18. Copyright 2001 American Chemical Society.)

4.4a presents various simulation cells of different percentages of molecular substitution by extending the unit cell in two dimensions [e.g., (1 × 1), (2 × 1), (3 × 1), and (2 × 2)], representing the structures with different substitution levels from 25 to 100%. They demonstrated that the optimal molecular packing was based on the consideration of three major factors: molecular substitution, substitution pattern, and molecular orientation on the Si(111) surface, and showed that a substitution level of 50% has the lowest energy among all substitutions they studied (25%, 33.3%, 50%, 66.7%, 75%, and 100%) (Figure 4.4b). Later in 2003, Yuan and co-workers calculated the structure of eight-carbon monolayers on the Si(111) surface and found that the best substitution levels on the Si(111) surface were 50% for octene or octyne-derived monolayers and 40% for the styrene or phenylacetylene-derived monolayers.[213]

4.1.3 Techniques for the Determination of Substitution Levels

A series of techniques was used to determine the substitution level of Si–H by functional groups on silicon surfaces. In 2003, Allongue and co-workers used scanning tunneling microscopy (STM) to observe bromophenyl monolayers on Si(111) surfaces.[233] The STM technique was harnessed to image the methyl-terminated Si(111) surfaces that were prepared through a chlorination/alkylation procedure in 2005 by the Lewis group, revealing a high degree of order and an ∼100% coverage of the Si(111) surface by methyl groups.[16] However, STM is ineffective in the case of long carbon chain organic monolayers on silicon surfaces because the layers generally are disordered on the molecular scale.

Fourier-transform infrared spectroscopy (FTIR) is a commonly used method to semi-quantify the substitution level of Si–H on the silicon surface by organic groups.[9,10,19,124,125,234] The decrease in the integrated intensity of the ν(Si–H_x) peak can be converted easily to the efficiency, $\%E$, of the reaction via the following equation[124,125]

$$\%E = \frac{(A_{\text{Si–H, before}} - A_{\text{Si–H, after}})}{A_{\text{Si–H, before}}} = \frac{\Delta A_{\text{Si–H}} \times 100}{A_{\text{Si–H, before}}} \tag{4.1}$$

where A is the area of the integrated intensity of the absorption of the specified feature. Figure 4.5a and b show the FTIR spectra of porous Si(100) surfaces before and after reaction with 1-dodecene, respectively, using white-light hydrosilylation in the presence

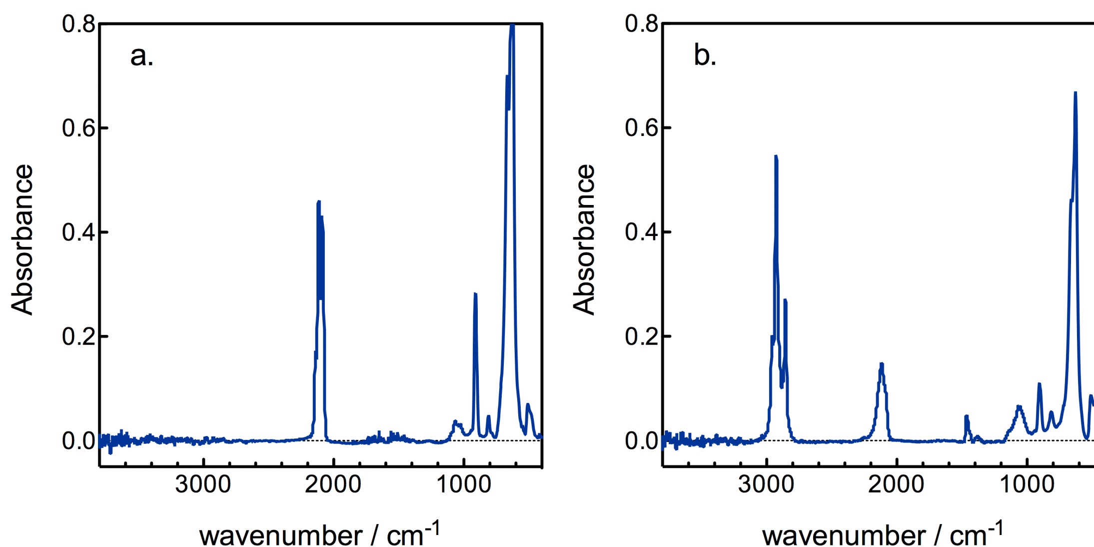

Figure 4.5. FTIR spectra of porous silicon coated with 0.5 M CBr_4 in dodecene (a) before and (b) after an 8-min white light photolysis (∼175 mW cm^{-2}). (Reprinted with permission from ref 9. Copyright 2011 American Chemical Society.)

of CBr_4.[9] A substitution level of 55–60% was obtained using the intensity difference of the ν(Si–H_x) peak centered around 2100 cm^{-1}. The disadvantage of this semiquantitative analysis is that the Si–H_x area changes very little at very low conversions; this problem is compounded by the broadening of the Si–H_x peak, as the yield of hydrosilylation increases, coupled with the curved baseline typically associated with these porous silicon samples.

X-ray photoelectron spectroscopy (XPS) is evidently a central surface technique combining both chemical and thickness sensitivity. XPS has been shown to be a powerful tool for the determination of the substitution level of alkyl groups on silicon bound through silicon–carbon bonds.[15,20,89,104,125,141] In 2000, Linford and Chidsey reported the functionalization of Si(111) with unsaturated hydrocarbons via UV illumination.[89] By using XPS narrow data, they calculated the substitution levels for all the modified silicon surfaces and got the highest, 45%, for the octadecyl-modified silicon surfaces. In 2005, Allongue and co-workers developed a quantitative angle-resolved XPS characterization method of alkyl and alkoxy monolayers on Si(111) surfaces.[141] Substitution levels of 48% for the $\equiv$Si$-$$C_{10}$ surface and 52% for the $\equiv$Si$-$O$-$$C_{10}$ surface were obtained according to their XPS measurements, very close to the maximum theoretical limits. This XPS quantification method was followed by research from the Zuilhof group on alkynes- and alkenes-modified silicon surfaces with chain lengths from C_{12} to C_{18}.[15] Using the atomic C/Si ratio from XPS data, they measured the substitution levels and found that the Si(111) surfaces were covered with 50–55% alkyl monolayers or 55–65% alkenyl monolayers. Later in 2013, the Zuilhof group also prepared monolayers on Si(111) surfaces from ω-fluoro-1-alkynes with varying carbon chain lengths (C_{10}–C_{18}), all of which have substitution levels in the range of 51–58%.[20]

The quantification of substitution levels of Si–H groups by alkyl groups using the XPS method is based upon a model that assumes that an XPS signal is attenuated as it passes through a material, according to the Beer–Lambert law, and usually uses the intensities of carbon and silicon signals from XPS for the calculation. Recently, however, questions have been raised as to the reliability of XPS for making such determinations. In 2017, Lewis and co-workers noted that values for coverage of methoxy groups on Si(111), as determined by XPS and FTIR differed substantially; XPS yielded values as high as 50% (Figure 4.6b), whereas FTIR was ∼30% (Figure 4.6a).[19] They attributed the difference to adventitious adsorption of residual solvent (methanol and/or THF), which would lead to an overestimation of the carbon:silicon ratio, and hence result in an inaccurate value of surface coverage. Adventitious carbon has also been noted by Yamazaki to be a potential problem in XPS measurements of surface coverage of alkyl

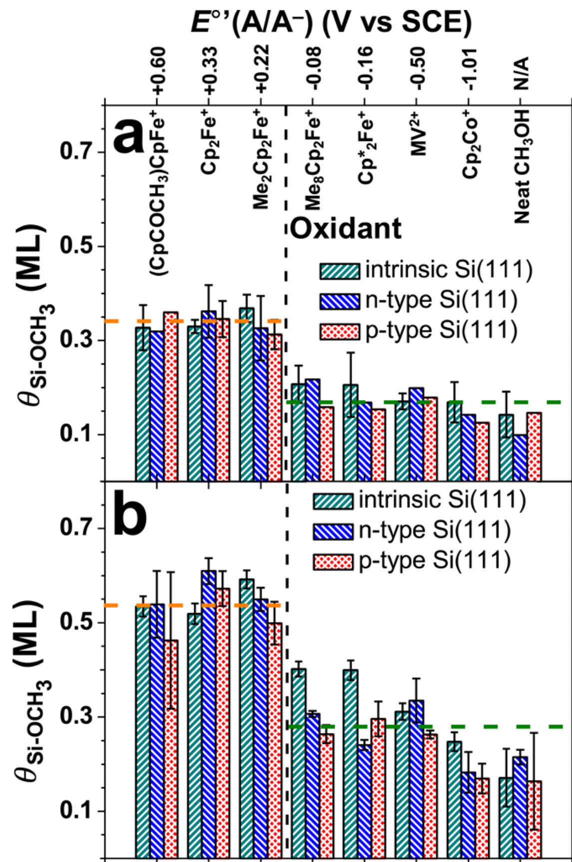

Figure 4.6. Monolayer coverages of $\equiv$Si$-$OCH$_3$ surfaces determined from (a) transmission infrared spectroscopy measurements and (b) X-ray photoelectron spectroscopy measurements as a function of the oxidizing conditions. (Reprinted with permission from ref 19. Copyright 2017 American Chemical Society.)

groups on silicon if one relies rely solely upon the ratio of carbon:silicon.[235] This group examined hydrosilylation of alkenes that contained fluorine- and nitrogen-containing groups that were used as atomic labels to quantify coverage, as opposed to the reliance upon the C 1s peaks in XPS. Our group also noted a discrepancy between the 'standard approach' in XPS that relies upon the silicon:carbon ratio when determining the coverage of an octadecanethiol linkage, $\equiv$Si$-$S$-$C$_{18}$ on Si(111)–H: the calculation using the silicon:carbon ratio indicated that $\sim$50% of the $\equiv$Si$-$H groups were replaced with $\equiv$Si$-$S$-$C$_{18}$, whereas using the Si:S ratio resulted in a substantially lower value of 27%. Adjusting the value by subtracting the same quantity of adventitious carbon determined to have been gathered on a hydrophobic Si(111)–H surface, however, led to a similar value of 27% substitution.[215]

In this chapter, we take a closer look at the assumptions made by earlier researchers who used XPS data for the quantification of the substitution levels of Si–H on Si(111)–H

surfaces by functional alkyl groups. The effect of adventitious carbon in these calculations is considered, the original calculations used previously to determine coverage are thoroughly reconsidered, and a revised approach is outlined. Three types of molecules were studied, including three simple aliphatic alkene molecules with different carbon chain lengths, 1-octene ($CH_2{=}CH{-}(CH_2)_5{-}CH_3$), 1-dodecene ($CH_2{=}CH{-}(CH_2)_9{-}CH_3$), and 1-octadecene ($CH_2{=}CH{-}(CH_2)_{15}{-}CH_3$), and two molecules with different atomic labels (F and S), 11-fluoro-1-undecene ($CH_2{=}CH{-}(CH_2)_9{-}F$) and di-*n*-octadecyl disulfide ($CH_3{-}(CH_2)_{17}{-}SS{-}(CH_2)_{17}{-}CH_3$). Conventional reaction conditions, including direct thermal heating (with neat molecules or molecules dissolved in mesitylene) and UV irradiation, are employed to functionalize the flat Si(111)–H surface with alkenes. For di-*n*-octadecyl disulfide, the functionalization method and XPS data used for quantification are from Chapter 3. In our previous work, a chalcogenide linker atom was used as the atomic label for the quantification of substitution levels. Here, two sets of formulae are derived for the quantification, using either the C/Si ratio or the E/Si ratio (E = F or S). Comparison and connection of different formulae are discussed. We hope that the new models will be more accurate and provide insights into the future directions for a better quantification of the substitution level of organic monolayers on silicon surfaces.

4.2 Materials and Methods

4.2.1 Materials

Si(111) wafers (n-type, phosphorus doped, 1–10 Ω·cm, 525 ± 25 μm) were obtained from Virginia Semiconductor, Inc. 1-Octene (98%), 1-dodencene (≥99.0%), and 1-octadecene (≥95.0%) were purchased from Sigma-Aldrich. 11-Fluoro-1-undecene (≥95%) was obtained from HongKong Chemhere Co.,Ltd. All reagents were stored in a –20 °C freezer inside an argon-filled glovebox. Dichloromethane was purified by a solvent purification system (Innovative Technology, Inc.) and dried over molecular sieves for 24 h in a glovebox prior to use. Molecular sieves (type 4A, 1/16 in. pellets, for selective adsorption), NH_4OH (aqueous, 30%), and HCl (aqueous, 37%) were purchased from Caledon Laboratories, Ltd. NH_4F(aqueous, 40%, semiconductor grade) was purchased from Transene Company, Inc. H_2O_2 (aqueous, 30%) and 2-propanol (≥99.5%) were obtained from Sigma-Aldrich. HF (49% aqueous, semiconductor grade) was purchased from J. T. Baker. $KAuCl_4{\cdot}xH_2O$ was purchased from Strem Chemicals.

4.2.2 Preparation of Flat Si(111)–H

Silicon wafers were cut into 1 cm $\times$ 1 cm squares using a dicing saw (Disco DAD 321). The diced chips were cleaned by a standard RCA procedure: the chips were sonicated first in 2-propanol for 10 min, then immersed in a fresh solution of H_2O/30% NH_4OH (aq)/30% H_2O_2 (aq) (6:1:1) at 80 °C for 10 min, and next in a fresh solution of H_2O/37% HCl (aq)/30% H_2O_2 (aq) (5:1:1) at 80 °C for another 10 min. The chips were rinsed thoroughly with deionized water between each step. The chips finally were rinsed with water and dried with a stream of argon gas. The cleaned silicon chips were immersed in argon-saturated 40% NH_4F for 5 min and then dipped into deionized water for 10 s. After being dried with an argon stream, each chip was put into an argon-filled vial, sealed, and immediately transferred into a glovebox.

4.2.3 Reactions with Organic Molecules

All reactions, except for the etching of silicon surfaces, were performed in the argon-filled glovebox. All the liquid molecules, including 1-octene, 1-dodencene, 1-octadecene, and 11-fluoro-1-undecene, were passed through a fresh column of alumina before use to remove peroxides. Figure 4.7a, b, and c show the reaction scheme of the hydride-terminated Si(111) surfaces with three pure alkenes, the fluoro-terminated alkene, and the di-*n*-octadecyl disulfide. Three methods were used to obtain the monolayer-grafted silicon surfaces, including direct heating using neat molecules, UV irradiation, and direct heating with molecules diluted in mesitylene, as shown in Figure 4.7d, e, and f. After reaction, the silicon samples were soaked in dry dichloromethane for 5 min and rinsed three times with a forceful stream of dry dichloromethane from a pipet to remove excess unreacted reagents. The samples were removed from the glovebox (in the sealed glass vial), dried with argon gas, and then analyzed immediately.

Direct Heating with Neat Alkenes

Twenty drops of liquid reagent were placed on a freshly etched flat silicon substrate inside a 20-mL glass vial, as shown in Figure 4.7d. The face of the silicon with the etched side was placed upside down to enforce spreading of the reagent, thus forming a sandwich of glass–reagent–etched silicon. Then, the glass vials were sealed with multilayers of parafilm entwined around the cap to seal it. The sealed glass vial containing the reagent and the porous silicon substrate was put on a 200 °C hot plate for a desired reaction time.

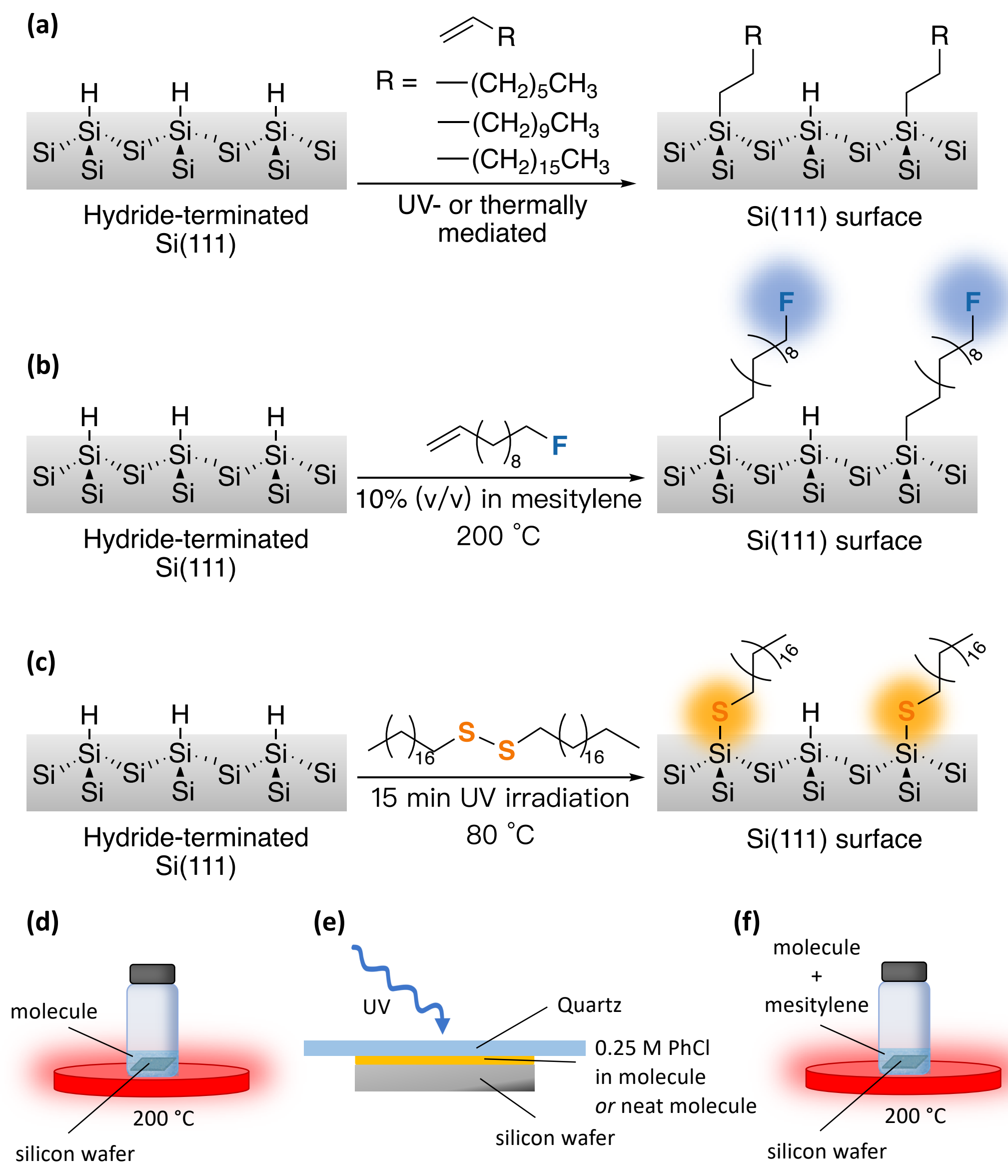

Figure 4.7. Reaction of Si(111)–H with (a) neat alkenes, (b) 11-fluoro-1-undecene diluted in mesitylene, and (c) di-*n*-octadecyl disulfide. Overview of experimental setup for reaction of Si(111)–H with an alkene via (d) direct heating using neat molecules, (e) UV irradiation, and (f) direct heating with an alkene diluted in mesitylene.

UV Irradiation

In 2012, our group demonstrated that the presence of chlorobenzene (PhCl) induces an increase of the pseudo-first-order rate coefficient, κ_{obs}, of UV-initiated hydrosilylation of hexadecene to increase 200-fold compared to that observed in neat hexadecene.[101] Here, PhCl was dissolved first into the alkene of interest to yield a solution with a concentration of 0.25 M PhCl in the molecules. Approximately 5 µL of the alkene/PhCl solution was placed on the silicon wafer, which then was covered with a quartz disc, forming a

sandwich of quartz coverslip–reagent(s)–silicon wafer (Figure 4.7e). The quartz disc minimized the concentration changes due to evaporation and prevented dewetting of the surface as the monolayer yield increases. Next, the samples were irradiated with the light from a UVP Pen-Ray lamp (254 nm, model 11SC-1) that was held 1 cm above the samples for various lengths of times. The intensity of the 254-nm light reaching the quartz surface was measured to be $\sim$2 mW cm^{-2}.

Direct Heating with Diluted Alkenes

For less common (more expensive) reagents, such as 11-fluoro-1-undecene, an improved method frequently was used by diluting the desired reagent in a solvent that would not react with the hydrogen-terminated surface and would not be incorporated into the monolayers. Among a variety of solvents, mesitylene proved to be one of the most suitable solvents for successful preparation of well-ordered monolayers on a silicon surface. As shown in Figure 4.7f, the alkene of interest was dissolved in mesitylene at a dilution ratio of 1:9 reagent:solvent, about 400 µL of the solution were placed on a freshly etched silicon wafer inside a 20-mL glass vial, and the vial was sealed and put on a 200 °C hot plate for a desired reaction time.

4.2.4 Analytical Techniques

The intensity of the 254 nm UV light was measured by a Solo 2 energy and power meter with a XLPF12-3S-H2-D0 head (Gentec Electro-Optics Inc.). Sessile drop contact angles and advancing and receding contact angle measurements were taken on an FTA200 video system. X-ray photoelectron spectroscopy (XPS) spectra were taken on a Kratos Axis Ultra X-ray photoelectron spectroscopy system with a power of 14 kV, 12 mA, and 168 W using an Al source with an energy of 1487 eV, in the University of Alberta NanoFAB, with binding energies calibrated to Au $4f_{7/2}$ = 84.0 eV. Photoelectrons were collected using a takeoff angle of 90° relative to the sample surface.

4.3 Results and Discussion

The reaction conditions differ from reagent to reagent. Direct heating with mesitylene solution is considered as one of the reaction conditions that applies to all the molecules we study here. For 1-octadecene, together with the mesitylene reflux condition, thermal heating with neat molecules and UV irradiation also are used for the achievement of

best coverage. In addition, UV irradiation is harnessed for the reaction of 11-fluoro-1-undecene with the Si(111)–H surface.

4.3.1 Functionalized Silicon Surface: Contact Angle Measurements

To ensure that the monolayers produced via alkene hydrosilylation or reaction with the dialkyl disulfide were of high quality, the functionalized silicon surfaces were analyzed first by goniometry (water contact angle measurements) to probe the hydrophobicity and order (Table 4.1 and Figure 4.8). The static contact angle for the starting hydride-terminated silicon surface is $\sim$83°. After reaction with 1-octene, 1-dodecene, and 1-octadecene, the maximum contact angles measured were $\sim$103°, $\sim$102°, and $\sim$106°, respectively; these values are similar to those of other silicon surfaces functionalized with long alkyl chains from the literature.[81,147] For the $\equiv$Si$-$(CH$_2$)$_{11}$$-$F surface obtained via refluxing in a 10% solution in mesitylene, the water contact angle is $\sim$93°, similar to that previously observed for $\equiv$Si$-$(CH$_2$)$_{10}$$-$F on Si(111) ($\sim$94°).[20] The relatively small contact angle of the $\equiv$Si$-$(CH$_2$)$_{11}$$-$F surface compared to the long alkyl-terminated silicon surfaces may result from the polar single C–F bond.

Water contact angles are useful to determine reaction kinetics to ensure completeness, as shown in Figure 4.9 for UV-mediated irradiation of 1-octadecene; the kinetics follow classic Langmuir kinetics, and a maximum contact angle of 105° was reached after 45 s.

Table 4.1. Static and Dynamic Contact Angles for the Functionalized Silicon Surfaces Reacted with the Indicated Reagents under Different Reaction Conditions

Reagent	Reaction Condition	θ_e^{wa} (°)	θ_a^{wa} (°)/θ_r^{wa} (°)
Si(111) surface	N/A	83.3 ± 0.9	95 ± 0.8/75 ± 0.8
1-Octene	10% in mesitylene, 200 °C, 2 h	103.3 ± 1.9	105 ± 0.4/100 ± 0.2
1-Dodecene	10% in mesitylene, 200 °C, 2 h	102.3 ± 1.3	109 ± 1.0/101 ± 0.9
1-Octadecene	excess neat molecule, 200 °C, 2 h	105.4 ± 1.3	110 ± 0.8/100 ± 0.4
	0.25 M PhCl in molecule, UV, 1 min	105.4 ± 0.8	109 ± 1.0/100 ± 0.9
	10% in mesitylene, 200 °C, 2 h	106.0 ± 0.9	112 ± 0.5/98 ± 0.7
11-Fluoro-1-undecene	0.25 M PhCl in molecule, UV, 1 min	88.4 ± 1.2	94 ± 0.9/87 ± 0.4
	10% in mesitylene, 200 °C, 2 h	93.0 ± 1.4	95 ± 0.6/90 ± 0.2
Di-*n*-octadecyl disulfide[b]	UV, 80 °C, 15 min	105.1 ± 0.4	108 ± 1.0/88 ± 0.8

[a]e, a, and r refer to equilibrium, advancing, and receding, respectively, and w and HD represent water and hexadecane, respectively. Each value is the average of five separate measurements, and the error listed is the standard deviation. [b]The data for di-*n*-octadecyl disulfide-functionalized silicon surface has been previously published (reference 215) and described in Chapter 3.

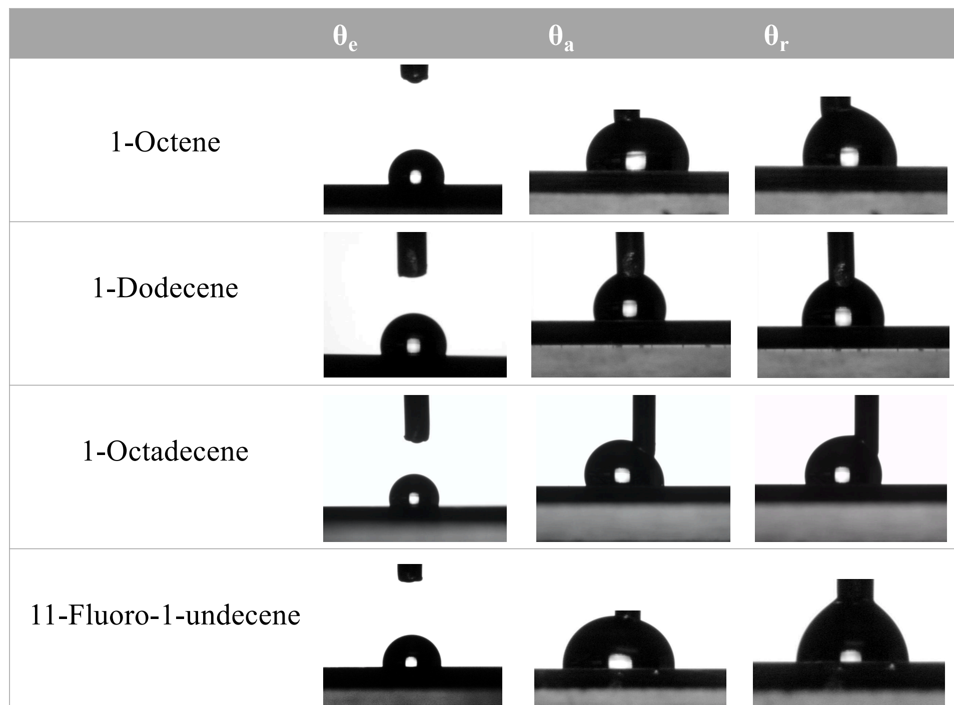

Figure 4.8. Water contact angle images of a Si(111)–H surface reacted with indicated reagents corresponding to Table 4.1.

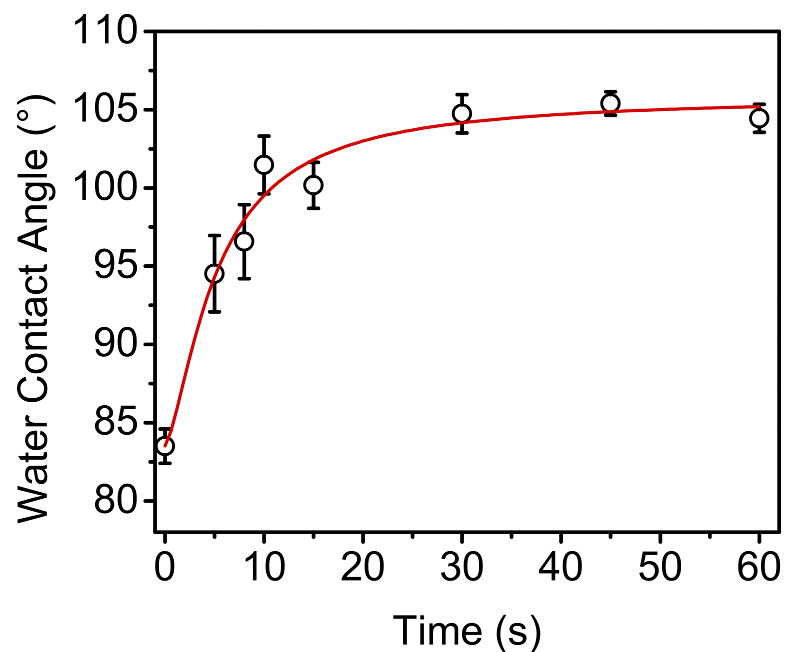

Figure 4.9. Kinetic profile of hydrosilylation of 1-octadecene on Si(111)–H with UV irradiation. Each black dot represents a unique sample that had been reacted for the indicated reaction time. The error bars represent the standard deviation of five measurements on the same sample.

4.3.2 Functionalized Silicon Surface: XPS

XPS was carried out on the silicon samples reacted with the four molecules, 1-octene, 1-dodecene, 1-octadecene, and 11-fluoro-1-undecene. A gold-on-silicon sample was used as the reference for XPS calibration (and not the C 1s), as per Lewis and co-workers.[40] As shown in Figure 4.10, the Si 2p spectra of all four silicon samples reveal no significant oxidation, which would appear as higher energy features above 102 eV due to the oxygen insertion into surface Si–Si and Si–H_x bonds.[25,125] All four C 1s spectra show the expected features representative of alkyl chains on silicon surfaces, with a main peak at 284.8 eV corresponding to the carbon in the alkyl chains. The feature at 287.8 eV is assigned to the carbon bound to fluorine for the $\equiv Si-(CH_2)_{11}-F$ surface. XPS data for the four functionalized surfaces are shown in Table 4.2.

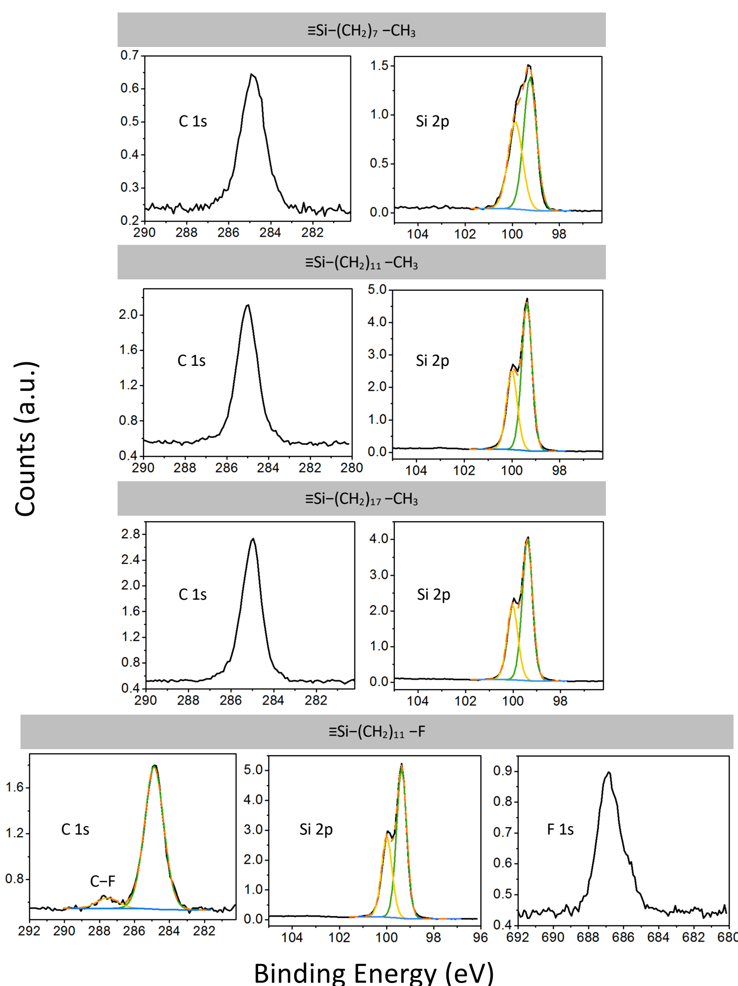

Figure 4.10. XPS spectra of Si(111)–H surfaces after thermal hydrosilylation with 1-octene, 1-dodecene, 1-octadecene, and 11-fluoro-1-undecene (10% in mesitylene solutions, v/v) at 200 °C for 2 h. Orange dashed curves are envelope fittings.

Table 4.2. Summary of XPS Data Corresponding to Figure 4.10

	Si $2p_{3/2}$	C 1s	C 1s (C–F)	F 1s
1-Octene	99.4	284.8		
1-Dodecene	99.4	285.0		
1-Octadecene	99.4	285.0		
11-Fluoro-1-undecene	99.4	284.9	287.5	686.8

4.3.3 $\equiv$Si$-$CH$=$CH$-$(CH_2)$_n$–F Surfaces from Literature

In 2013, the Zuilhof group reacted Si(111) surfaces with ω-fluoro-1-alkynes of varying carbon chain lengths (C_{10}–C_{18}), producing $\equiv$Si$-$CH$=$CH$-$(CH_2)$_n$–F surfaces (n = 8, 10, 12, 14, and 16).[20] Figure 4.11a and b show the XPS C 1s and Si 2p spectra, respectively, of the five surfaces. As shown in Figure 4.11a, the peak 283.7 eV corresponds to the carbon bound to the silicon, the large peak at 285 eV is assigned to the predominant aliphatic chain that was used as a reference peak, and a higher binding energy contribution at 287.9 eV belongs to the carbon bound to fluorine. The doublets at 99.5 eV and 100.1 eV in Figure 4.11b correspond to the Si $2p_{3/2}$ and Si $2p_{1/2}$ peaks, respectively. The binding energies of C 1s and Si 2p are very close to the those of our $\equiv$Si$-$(CH_2)$_{11}$$-$F surface (Table 4.2).

In the work of the Zuilhof group, XPS data was harnessed to obtain the substitution levels of the Si–H group by the monolayers. The atomic C/Si ratios were converted first into monolayer thicknesses, d_{ML}, using the following relationship

$$d_{\mathrm{ML}} = \lambda_{\mathrm{ML}}^{\mathrm{Si}} \sin(\theta) \ln(1 + \mathrm{C}/\mathrm{Si}) \tag{4.2}$$

where $\lambda_{\mathrm{ML}}^{\mathrm{Si}}$ is the attenuation length of Si 2p photoelectrons in the organic monolayers ($\lambda_{\mathrm{ML}}^{\mathrm{Si}}$ = 39.5 Å), and θ is the takeoff angle between the surface and the detector (θ =

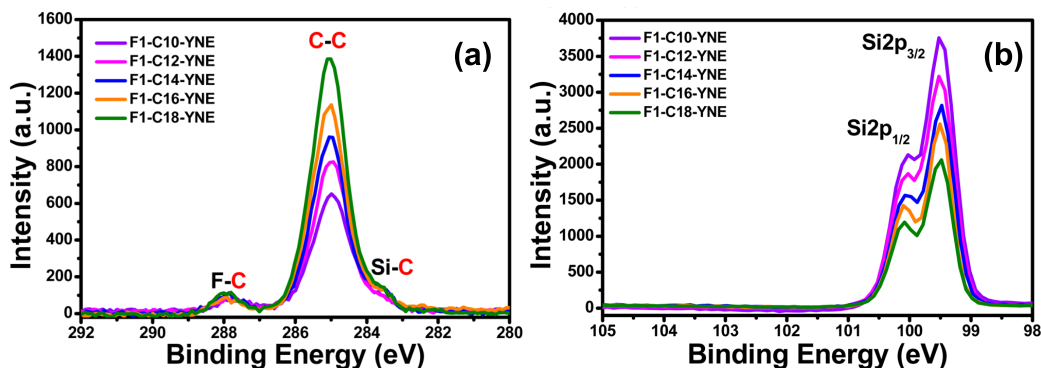

Figure 4.11. (a) C1s and (b) Si 2p XPS narrow scan of $\equiv$Si$-$CH$=$CH$-$(CH_2)$_n$–F surfaces. (Reprinted with permission from ref 20. Copyright 2013 American Chemical Society.)

90°). The surface coverage was calculated by comparing the formed monolayers with a previous study on alkane-thiol monolayer on gold. The surface coverage, ϕ, of the monolayers was given by

$$\phi = \frac{d_{\mathrm{ML}} \times D_{\mathrm{Au}}}{d_{\mathrm{TH}} \times D_{\mathrm{Si}}} \tag{4.3}$$

where D_{Au} is the surface density of chains in a perfect alkanethiol monolayer on gold with a tilt angle of 30° ($D_{\mathrm{Au}} = 4.65 \times 10^{14}$ cm^{-2}), D_{Si} is the surface atom density on Si(111) ($D_{\mathrm{Si}} = 7.8 \times 10^{14}$ cm^{-2}), and $d_{\mathrm{TH}(30°)}$ is the theoretical thickness of an organic monolayer on Si with a tilt angle of 30°. The atomic C/Si ratio and calculated surface coverage for the prepared monolayers are shown in Table 4.3.

Table 4.3. Quantitative XPS Data of Indicated $\equiv$Si$-$CH=CH$-$(CH$_2$)$_n-$F Surfaces from Reference 20

Surface	C/Si ratio	SAM thickness, expt. (d_{ML}, Å)	SAM thickness, theory (d_{TH}, Å)	surface coverage, ϕ_{ML} (%)
$\equiv$Si$-$CH=CH$-$(CH$_2$)$_8-$F	23.8/76.2	10.6	12.3	51
$\equiv$Si$-$CH=CH$-$(CH$_2$)$_{10}-$F	28.5/71.5	13.1	14.5	54
$\equiv$Si$-$CH=CH$-$(CH$_2$)$_{12}-$F	32.7/67.3	15.5	16.8	55
$\equiv$Si$-$CH=CH$-$(CH$_2$)$_{14}-$F	37.1/62.9	18.1	19.1	56
$\equiv$Si$-$CH=CH$-$(CH$_2$)$_{16}-$F	41.2/58.8	20.7	21.3	58

For all their functionalized silicon surfaces, the obtained coverages are in the range of 51–58%. As a matter of fact, Equation 4.2 is a simplified version from the work by Wallart et al.,[141] neglecting some important parameters, such as the atomic volume density of silicon, the relative sensitivity factor for each elements from XPS, and the difference between the attenuation length of carbon and silicon (see Chapter 3 for more details). These parameters could be important for a more accurate quantification of substitution levels. Furthermore, their work used the total carbon intensity for obtaining the C/Si ratio. It could be possible that a part of the carbon signal comes from the adventitious carbon above the monolayer, artificially increasing the surface coverage, as mentioned in the work from the Lewis group.[19]

In Chapter 3, we described the use of XPS for the estimation of the substitution level of the chalcogenide group on silicon via a Si–E bond (E = S, Se or Te) and showed that the chalcogen atom in the monolayer could be used as an atomic label for the calculation of substitution level.[215] It is promising to use the F/Si ratio from the XPS data of the fluorine-contained monolayer for a more precise coverage calculation because all the ratios are directly from the monolayers. In order to correct the assumption made by other researchers and give a more accurate calculation, we developed a new revised set of models that would be more accurate for the quantification of the substitution levels on Si(111) surfaces.

4.4 Reconsideration of the Models and Calculations used for XPS-based Determination of Surface Coverage

Here, we reconsider the model, starting from a structural profile of the resulting organic monolayers. Schematics of the cross-sectional profiles of the monolayers comprising $\equiv$Si$-$$(CH_2)_{11}$$-$F surface, the $\equiv$Si$-$$(CH_2)_n$$-$$CH_3$ surfaces, and the $\equiv$Si$-$S$-$$(CH_2)_{17}$$-$$CH_3$ are shown in Figure 4.12. They are composed of at least three sublayers, the silicon substrate at the bottom, the organic monolayer in the middle, and the possible adventitious carbon layer at the top. For the $\equiv$Si$-$$(CH_2)_{11}$$-$F surface, the organic layer is further divided into the very thin top monofluorine "layer", and the underlying alkyl layer. Similarly, the organic layer of the $\equiv$Si$-$S$-$$(CH_2)_{17}$$-$$CH_3$ surface is composed of the overlying alkyl layer and the thin "layer" containing the sulfur atoms at the bottom. Quantitative XPS data of the five silicon surfaces are shown in Table 4.4.

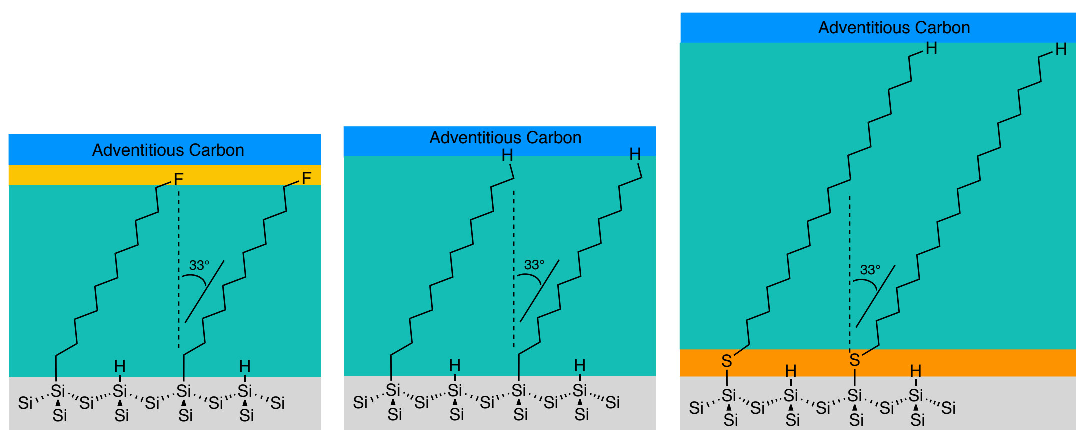

Figure 4.12. Schematic models of the $\equiv$Si$-$$(CH_2)_{11}$$-$F, $\equiv$Si$-$$(CH_2)_n$–$CH_3$, and $\equiv$Si$-$S$-$$(CH_2)_{17}$$-$$CH_3$ surfaces, from left to right, respectively.

Table 4.4. Quantitative XPS Data of Indicated Functionalized Silicon Surfaces

Surface	C/Si ratio	F/Si ratio	S/Si ratio
$\equiv$Si–$(CH_2)_{11}$–F	0.441	0.187	- -
$\equiv$Si–$(CH_2)_7$–CH_3	0.362	- -	- -
$\equiv$Si–$(CH_2)_{11}$–CH_3	0.523	- -	- -
$\equiv$Si–$(CH_2)_{17}$–CH_3	0.790	- -	- -
$\equiv$Si–S–$(CH_2)_{17}$–CH_3	0.749	- -	0.052

4.4.1 Calculations of Constants

This section describes the detailed calculations of the constants that will be applied in the quantification of substitution levels for all the functionalized silicon surfaces, including

the atomic density of carbon on a gold substrate, ρ_C^{Au}, the attenuation length of the Si 2p electron travelling through an alkyl monolayer on gold, λ_{SiC}^{Au}, and the attenuation length of C 1s electron in an alkyl monolayer on gold, λ_{CC}^{Au}. The atomic density of carbon on gold, ρ_C^{Au}, can be calculated by assuming that the functional layer would have the same surface density as the surface of Au, n_{Au} (4.6×10^{14} atoms/cm^2), and dividing that by the average thickness per carbon atomic plane or the theoretical thickness (1.32 nm) of each chain normalized by the number of carbons per chain, N_{chain} (12).

$$\rho_C^{Au} = \frac{n_{Au}}{d_C^{Au}/N_{chain}} = \frac{4.6 \times 10^{14}}{1.32 \times 10^{-7}/12} = 4.1 \times 10^{22} \text{ atoms/cm}^3 \tag{4.4}$$

The atomic density of carbon on silicon substrate, ρ_C^{Si}, is given by

$$\rho_C^{Si} = \frac{\phi n_{Si}}{d_C^{Si}/N_{chain}} = \frac{\phi n_{Si} N_{chain}}{d_C^{Si}} \tag{4.5}$$

where n_{Si} is the atomic surface density of silicon, and the attenuation length of photoelectrons in alkyl monolayers on gold, λ_{ML}^{Au}, can be calculated using the empirical formula from the Whitesides group[214]

$$\lambda_{ML}^{Au} = 9 + 0.022 E_k \tag{4.6}$$

where E_k is the kinetic energy of a specific element, and the result is in Å. Therefore, the attenuation length of Si 2p electrons in an alkyl monolayer on gold is given by

$$\lambda_{SiC}^{Au} = 9 + 0.022 E_k = 9 + 0.022(1487 - 99.4 \text{ eV}) = 39.5 \text{ Å} \tag{4.7}$$

The attenuation length of C 1s electrons in an alkyl monolayer on gold is given by

$$\lambda_{CC}^{Au} = 9 + 0.022 E_k = 9 + 0.022(1487 - 284.8 \text{ eV}) = 35.4 \text{ Å} \tag{4.8}$$

All of the utilized constants are listed in Table 4.5. These values will be used in the model of alkyl-based monolayers on silicon.

Table 4.5. List of All Constants Used for the Calculation of Substitution Levels from XPS Data

Constant	Value
Sensitivity factor σ_{Si}, σ_F, σ_C	0.328, 1.000, 0.278
Atomic surface density n_{Si}, $^{a}n_{Au}$	7.8×10^{14} atoms/cm^2, 4.6×10^{14} atoms/cm^2
Attenuation coefficients λ_{SiSi}, $^{b}\lambda_{SiC}^{Au}$, $^{b}\lambda_{CC}^{Au}$	1.8 nm, 3.95 nm, 3.54 nm
Atomic density ρ_{Si}, $^{c}\rho_{C}^{Au}$	5×10^{22} atoms/cm^3, 4.1×10^{22} atoms/cm^3

$^{a}(\sqrt{3}\times\sqrt{3})R30$ surface of (111). ^{b}Calculated based on an empirical formula from Whitesides (reference 214). ^{c}Calculated based on the gold surface.

4.4.2 Connection between Attenuation Length and Atomic Density

To estimate the value of λ_{SiC}^{Si}, the scaling the values for gold surfaces was used as a starting point. According to the work of Tanuma and co-workers,[236] for an electron emitted from element x, going through a material y with a structure α, the product of the attenuation coefficient, λ_{xy}^{α}, times density, ρ_{y}^{α}, will be a constant, specifically if the electron is traveling through a different structure of y, β, that has a different density, ρ_{y}^{β}

$$\lambda_{xy}^{\alpha}\rho_{y}^{\alpha} = \lambda_{xy}^{\beta}\rho_{y}^{\beta} \tag{4.9}$$

When Eq 4.9 was applied to the case of the attenuation length of an element (Si or C) on silicon and gold substrates, the attenuation length of an electron emitted from Si, traveling through an organic carbon layer on a silicon substrate, λ_{SiC}^{Si}, is given by

$$\lambda_{SiC}^{Si}\rho_{C}^{Si} = \lambda_{SiC}^{Au}\rho_{C}^{Au}$$

$$\lambda_{SiC}^{Si} = \frac{\rho_{C}^{Au}}{\rho_{C}^{Si}}\lambda_{SiC}^{Au} \tag{4.10}$$

The attenuation length of Si going through the adventitious carbon layer on a silicon substrate, λ_{SiA}, is given by

$$\lambda_{SiA}\rho_{A} = \lambda_{SiC}^{Au}\rho_{C}^{Au}$$

$$\lambda_{SiA} = \frac{\rho_{C}^{Au}}{\rho_{A}}\lambda_{SiC}^{Au} \tag{4.11}$$

The attenuation length of C going through the organic carbon layer on a silicon substrate, λ_{CC}^{Si}, is given by

$$\lambda_{CC}^{Si}\rho_{C}^{Si} = \lambda_{CC}^{Au}\rho_{C}^{Au}$$

$$\lambda_{CC}^{Si} = \frac{\rho_C^{Au}}{\rho_C^{Si}} \lambda_{CC}^{Au} \tag{4.12}$$

The attenuation length of C going through the adventitious carbon layer on a silicon substrate, λ_{CA}, is given by

$$\lambda_{CA}\rho_A = \lambda_{CC}^{Au}\rho_C^{Au}$$

$$\lambda_{CA} = \frac{\rho_C^{Au}}{\rho_A} \lambda_{CC}^{Au} \tag{4.13}$$

The obtained equations above show that, the attenuation length for Si or C passing through a specific carbon layer (the carbon in alkyl chains, or adventitious carbon) on a silicon substrate can be estimated as the product of the attenuation length on a gold substrate multiplied by the ratio of the atomic density of carbon on gold relative to carbon's atomic density on silicon. These equations will be used in the section regarding the quantification of the substitution levels.

4.4.3 Monolayer with an ω-Fluorine Tag: the $\equiv$Si–$(CH_2)_{11}$–F Surface

Because of the presence of multiple layers, as shown in Figure 4.13, a continuum substrate-overlayer model was used to determine the substitution level, ϕ, of the alkyl overlayer on silicon, where it is assumed that each layer has a uniform atomic density, ρ_i, electron attenuation coefficient, λ_i, and thickness, d_i. It is worth noting that the attenuation length of Si penetrating the organic carbon layer, λ_{SiC}^{Si}, is no longer a constant but a function of the atomic density of carbon on the silicon substrate, which depends on the substitution level ϕ and also has taken the tilt angle into consideration (vide infra). Conventionally, the substitution level is obtained through dividing the effective thickness, d, by the theoretical monolayer thickness, d_{TH}. Here in our revised formulae, the thickness of the alkyl layer no longer needs to be calculated because we always have the product of thickness and density in all the equations, which is $\phi \times n_{Si} \times N_{chain}$, and the substitution level will be calculated directly from the revised formula (vide infra).

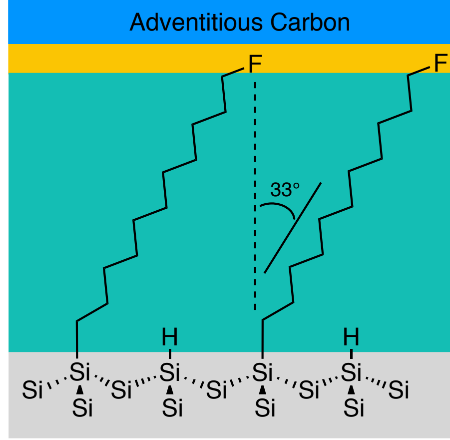

Figure 4.13. Scheme of the cross-section of the organic monolayer comprising ≡Si–$(CH_2)_{11}$–F groups, an ω-heteroatomic tag.

Within the continuum model, the total Si 2p signal intensity at the alkyl chain-modified surface is given by

$$I_{\mathrm{Si}} = \sigma_{\mathrm{Si}}\rho_{\mathrm{Si}}(\int_0^{\infty} \exp(-x/\lambda_{\mathrm{SiSi}})\mathrm{d}x)\exp(-d_{\mathrm{C}}/\lambda_{\mathrm{SiC}})\exp(-d_{\mathrm{F}}/\lambda_{\mathrm{SiF}})\exp(-d_{\mathrm{A}}/\lambda_{\mathrm{SiA}})$$

$$I_{\mathrm{Si}} = \sigma_{\mathrm{Si}}\rho_{\mathrm{Si}}\lambda_{\mathrm{SiSi}}\exp(d_{\mathrm{C}}^{\mathrm{Si}}/\lambda_{\mathrm{SiC}} - d_{\mathrm{F}}/\lambda_{\mathrm{SiF}} - d_{\mathrm{A}}/\lambda_{\mathrm{SiA}}) \tag{4.14}$$

If we assume $d_{\mathrm{F}}/\lambda_{\mathrm{SiF}} \ll 1$, and $\lambda_{\mathrm{SiC}}^{\mathrm{Si}} = \frac{\rho_{\mathrm{C}}^{\mathrm{Au}}}{\rho_{\mathrm{C}}^{\mathrm{Si}}}\lambda_{\mathrm{SiC}}^{\mathrm{Au}}$, Eq 4.14 can be written as

$$I_{\mathrm{Si}} = \sigma_{\mathrm{Si}}\rho_{\mathrm{Si}}\lambda_{\mathrm{SiSi}}\exp(\frac{-d_{\mathrm{C}}^{\mathrm{Si}}\rho_{\mathrm{C}}^{\mathrm{Si}}}{\rho_{\mathrm{C}}^{\mathrm{Au}}\lambda_{\mathrm{SiC}}^{\mathrm{Au}}})\exp(-d_{\mathrm{A}}/\lambda_{\mathrm{SiA}}) \tag{4.15}$$

Since $\rho_{\mathrm{C}}^{\mathrm{Si}} = \frac{\phi n_{\mathrm{Si}}N_{\mathrm{chain}}}{d_{\mathrm{C}}^{\mathrm{Si}}}$, the Eq 4.15 becomes

$$I_{\mathrm{Si}} = \sigma_{\mathrm{Si}}\rho_{\mathrm{Si}}\lambda_{\mathrm{SiSi}}\exp(-d_{\mathrm{A}}/\lambda_{\mathrm{SiA}})\exp(\frac{-\phi n_{\mathrm{Si}}N_{\mathrm{chain}}}{\rho_{\mathrm{C}}^{\mathrm{Au}}\lambda_{\mathrm{SiC}}^{\mathrm{Au}}}) \tag{4.16}$$

The carbon signal from the alkyl group is given by

$$I_{\mathrm{C}}^{\mathrm{Si}} = \sigma_{\mathrm{C}}^{\mathrm{Si}}\rho_{\mathrm{C}}^{\mathrm{Si}}[\int_0^{d_{\mathrm{C}}^{\mathrm{Si}}} \exp(-x/\lambda_{\mathrm{CC}})\mathrm{d}x]\exp(-d_{\mathrm{F}}/\lambda_{\mathrm{CF}})\exp(-d_{\mathrm{A}}/\lambda_{\mathrm{CA}})$$

$$I_{\mathrm{C}}^{\mathrm{Si}} = \sigma_{\mathrm{C}}\rho_{\mathrm{C}}^{\mathrm{Si}}\lambda_{\mathrm{CC}}^{\mathrm{Si}}[1 - \exp(-d_{\mathrm{C}}^{\mathrm{Si}}/\lambda_{\mathrm{CC}}^{\mathrm{Si}})]\exp(-d_{\mathrm{F}}/\lambda_{\mathrm{CF}} - d_{\mathrm{A}}/\lambda_{\mathrm{CA}})$$

$$I_{\mathrm{C}}^{\mathrm{Si}} = \sigma_{\mathrm{C}}\rho_{\mathrm{C}}^{\mathrm{Au}}\lambda_{\mathrm{CC}}^{\mathrm{Au}}\left[1 - \exp\left(\frac{-d_{\mathrm{C}}^{\mathrm{Si}}\rho_{\mathrm{C}}^{\mathrm{Si}}}{\rho_{\mathrm{C}}^{\mathrm{Au}}\lambda_{\mathrm{CC}}^{\mathrm{Au}}}\right)\right]\exp(-d_{\mathrm{A}}/\lambda_{\mathrm{CA}})$$

$$I_{\mathrm{C}}^{\mathrm{Si}} = \sigma_{\mathrm{C}}\rho_{\mathrm{C}}^{\mathrm{Au}}\lambda_{\mathrm{CC}}^{\mathrm{Au}}\left[1-\exp\left(\frac{-\phi n_{\mathrm{Si}}N_{\mathrm{chain}}}{\rho_{\mathrm{C}}^{\mathrm{Au}}\lambda_{\mathrm{CC}}^{\mathrm{Au}}}\right)\right]\exp(-d_{\mathrm{A}}/\lambda_{\mathrm{CA}}) \tag{4.17}$$

The signal from the fluorine layer is given by

$$I_{\mathrm{F}} = \sigma_{\mathrm{F}}\rho_{\mathrm{F}}[\int_0^{d_{\mathrm{F}}}\exp(-x/\lambda_{\mathrm{FF}})\mathrm{d}x]\exp(-d_{\mathrm{A}}/\lambda_{\mathrm{FA}})$$

$$I_{\mathrm{F}} = \sigma_{\mathrm{F}}\rho_{\mathrm{F}}\lambda_{\mathrm{FF}}^{\mathrm{Si}}[1-\exp(-d_{\mathrm{F}}/\lambda_{\mathrm{FF}}^{\mathrm{Si}})]\exp(-d_{\mathrm{A}}/\lambda_{\mathrm{FA}}) \tag{4.18}$$

We can assume that $1-\exp(-d_{\mathrm{F}}/\lambda_{\mathrm{FF}}^{\mathrm{Si}}) \approx d_{\mathrm{F}}/\lambda_{\mathrm{FF}}^{\mathrm{Si}}$, so Eq 4.18 becomes

$$I_{\mathrm{F}} = \sigma_{\mathrm{F}}\rho_{\mathrm{F}}\lambda_{\mathrm{FF}}^{\mathrm{Si}}\frac{d_{\mathrm{F}}}{\lambda_{\mathrm{FF}}^{\mathrm{Si}}}\exp(-d_{\mathrm{A}}/\lambda_{\mathrm{FA}}) = \sigma_{\mathrm{F}}\rho_{\mathrm{F}}d_{\mathrm{F}}\exp(-d_{\mathrm{A}}/\lambda_{\mathrm{FA}})$$

Given that $\rho_{\mathrm{F}}^{\mathrm{Si}} = \frac{\phi n_{\mathrm{Si}}}{d_{\mathrm{F}}}$, the signal from the fluorine layer is given by

$$I_{\mathrm{F}} = \sigma_{\mathrm{F}}\phi n_{\mathrm{Si}}\exp(-d_{\mathrm{A}}/\lambda_{\mathrm{FA}}) \tag{4.19}$$

The intensity of adventitious carbon signal is given by

$$I_{\mathrm{A}} = \sigma_{\mathrm{C}}\rho_{\mathrm{A}}[\int_0^{d_{\mathrm{A}}}\exp(-x/\lambda_{\mathrm{CA}})\mathrm{d}x]$$

$$I_{\mathrm{A}} = \sigma_{\mathrm{C}}\rho_{\mathrm{A}}\lambda_{\mathrm{CA}}[1-\exp(-d_{\mathrm{A}}/\lambda_{\mathrm{CA}})]$$

$$I_{\mathrm{A}} = \sigma_{\mathrm{C}}\rho_{\mathrm{A}}^{\mathrm{Au}}\lambda_{\mathrm{CC}}^{\mathrm{Au}}[1-\exp(-d_{\mathrm{A}}/\lambda_{\mathrm{CA}})]$$

The total intensity of carbon signal is

$$I_{\mathrm{C}}^{\mathrm{total}} = I_{\mathrm{C}}^{\mathrm{Si}} + I_{\mathrm{A}} = \sigma_{\mathrm{C}}\rho_{\mathrm{C}}^{\mathrm{Au}}\lambda_{\mathrm{CC}}^{\mathrm{Au}}\exp(-d_{\mathrm{A}}/\lambda_{\mathrm{CA}})\left[1-\exp\left(\frac{-\phi n_{\mathrm{Si}}N_{\mathrm{chain}}}{\rho_{\mathrm{C}}^{\mathrm{Au}}\lambda_{\mathrm{CC}}^{\mathrm{Au}}}\right)+\exp(d_{\mathrm{A}}/\lambda_{\mathrm{CA}})-1\right]$$

$$= \sigma_{\mathrm{C}}\rho_{\mathrm{C}}^{\mathrm{Au}}\lambda_{\mathrm{CC}}^{\mathrm{Au}}\exp(-d_{\mathrm{A}}/\lambda_{\mathrm{CA}})\left[\exp(-d_{\mathrm{A}}/\lambda_{\mathrm{CA}})-\exp\left(\frac{-\phi n_{\mathrm{Si}}N_{\mathrm{chain}}}{\rho_{\mathrm{C}}^{\mathrm{Au}}\lambda_{\mathrm{CC}}^{\mathrm{Au}}}\right)\right]$$

$$I_{\mathrm{C}}^{\mathrm{total}} = \sigma_{\mathrm{C}}\rho_{\mathrm{C}}^{\mathrm{Au}}\lambda_{\mathrm{CC}}^{\mathrm{Au}}\left[1-\exp\left(-d_{\mathrm{A}}/\lambda_{\mathrm{CA}}-\frac{\phi n_{\mathrm{Si}}N_{\mathrm{chain}}}{\rho_{\mathrm{C}}^{\mathrm{Au}}\lambda_{\mathrm{CC}}^{\mathrm{Au}}}\right)\right] \tag{4.20}$$

After obtaining the intensity of the Si signal, I_{Si} (Eq 4.16), the intensity of F signal, I_{F} (Eq 4.19), and the total intensity of C signal, $I_{\mathrm{C}}^{\mathrm{total}}$ (Eq 4.20), two quantification methods for the substitution level, using the ratio $I_{\mathrm{C}}^{\mathrm{total}}/I_{\mathrm{Si}}$, or the ratio $I_{\mathrm{F}}/I_{\mathrm{Si}}$, will be derived as shown below.

Substitution Level from the Ratio of C to Si

Dividing Eq 4.16 by Eq 4.20 gives the ratio of the total carbon intensity to the silicon intensity

$$\frac{I_C^{total}}{I_{Si}} = \left(\frac{\sigma_C \rho_C^{Au} \lambda_{CC}^{Au}}{\sigma_{Si} \rho_{Si} \lambda_{SiSi}}\right) \left[\exp\left(\frac{d_A}{\lambda_{SiA}} + \frac{\phi n_{Si} N_{chain}}{\rho_C^{Au} \lambda_{SiC}^{Au}}\right) - \exp\left(\left(\frac{d_A}{\lambda_{SiA}} - \frac{d_A}{\lambda_{CA}}\right) + \frac{\phi n_{Si} N_{chain}}{\rho_C^{Au}} \left(\frac{1}{\lambda_{SiC}^{Au}} - \frac{1}{\lambda_{CC}^{Au}}\right)\right)\right] \quad (4.21)$$

Note that if $\frac{\phi n_{Si} N_{chain}}{\rho_C^{Au}} \left(\frac{1}{\lambda_{SiC}^{Au}} - \frac{1}{\lambda_{CC}^{Au}}\right) = \phi N_{chain}(-0.00558)$ and $N_{chain} \leq 18$, we obtain

$$0.9 < \exp\left[\frac{\phi n_{Si} N_{chain}}{\rho_C^{Au}} \left(\frac{1}{\lambda_{SiC}^{Au}} - \frac{1}{\lambda_{CC}^{Au}}\right)\right] < 1$$

Eq 4.21 becomes

$$\frac{I_C^{total}}{I_{Si}} \approx \left(\frac{\sigma_C \rho_C^{Au} \lambda_{CC}^{Au}}{\sigma_{Si} \rho_{Si} \lambda_{SiSi}}\right) \left[\exp\left(\frac{d_A}{\lambda_{SiA}} + \frac{\phi n_{Si} N_{chain}}{\rho_C^{Au} \lambda_{SiC}^{Au}}\right) - 1\right]$$

$$\frac{d_A}{\lambda_{SiA}} + \frac{\phi n_{Si} N_{chain}}{\rho_C^{Au} \lambda_{SiC}^{Au}} = \ln\left[\frac{I_C^{total}}{I_{Si}} \left(\frac{\sigma_{Si} \rho_{Si} \lambda_{SiSi}}{\sigma_C \rho_C^{Au} \lambda_{CC}^{Au}}\right) + 1\right]$$

ϕ can be calculated as

$$\phi = \frac{\rho_C^{Au} \lambda_{SiC}^{Au}}{n_{Si} N_{chain}} \ln\left[\frac{I_C^{total}}{I_{Si}} \left(\frac{\sigma_{Si} \rho_{Si} \lambda_{SiSi}}{\sigma_C \rho_C^{Au} \lambda_{CC}^{Au}}\right) + 1\right] - \frac{\rho_C^{Au} \lambda_{SiC}^{Au} d_A}{n_{Si} N_{chain} \lambda_{SiA}}$$

$$\phi = \frac{\rho_C^{Au} \lambda_{SiC}^{Au}}{n_{Si} N_{chain}} \ln\left[\frac{I_C^{total}}{I_{Si}} \left(\frac{\sigma_{Si} \rho_{Si} \lambda_{SiSi}}{\sigma_C \rho_C^{Au} \lambda_{CC}^{Au}}\right) + 1\right] - \frac{\rho_A d_A}{n_{Si} N_{chain}} \quad (4.22)$$

Eq 4.22 shows the relation between the substitution level and all the related parameters, derived from the C/Si ratio. If we assume k is the ratio of the atomic density of adventitious carbon on silicon, ρ_A, to the atomic density of carbon on gold, ρ_C^{Au}, in other words, $\rho_A = k\rho_C^{Au}$, and put all the constants from Table 4.5 into Eq 4.22

$$\phi = \frac{(4.1 \times 10^{22})(3.95 \times 10^{-7})}{(7.8 \times 10^{14}) N_{chain}} \ln\left[\frac{I_C^{total}}{I_{Si}}(0.732) + 1\right] - \frac{k\rho_C^{Au} d_A(\text{nm}) \times 10^{-7}}{(7.8 \times 10^{14}) N_{chain}}$$

$$\phi = \frac{20.76}{N_{\text{chain}}} \ln\left(0.732\frac{I_{\text{C}}^{\text{total}}}{I_{\text{Si}}} + 1\right) - 5.26\frac{kd_{\text{A}}}{N_{\text{chain}}} \tag{4.23}$$

If we assume $k = 0.8$, $N_{\text{chain}} = 11$ for the $\equiv$Si$-$(CH$_2$)$_{11}-$F surface, and $I_{\text{C}}^{\text{total}}/I_{\text{Si}} = 0.441$ (Table 4.4), Eq 4.23 becomes

$$\phi = 0.527 - 0.38d_{\text{A}} \tag{4.24}$$

Substitution Level from the Ratio of F to Si

Since the $\equiv$Si$-$(CH$_2$)$_{11}-$F surface contains another element, fluorine, the substitution level also can be obtained using the F/Si ratio. Taking the ratio of the fluorine and silicon intensities gives (Eqs 4.19 and 4.16)

$$\frac{I_{\text{F}}}{I_{\text{Si}}} = \frac{\sigma_{\text{F}}\phi n_{\text{Si}} \exp(-d_{\text{A}}/\lambda_{\text{FA}})}{\sigma_{\text{Si}}\rho_{\text{Si}}\lambda_{\text{SiSi}} \exp(-d_{\text{A}}/\lambda_{\text{SiA}}) \exp\left(\frac{-\phi n_{\text{Si}} N_{\text{chain}}}{\rho_{\text{C}}^{\text{Au}}\lambda_{\text{SiC}}^{\text{Au}}}\right)}$$

$$\frac{I_{\text{F}}}{I_{\text{Si}}}\frac{\sigma_{\text{Si}}\rho_{\text{Si}}\lambda_{\text{SiSi}}}{\sigma_{\text{F}}n_{\text{Si}}} \exp\left[d_{\text{A}}\left(\frac{1}{\lambda_{\text{FA}}} - \frac{1}{\lambda_{\text{SiA}}}\right)\right] = \phi \exp\left(\frac{n_{\text{Si}}N_{\text{chain}}}{\rho_{\text{C}}^{\text{Au}}\lambda_{\text{SiC}}^{\text{Au}}}\phi\right) \tag{4.25}$$

If we first-order Taylor expand

$$\exp\left(\frac{n_{\text{Si}}N_{\text{chain}}}{\rho_{\text{C}}^{\text{Au}}\lambda_{\text{SiC}}^{\text{Au}}}\phi\right) \approx 1 + \frac{n_{\text{Si}}N_{\text{chain}}}{\rho_{\text{C}}^{\text{Au}}\lambda_{\text{SiC}}^{\text{Au}}}\phi$$

Eq 4.25 becomes

$$\frac{I_{\text{F}}}{I_{\text{Si}}}\frac{\sigma_{\text{Si}}\rho_{\text{Si}}\lambda_{\text{SiSi}}}{\sigma_{\text{F}}n_{\text{Si}}} \exp\left[d_{\text{A}}\left(\frac{1}{\lambda_{\text{FA}}} - \frac{1}{\lambda_{\text{SiA}}}\right)\right] = \phi\left(1 + \frac{n_{\text{Si}}N_{\text{chain}}}{\rho_{\text{C}}^{\text{Au}}\lambda_{\text{SiC}}^{\text{Au}}}\phi\right) \tag{4.26}$$

Eq 4.26 shows the relationship between the substitution level and all the related parameters, derived from the F/Si ratio. If we put all the constants from Table 4.5 into Eq 4.26

$$\frac{I_{\text{F}}}{I_{\text{Si}}}\frac{(0.328)(5\times10^{22})(1.8\times10^{-7})}{(1)(7.8\times10^{14})} \exp\left[d_A\left(\frac{1}{2.66} - \frac{1}{3.95}\right)\right] = \phi\left[1 + \frac{(7.8\times10^{14})(11)}{(4.1\times10^{22})(3.95\times10^{-7})}\phi\right]$$

$$\frac{I_{\text{F}}}{I_{\text{Si}}}(3.78)\exp(0.1d_{\text{A}}) = \phi(1 + 0.53\phi) \tag{4.27}$$

We can solve the quadratic Eq 4.27 for ϕ

$$\phi = \frac{\sqrt{1+8\frac{I_F}{I_{Si}}\exp(0.1d_A)}-1}{1.06} \tag{4.28}$$

If we first-order Taylor expand $\exp(0.1d_A) \approx 1+0.1d_A$ and designate the fluorine to silicon intensity ratio as 0.187 from the XPS data (Table 4.4) into Eq 4.28, then, Eq 4.28 becomes

$$\phi = \frac{\sqrt{2.5+0.15d_A}-1}{1.06} \tag{4.29}$$

Taylor expanding the square root of Eq 4.29 gives

$$\phi = 0.547+0.045d_A \tag{4.30}$$

4.4.4 Monolayers without Heteroatomic Tags: $\equiv$Si–(CH$_2$)$_n$–CH$_3$ Surfaces

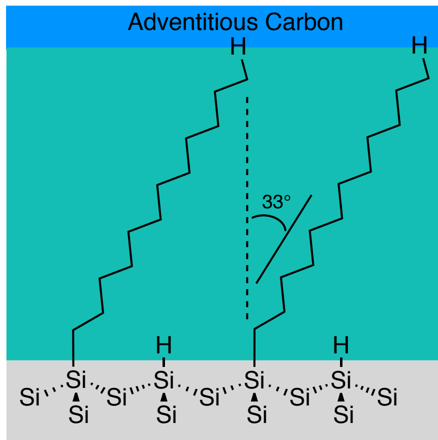

Figure 4.14. A representative scheme of the Si–(CH$_2$)$_n$–CH$_3$ surface.

A three layer model is used for the $\equiv$Si$-$(CH$_2$)$_n$$-CH_3$ surfaces, including the silicon layer at the bottom, an organic alkyl monolayer, and an adventitious carbon layer, as shown in Figure 4.14. Similarly, the signal from silicon layer is given by

$$I_{Si} = \sigma_{Si}\rho_{Si}\left[\int_0^{\infty}\exp(-x/\lambda_{SiSi})\mathrm{d}x\right]\exp(-d_C/\lambda_{SiC})\exp(-d_A/\lambda_{SiA})$$

$$I_{Si} = \sigma_{Si}\rho_{Si}\lambda_{SiSi}\exp(-d_C/\lambda_{SiC}-d_A/\lambda_{SiA}) \tag{4.31}$$

The carbon signal from the alkyl group is given by

$$I_{\mathrm{C}}^{\mathrm{Si}} = A\sigma_{\mathrm{C}}\rho_{\mathrm{C}}\lambda_{\mathrm{CC}}[1-\exp(-d_{\mathrm{C}}/\lambda_{\mathrm{CC}})]\exp(-d_{\mathrm{A}}/\lambda_{\mathrm{CA}}) \tag{4.32}$$

The signal of adventitious carbon is given by

$$I_{\mathrm{A}} = \sigma_{\mathrm{C}}\rho_{\mathrm{A}}\lambda_{\mathrm{CA}}[1-\exp(-d_{\mathrm{A}}/\lambda_{\mathrm{CA}})] \tag{4.33}$$

Similar to the $\equiv$Si$-$(CH$_2$)$_{11}$$-$F surface, the ratio of the total carbon intensity to the silicon intensity finally is given by

$$\phi = \frac{20.76}{N_{\mathrm{chain}}}\ln\left(0.732\frac{I_{\mathrm{C}}^{\mathrm{total}}}{I_{\mathrm{Si}}}+1\right) - 5.26\frac{kd_{\mathrm{A}}}{N_{\mathrm{chain}}} \tag{4.34}$$

For the $\equiv$Si$-$(CH$_2$)$_7$$-CH_3$ surface, the carbon to silicon ratio obtained from XPS is 0.362 (Table 4.4), $N_{\mathrm{chain}} = 8$, and if we again assume $k = 0.8$, then the coverage is given by

$$\phi = 0.61 - 0.53d_{\mathrm{A}}$$

For the $\equiv$Si$-$(CH$_2$)$_{11}$$-CH_3$ surface, the carbon to silicon ratio obtained from XPS is 0.523 (Table 4.4), $N_{\mathrm{chain}} = 12$, and if we again assume $k = 0.8$, then the coverage is given by

$$\phi = 0.56 - 0.35d_{\mathrm{A}}$$

For the $\equiv$Si$-$(CH$_2$)$_{17}$$-CH_3$ surface, the carbon to silicon ratio obtained from XPS is 0.790 (Table 4.4), $N_{\mathrm{chain}} = 18$, and if we again assume $k = 0.8$, then the coverage is given by

$$\phi = 0.53 - 0.23d_{\mathrm{A}}$$

4.4.5 Monolayers with an α-Heteroatom, Surface-Bound Tag: the $\equiv$Si$-$S$-$(CH$_2$)$_{17}$$-CH_3$ Surface

In Chapter 3, we derived two expressions for the substitution level, using the ratio of carbon to silicon or the ratio of sulfur to silicon. The scheme of the layered model is shown in Figure 4.15. Here, an updated formula for the $\equiv$Si$-$S$-$(CH$_2$)$_{17}$$-CH_3$ surface is derived.

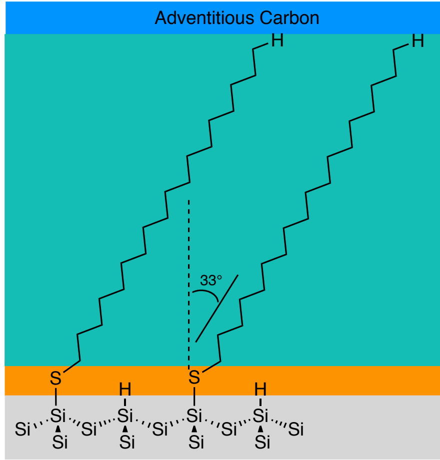

Figure 4.15. Scheme of the cross-section of the organic monolayer comprising ≡Si–S–$(CH_2)_{17}$–CH_3 groups.

The signal of silicon is given by

$$I_{\mathrm{Si}} = \sigma_{\mathrm{Si}}\rho_{\mathrm{Si}}\left[\int_0^{\infty}\exp(-x/\lambda_{\mathrm{SiSi}})\mathrm{d}x\right]\exp(-d_{\mathrm{S}}/\lambda_{\mathrm{SiS}})\exp(-d_{\mathrm{C}}/\lambda_{\mathrm{SiC}})\exp(-d_{\mathrm{A}}/\lambda_{\mathrm{SiA}})$$

$$I_{\mathrm{Si}} = \sigma_{\mathrm{Si}}\rho_{\mathrm{Si}}\lambda_{\mathrm{SiSi}}\exp(-d_{\mathrm{C}}/\lambda_{\mathrm{SiC}} - d_{\mathrm{A}}/\lambda_{\mathrm{SiA}}) \tag{4.35}$$

The signal of sulfur atom is given by

$$I_{\mathrm{S}} = \sigma_{\mathrm{S}}\rho_{\mathrm{S}}\left[\int_0^{d_{\mathrm{S}}}\exp(-x/\lambda_{\mathrm{SS}})\mathrm{d}x\right]\exp(-d_{\mathrm{C}}/\lambda_{\mathrm{SC}})\exp(-d_{\mathrm{A}}/\lambda_{\mathrm{SA}})$$

$$I_{\mathrm{S}} = \sigma_{\mathrm{S}}\rho_{\mathrm{S}}\lambda_{\mathrm{SS}}\left[1-\exp(-d_{\mathrm{S}}/\lambda_{\mathrm{SS}})\right]\exp(-d_{\mathrm{C}}/\lambda_{\mathrm{SC}})\exp(-d_{\mathrm{A}}/\lambda_{\mathrm{SA}}) \tag{4.36}$$

The carbon signal from the alkyl group is given by

$$I_{\mathrm{C}}^{\mathrm{Si}} = A\sigma_{\mathrm{C}}\rho_{\mathrm{C}}\lambda_{\mathrm{CC}}[1-\exp(-d_{\mathrm{C}}/\lambda_{\mathrm{CC}})]\exp(-d_{\mathrm{A}}/\lambda_{\mathrm{CA}}) \tag{4.37}$$

The signal of adventitious carbon is given by

$$I_{\mathrm{A}} = \sigma_{\mathrm{C}}\rho_{\mathrm{A}}\lambda_{\mathrm{CA}}[1-\exp(-d_{\mathrm{A}}/\lambda_{\mathrm{CA}})] \tag{4.38}$$

Substitution Level from the Ratio of C to Si

Similar to the ≡Si$-(CH_2)_{11}-$F surface, the substitution level is finally given by

$$\phi = \frac{\rho_{\mathrm{C}}^{\mathrm{Au}}\lambda_{\mathrm{SiC}}^{\mathrm{Au}}}{n_{\mathrm{Si}}N_{\mathrm{chain}}}\ln\left[\frac{I_{\mathrm{C}}^{\mathrm{total}}}{I_{\mathrm{Si}}}\left(\frac{\sigma_{\mathrm{Si}}\rho_{\mathrm{Si}}\lambda_{\mathrm{SiSi}}}{\sigma_{\mathrm{C}}\rho_{\mathrm{C}}^{\mathrm{Au}}\lambda_{\mathrm{CC}}^{\mathrm{Au}}}\right)+1\right]-\frac{\rho_{\mathrm{A}}d_{\mathrm{A}}}{n_{\mathrm{Si}}N_{\mathrm{chain}}}$$

and after putting all the constants into the equation above, the coverage is given by

$$\phi = \frac{20.76}{N_{chain}} \ln\left(0.732\frac{I_C^{total}}{I_{Si}} + 1\right) - 5.26\frac{kd_A}{N_{chain}} \tag{4.39}$$

For $\equiv$Si$-$S$-$(CH$_2$)$_{17}$$-CH_3$ surface, the carbon to silicon ratio is 0.749 (Table 4.4), $N_{chain} = 18$, $k = 0.8$, and Eq 4.39 becomes

$$\phi = 0.50 - 0.23d_A \tag{4.40}$$

Substitution Level from the Ratio of S to Si

Since the $\equiv$Si$-$S$-$(CH$_2$)$_{17}$$-CH_3$ surface contains another element, sulfur, the substitution level also can be obtained using the S/Si ratio. Taking the ratio of sulfur (Eq 4.36) to silicon (Eq 4.35) intensities gives

$$\frac{I_S}{I_{Si}} = \frac{\sigma_E \rho_S \lambda_{SS} [1 - \exp(-d_S/\lambda_{SS})] \exp(-d_C/\lambda_{SC}) \exp(-d_A/\lambda_{SA})}{\sigma_{Si} \rho_{Si} \lambda_{SiSi} \exp(-d_C/\lambda_{SiC} - d_A/\lambda_{SiA})}$$

If we again assume that $\exp[d_S(1/\lambda_{SiS} - 1/\lambda_{SS})] \approx 1$, $\exp[d_C(1/\lambda_{SiC} - 1/\lambda_{SC})] \approx 1$, and $d_S/\lambda_{SiS} \ll 1$, we arrive at the simplified expression of

$$\frac{I_S}{I_{Si}} = \frac{\sigma_S \rho_S d_S}{\sigma_{Si} \rho_{Si} \lambda_{SiSi}}$$

Given that $\rho_S d_S = n_S$, where n_S is the atomic surface density of sulfur atoms, and the substitution level is defined as $\Theta = n_S/n_{Si}$, we can solve for the substitution level

$$\phi = \frac{\sigma_{Si} \rho_{Si} \lambda_{SiSi} I_S}{n_{Si} \sigma_S I_{Si}} \tag{4.41}$$

After putting the constants from Table 4.5, and S/Si ratio of 0.052 into Eq 4.41, the substitution level was found to be 27% (Chapter 3).

4.4.6 Results and Discussion

The formulae derived for the quantification of substitution levels for the three types of functionalized silicon surfaces, as derived vide supra, are summarized in Table 4.6. According to the formulae using the C/Si ratio, assuming no adventitious carbon on the surfaces, the substitution levels of the five surfaces are all in the 50–60% range, in good agreement with those from the literature.

Table 4.6. Quantification of Substitution Level for Different Functionalized Silicon Surfaces

Surface	C to Si[a]	F to Si[a]	S to Si[a]
$\equiv$Si–$(CH_2)_{11}$–F	$\phi = 0.527 - 0.38d_A$	$\phi = 0.547 + 0.045d_A$	- -
$\equiv$Si–$(CH_2)_7$–CH_3	$\phi = 0.61 - 0.53d_A$	- -	- -
$\equiv$Si–$(CH_2)_{11}$–CH_3	$\phi = 0.56 - 0.35d_A$	- -	- -
$\equiv$Si–$(CH_2)_{17}$–CH_3	$\phi = 0.53 - 0.23d_A$	- -	- -
$\equiv$Si–S–$(CH_2)_{17}$–CH_3	$\phi = 0.50 - 0.23d_A$	- -	$\phi = 27\%$

[a] ϕ is the substution level and d_A is the thickness of adventitious carbon layer.

For the $\equiv$Si$-(CH_2)_{11}-$F surface, two equations are derived for the calculation of substitution level, using the C/Si ratio and F/Si ratio from XPS, as shown in Table 4.6. The two formulae point in opposite directions with respect to the amount of adventitious carbon, and the substitution levels only agree when the adventitious carbon is zero, which gives the value of the substitution level as $\sim$53% for the $\equiv$Si$-(CH_2)_{11}-$F surface. This result suggests that the fluorine-terminated surface has almost no adventitious carbon, which may be due to the C–F termination and the dense packing of the monolayers. The effect of photodiffraction of needs to be considered as it could lead to a lowered intensity for the silicon signal. Rotational XPS was used in literature to correct for any diffraction effects caused by the crystallinity of the Si when quantifying the substitution level. In our previous work, multiple measurements of identically prepared samples in separate XPS runs were used for all quantitative XPS calculations, and it was found that there was generally less than a 10% difference in calculated substitution levels. Although our samples were not rotated during XPS measurements, to lower the substitution level to, for instance, $\sim$30%, however, the silicon intensity would have to be off by a factor of two, which is unlikely given the previous measurements in Chapter 3 and other literature references on photodiffraction (which show that the error arising from photodiffraction is generally 10–20%).

For the three aliphatic $\equiv$Si$-(CH_2)_n-CH_3$ surfaces, the substitution levels are all in the range of 53–61%, assuming no adventitious carbon on the surface. From the three formulae derived from C/Si ratios, we can see that the effect from adventitious carbon on calculated coverage decreases as the chain length increases from 8 carbons to 18 carbons. If there is 1 nm adventitious carbon on the surface, compared to the no adventitious carbon regime, the substitution level will decrease from 61% to 8% for the $\equiv$Si$-(CH_2)_7-CH_3$ surface, from 56% to 21% for the $\equiv$Si$-(CH_2)_{11}-CH_3$ surface, and from 53% to 27% for the $\equiv$Si$-(CH_2)_{17}-CH_3$ surface. Every Angstrom difference in adventitious carbon changes the coverage of C_{18} by 2%, while it changes that of C_8 by 5%. Because of the higher thickness and presumably more dense packing of the C_{18} monolayer compared to the C_8 monolayer, the influence of the adventitious carbon to

C_{18} is significantly less with respect to the quantification of the substitution level.

For the $\equiv Si-S-(CH_2)_{17}-CH_3$ surface, two formulae can be used to quantify the substitution level, based on the C/Si ratio, or on the S/Si ratio, as shown in Table 4.6. The substitution level from the updated formula using C/Si ratio, $\phi = 0.50 - 0.23d_A$, still depends on the thickness of the adventitious carbon on the surface. Assuming no adventitious carbon on the surface, the substitution level is ~50%. However, every Angstrom difference in adventitious carbon changes the substitution level of the $\equiv Si-S-(CH_2)_{17}-CH_3$ surface by 2%. For the formula using the S/Si ratio, the substitution level is independent of the thickness of adventitious carbon, but relies on the S/Si ratio from XPS, after the reasonable simplifying assumptions, as shown in Chapter 3. The substitution level calculated is ~27% using the ratio of S:Si. According to the updated formula using the C:Si ratio (Table 4.6), $\phi = 0.50 - 0.23d_A$, and thus we would need to have ~1 nm of adventitious carbon to have 27% coverage. For all the calculations, we assume that the packing density ratio of adventitious carbon to the alkyl chain is 0.8, $\rho_A = 0.8\rho_C^{Au}$, which will increase the estimated adventitious carbon thickness by 25%; this is not a large difference in coverage. The relatively lower coverage of $\equiv Si-S-(CH_2)_{17}-CH_3$ compared to $\equiv Si-(CH_2)_{11}-F$ is almost certainly due to the larger surface-bound sulfur atoms compared to the surface-bound carbon atoms on the silicon that obstruct the neighbouring Si–H from further reactivity, leading to the lower substitution level and a rougher surface, giving more opportunity for adventitious carbon to be adsorbed on silicon.

The most important conclusion from the updated quantification method is that the error in estimating the substitution level is an order of magnitude lower when using a functional tag, such as S or F, compared to using the C/Si ratio. Figure 4.16a shows the substitution levels of the $\equiv Si-(CH_2)_{11}-F$ surface using the formulae derived from F/Si ratio or C/Si ratio. From the C/Si ratio formula, the prefactor in front of the adventitious carbon thickness is 0.38 1/nm, compared to 0.045 1/nm for the F/Si formula. Therefore, if the adventitious carbon thickness is assumed to be anywhere between 0 and 1 nm, the C/Si formula predicts that the coverage is between the massive range of 15–53% coverage compared to the F/Si formula, which predicts a range of 55–59%, as shown in Figure 4.16a. It shows that when using the C/Si ratio, small differences in adventitious carbon thickness make a big difference (every Angstrom difference in adventitious carbon changes the substitution level by 4%), while there is only a 0.5% change when using the F/Si ratio. Similar results are observed for the $\equiv Si-S-(CH_2)_{17}-CH_3$ surface when using C/Si ratio or S/Si ratio for quantification, as shown in Figure 4.16b.

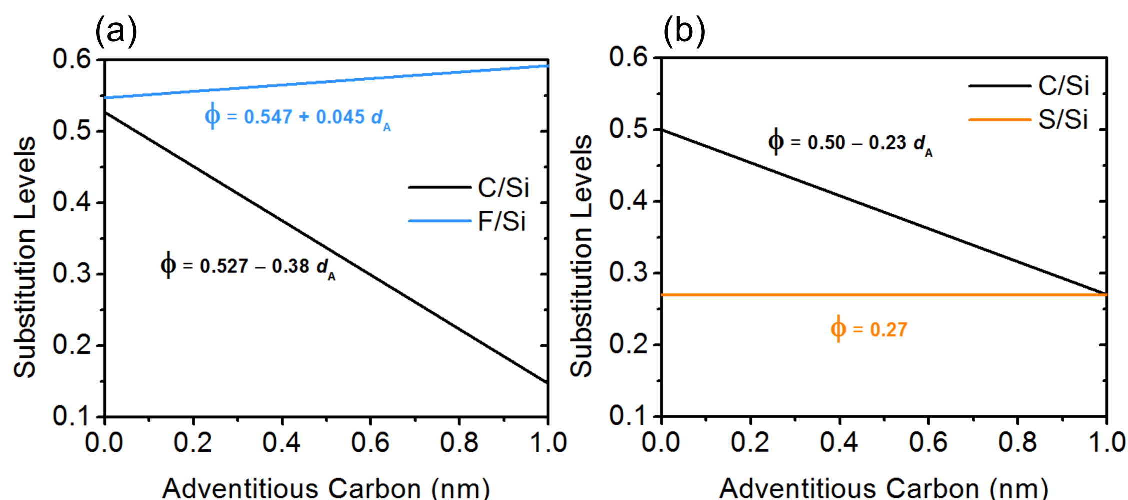

Figure 4.16. A scheme of the relationship between substitution levels and the thickness of adventitious carbon of (a) the $\equiv$Si$-$(CH_2)$_{11}$$-$F surface, derived using the C/Si ratio (black) or the F/Si ratio (blue) from XPS data, and (b) the $\equiv$Si$-$S$-$(CH_2)$_{17}$$-$$CH_3$ surface, derived using the C/Si ratio (black) or the S/Si ratio (orange) from XPS data.

4.5 Conclusions

In this work, we examined the reactivity of the Si(111)–H surfaces with 1-octene, 1-dodecene, 1-octadecene, and 11-fluoro-1-undecene via hydrosilylation under different reaction conditions in order to obtain the maximum coverages. Water contact angles of the functionalized silicon surfaces show the changes of the surface energy, which agree very well with those from literature. XPS spectra show the successful incorporation of C and F elements on silicon surfaces, with little oxidation. A new revised set of models and formulae for the quantification of substitution levels of five silicon surfaces, including $\equiv$Si$-$(CH_2)$_{11}$$-$F, $\equiv$Si$-$(CH_2)$_7$$-$$CH_3$, $\equiv$Si$-$(CH_2)$_{11}$$-$$CH_3$, $\equiv$Si$-$(CH_2)$_{17}$$-$$CH_3$, and $\equiv$Si$-$S$-$(CH_2)$_{17}$$-$$CH_3$ surfaces, was developed. The substitution level of the fluorine-terminated surface has a value of $\sim$53%, as determined by the formulae using the C/Si and F/Si ratio from XPS. The three pure alkene-functionalized silicon surfaces all have a substitution level of around 50–60%, assuming no adventitious carbon on the surface. The substitution level of $\equiv$Si$-$S$-$(CH_2)$_{17}$$-$$CH_3$ surface is 27%, which is significantly lower that of the alkyl monolayers bound through Si–C linkage and might be due to the larger sulfur atom directly bound to silicon that further blocks the neighbouring Si–H from reaction. It is found that the usage of a heteroatom such as F and S, will reduce the error in the quantification of the substitution level resulting from the effect of adventitious carbon largely. In future, molecules with different atomic labels (e.g., S, Se, F) need to be investigated to obtain a deep understanding of the effect of adventitious

carbon on the coverage calculation in order to better control the electronic properties of silicon by changing the true surface coverage for the applications of various devices.

Chapter 5

Thesis Summary and Outlook

5.1 Summary of Chapters

In this thesis, self-assembled monolayers through ≡Si−ER (E = S, Se and Te) bonds are formed on porous Si(100) surfaces via very fast microwave or hot plate thermal heating with synthetically practical dialkyl/diaryl dichalcogenide compounds that contain S–S, Se–Se, or Te–Te bonds. UV irradiation and gentle thermal heating with dichalcogenide also leads to the formation of ≡Si−ER bond on flat Si(111) surfaces. The mechanism of reactivity of the dichalcogenides appears to be radical in nature under both thermal and UV light conditions, and it is closely related to the observed reactivity in silane molecules. For functionalized flat Si(111) surfaces, the substitution level of the phenyl chalcogenide derivatives (≡Si−E−Ph) was lower than that of the aliphatic chalcogenide (≡Si−S−*n*-octadecyl) group due to the bulky phenyl group shielding a significant number of Si–H bonds from further reactivity. The substitution levels of alkenes with various chain lengths and with fluorine as an atomic label on silicon surfaces were measured to give insights into the better control of electronic propeties of modified silicon surfaces.

5.1.1 Chapter 1

Chapter 1 gives a brief introduction to the basic principles of silicon surface chemistry and describes the development and mechanisms of formation of silicon–chalcogen bonds on silicon surfaces. The chapter starts with the properties of two types of the most investigated bulk silicon surfaces, flat silicon and nanostructured porous silicon. Next, various functionalization strategies of silicon surfaces are introduced, including direct heating, microwave irradiation, thermolytic grafting, radical initiation, and UV or white

light illumination. This summary is followed by the history of silicon–chalcogen bond formation, starting from a molecular perspective and moving to the chemistry of Si–E (E = S, Se and Te) on silicon surfaces. Characterization techniques for modifying silicon surfaces, including Fourier-transform infrared spectroscopy (FTIR), X-ray photoelectron spectroscopy (XPS), time-of-flight secondary ion mass spectrometry (ToF-SIMS), contact angle measurements, and atomic force microscopy (AFM) scribing are described. Finally, this chapter concludes with a brief summary and future research directions for silicon–chalcogen bond formation on silicon surfaces and an improved method for the calculation of the substitution level of silicon–hydrogen bonds with organic and organochalcogen compounds.

5.1.2 Chapter 2

Chapter 2 describes the chemistry to produce $\equiv$Si$-$E bonds (E = S, Se, and Te) through very fast microwave heating (10–15 s) and direct thermal heating (hot plate, 2 min) through the reaction of hydride-terminated silicon surfaces with dialkyl or diaryl dichalcogenides. The chemistry produces surface-bound $\equiv$Si$-$SR, $\equiv$Si$-$SeR, and $\equiv$Si$-$TeR groups. Although the interfacing of molecules through $\equiv$Si$-$SR and $\equiv$Si$-$SeR bonds is known, to the best of our knowledge, the heavier chalcogenide variant, $\equiv$Si$-$TeR, has not been described previously. Fourier transform infrared (FTIR) spectroscopy, X-ray photoelectron spectroscopy (XPS), and depth profiling with time-of-flight-secondary ionization mass spectrometry (ToF-SIMS) were carried out to identify the surface groups bound to silicon, the uniformity of functionalization throughout the layer, and comparative information regarding the substitution levels. Possible mechanisms are outlined, and the most likely ones, based upon parallels with well-established molecular literature, involve surface silyl radicals or dangling bonds that react with either the alkyl or aryl dichalcogenide directly, REER, or its homolysis product, the alkyl or aryl chalcogenyl radical, RE· (where E = S, Se, and Te).

5.1.3 Chapter 3

Chapter 3 presents the formation of silicon–chalcogenide bonds, $\equiv$Si$-$E$-$R (where E = S, Se, and Te) on flat silicon(111) surfaces, initiated by a 254-nm light, coupled with gentle heating to melt and liquefy the chalcogenide precursors for 15 min. Substitution levels of the silicon-hydride on the starting $\equiv$Si(111)$-$H surface by an organochalcogen were quantified by XPS, using the chalcogenide linker atom as the atomic label, where average substitution levels of $\sim$15% were found for all $\equiv$Si$-$E$-$Ph groups. These mea-

sured substitution levels were found to agree with 2-dimensional stochastic simulations assuming kinetically irreversible silicon–chalcogen bond formation. Because of the small bond angle about the chalcogen atom, the phenyl rings in the case of ≡Si−E−Ph effectively block otherwise reactive Si−H bonds, leading to the observed lower substitution levels. The linear aliphatic dialkyl disulfide version, ≡Si−S–*n*-octadecyl, is less limited by steric blocking of surface Si−H groups, as is the case with a phenyl group, and has a much higher substitution level of ∼29%. XPS and UPS were carried out on ≡Si−E−Ph surfaces to determine the effect of chalcogenide substitution on the electronics of the silicon, including surface dipoles and work function. The electronics did not change significantly from the starting ≡Si−H surface, which may be due to the low level of substitution that is believed to be caused by steric blocking by the phenyl groups as well as the relatively similar electronegativities of these elements relative to silicon.

5.1.4 Chapter 4

Chapter 4 describes the quantification of the substitution levels of self-assembled organic monolayers on flat silicon (111) surfaces. 1-Octene, 1-dodecene, 1-octadecene, and 11-fluoro-1-undecene were reacted with Si(111)–H surfaces via hydrosilylation under different reaction conditions to obtain the maximum coverages for calculation. Water contact angle measurements, including static, advancing, and receding contact angles were carried out to obtain information regarding surface energy, monolayer order, and kinetics. The values agree very well with those from the literature. XPS spectra showed the successful incorporation of C and F elements on silicon surfaces with little oxidation. A new revised set of models and formulae for the quantification of the substitution levels of the four functionalized silicon surfaces as well as an octadecyl sulfide-terminated silicon surface was developed. The error in estimating the substitution level is an order of magnitude lower when using a functional tag, such as S or F, compared to using the carbon to silicon ratio. The calculation shows that when using the carbon to silicon ratio, small differences in adventitious carbon thickness make a big difference to the value of the substitution level (every Angstrom difference in adventitious carbon changes the substitution level by 4%), while there is only a 0.5% change when using the fluorine to silicon ratio. In order to quantify the coverage of the silicon surface precisely for a better control of the electronic properties, molecules with different atomic labels (e.g., S, Se, F), and various chain lengths need to be investigated.

5.2 Future Work

5.2.1 Control of the Electronic Properties of Chalcogenide-modified Silicon Surfaces

Controlling the structure of silicon surfaces as well as their chemical and physical properties is scientifically interesting and particularly important for technology. The Fagas group calculated the electronic properties of ≡Si−SH, ≡Si−SeH and ≡Si−TeH surfaces using first principles.[42] They predicted that the work function will increase to 4.8 eV for the ≡Si−SH surface from the starting value of 4.3 eV for the hydride-terminated surface, while it will decrease to 3.8 eV for the ≡Si−TeH surface if the coverage reaches 100%. In Chapter 3, we measured the electronic properties (work function, surface dipole, and surface electron affinity) of ≡Si−S−Ph, ≡Si−Se−Ph, and ≡Si−Te−Ph surfaces using XPS and UPS. However, due to the low substitution levels (∼15%) of ≡Si−H by the bulky phenyl-chalcogen groups on silicon, the electronics of the silicon surfaces are still dominated by the ≡Si−H termination groups, leading to data for the three surfaces that are similar to that of the starting ≡Si−H-terminated surface. In order to produce a chalcogen-bound silicon surface with higher surface coverage, with a noticeable change of electronic properties, chalcogenides with smaller sizes, such as dimethyl disulfide, dimethyl diselenide, and dimethyl ditelluride, should be used for the reaction. Figure 5.1 shows the FTIR spectra of porous silicon before and after reaction with dimethy disulfide at 100 °C for 1 h. The decrease in Si–H peak at ∼2100 cm^{-1} and the increase of the C–H stretching mode around 2900 cm^{-1} show the formation of a ≡Si−SCH_3 surface. For future research, dimethyl diselenide and dimethyl ditelluride also should be reacted with porous silicon under various conditions for the reactivity study, followed by the reaction with a flat silicon surface for the measurement of electronic properties.

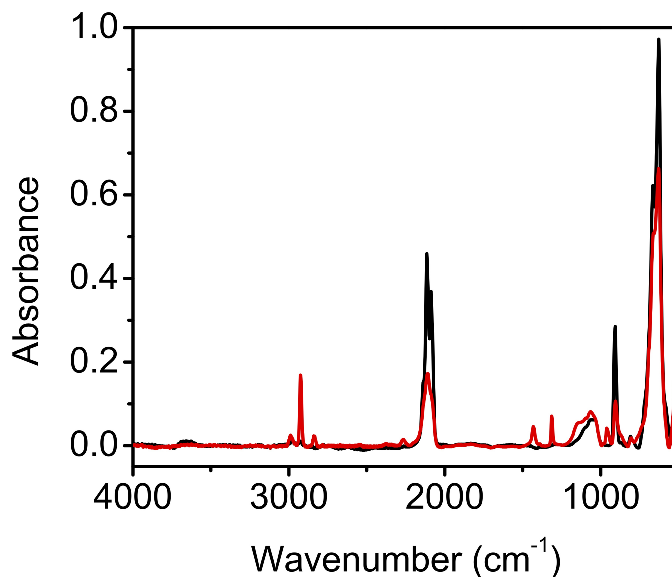

Figure 5.1. FTIR spectra of freshly prepared hydride-terminated porous silicon (red), and the porous silicon after reaction with dimethyl disulfide on a 100 °C hot plate for 1 h (black).

Furthermore, the doping density and type determine the initial Fermi level relative to the valence and conduction bands in the bulk silicon, thus affecting the interface dipole between the silicon surface and alkyl/alkenyl monolayers. In the future, different doping density-type combinations can be used, including heavily doped n-type, moderately doped n-type, heavily doped p-type, and moderately doped p-type silicons, for a more comprehensive investigation of the effect of chalcogen-terminated silicon surfaces.

5.2.2 Monolayer Doping of Silicon Surfaces with Chalcogens for Water Splitting

The depletion of fossil fuels and increasing environmental concerns have triggered an urgent demand for sustainable alternative energy sources. Solar light is an inexhaustible natural energy source that is expected to be used heavily for resolving the above problems. However, it is still a great challenge to develop effective techniques for the utilization of solar energy cheaply, conveniently, and efficiently. Silicon is a promising candidate material for use in water splitting systems to produce hydrogen gas (H_2), a clean-burning fuel, due to its wide availability as a low cost, high purity crystalline material, as well as its excellent electronic properties.[237] Silicon has a small band gap (1.12 eV), which is suitable for absorbing visible illumination, and a more negative conduction band edge compared with the hydrogen evolution reaction potential, E^0 (H^+/H_2), for reduction of water to H_2.[238] Nano- and micro-crystalline silicon-based light absorbers,

in particular nanowire structures, are being functionalized with inorganic, organic, and bacterial catalysts for generation of H_2.[239,240] Figure 5.2 shows an example of the single silicon nanowire for the photoelectrochemical process to produce H_2, where silicon and platinum are selected as the light-absorbing semiconductor and proton-reduction electrocatalyst, respectively.[21]

In order to tune the interfacial electrical properties of a silicon surface precisely for a higher water splitting efficiency, monolayer doping (MLD), a precise method that introduces a very thin (few nanometers) layer of dopant onto the device, was developed.[241,242] At present, MLD has been used for electronic device applications, in which a molecule attached via a silicon–carbon or silicon–oxygen bond is used to introduce dopants onto the silicon surface. The C–Si and O–Si surface linkers, however, lead to substantial contamination of the device. There has been far less attention for dopants involving group VI atoms (S, Se, Te), although theoretical calculations have predicted that surface-localized S, Se, and Te atoms should be able to exert dramatic control over the electronics of the silicon.[42]

In the future, highly efficient chalcogens, (S, Se and Te)-doped silicon photocathodes, could be developed via monolayer doping for water splitting. Figure 5.3 shows a monolayer doping (MLD) process scheme. A clean, freshly etched Si–H bond-terminated wafer will be reacted with dialkyl and diaryl dichalcogenide molecules (R–EE–R, where E = S, Se, Te atoms) under UV irradiation on an 80 °C hot plate for 15 min (Figure 5.3b), as introduced in Chapter 3. A monolayer containing dopant atoms is formed via

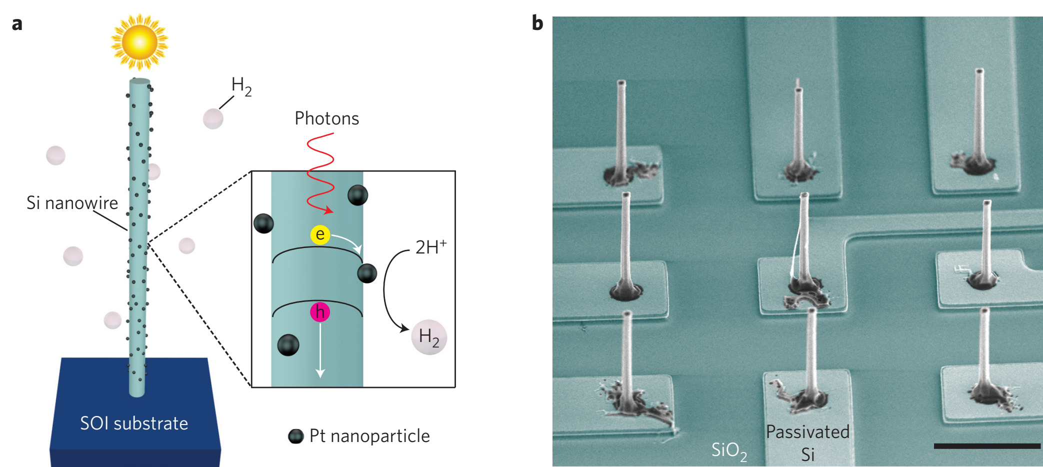

Figure 5.2. (a) Schematic illustration of the single silicon nanowire for the photoelectrochemical process. Photoexcited electron-hole pairs are produced under illumination and are subsequently separated at the nanowire/electrolyte interface because of band bending. The electrons then move to the platinum catalytic sites and carry out proton reduction. (b) Scanning electron microscope (SEM) image of individually addressable single nanowires. Scale bar is 10 µm. (Reprinted with permission from ref 21. Copyright 2016 Springer Nature.)

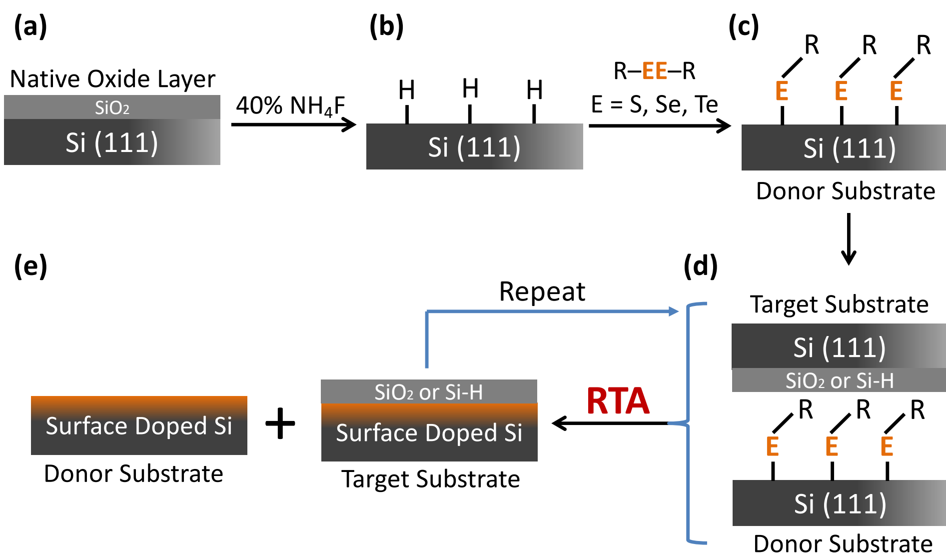

Figure 5.3. Schematic diagram of the monolayer contact doping process for Si substrates.

Si–E bonds on a separate substrate (termed donor substrate) that is distinct from the Si interface intended for doping (Figure 5.3c). Sheet resistance values (Rs) will be determined by four-point probe measurements. The prepared donor substrate will be brought in direct contact with the pristine substrate intended for surface doping (termed target substrate) and annealed using rapid thermal anneal (RTA, Figure 5.3d). Two doped silicon products will be obtained, one is from monolayer doping (donor substrate), and the other one is from contact doping (target substrate) (Figure 5.3e). By repeating the reaction–contact–anneal cycle on the same target substrate, higher levels of chalcogenide doping can be achieved, if needed. Finally, the doped silicon will be assembled into an integrated photoelectrode device, as has been developed thoroughly in our lab,[243] with appropriate stable protective and conductive layers, followed by the photoelectrochemical characterization for solar-driven water splitting. The chemistry will be extended to other doping elements of interest, including B, P, and As. The fabricated water splitting devices with new electrode materials are expected to increase the H_2 conversion efficiency, reducing the pressure and cost stemming from the large-scale production of energy from these newer, alternative sources.

5.2.3 Functionalization of Porous and Flat Germanium Surfaces with Dichalcogenides

In addition to silicon, significant attention also has been given to another semiconductor from group IV, germanium. The small band gap (0.67 eV), and the higher electron

and hole mobilities, ∼2.5× and ∼4×, respectively,[244] than those of silicon, allow germanium to be a promising candidate for semiconductor-based technologies. These properties are useful for faster devices and an absorption spectrum that extends into the infrared. However, in contrast to the native oxide of Si, which provides a stable passivating layer, the native oxide of Ge is water soluble and forms a poor interface with Ge, resulting in a high density of electronic defects.[245–247] Various methods for removing germaniums' oxide layer have been developed, mainly through etching and then attaching an organic monolayer on the germanium surface to suppress oxide formation.[248] Our group prepared porous germanium by a bipolar electrochemical etching technique,[22] as shown in Figure 5.4a. Initially, the germanium surface is anodized at 350 mA cm^{-2} for 5 min, followed by cathodization for 1 min with a negative bias at the same current density. Figure 5.5 shows the top view and cross-sectional view of the prepared porous germanium wafer. A hydride-terminated flat germanium suface was prepared by etching shards of Ge(100) wafers in an aqueous 10% HF solution for 10 min, after being pretreated by immersion in 30% H_2O_2 for 10 s to remove trace organics,[249] as shown in Figure 5.4b.

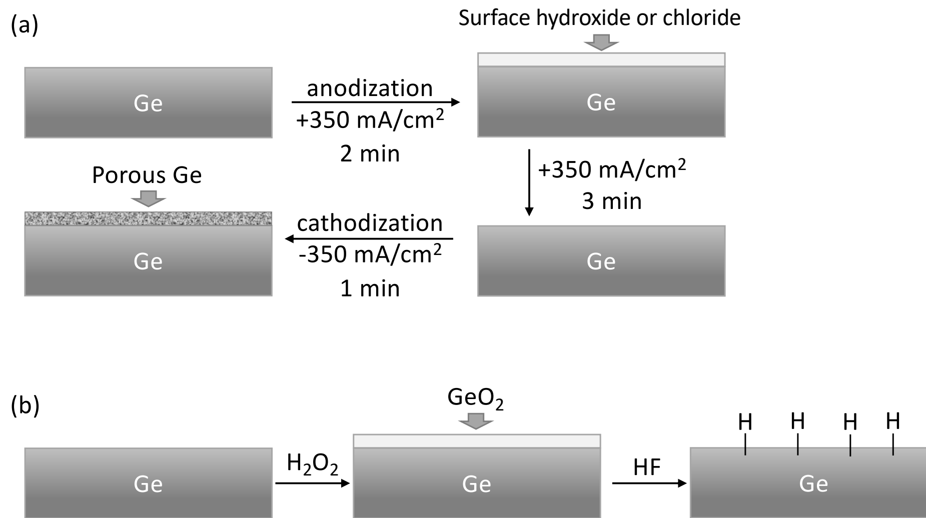

Figure 5.4. (a) Schematic representation of the bipolar electrochemical etching to produce porous Ge(100) wafers. (b) Schematic representation of preparation of hydride-terminated flat Ge(100) wafers.

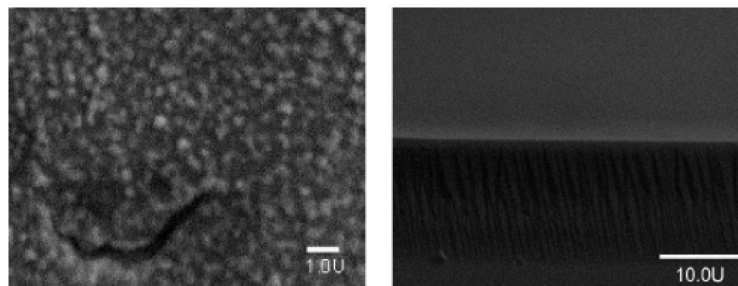

Figure 5.5. Top (left) and cross-sectional (right) views of n^+ type derived porous germanium. Reprinted with permission of ref 22. Copyright 2000 the Royal Society of Chemistry.

A hydride-terminated germanium surface can be stabilized or passivated via functionalization with organic monolayers. Sulfide termination has provided one of the best passivations of germanium.[250,251] Chapter 2 shows the first report to produce the ≡Si−E bonds (E = S, Se, and Te) through the reaction of hydride-terminated silicon surfaces with dialkyl or diaryl dichalcogenides, and Chapter 3 introduces the formation of the same ≡Si−E bonds on flat silicon surfaces. However, there are no reports of self-assembled monolayers attached to germanium through ≡Ge−Te bonds. As shown in Figure 5.6, hydride-terminated germanium can react with various dichalcogenides, producing a ≡Ge−E bond. It is promising that the formation of the ≡Ge−E bond will give the germanium surface a better oxidation resistance, improve its electronic characteristics, and stabilize the dispersibility.

Furthermore, the chemistry can be applied to germanium nanowires and germanium nanoparticles, offering enormous potential in a range of biomedical (cellular imaging and drug delivery), photovoltaic (light-emitting diodes and solar cells), and energy (battery anodes) applications.

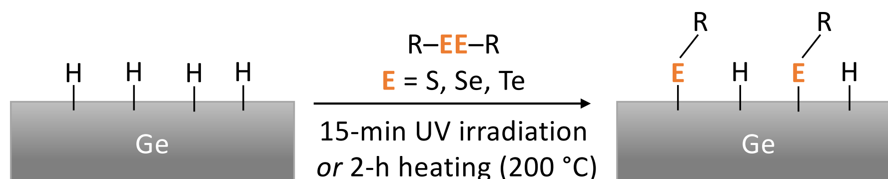

Figure 5.6. Functionalization of hydride-terminated germanium with dialkyl/diaryl dichalcogenides under UV irradiation or thermal heating.

Bibliography

[1] Dasog, M.; Thompson, J. R.; Lewis, N. S. Oxidant-Activated Reactions of Nucleophiles with Silicon Nanocrystals. *Chemistry of Materials* **2017**, *29*, 7002–7013.

[2] Gallant, B. M.; Gu, X. W.; Chen, D. Z.; Greer, J. R.; Lewis, N. S. Tailoring of Interfacial Mechanical Shear Strength by Surface Chemical Modification of Silicon Microwires Embedded in Nafion Membranes. *ACS Nano* **2015**, *9*, 5143–5153.

[3] Jeong, H. E.; Kim, I.; Karam, P.; Choi, H.-J.; Yang, P. Bacterial Recognition of Silicon Nanowire Arrays. *Nano Letters* **2013**, *13*, 2864–2869.

[4] Arefi, H. H.; Nolan, M.; Fagas, G. Role of the Head and/or Tail Groups of Adsorbed-[$X^{\text{head group}}$]–Alkyl–[$X^{\text{tail group}}$][X= O(H), S(H), $NH_{(2)}$] Chains in Controlling the Work Function of the Functionalized H:Si (111) Surface. *The Journal of Physical Chemistry C* **2015**, *119*, 11588–11597.

[5] Vogl, U. S.; Lux, S. F.; Das, P.; Weber, A.; Placke, T.; Kostecki, R.; Winter, M. The Mechanism of SEI Formation on Single Crystal Si(100), Si(110) and Si(111) Electrodes. *Journal of The Electrochemical Society* **2015**, *162*, A2281–A2288.

[6] Rumpf, K.; Granitzer, P.; Poelt, P.; Krenn, H. Transition Metals Specifically Electrodeposited into Porous Silicon. *Physica Status Solidi C* **2009**, *6*, 1592–1595.

[7] Granitzer, P.; Rumpf, K.; Pölt, P.; Reichmann, A.; Krenn, H. Self-Assembled Mesoporous Silicon in the Crossover between Irregular and Regular Arrangement Applicable for Ni Filling. *Physica E: Low-dimensional Systems and Nanostructures* **2007**, *38*, 205–210.

[8] Higashi, G.; Chabal, Y.; Trucks, G.; Raghavachari, K. Ideal Hydrogen Termination of the Si(111) Surface. *Applied Physics Letters* **1990**, *56*, 656–658.

[9] Huck, L. A.; Buriak, J. M. Toward a Mechanistic Understanding of Exciton-Mediated Hydrosilylation on Nanocrystalline Silicon. *Journal of the American Chemical Society* **2012**, *134*, 489–497.

[10] Buriak, J. M.; Sikder, M. D. H. From Molecules to Surfaces: Radical-Based Mechanisms of Si–S and Si–Se Bond Formation on Silicon. *Journal of the American Chemical Society* **2015**, *137*, 9730–9738.

[11] Plymale, N. T.; Ramachandran, A. A.; Lim, A.; Brunschwig, B. S.; Lewis, N. S. Control of the Band-Edge Positions of Crystalline Si(111) by Surface Functionalization with 3,4,5-Trifluorophenylacetylenyl Moieties. *The Journal of Physical Chemistry C* **2016**, *120*, 14157–14169.

[12] Li, Y.-H.; Buriak, J. M. Dehydrogenative Silane Coupling on Silicon Surfaces via Early Transition Metal Catalysis. *Inorganic Chemistry* **2006**, *45*, 1096–1102.

[13] Wang, D.; Buriak, J. M. Electrochemically Driven Organic Monolayer Formation on Silicon Surfaces using Alkylammonium and Alkylphosphonium Reagents. *Surface Science* **2005**, *590*, 154–161.

[14] Sayed, S. Y.; Wang, F.; Malac, M.; Meldrum, A.; Egerton, R. F.; Buriak, J. M. Heteroepitaxial Growth of Gold Nanostructures on Silicon by Galvanic Displacement. *ACS Nano* **2009**, *3*, 2809–2817.

[15] Scheres, L.; Giesbers, M.; Zuilhof, H. Organic Monolayers onto Oxide-Free Silicon with Improved Surface Coverage: Alkynes versus Alkenes. *Langmuir* **2010**, *26*, 4790–4795.

[16] Yu, H.; Webb, L. J.; Ries, R. S.; Solares, S. D.; Goddard, W. A.; Heath, J. R.; Lewis, N. S. Low-Temperature STM Images of Methyl-terminated Si (111) Surfaces. *The Journal of Physical Chemistry B* **2005**, *109*, 671–674.

[17] Sieval, A. B.; van den Hout, B.; Zuilhof, H.; Sudhölter, E. J. R. Molecular Modeling of Covalently Attached Alkyl Monolayers on the Hydrogen-Terminated Si(111) Surface. *Langmuir* **2001**, *17*, 2172–2181.

[18] Zhang, L.; Wesley, K.; Jiang, S. Molecular Simulation Study of Alkyl Monolayers on Si (111). *Langmuir* **2001**, *17*, 6275–6281.

[19] Plymale, N. T.; Dasog, M.; Brunschwig, B. S.; Lewis, N. S. A Mechanistic Study of the Oxidative Reaction of Hydrogen-Terminated Si (111) Surfaces with Liquid Methanol. *The Journal of Physical Chemistry C* **2017**, *121*, 4270–4282.

[20] Pujari, S. P.; van Andel, E.; Yaffe, O.; Cahen, D.; Weidner, T.; van Rijn, C. J. M.; Zuilhof, H. Mono-Fluorinated Alkyne-Derived SAMs on Oxide-Free Si(111) Surfaces: Preparation, Characterization and Tuning of the Si Workfunction. *Langmuir* **2013**, *29*, 570–580.

[21] Su, Y.; Liu, C.; Brittman, S.; Tang, J.; Fu, A.; Kornienko, N.; Kong, Q.; Yang, P. Single-Nanowire Photoelectrochemistry. *Nature Nanotechnology* **2016**, *11*, 609.

[22] Choi, H. C.; Buriak, J. M. Preparation and Functionalization of Hydride Terminated Porous Germanium. *Chemical Communications* **2000**, 1669–1670.

[23] Ieong, M.; Doris, B.; Kedzierski, J.; Rim, K.; Yang, M. Silicon Device Scaling to the Sub-10-nm Regime. *Science* **2004**, *306*, 2057–2060.

[24] Tao, F. F.; Zhu, Y.; Bernasek, S. L. In *Functionalization of Semiconductor Surfaces*; Tao, F. F., Bernasek, S. L., Eds.; John Wiley & Sons, Inc., 2012; pp 1–10.

[25] Bruce, J. P.; Oliver, D. R.; Lewis, N. S.; Freund, M. S. Electrical Characteristics of the Junction between PEDOT:PSS and Thiophene-Functionalized Silicon Microwires. *ACS Applied Materials & Interfaces* **2015**, *7*, 27160–27166.

[26] Kang, O. S.; Bruce, J. P.; Herbert, D. E.; Freund, M. S. Covalent Attachment of Ferrocene to Silicon Microwire Arrays. *ACS Applied Materials & Interfaces* **2015**, *7*, 26959–26967.

[27] Ciampi, S.; Choudhury, M. H.; Ahmad, S. A. B. A.; Darwish, N.; Brun, A. L.; Gooding, J. J. The Impact of Surface Coverage on the Kinetics of Electron Transfer through Redox Monolayers on a Silicon Electrode Surface. *Electrochimica Acta* **2015**, *186*, 216–222.

[28] Vilan, A.; Yaffe, O.; Biller, A.; Salomon, A.; Kahn, A.; Cahen, D. Molecules on Si: Electronics with Chemistry. *Advanced Materials* **2010**, *22*, 140–159.

[29] Dasog, M.; Bader, K.; Veinot, J. G. C. Influence of Halides on the Optical Properties of Silicon Quantum Dots. *Chemistry of Materials* **2015**, *27*, 1153–1156.

[30] Fermi, A.; Locritani, M.; Carlo, G. D.; Pizzotti, M.; Caramori, S.; Yu, Y.; Korgel, B. A.;

Bergamini, G.; Ceroni, P. Light-Harvesting Antennae based on Photoactive Silicon Nanocrystals Functionalized with Porphyrin Chromophores. *Faraday Discussions* **2015**, *185*, 481–495.

[31] Wang, J.; Zhou, Y.; Watkinson, M.; Gautrot, J.; Krause, S. High-Sensitivity Light-Addressable Potentiometric Sensors using Silicon on Sapphire Functionalized with Self-Assembled Organic Monolayers. *Sensors and Actuators B: Chemical* **2015**, *209*, 230–236.

[32] Kanyong, P.; Sun, G.; Rösicke, F.; Syritski, V.; Panne, U.; Hinrichs, K.; Rappich, J. Maleimide Functionalized Silicon Surfaces for Biosensing Investigated by In-Situ IRSE and EQCM. *Electrochemistry Communications* **2015**, *51*, 103–107.

[33] Peng, W.; Rupich, S. M.; Shafiq, N.; Gartstein, Y. N.; Malko, A. V.; Chabal, Y. J. Silicon Surface Modification and Characterization for Emergent Photovoltaic Applications Based on Energy Transfer. *Chemical Reviews* **2015**, *115*, 12764–12796.

[34] Wong, K. T.; Lewis, N. S. What a Difference a Bond Makes: The Structural, Chemical, and Physical Properties of Methyl-Terminated Si(111) Surfaces. *Accounts of Chemical Research* **2014**, *47*, 3037–3044.

[35] Kroemer, H. Nobel Lecture: Quasielectric Fields and Band Offsets: Teaching Electrons New Tricks. *Reviews of Modern Physics* **2001**, *73*, 783–793.

[36] Schmidt, V.; Wittemann, J. V.; Senz, S.; Gösele, U. Silicon Nanowires: A Review on Aspects of their Growth and their Electrical Properties. *Advanced Materials* **2009**, *21*, 2681–2702.

[37] Smaali, K.; Guérin, D.; Passi, V.; Ordronneau, L.; Carella, A.; Mélin, T.; Dubois, E.; Vuillaume, D.; Simonato, J.; Lenfant, S. Physical Study by Surface Characterizations of Sarin Sensor on the Basis of Chemically Functionalized Silicon Nanoribbon Field Effect Transistor. *The Journal of Physical Chemistry C* **2016**, *120*, 11180–11191.

[38] Bashouti, M. Y.; Pietsch, M.; Brönstrup, G.; Sivakov, V.; Ristein, J.; Christiansen, S. Heterojunction Based Hybrid Silicon Nanowire Solar Cell: Surface Termination, Photoelectron and Photoemission Spectroscopy Study. *Progress in Photovoltaics: Research and Applications* **2014**, *22*, 1050–1061.

[39] Pluchery, O.; Zhang, Y.; Benbalagh, R.; Caillard, L.; Gallet, J. J.; Bournel, F.; Lamic-Humblot, A.-F.; Salmeron, M.; Chabal, Y. J.; Rochet, F. Static and Dynamic Electronic Characterization of Organic Monolayers Grafted on a Silicon Surface. *Physical Chemistry Chemical Physics* **2016**, *18*, 3675–3684.

[40] Gleason-Rohrer, D. C.; Brunschwig, B. S.; Lewis, N. S. Measurement of the Band Bending and Surface Dipole at Chemically Functionalized Si(111)/Vacuum Interfaces. *The Journal of Physical Chemistry C* **2013**, *117*, 18031–18042.

[41] Pluchery, O.; Caillard, L.; Dollfus, P.; Chabal, Y. J. Gold Nanoparticles on Functionalized Silicon Substrate under Coulomb Blockade Regime: An Experimental and Theoretical Investigation. *The Journal of Physical Chemistry B* **2018**, *122*, 897–903.

[42] Arefi, H. H.; Fagas, G. Chemical Trends in the Work Function of Modified Si(111) Surfaces: A DFT Study. *The Journal of Physical Chemistry C* **2014**, *118*, 14346–14354.

[43] Nishinaga, T. *Handbook of Crystal Growth: Fundamentals*; Elsevier, 2014.

[44] Koval, C. A.; Howard, J. N. Electron Transfer at Semiconductor Electrode-Liquid Electrolyte Interfaces. *Chemical Reviews* **1992**, *92*, 411–433.

[45] Morrison, S. R. *Electrochemistry at Semiconductor and Oxidized Metal Electrodes*; Springer US,

1980.

[46] Zhang, X. G. *Electrochemistry of Silicon and its Oxide*; Springer Science & Business Media, 2007.

[47] Bean, K. E.; Gleim, P. S. The Influence of Crystal Orientation on Silicon Semiconductor Processing. *Proceedings of the IEEE* **1969**, *57*, 1469–1476.

[48] Buriak, J. M. Organometallic Chemistry on Silicon and Germanium Surfaces. *Chemical Reviews* **2002**, *102*, 1271–1308.

[49] Neergaard Waltenburg, H.; Yates, J. T. Surface Chemistry of Silicon. *Chemical Reviews* **1995**, *95*, 1589–1673.

[50] Hamers, R. J.; Wang, Y. Atomically-Resolved Studies of the Chemistry and Bonding at Silicon Surfaces. *Chemical Reviews* **1996**, *96*, 1261–1290.

[51] Canham, L. T. Silicon Quantum Wire Array Fabrication by Electrochemical and Chemical Dissolution of Wafers. *Applied Physics Letters* **1990**, *57*, 1046–1048.

[52] Bsiesy, A.; Vial, J. C.; Gaspard, F.; Herino, R.; Ligeon, M.; Muller, F.; Romestain, R.; Wasiela, A.; Halimaoui, A.; Bomchil, G. Photoluminescence of High Porosity and of Electrochemically Oxidized Porous Silicon Layers. *Surface Science* **1991**, *254*, 195–200.

[53] Tsai, C.; Li, K.; Sarathy, J.; Shih, S.; Campbell, J. C.; Hance, B. K.; White, J. M. Thermal Treatment Studies of the Photoluminescence Intensity of Porous Silicon. *Applied Physics Letters* **1991**, *59*, 2814–2816.

[54] Robinson, M. B.; Dillon, A. C.; Haynes, D. R.; George, S. M. Effect of Thermal Annealing and Surface Coverage on Porous Silicon Photoluminescence. *Applied Physics Letters* **1992**, *61*, 1414–1416.

[55] Tsybeskov, L.; Vandyshev, J. V.; Fauchet, P. M. Blue Emission in Porous Silicon: Oxygen-Related Photoluminescence. *Physical Review B* **1994**, *49*, 7821–7824.

[56] Canham, L. *Handbook of Porous Silicon*; Springer: New York, 2014.

[57] Sailor, M. J. *Porous Silicon in Practice: Preparation, Characterization and Applications*; John Wiley & Sons, 2012.

[58] Granitzer, P.; Rumpf, K. Porous Silicon—A Versatile Host Material. *Materials* **2010**, *3*, 943–998.

[59] Doan, V. V.; Sailor, M. J. Photolithographic Fabrication of Micron-Dimension Porous Si Structures Exhibiting Visible Luminescence. *Applied Physics Letters* **1992**, *60*, 619–620.

[60] Li, X.; Suwa, T.; Teramoto, A.; Kuroda, R.; Sugawa, S.; Ohmi, T. Atomically Flattening Technology at 850 ^{o}C for Si(100) Surface. *ECS Transactions* **2010**, *28*, 299–309.

[61] Kuroda, R.; Suwa, T.; Teramoto, A.; Hasebe, R.; Sugawa, S.; Ohmi, T. Atomically Flat Silicon Surface and Silicon/Insulator Interface Formation Technologies for (100) Surface Orientation Large-Diameter Wafers Introducing High Performance and Low-Noise Metal–Insulator–Silicon FETs. *IEEE Transactions on Electron Devices* **2009**, *56*, 291–298.

[62] Higashi, G. S.; Becker, R. S.; Chabal, Y. J.; Becker, A. J. Comparison of Si(111) Surfaces Prepared using Aqueous Solutions of NH_4F versus HF. *Applied Physics Letters* **1991**, *58*, 1656–1658.

[63] Newton, T. A.; Boiani, J. A.; Hines, M. A. The Correlation between Surface Morphology and Spectral Lineshape: a Re-examination of the H–Si(111) Stretch Vibration. *Surface Science* **1999**,

430, 67–79.

[64] Anderson, R. C.; Muller, R. S.; Tobias, C. W. Chemical Surface Modification of Porous Silicon. *Journal of the Electrochemical Society* **1993**, *140*, 1393–1396.

[65] Boukherroub, R.; Szunerits, S. In *Electrochemistry at the Nanoscale*; Schmuki, P., Virtanen, S., Eds.; Nanostructure Science and Technology; Springer New York: New York, NY, 2009; pp 183–248.

[66] Mastronardi, M. L.; Hennrich, F.; Henderson, E. J.; Maier-Flaig, F.; Blum, C.; Reichenbach, J.; Lemmer, U.; Kübel, C.; Wang, D.; Kappes, M. M.; Ozin, G. A. Preparation of Monodisperse Silicon Nanocrystals Using Density Gradient Ultracentrifugation. *Journal of the American Chemical Society* **2011**, *133*, 11928–11931.

[67] Dasog, M.; Rachinsky, C.; Veinot, J. G. C. From Si and C encapsulated SiO_2 to SiC: Exploring the Influence of Sol–Gel Polymer Substitution on Thermally Induced Nanocrystal Formation. *Journal of Materials Chemistry* **2011**, *21*, 12422–12427.

[68] Pi, X. D.; Liptak, R. W.; Nowak, J. D.; Wells, N. P.; Carter, C. B.; Campbell, S. A.; Kortshagen, U. Air-Stable Full-Visible-Spectrum Emission from Silicon Nanocrystals Synthesized by an All-Gas-Phase Plasma Approach. *Nanotechnology* **2008**, *19*, 245603.

[69] Huisken, F.; Ledoux, G.; Guillois, O.; Reynaud, C. Light-Emitting Silicon Nanocrystals from Laser Pyrolysis. *Advanced Materials* **2002**, *14*, 1861–1865.

[70] Zhang, X.; Chabal, Y.; Christman, S.; Chaban, E.; Garfunkel, E. Oxidation of H-Covered Flat and Vicinal Si (111)-1$\times$1 Surfaces. *Journal of Vacuum Science & Technology A: Vacuum, Surfaces, and Films* **2001**, *19*, 1725–1729.

[71] Zhang, X.; Garfunkel, E.; Chabal, Y.; Christman, S.; Chaban, E. Stability of HF-Etched Si(100) Surfaces in Oxygen Ambient. *Applied Physics Letters* **2001**, *79*, 4051–4053.

[72] Dai, M.; Wang, Y.; Kwon, J.; Halls, M. D.; Chabal, Y. J. Nitrogen Interaction with Hydrogen-Terminated Silicon Surfaces at the Atomic Scale. *Nature Materials* **2009**, *8*, 825.

[73] Ciampi, S.; Harper, J. B.; Gooding, J. J. Wet Chemical Routes to the Assembly of Organic Monolayers on Silicon Surfaces via the Formation of Si–C Bonds: Surface Preparation, Passivation and Functionalization. *Chemical Society Reviews* **2010**, *39*, 2158–2183.

[74] Haick, H.; Hurley, P. T.; Hochbaum, A. I.; Yang, P.; Lewis, N. S. Electrical Characteristics and Chemical Stability of Non-Oxidized, Methyl-Terminated Silicon Nanowires. *Journal of the American Chemical Society* **2006**, *128*, 8990–8991.

[75] Li, Y.; Calder, S.; Yaffe, O.; Cahen, D.; Haick, H.; Kronik, L.; Zuilhof, H. Hybrids of Organic Molecules and Flat, Oxide-Free Silicon: High-Density Monolayers, Electronic Properties, and Functionalization. *Langmuir* **2012**, *28*, 9920–9929.

[76] Fabre, B. Functionalization of Oxide-Free Silicon Surfaces with Redox-Active Sssemblies. *Chemical reviews* **2016**, *116*, 4808–4849.

[77] DeBenedetti, W. J.; Chabal, Y. J. Functionalization of Oxide-Free Silicon Surfaces. *Journal of Vacuum Science & Technology A: Vacuum, Surfaces, and Films* **2013**, *31*, 050826.

[78] Ballestri, M.; Chatgilialoglu, C.; Clark, K. B.; Griller, D.; Giese, B.; Kopping, B. Tris(trimethylsilyl)silane as a Radical-Based Reducing Agent in Synthesis. *The Journal of Organic Chemistry* **1991**, *56*, 678–683.

[79] Chatgilialoglu, C.; Griller, D.; Lesage, M. Rate Constants for the Reactions of Tris(trimethylsilyl) silyl Radicals with Organic Halides. *The Journal of Organic Chemistry* **1989**, *54*, 2492–2494.

[80] Linford, M. R.; Chidsey, C. E. D. Alkyl Monolayers Covalently Bonded to Silicon Surfaces. *Journal of the American Chemical Society* **1993**, *115*, 12631–12632.

[81] Linford, M. R.; Fenter, P.; Eisenberger, P. M.; Chidsey, C. E. D. Alkyl Monolayers on Silicon Prepared from 1-Alkenes and Hydrogen-Terminated Silicon. *Journal of the American Chemical Society* **1995**, *117*, 3145–3155.

[82] Wang, D.; Buriak, J. M. Trapping Silicon Surface-Based Radicals. *Langmuir* **2006**, *22*, 6214–6221.

[83] Hu, M.; Liu, F.; Buriak, J. M. Expanding the Repertoire of Molecular Linkages to Silicon: Si–S, Si–Se, and Si–Te Bonds. *ACS Applied Materials & Interfaces* **2016**, *8*, 11091–11099.

[84] Terry, J.; Linford, M. R.; Wigren, C.; Cao, R.; Pianetta, P.; Chidsey, C. E. D. Determination of the Bonding of Alkyl Monolayers to the Si(111) Surface using Chemical-Shift, Scanned-Energy Photoelectron Diffraction. *Applied Physics Letters* **1997**, *71*, 1056–1058.

[85] Terry, J.; Linford, M. R.; Wigren, C.; Cao, R.; Pianetta, P.; Chidsey, C. E. Alkyl-Terminated Si (111) Surfaces: a High-Resolution, Core Level Photoelectron Spectroscopy Study. *Journal of Applied Physics* **1999**, *85*, 213–221.

[86] Walsh, R. Bond Dissociation Energy Values in Silicon-Containing Compounds and Some of Their Implications. *Accounts of Chemical Research* **1981**, *14*, 246–252.

[87] Stewart, M. P.; Buriak, J. M. Photopatterned Hydrosilylation on Porous Silicon. *Angewandte Chemie International Edition* **1998**, *37*, 3257–3260.

[88] Zavitsas, A. A.; Chatgilialoglu, C. Energies of Activation. The Paradigm of Hydrogen Abstractions by Radicals. *Journal of the American Chemical Society* **1995**, *117*, 10645–10654.

[89] Cicero, R. L.; Linford, M. R.; Chidsey, C. E. D. Photoreactivity of Unsaturated Compounds with Hydrogen-Terminated Silicon(111). *Langmuir* **2000**, *16*, 5688–5695.

[90] Wang, X.; Ruther, R. E.; Streifer, J. A.; Hamers, R. J. UV-Induced Grafting of Alkenes to Silicon Surfaces: Photoemission versus Excitons. *Journal of the American Chemical Society* **2010**, *132*, 4048–4049.

[91] Sieval, A. B.; van den Hout, B.; Zuilhof, H.; Sudhölter, E. J. R. Molecular Modeling of Alkyl Monolayers on the Si(111) Surface. *Langmuir* **2000**, *16*, 2987–2990.

[92] Peng, W.; DeBenedetti, W. J.; Kim, S.; Hines, M. A.; Chabal, Y. J. Lowering the Density of Electronic Defects on Organic-Functionalized Si(100) Surfaces. *Applied Physics Letters* **2014**, *104*, 241601.

[93] Aureau, D.; Rappich, J.; Moraillon, A.; Allongue, P.; Ozanam, F.; Chazalviel, J.-N. In situ Monitoring of the Electronic Properties and the pH Stability of Grafted Si(111). *Journal of Electroanalytical Chemistry* **2010**, *646*, 33–42.

[94] Eves, B. J.; Lopinski, G. P. Formation of Organic Monolayers on Silicon via Gas-Phase Photochemical Reactions. *Langmuir* **2006**, *22*, 3180–3185.

[95] Boukherroub, R.; Petit, A.; Loupy, A.; Chazalviel, J.-N.; Ozanam, F. Microwave-Assisted Chemical Functionalization of Hydrogen-Terminated Porous Silicon Surfaces. *The Journal of Physical Chemistry B* **2003**, *107*, 13459–13462.

[96] Petit, A.; Delmotte, M.; Loupy, A.; Chazalviel, J.-N.; Ozanam, F.; Boukherroub, R. Microwave Effects on Chemical Functionalization of Hydrogen-Terminated Porous Silicon Nanostructures. *The Journal of Physical Chemistry C* **2008**, *112*, 16622–16628.

[97] Stewart, M. P.; Buriak, J. M. Exciton-Mediated Hydrosilylation on Photoluminescent Nanocrystalline Silicon. *Journal of the American Chemical Society* **2001**, *123*, 7821–7830.

[98] Cullis, A.; Canham, L.; Calcott, P. The Structural and Luminescence Properties of Porous Silicon. *Journal of Applied Physics* **1997**, *82*, 909–965.

[99] Baierle, R.; Caldas, M.; Molinari, E.; Ossicini, S. Optical Emission from Small Si Particles. *Solid State Communications* **1997**, *102*, 545–549.

[100] Buda, F.; Kohanoff, J.; Parrinello, M. Optical Properties of Porous Silicon: A First-Principles Study. *Physical Review Letters* **1992**, *69*, 1272.

[101] Huck, L. A.; Buriak, J. M. UV-Initiated Hydrosilylation on Hydrogen-Terminated Silicon (111): Rate Coefficient Increase of Two Orders of Magnitude in the Presence of Aromatic Electron Acceptors. *Langmuir* **2012**, *28*, 16285–16293.

[102] Sun, Q.-Y.; de Smet, L. C.; van Lagen, B.; Wright, A.; Zuilhof, H.; Sudhölter, E. J. Covalently Attached Monolayers on Hydrogen-Terminated Si (100): Extremely Mild Attachment by Visible Light. *Angewandte Chemie International Edition* **2004**, *43*, 1352–1355.

[103] Sun, Q.-Y.; de Smet, L. C.; van Lagen, B.; Giesbers, M.; Thüne, P. C.; van Engelenburg, J.; de Wolf, F. A.; Zuilhof, H.; Sudhölter, E. J. Covalently Attached Monolayers on Crystalline Hydrogen-Terminated Silicon: Extremely Mild Attachment by Visible Light. *Journal of the American Chemical Society* **2005**, *127*, 2514–2523.

[104] Rijksen, B.; Pujari, S. P.; Scheres, L.; van Rijn, C. J.; Baio, J.; Weidner, T.; Zuilhof, H. Hexadecadienyl Monolayers on Hydrogen-Terminated Si (111): Faster Monolayer Formation and Improved Surface Coverage using the Enyne Moiety. *Langmuir* **2012**, *28*, 6577–6588.

[105] Balakumar, A.; Lysenko, A. B.; Carcel, C.; Malinovskii, V. L.; Gryko, D. T.; Schweikart, K.-H.; Loewe, R. S.; Yasseri, A. A.; Liu, Z.; Bocian, D. F.; Lindsey, J. S. Diverse Redox-Active Molecules Bearing O-, S-, or Se-Terminated Tethers for Attachment to Silicon in Studies of Molecular Information Storage. *The Journal of Organic Chemistry* **2004**, *69*, 1435–1443.

[106] Yasseri, A. A.; Syomin, D.; Loewe, R. S.; Lindsey, J. S.; Zaera, F.; Bocian, D. F. Structural and Electron-Transfer Characteristics of O-, S-, and Se-Tethered Porphyrin Monolayers on Si(100). *Journal of the American Chemical Society* **2004**, *126*, 15603–15612.

[107] Chatgilialoglu, C. Structural and Chemical Properties of Silyl Radicals. *Chemical Reviews* **1995**, *95*, 1229–1251.

[108] Chatgilialoglu, C. $(Me_3Si)_3SiH$: Twenty Years After Its Discovery as a Radical-Based Reducing Agent. *Chemistry – A European Journal* **2008**, *14*, 2310–2320.

[109] Coulter, S. K.; Schwartz, M. P.; Hamers, R. J. Sulfur Atoms as Tethers for Selective Attachment of Aromatic Molecules to Silicon(001) Surfaces. *The Journal of Physical Chemistry B* **2001**, *105*, 3079–3087.

[110] Yu, L. H.; Gergel-Hackett, N.; Zangmeister, C. D.; Hacker, C. A.; Richter, C. A.; Kushmerick, J. G. Molecule-Induced Interface States Dominate Charge Transport in Si–Alkyl–Metal Junctions. *Journal of Physics: Condensed Matter* **2008**, *20*, 374114.

[111] Lou, J. L.; Shiu, H. W.; Chang, L. Y.; Wu, C. P.; Soo, Y.-L.; Chen, C.-H. Preparation and Characterization of an Ordered 1-Dodecanethiol Monolayer on Bare Si(111) Surface. *Langmuir* **2011**, *27*, 3436–3441.

[112] Huang, Y.-S.; Chen, C.-H.; Chen, C.-H.; Hung, W.-H. Fabrication of Octadecyl and Octadecanethiolate Self-Assembled Monolayers on Oxide-Free Si(111) with a One-Cell Process. *ACS Applied Materials & Interfaces* **2013**, *5*, 5771–5776.

[113] Hacker, C. A. Modifying Electronic Properties at the Silicon–Molecule Interface using Atomic Tethers. *Solid-State Electronics* **2010**, *54*, 1657–1664.

[114] Sano, H.; Ohno, K.; Ichii, T.; Murase, K.; Sugimura, H. Alkanethiol Self-Assembled Monolayers Formed on Silicon Substrates. *Japanese Journal of Applied Physics* **2010**, *49*, 01AE09.

[115] Bhartia, B.; Puniredd, S. R.; Jayaraman, S.; Gandhimathi, C.; Sharma, M.; Kuo, Y.-C.; Chen, C.-H.; Reddy, V. J.; Troadec, C.; Srinivasan, M. P. Highly Stable Bonding of Thiol Monolayers to Hydrogen-Terminated Si via Supercritical Carbon Dioxide: Toward a Super Hydrophobic and Bioresistant Surface. *ACS Applied Materials & Interfaces* **2016**, *8*, 24933–24945.

[116] Soundararajan, N.; Jackson, J. E.; Platz, M. S. Reaction of Triethylsilyl Radical with Sulfides, a Laser Flash Photolysis Study. *Journal of Physical Organic Chemistry* **1988**, *1*, 39–46.

[117] Ogawa, A.; Doi, M.; Ogawa, I.; Hirao, T. Highly Selective Three-Component Coupling of Ethyl Propiolate, Alkenes, and Diphenyl Diselenide under Visible-Light Irradiation. *Angewandte Chemie International Edition* **1999**, *38*, 2027–2029.

[118] Russell, G. A.; Tashtoush, H. Free-Radical Chain-Substitution Reactions of Alkylmercury Halides. *Journal of the American Chemical Society* **1983**, *105*, 1398–1399.

[119] Ogawa, A. In *Main Group Metals in Organic Synthesis*; Yamamoto, H., Oshima, K., Eds.; Wiley-VCH Verlag GmbH & Co. KGaA, 2004; pp 813–866.

[120] Nogueira, C. W.; Zeni, G.; Rocha, J. B. Organoselenium and organotellurium compounds: toxicology and pharmacology. *Chemical Reviews* **2004**, *104*, 6255–6286.

[121] Bowman, W. R. In *Organoselenium Chemistry*; Wirth, T., Ed.; Wiley-VCH Verlag GmbH & Co. KGaA, 2011; pp 111–146.

[122] Chatgilialoglu, C. The Tris(trimethylsilyl)silane/Thiol Reducing System: A Tool for Measuring Rate Constants for Reactions of Carbon-Centered Radicals with Thiols. *Helvetica Chimica Acta* **2006**, *89*, 2387–2398.

[123] Wittenberg, D.; McNinch, H. A.; Gilman, H. The Reaction of Some Silicon Hydrides with Sulfur-containing Heterocycles and Related Compounds. *Journal of the American Chemical Society* **1958**, *80*, 5418–5422.

[124] de Smet, L. C.; Zuilhof, H.; Sudhölter, E. J.; Lie, L. H.; Houlton, A.; Horrocks, B. R. Mechanism of the Hydrosilylation Reaction of Alkenes at Porous Silicon: Experimental and Computational Deuterium Labeling Studies. *The Journal of Physical Chemistry B* **2005**, *109*, 12020–12031.

[125] Nemanick, E. J.; Hurley, P. T.; Webb, L. J.; Knapp, D. W.; Michalak, D. J.; Brunschwig, B. S.; Lewis, N. S. Chemical and Electrical Passivation of Single-Crystal Silicon(100) Surfaces through a Two-Step Chlorination/Alkylation Process. *The Journal of Physical Chemistry B* **2006**, *110*, 14770–14778.

[126] Huck, L. A.; Buriak, J. M. In *Handbook of Porous Silicon*; Canham, L., Ed.; Springer International

Publishing, 2014; pp 683–693.

[127] Scheres, L.; Rijksen, B.; Giesbers, M.; Zuilhof, H. Molecular Modeling of Alkyl and Alkenyl Monolayers on Hydrogen-Terminated Si (111). *Langmuir* **2011**, *27*, 972–980.

[128] Vickerman, J. C.; Briggs, D. *ToF-SIMS: Surface Analysis by Mass Spectrometry*; IM, 2001.

[129] Brison, J.; Muramoto, S.; Castner, D. G. ToF-SIMS Depth Profiling of Organic Films: A Comparison between Single-Beam and Dual-Beam Analysis. *The Journal of Physical Chemistry C* **2010**, *114*, 5565–5573.

[130] Sodhi, R. N. Time-of-flight Secondary Ion Mass Spectrometry (TOF-SIMS):—Versatility in Chemical and Imaging Surface Analysis. *Analyst* **2004**, *129*, 483–487.

[131] Yuan, Y.; Lee, T. R. *Surface Science Techniques*; Springer, 2013; pp 3–34.

[132] Shi, Z.; Zhang, Y.; Liu, M.; Hanaor, D. A.; Gan, Y. Dynamic Contact Angle Hysteresis in Liquid Bridges. *Colloids and Surfaces A: Physicochemical and Engineering Aspects* **2018**, *555*, 365–371.

[133] Liu, F.; Hauger, T. C.; Olsen, B. C.; Luber, E. J.; Buriak, J. M. Polymers, Plasmons, and Patterns: Mechanism of Plasmon-Induced Hydrosilylation on Silicon. *Chemistry of Materials* **2016**, *28*, 9158–9168.

[134] Yam, C. M.; Tong, S. S.; Kakkar, A. K. Simple Acid- Base Hydrolytic Chemistry Approach to Molecular Self-Assembly: Thin Films of Long Chain Alcohols Terminated with Alkyl, Phenyl, and Acetylene Groups on Inorganic Oxides Surfaces. *Langmuir* **1998**, *14*, 6941–6947.

[135] Popoff, R. T.; Zavareh, A. A.; Kavanagh, K. L.; Yu, H.-Z. Reduction of Gold Penetration through Phenyl-Terminated Alkyl Monolayers on Silicon. *The Journal of Physical Chemistry C* **2012**, *116*, 17040–17047.

[136] Chibowski, E. J. Surface Free Energy and Wettability of Silyl Layers on Silicon Determined from Contact Angle Hysteresis. *Advances in Colloid and Interface Science* **2005**, *113*, 121–131.

[137] Janssen, D.; De Palma, R.; Verlaak, S.; Heremans, P.; Dehaen, W. Static Solvent Contact Angle Measurements, Surface Free Energy and Wettability Determination of Various Self-Assembled Monolayers on Silicon Dioxide. *Thin Solid Films* **2006**, *515*, 1433–1438.

[138] Anariba, F.; DuVall, S. H.; McCreery, R. L. Mono- and Multilayer Formation by Diazonium Reduction on Carbon Surfaces Monitored with Atomic Force Microscopy “Scratching”. *Analytical Chemistry* **2003**, *75*, 3837–3844.

[139] Peng, F.; Su, Y.; Zhong, Y.; Fan, C.; Lee, S.-T.; He, Y. Silicon Nanomaterials Platform for Bioimaging, Biosensing, and Cancer Therapy. *Accounts of Chemical Research* **2014**, *47*, 612–623.

[140] Cheng, X.; Hinde, E.; Owen, D. M.; Lowe, S. B.; Reece, P. J.; Gaus, K.; Gooding, J. J. Enhancing Quantum Dots for Bioimaging using Advanced Surface Chemistry and Advanced Optical Microscopy: Application to Silicon Quantum Dots (SiQDs). *Advanced Materials* **2015**, *27*, 6144–6150.

[141] Wallart, X.; Henry de Villeneuve, C.; Allongue, P. Truly Quantitative XPS Characterization of Organic Monolayers on Silicon: Study of Alkyl and Alkoxy Monolayers on H–Si(111). *Journal of the American Chemical Society* **2005**, *127*, 7871–7878.

[142] Brown, E. S.; Hlynchuk, S.; Maldonado, S. Chemically Modified Si(111) Surfaces Simultaneously Demonstrating Hydrophilicity, Resistance against Oxidation, and Low Trap State Densities. *Surface*

Science **2016**, *645*, 49–55.

[143] Toledano, T.; Garrick, R.; Sinai, O.; Bendikov, T.; Haj-Yahia, A.-E.; Lerman, K.; Alon, H.; Sukenik, C. N.; Vilan, A.; Kronik, L.; Cahen, D. Effect of Binding Group on Hybridization across the Silicon/Aromatic-Monolayer Interface. *Journal of Electron Spectroscopy and Related Phenomena* **2015**, *204, Part A*, 149–158.

[144] Li, F.; Basile, V. M.; Rose, M. J. Electron Transfer through Surface-Grown, Ferrocene-Capped Oligophenylene Molecular Wires (5–50 Å) on n-Si(111) Photoelectrodes. *Langmuir* **2015**, *31*, 7712–7716.

[145] DeBenedetti, W. J. I.; Chiu, S.-K.; Radlinger, C. M.; Ellison, R. J.; Manhat, B. A.; Zhang, J. Z.; Shi, J.; Goforth, A. M. Conversion from Red to Blue Photoluminescence in Alcohol Dispersions of Alkyl-Capped Silicon Nanoparticles: Insight into the Origins of Visible Photoluminescence in Colloidal Nanocrystalline Silicon. *The Journal of Physical Chemistry C* **2015**, *119*, 9595–9608.

[146] Cooper, A. J.; Keyvanfar, K.; Deberardinis, A.; Pu, L.; Bean, J. C. Dopant Passivation and Work Function Tuning through Attachment of Heterogeneous Organic Monolayers on Silicon in Ultrahigh Vacuum. *Applied Surface Science* **2011**, *257*, 6138–6144.

[147] Sieval, A.; Demirel, A.; Nissink, J.; Linford, M.; Van der Maas, J.; De Jeu, W.; Zuilhof, H.; Sudhölter, E. Highly Stable Si–C linked Functionalized Monolayers on the Silicon (100) Surface. *Langmuir* **1998**, *14*, 1759–1768.

[148] Yang, Z.; Gonzalez, C. M.; Purkait, T. K.; Iqbal, M.; Meldrum, A.; Veinot, J. G. C. Radical Initiated Hydrosilylation on Silicon Nanocrystal Surfaces: An Evaluation of Functional Group Tolerance and Mechanistic Study. *Langmuir* **2015**, *31*, 10540–10548.

[149] Steinrück, H.-G.; Schiener, A.; Schindler, T.; Will, J.; Magerl, A.; Konovalov, O.; Li Destri, G.; Seeck, O. H.; Mezger, M.; Haddad, J.; Deutsch, M.; Checco, A.; Ocko, B. M. Nanoscale Structure of Si/SiO_2/Organics Interfaces. *ACS Nano* **2014**, *8*, 12676–12681.

[150] Gusev, E. P.; Lu, H. C.; Gustafsson, T.; Garfunkel, E. Growth Mechanism of Thin Silicon Oxide Films on Si(100) Studied by Medium-Energy Ion Scattering. *Physical Review B* **1995**, *52*, 1759–1775.

[151] Yu, Y.; Rowland, C. E.; Schaller, R. D.; Korgel, B. A. Synthesis and Ligand Exchange of Thiol-Capped Silicon Nanocrystals. *Langmuir* **2015**, *31*, 6886–6893.

[152] Dabbousi, B. O.; Bonasia, P. J.; Arnold, J. Tris(trimethylsilyl)silanetellurol: Preparation, Characterization, and Synthetic Utility of a Remarkably Stable Tellurol. *Journal of the American Chemical Society* **1991**, *113*, 3186–3188.

[153] Sadekov, I. D.; Zakharov, A. V. Stable Tellurols and Their Metal Derivatives. *Russian Chemical Reviews* **1999**, *68*, 909–923.

[154] Ferreira, J. T. B.; Oliveira, A. R. M. D.; Comasseto, J. V. A Convenient Method of Synthesis of Dialkyltellurides and Dialkylditellurides. *Synthetic Communications* **1989**, *19*, 239–244.

[155] Buriak, J. M.; Stewart, M. P.; Geders, T. W.; Allen, M. J.; Choi, H. C.; Smith, J.; Raftery, D.; Canham, L. T. Lewis Acid Mediated Hydrosilylation on Porous Silicon Surfaces. *Journal of the American Chemical Society* **1999**, *121*, 11491–11502.

[156] Sailor, M. J. *Porous Silicon in Practice*; Wiley-VCH Verlag GmbH & Co. KGaA, 2011; pp 43–76.

[157] Jin, C.; Murphy, J. N.; Harris, K. D.; Buriak, J. M. Deconvoluting the Mechanism of Microwave

Annealing of Block Copolymer Thin Films. *ACS Nano* **2014**, *8*, 3979–3991.

[158] Sailor, M. J. In *Handbook of Porous Silicon*; Canham, L., Ed.; Springer International Publishing, 2014; pp 355–380.

[159] Ogata, Y. H. In *Handbook of Porous Silicon*; Canham, L., Ed.; Springer International Publishing, 2014; pp 473–480.

[160] Chabal, Y. J.; Higashi, G. S.; Raghavachari, K.; Burrows, V. A. Infrared Spectroscopy of Si(111) and Si(100) Surfaces After HF Treatment: Hydrogen Termination and Surface Morphology. *Journal of Vacuum Science & Technology A* **1989**, *7*, 2104–2109.

[161] Yu, Y.; Hessel, C. M.; Bogart, T. D.; Panthani, M. G.; Rasch, M. R.; Korgel, B. A. Room Temperature Hydrosilylation of Silicon Nanocrystals with Bifunctional Terminal Alkenes. *Langmuir* **2013**, *29*, 1533–1540.

[162] Yu, Y.; Korgel, B. A. Controlled Styrene Monolayer Capping of Silicon Nanocrystals by Room Temperature Hydrosilylation. *Langmuir* **2015**, *31*, 6532–6537.

[163] Riikonen, J.; Salomäki, M.; van Wonderen, J.; Kemell, M.; Xu, W.; Korhonen, O.; Ritala, M.; MacMillan, F.; Salonen, J.; Lehto, V.-P. Surface Chemistry, Reactivity, and Pore Structure of Porous Silicon Oxidized by Various Methods. *Langmuir* **2012**, *28*, 10573–10583.

[164] Santucci, S.; Di Nardo, S.; Lozzi, L.; Passacantando, M.; Picozzi, P. XPS, LEED and AFM Investigation of the Si(100) Surface after the Deposition and Annealing of Tellurium Thin Films. *Surface Science* **1996**, *352-354*, 1027–1032.

[165] Ishida, T.; Choi, N.; Mizutani, W.; Tokumoto, H.; Kojima, I.; Azehara, H.; Hokari, H.; Akiba, U.; Fujihira, M. High-Resolution X-Ray Photoelectron Spectra of Organosulfur Monolayers on Au(111): S (2p) Spectral Dependence on Molecular Species. *Langmuir* **1999**, *15*, 6799–6806.

[166] Maddanimath, T.; Khollam, Y. B.; Aslam, M.; Mulla, I. S.; Vijayamohanan, K. Self-Assembled Monolayers of Diphenyl Disulphide: a Novel Cathode Material for Rechargeable Lithium Batteries. *Journal of Power Sources* **2003**, *124*, 133–142.

[167] Guo, J.; Wang, Q.; Jin, J.; Chen, C.; Wen, Z. Analysis of Structure and Electrochemistry of Selenium-Containing Conductive Polymer Materials for Rechargeable Lithium Batteries. *Journal of The Electrochemical Society* **2016**, *163*, A654–A659.

[168] Bahl, M. K.; Watson, R. L.; Irgolic, K. J. X-Ray Photoemission Studies of Tellurium and Some of its Compounds. *The Journal of Chemical Physics* **1977**, *66*, 5526–5535.

[169] Wheeler, L. M.; Anderson, N. C.; Palomaki, P. K. B.; Blackburn, J. L.; Johnson, J. C.; Neale, N. R. Silyl Radical Abstraction in the Functionalization of Plasma-Synthesized Silicon Nanocrystals. *Chemistry of Materials* **2015**, *27*, 6869–6878.

[170] Dénès, F.; Pichowicz, M.; Povie, G.; Renaud, P. Thiyl Radicals in Organic Synthesis. *Chemical Reviews* **2014**, *114*, 2587–2693.

[171] McDonough, J. E.; Weir, J. J.; Sukcharoenphon, K.; Hoff, C. D.; Kryatova, O. P.; Rybak-Akimova, E. V.; Scott, B. L.; Kubas, G. J.; Mendiratta, A.; Cummins, C. C. Comparison of Thermodynamic and Kinetic Aspects of Oxidative Addition of PhE-EPh (E = S, Se, Te) to $Mo(CO)_3(PR_3)_2$, $W(CO)_3(PR_3)_2$, and $Mo(N[^tBu]Ar)_3$ Complexes. The Role of Oxidation State and Ancillary Ligands in Metal Complex Induced Chalcogenyl Radical Generation. *Journal of the American Chemical Society* **2006**, *128*, 10295–10303.

[172] Subramanian, H.; Moorthy, R.; Sibi, M. P. Thiyl Radicals: From Simple Radical Additions to Asymmetric Catalysis. *Angewandte Chemie International Edition* **2014**, *53*, 13660–13662.

[173] Renaud, P. In *Organoselenium Chemistry*; Wirth, D. T., Ed.; Topics in Current Chemistry 208; Springer Berlin Heidelberg, 2000; pp 81–112.

[174] Oae, S.; Doi, J. T. *Organic Sulfur Chemistry: Structure and Mechanism*; CRC Press Boca Raton, FL, 1991; Vol. 1.

[175] Walter, M. G.; Warren, E. L.; McKone, J. R.; Boettcher, S. W.; Mi, Q.; Santori, E. A.; Lewis, N. S. Solar Water Splitting Cells. *Chemical Reviews* **2010**, *110*, 6446–6473.

[176] Zhang, Z.; Yates, J. T. Band Bending in Semiconductors: Chemical and Physical Consequences at Surfaces and Interfaces. *Chemical Reviews* **2012**, *112*, 5520–5551.

[177] Hu, S.; Richter, M. H.; Lichterman, M. F.; Beardslee, J.; Mayer, T.; Brunschwig, B. S.; Lewis, N. S. Electrical, Photoelectrochemical, and Photoelectron Spectroscopic Investigation of the Interfacial Transport and Energetics of Amorphous TiO_2/Si Heterojunctions. *The Journal of Physical Chemistry C* **2016**, *120*, 3117–3129.

[178] Yaffe, O.; Pujari, S.; Sinai, O.; Vilan, A.; Zuilhof, H.; Kahn, A.; Kronik, L.; Cohen, H.; Cahen, D. Effect of Doping Density on the Charge Rearrangement and Interface Dipole at the Molecule–Silicon Interface. *The Journal of Physical Chemistry C* **2013**, *117*, 22422–22427.

[179] Urrabazo, D.; Overzet, L. J. The Effects of the Fermi Level on Ion Induced Electron Emission from Chemically and Sputter Cleaned Semiconductors. *Journal of Physics D: Applied Physics* **2015**, *48*, 345203.

[180] Vilan, A.; Cahen, D. Chemical Modification of Semiconductor Surfaces for Molecular Electronics. *Chemical Reviews* **2017**, *117*, 4624–4666.

[181] Rakshit, T.; Liang, G.-C.; Ghosh, A. W.; Datta, S. Silicon-based Molecular Electronics. *Nano Letters* **2004**, *4*, 1803–1807.

[182] Maldonado, S.; Plass, K. E.; Knapp, D.; Lewis, N. S. Electrical Properties of Junctions between Hg and Si(111) Surfaces Functionalized with Short-Chain Alkyls. *The Journal of Physical Chemistry C* **2007**, *111*, 17690–17699.

[183] Takeuchi, N.; Kanai, Y.; Selloni, A. Surface Reaction of Alkynes and Alkenes with H-Si (111): A Density Functional Theory Study. *Journal of the American Chemical Society* **2004**, *126*, 15890–15896.

[184] Arefi, H. H.; Nolan, M.; Fagas, G. Binary Functionalization of H:Si(111) Surfaces by Alkyl Monolayers with Different Linker Atoms Enhances Monolayer Stability and Packing. *Physical Chemistry Chemical Physics* **2016**, *18*, 12952–12963.

[185] Sze, S. *Physics of Semiconductor Devices, 2nd Ed*; John wiley & sons, 1981.

[186] Hunger, R.; Fritsche, R.; Jaeckel, B.; Jaegermann, W.; Webb, L. J.; Lewis, N. S. Chemical and Electronic Characterization of Methyl-Terminated Si(111) Surfaces by High-Resolution Synchrotron Photoelectron Spectroscopy. *Physical Review B* **2005**, *72*, 045317.

[187] Chu, J. Y. C.; Lewicki, J. W. Thermal Decomposition of Bis(diphenylmethyl) Diselenide. *The Journal of Organic Chemistry* **1977**, *42*, 2491–2493.

[188] Chaudhury, M. K.; Whitesides, G. M. Correlation Between Surface Free Energy and Surface

Constitution. *Science* **1992**, *255*, 1230–1232.

[189] Bain, C. D.; Whitesides, G. M. Molecular-Level Control over Surface Order in Self-Assembled Monolayer Films of Thiols on Gold. *Science* **1988**, *240*, 62–63.

[190] Biebuyck, H. A.; Bain, C. D.; Whitesides, G. M. Comparison of Organic Monolayers on Polycrystalline Gold Spontaneously Assembled from Solutions Containing Dialkyl Disulfides or Alkanethiols. *Langmuir* **1994**, *10*, 1825–1831.

[191] Bain, C. D.; Evall, J.; Whitesides, G. M. Formation of Monolayers by the Coadsorption of Thiols on Gold: Variation in the Head Group, Tail group, and Solvent. *Journal of the American Chemical Society* **1989**, *111*, 7155–7164.

[192] Liu, Y.; Shen, L. From Langmuir Kinetics to First- and Second-Order Rate Equations for Adsorption. *Langmuir* **2008**, *24*, 11625–11630.

[193] Escorihuela, J.; Zuilhof, H. Rapid Surface Functionalization of Hydrogen-Terminated Silicon by Alkyl Silanols. *Journal of the American Chemical Society* **2017**, *139*, 5870–5876.

[194] Sieval, A. B.; Opitz, R.; Maas, H. P. A.; Schoeman, M. G.; Meijer, G.; Vergeldt, F. J.; Zuilhof, H.; Sudhölter, E. J. R. Monolayers of 1-Alkynes on the H-Terminated Si(100) Surface. *Langmuir* **2000**, *16*, 10359–10368.

[195] Lenfant, S.; Guerin, D.; Tran Van, F.; Chevrot, C.; Palacin, S.; Bourgoin, J.-P.; Bouloussa, O.; Rondelez, F.; Vuillaume, D. Electron Transport through Rectifying Self-Assembled Monolayer Diodes on Silicon: Fermi-Level Pinning at the Molecule–Metal Interface. *The Journal of Physical Chemistry B* **2006**, *110*, 13947–13958.

[196] Srivastava, P.; Chapman, W. G.; Laibinis, P. E. Odd–Even Variations in the Wettability of *n*-Alkanethiolate Monolayers on Gold by Water and Hexadecane: A Molecular Dynamics Simulation Study. *Langmuir* **2005**, *21*, 12171–12178.

[197] Ulman, A. Self-Assembled Monolayers of Alkyltrichiorosilanes: Building Blocks for Future Organic Materials. *Advanced Materials* **1990**, *2*, 573–582.

[198] Sabatani, E.; Cohen-Boulakia, J.; Bruening, M.; Rubinstein, I. Thioaromatic Monolayers on Gold: A New Family of Self-Assembling Monolayers. *Langmuir* **1993**, *9*, 2974–2981.

[199] Fadeev, A. Y.; McCarthy, T. J. Trialkylsilane Monolayers Covalently Attached to Silicon Surfaces: Wettability Studies Indicating that Molecular Topography Contributes to Contact Angle Hysteresis. *Langmuir* **1999**, *15*, 3759–3766.

[200] Li, S. L.; Truhlar, D. G. Full-Dimensional Ground- and Excited-State Potential Energy Surfaces and State Couplings for Photodissociation of Thioanisole. *The Journal of Chemical Physics* **2017**, *146*, 064301.

[201] Schweig, A.; Thon, N. Measurement of Relative Conformational Stabilities by Variable Temperature Photoelectron Spectroscopy. A Study of Rotational Isomerism in Thioanisole. *Chemical Physics Letters* **1976**, *38*, 482–485.

[202] Leroux, Y. R.; Fei, H.; Noël, J.-M.; Roux, C.; Hapiot, P. Efficient Covalent Modification of a Carbon Surface: Use of a Silyl Protecting Group To Form an Active Monolayer. *Journal of the American Chemical Society* **2010**, *132*, 14039–14041.

[203] Bandoli, G.; Clemente, D. A.; Tondello, E.; Dondoni, A. Crystal, Molecular, and Electronic Structure of 4-Dimethylaminophenyl Phenyl Sulphide. *Journal of the Chemical Society, Perkin*

Transactions 2 **1974**, *0*, 157–160.

[204] Hamed, E. A.; El-Bardan, A. A.; Saad, E. F.; Gohar, G. A.; Hassan, G. M. Nucleophilic Substitutions at the Pyridine ring. Conformational Preference of the Products and Kinetics of the Reactions of 2-Chloro-3-nitro- and 2-Chloro-5-nitro-pyridines with Arenethiolates. *Journal of the Chemical Society, Perkin Transactions 2* **1997**, *0*, 2415–2422.

[205] Van Der Heijden, S. P.; Chandler, W. D.; Robertson, B. E. Conformations of Bridged Diphenyls. IX. Crystal Structure of 2-(4'-Carbomethoxy-2'-nitrothiophenyl)-1,3,5-trimethylbenzene. *Canadian Journal of Chemistry* **1975**, *53*, 2102–2107.

[206] Bzhezovskii, V. M.; Kapustin, E. G. Steric and Electronic Structure of Selenoanisole: A Quantum-Chemical Study. *Russian Journal of General Chemistry* **2003**, *73*, 54–60.

[207] Fujihara, H.; Mima, H.; Ikemori, M.; Furukawa, N. New Hypervalent σ-Selenanes with a Transannular Se–N Bond from *N*-Methyl-5*H*,7*H*-dibenzo[*b*,*g*][1,5]Selenazocine. *Journal of the American Chemical Society* **1991**, *113*, 6337–6338.

[208] Frisell, H.; Engman, L. Molecular Modelling of Some Para-Substituted Aryl Methyl Telluride and Diaryl Telluride Antioxidants. *Journal of Molecular Structure* **2000**, *526*, 103–114.

[209] Herman, A.; Godlewska, S.; Ponikiewski, Ł.; Kruczyński, T.; Dołęga, A. Propeller-Like Chirality of Methyl-Tris(2,6-diisopropylphenoxy) Silylsulfide. *Silicon* **2016**, *8*, 105–110.

[210] Marynowski, W.; Klucznik, T.; Baranowska, K.; Dołęga, A.; Wojnowski, W. Tri(mesityloxy)silanethiol–The First Structurally Characterized Organoxysilanethiol (Contributions to the Chemistry of Silicon–Sulfur Compounds.). *Zeitschrift für anorganische und allgemeine Chemie* **2010**, *636*, 685–687.

[211] Harada, Y.; Koitaya, T.; Mukai, K.; Yoshimoto, S.; Yoshinobu, J. Spectroscopic Characterization and Transport Properties of Aromatic Monolayers Covalently Attached to Si(111) Surfaces. *The Journal of Physical Chemistry C* **2013**, *117*, 7497–7505.

[212] Plymale, N. T.; Kim, Y.-G.; Soriaga, M. P.; Brunschwig, B. S.; Lewis, N. S. Synthesis, Characterization, and Reactivity of Ethynyl- and Propynyl-Terminated Si(111) Surfaces. *The Journal of Physical Chemistry C* **2015**, *119*, 19847–19862.

[213] Yuan, S.-L.; Cai, Z.-T.; Jiang, Y.-S. Molecular Simulation Study of Alkyl Monolayers on the Si(111) Surface. *New Journal of Chemistry* **2003**, *27*, 626–633.

[214] Laibinis, P. E.; Bain, C. D.; Whitesides, G. M. Attenuation of Photoelectrons in Monolayers of *n*-Alkanethiols Adsorbed on Copper, Silver, and Gold. *The Journal of Physical Chemistry* **1991**, *95*, 7017–7021.

[215] Hu, M.; Hauger, T. C.; Olsen, B. C.; Luber, E. J.; Buriak, J. M. UV-Initiated Si–S, Si–Se, and Si–Te Bond Formation on Si (111): Coverage, Mechanism, and Electronics. *The Journal of Physical Chemistry C* **2018**, *122*, 13803–13814.

[216] Sieval, A. B.; Vleeming, V.; Zuilhof, H.; Sudhölter, E. J. R. An Improved Method for the Preparation of Organic Monolayers of 1-Alkenes on Hydrogen-Terminated Silicon Surfaces. *Langmuir* **1999**, *15*, 8288–8291.

[217] McDonough, J. E.; Weir, J. J.; Carlson, M. J.; Hoff, C. D.; Kryatova, O. P.; Rybak-Akimova, E. V.; Clough, C. R.; Cummins, C. C. Solution Calorimetric and Stopped-Flow Kinetic Studies of the Reaction of $\bullet Cr(CO)_3C_5Me_5$ with PhSe–SePh and PhTe–TePh. Experimental and Theoretical Estimates of the Se–Se, Te–Te, H–Se, and H–Te Bond Strengths. *Inorganic Chemistry* **2005**, *44*,

3127–3136.

[218] Terry, J.; Mo, R.; Wigren, C.; Cao, R.; Mount, G.; Pianetta, P.; Linford, M. R.; Chidsey, C. E. D. Reactivity of the H–Si (111) Surface. *Nuclear Instruments and Methods in Physics Research Section B: Beam Interactions with Materials and Atoms* **1997**, *133*, 94–101.

[219] Giesbrecht, P. K.; Bruce, J. P.; Freund, M. S. Electric and Photoelectric Properties of 3,4–Ethylenedioxythiophene-Functionalized n-Si/PEDOT:PSS Junctions. *ChemSusChem* **2016**, *9*, 109–117.

[220] Garner, L. E.; Steirer, K. X.; Young, J. L.; Anderson, N. C.; Miller, E. M.; Tinkham, J. S.; Deutsch, T. G.; Sellinger, A.; Turner, J. A.; Neale, N. R. Covalent Surface Modification of Gallium Arsenide Photocathodes for Water Splitting in Highly Acidic Electrolyte. *ChemSusChem* **2017**, *10*, 767–773.

[221] MacLeod, B. A.; Steirer, K. X.; Young, J. L.; Koldemir, U.; Sellinger, A.; Turner, J. A.; Deutsch, T. G.; Olson, D. C. Phosphonic Acid Modification of $GaInP_2$ Photocathodes Toward Unbiased Photoelectrochemical Water Splitting. *ACS Applied Materials & Interfaces* **2015**, *7*, 11346–11350.

[222] Rangan, S.; Batarseh, A.; Chitre, K. P.; Kopecky, A.; Galoppini, E.; Bartynski, R. A. Tuning Energy Level Alignment At Organic/Semiconductor Interfaces Using a Built-In Dipole in Chromophore–Bridge–Anchor Compounds. *The Journal of Physical Chemistry C* **2014**, *118*, 12923–12928.

[223] Li, Y.; O'Leary, L. E.; Lewis, N. S.; Galli, G. Combined Theoretical and Experimental Study of Band-Edge Control of Si through Surface Functionalization. *The Journal of Physical Chemistry C* **2013**, *117*, 5188–5194.

[224] Böcking, T.; Kilian, K. A.; Gaus, K.; Gooding, J. J. Modifying Porous Silicon with Self-Assembled Monolayers for Biomedical Applications: The Influence of Surface Coverage on Stability and Biomolecule Coupling. *Advanced Functional Materials* **2008**, *18*, 3827–3833.

[225] Woods, M.; Carlsson, S.; Hong, Q.; Patole, S.; Lie, L.; Houlton, A.; Horrocks, B. A Kinetic Model of the Formation of Organic Monolayers on Hydrogen-Terminated Silicon by Hydrosilation of Alkenes. *The Journal of Physical Chemistry B* **2005**, *109*, 24035–24045.

[226] Nemanick, E. J.; Solares, S. D.; Goddard, W. A.; Lewis, N. S. Quantum Mechanics Calculations of the Thermodynamically Controlled Coverage and Structure of Alkyl Monolayers on Si (111) Surfaces. *The Journal of Physical Chemistry B* **2006**, *110*, 14842–14848.

[227] Bansal, A.; Li, X.; Lauermann, I.; Lewis, N. S.; Yi, S. I.; Weinberg, W. Alkylation of Si Surfaces Using a Two-Step Halogenation/Grignard Route. *Journal of the American Chemical Society* **1996**, *118*, 7225–7226.

[228] Solares, S. D.; Yu, H.; Webb, L. J.; Lewis, N. S.; Heath, J. R.; Goddard, W. A. Chlorination-Methylation of the Hydrogen-Terminated Silicon (111) Surface Can Induce a Stacking Fault in the Presence of Etch Pits. *Journal of the American Chemical Society* **2006**, *128*, 3850–3851.

[229] Yu, H.; Webb, L. J.; Heath, J. R.; Lewis, N. S. Scanning Tunneling Spectroscopy of Methyl-and Ethyl-Terminated Si (111) Surfaces. *Applied Physics Letters* **2006**, *88*, 252111.

[230] Hurley, P. T.; Nemanick, E. J.; Brunschwig, B. S.; Lewis, N. S. Covalent Attachment of Acetylene and Methylacetylene Functionality to Si (111) Surfaces: Scaffolds for Organic Surface Functionalization while Retaining Si–C Passivation of Si (111) Surface Sites. *Journal of the American Chemical Society* **2006**, *128*, 9990–9991.

[231] Rohde, R. D.; Agnew, H. D.; Yeo, W.-S.; Bailey, R. C.; Heath, J. R. A Non-Oxidative Approach toward Chemically and Electrochemically Functionalizing Si (111). *Journal of the American Chemical Society* **2006**, *128*, 9518–9525.

[232] Pujari, S. P.; Filippov, A. D.; Gangarapu, S.; Zuilhof, H. High-Density Modification of H-Terminated Si (111) Surfaces Using Short-Chain Alkynes. *Langmuir* **2017**, *33*, 14599–14607.

[233] Allongue, P.; de Villeneuve, C. H.; Cherouvrier, G.; Cortes, R.; Bernard, M.-C. Phenyl Layers on H–Si (111) by Electrochemical Reduction of Diazonium Salts: Monolayer versus Multilayer Formation. *Journal of Electroanalytical Chemistry* **2003**, *550*, 161–174.

[234] Stewart, M.; Robins, E.; Geders, T.; Allen, M.; Cheul Choi, H.; Buriak, J. Three Methods for Stabilization and Functionalization of Porous Silicon Surfaces via Hydrosilylation and Electrografting Reactions. *Physica Status Solidi A* **2000**, *182*, 109–115.

[235] Liu, Y.; Yamazaki, S.; Yamabe, S.; Nakato, Y. A Mild and Efficient Si (111) Surface Modification via Hydrosilylation of Activated Alkynes. *Journal of Materials Chemistry* **2005**, *15*, 4906–4913.

[236] Tanuma, S.; Powell, C. J.; Penn, D. R. Calculations of Electron Inelastic Mean Free Paths. V. Data for 14 Organic Compounds over the 50–2000 eV Range. *Surface and interface analysis* **1994**, *21*, 165–176.

[237] King, L. A.; Hellstern, T. R.; Park, J.; Sinclair, R.; Jaramillo, T. F. Highly Stable Molybdenum Disulfide Protected Silicon Photocathodes for Photoelectrochemical Water Splitting. *ACS Applied Materials & Interfaces* **2017**, *9*, 36792–36798.

[238] Seitz, L. C.; Chen, Z.; Forman, A. J.; Pinaud, B. A.; Benck, J. D.; Jaramillo, T. F. Modeling Practical Performance Limits of Photoelectrochemical Water Splitting Based on the Current State of Materials Research. *ChemSusChem* **2014**, *7*, 1372–1385.

[239] Liu, C.; Gallagher, J. J.; Sakimoto, K. K.; Nichols, E. M.; Chang, C. J.; Chang, M. C.; Yang, P. Nanowire–Bacteria Hybrids for Unassisted Solar Carbon Dioxide Fixation to Value-Added Chemicals. *Nano Letters* **2015**, *15*, 3634–3639.

[240] Sakimoto, K. K.; Wong, A. B.; Yang, P. Self-Photosensitization of Nonphotosynthetic Bacteria for Solar-to-Chemical Production. *Science* **2016**, *351*, 74–77.

[241] Ho, J. C.; Yerushalmi, R.; Jacobson, Z. A.; Fan, Z.; Alley, R. L.; Javey, A. Controlled Nanoscale Doping of Semiconductors via Molecular Monolayers. *Nature Materials* **2008**, *7*, 62.

[242] van Druenen, M.; Collins, G.; Glynn, C.; O'Dwyer, C.; Holmes, J. D. Functionalization of SiO_2 Surfaces for Si Monolayer Doping with Minimal Carbon Contamination. *ACS Applied Materials & Interfaces* **2018**, *10*, 2191–2201.

[243] Bau, J. A.; Luber, E. J.; Buriak, J. M. Oxygen Evolution Catalyzed by Nickel–Iron Oxide Nanocrystals with a Nonequilibrium Phase. *ACS Applied Materials & Interfaces* **2015**, *7*, 19755–19763.

[244] Serino, A. C.; Anderson, M. E.; Saleh, L. M.; Dziedzic, R. M.; Mills, H.; Heidenreich, L. K.; Spokoyny, A. M.; Weiss, P. S. Work Function Control of Germanium through Carborane-Carboxylic Acid Surface Passivation. *ACS Applied Materials & Interfaces* **2017**, *9*, 34592–34596.

[245] Kingston, R. Review of Germanium Surface Phenomena. *Journal of Applied Physics* **1956**, *27*, 101–114.

[246] Schmeisser, D.; Schnell, R.; Bogen, A.; Himpsel, F.; Rieger, D.; Landgren, G.; Morar, J. Surface Oxidation States of Germanium. *Surface Science* **1986**, *172*, 455–465.

[247] Bodlaki, D.; Yamamoto, H.; Waldeck, D.; Borguet, E. Ambient Stability of Chemically Passivated Germanium Interfaces. *Surface Science* **2003**, *543*, 63–74.

[248] Yuan, F.-W.; Yang, H.-J.; Tuan, H.-Y. Alkanethiol-Passivated Ge Nanowires as High-Performance Anode Materials for Lithium-Ion Batteries: the Role of Chemical Surface Functionalization. *ACS Nano* **2012**, *6*, 9932–9942.

[249] Choi, K.; Buriak, J. M. Hydrogermylation of Alkenes and Alkynes on Hydride-Terminated Ge (100) Surfaces. *Langmuir* **2000**, *16*, 7737–7741.

[250] Kerr, A. T.; Placencia, D.; Gay, M. E.; Boercker, J. E.; Soto, D.; Davis, M. H.; Banek, N. A.; Foos, E. E. Sulfur-Capped Germanium Nanocrystals: Facile Inorganic Ligand Exchange. *The Journal of Physical Chemistry C* **2017**, *121*, 22597–22606.

[251] Wong, K. T.; Chopra, S. N.; Bent, S. F. Dissociative Adsorption of Dimethyl Sulfoxide at the Ge (100)-2×1 Surface. *The Journal of Physical Chemistry C* **2012**, *116*, 26422–26430.